QUANTUM MODELING OF HYBRID SYSTEMS FOR MOLECULAR MEMORIES

Adrian Calborean

École Doctorale Chimie et Sciences du Vivant

THESE

Pour obtenir le grade de

DOCTEUR DE L'UNIVERSITE JOSEPH FOURIER

Discipline : CHIMIE PHYSIQUE

Présentée par

Adrian CALBOREAN

MODELISATION PAR LA CHIMIE QUANTIQUE DES SYSTEMES HYBRIDES POUR DES MEMOIRES MOLECULAIRE

Thése soutenue le 27 octobre 2009

Composition du jury

Prof. Carlo ADAMO	*Ecole Normale Supérieure Chimie Paris*	Rapporteur
Dr. Dominique VUILLAUME	*CNRS – IEMN*	Rapporteur
Prof. Anne MILET	*Université Joseph Fourier*	Examinateur
Prof. Vasile CHIS	*Babes-Bolyai University*	Examinateur
Dr. Pascale MALDIVI	*CEA Grenoble*	Directeur de thèse
Dr. Philippe BLAISE	*CEA Grenoble*	Co-directeur de thèse

Service de Chimie Inorganique et Biologique
Institut Nanosciences et Cryogénie, CEA Grenoble, France

École Doctorale Chimie et Sciences du Vivant

THESIS

For obtaining the degree of

DOCTOR OF THE JOSEPH FOURIER UNIVERSITY

Specialty: PHYSICAL CHEMISTRY

Presented by

Adrian CALBOREAN

QUANTUM MODELING OF HYBRID SYSTEMS FOR MOLECULAR MEMORIES

Thesis defended on 28 April 2009

Composition of jury

Prof. Carlo ADAMO	*Ecole Normale Supérieure Chimie Paris*	Rapporteur
Dr. Dominique VUILLAUME	*CNRS – IEMN*	Rapporteur
Prof. Anne MILET	*Université Joseph Fourier*	Examinator
Prof. Vasile CHIS	*Babes-Bolyai University*	Examinator
Dr. Pascale MALDIVI	*CEA Grenoble*	Thesis director
Dr. Philippe BLAISE	*CEA Grenoble*	Thesis co-director

Service de Chimie Inorganique et Biologique
Institut Nanosciences et Cryogénie, CEA Grenoble, France

Résumé

Ce travail a été réalisé dans le cadre général du développement de nouveaux composants mémoires utilisant le stockage de charges grâce à des molécules rédox. Une collaboration combinant recherche fondamentale, dans notre laboratoire, et recherche appliquée avec des équipes du CEA/LETI a conduit à la conception de systèmes hybrides constitués d'une monocouche de molécules rédox greffées sur la surface de silicium, les différents états de charge des molécules servant à stocker l'information. Notre but était de comprendre les paramètres (molécule, lien) gouvernant les transferts de charge et les propriétés électriques de tels systèmes. L'objectif principal de la thèse a donc été de modéliser les propriétés électroniques de molécules rédox et des systèmes résultants de leur greffage sur Si, à l'aide de méthodes basées sur la Théorie de la Fonctionnelle de la Densité. Un premier volet a été consacré à l'étude de processus rédox dans des porphyrine métallées intéressantes pour leur bistabilité. Un deuxième volet rassemble toutes les études sur les systèmes de molécules rédox greffées sur Si. En raison de leur nature hybride, deux approches ont été utilisées. La première, basée sur une description moléculaire où la surface de Si est modélisée par un aggrégat, conduit à des données importantes telles que le gap HOMO-LUMO, la localisation des charges ou les propriétés structurales. La deuxième basée sur des calculs de système périodique où la surface de Si est infinie, donne accès aux densités d'états. Ces données ont été ensuite comparées aux calculs moléculaires et discutées en liaison avec les propriétés électriques déterminées sur des composants tests.

Mots-clés

mémoires moléculaire, molécules rédox, porphyrine métallées, bistabilité, ferrocene, systèmes hybrides, Théorie de la Fonctionnelle de la Densité, système périodique.

Discipline

Chimie physique moléculaire et structurale

Laboratoire

Laboratoire de Reconnaissance Ionique et Chimie de Coordination
Service de Chimie Inorganique et Biologique, UMR-E3 CEA-UJF
Institut Nanosciences et Cryogénie, CEA Grenoble
17 Rue des Martyrs, 38054 Grenoble Cedex, France

Abstract

The general context of this work is the development of new electronic devices that utilize charge storage properties of redox-active molecules for memory applications. A collaborative approach involving both fundamental research in our laboratory and applied research teams from the CEA/LETI has lead to the design of hybrid systems for molecular memories. Monolayers of redox-active molecules are formed on the semiconductor Si surface and the stable charged states of the molecules are utilized to store information. Our purpose was to understand the main parameters (molecule, linker) which govern the charge transfer between semiconducting Si surface and redox molecules and the electrical behaviour of such systems.

The main objective of this thesis has thus been to develop Density Functional Theory approaches to describe the electronic properties of redox-active molecules and hybrid systems for the purpose of information storage. The first axis was dedicated to the modeling of redox processes of molecules such as metalloporphyrins with bistability properties. The second part was devoted to the study of redox-active molecules grafted on Si surface. Due to the hybrid nature of the latter systems, two approaches were developed. One was based on a molecular description, using Si aggregates in place of a Si surface, yielding a molecular orbital description of some relevant features: Homo-Lumo gaps, charge localization or structural properties. The other approach was focused on periodical calculations, with molecules grafted on 'infinite' Si surface. The resulting DOS were compared to molecular results, and discussed in the light of experimental data on electrical properties.

Keywords

molecular memories, redox molecules, metallic porphyrin, bistability, ferrocene, hybrid systems, Density Functional Theory, periodical systems.

Specialty

Molecular and structurale physical chemistry

Laboratory

Laboratoire de Reconnaissance Ionique et Chimie de Coordination
Service de Chimie Inorganique et Biologique, UMR-E3 CEA-UJF
Institut Nanosciences et Cryogénie, CEA Grenoble
17 Rue des Martyrs, 38054 Grenoble Cedex, France

Acknowledgements

First and foremost, I would like to express my sincere appreciation to my advisor, Dr. Pascale Maldivi for her invaluable support, encouragement and guidance for the successful completion of my thesis.

I would also like to thank Dr. Philippe Blaise as thesis co-director, whose help and support during these three years were essential to me. I really appreciated his valuable advices and cordiality.

I would like to express my gratitude to Professor Carlo Adamo, Dr. Dominique Vuillaume Professor Anne Milet and Professor Vasile Chis for accepting to judge the quality of my work.

Particular thanks are addressed to Tiziana Pro, Julien Buckley, Florence Duclairoir and Lionel Dubois which brought a fundamental contribution to this work and have been patience and perseverance to discuss and work day after day.

I would like to acknowledge to Valentina Vetere, my office colleague, for her help and disponibility during the preparation of the thesis manuscript and the public defense. Also for the pleasant atmosphere that was in our office.

I would also like to thank Zohra Termache, the secretary the most effective I have encountered, for his availability and assistance.

Many thanks to former and present collaborators at the RICC Laboratory for their practical help, friendly support and encouragement during these years. Last but not least, I would like to thank my family and friends for their long-lasting patience and support.

The European Community through the Marie Curie CHEMtronics programme (MEST-CT-2005-020513) is deeply acknowledged for financial support.

Résumé étendu en français

En raison de l'augmentation constante de la densité des dispositifs à base de silicium, des limites physiques (effets quantiques et comportement non déterministe des faibles courants) et technologiques (comme la dissipation de la puissance, la complexité du design et l'effet tunnel des courants) peuvent intervenir et bloquer les possibilités de futur progrès de la microélectronique. Pour ces raisons, il est admis que la loi de Moore n'est plus valable ou que les lois d'échelle du CMOS sont désormais obsolètes.

L'électronique moléculaire a pour ambition de remplacer les technologies actuelles par des systèmes comportant une ou plusieurs molécules qui peuvent être utilisées comme interrupteurs, connections ou comme dispositifs logiques ou comme mémoires. L'approche aussi dit « bottom-up » consiste à créer des éléments fonctionnels à partir des plus petits éléments de construction, les molécules, avec l'opportunité supplémentaire d'obtenir un ordre structural à plus large échelle comme pour les transistors.

Les recommandations actuelles pour le développement des mémoires « flash » non-volatiles peuvent être résumées en deux voies distinctes. D'un coté il s'agit de rechercher de nouveaux matériaux et des nouvelles architectures de transistors afin de réduire les dimensions des dispositifs actuels. D'un autre coté, la recherche de nouvelles technologies s'appuie sur une électronique à l'échelle de la molécule ou de l'atome. Ces dernières technologies sont essentiellement fondées sur des mémoires moléculaires, qui peuvent être des dispositifs capacitifs (comme les mémoires Flash ou DRAM) ou des mémoires interrupteurs résistives qui utilisent une architecture dite « crossbar ». Dans ce projet, nous nous sommes intéressés au développement d'un dispositif capacitif hybride moléculaire qui utilise des molécules rédox comme composants actifs de stockage de charge.

Ces dernières années, beaucoup d'efforts ont été focalisés vers de nouveaux dispositifs de mémoires qui utilisent une approche hybride molecule/silicium et qui tiennent compte de l'incorporation de molécules organiques à des semi-conducteurs de Si. Ces types de

développements sont intéressants parce qu'ils donnent la possibilité de dépasser les limitations (augmentations des couts de développement, fiabilité et variabilité) des technologies actuelles.

Dans ce cadre, nous avons décidé d'étudier des monocouches de molécules redox-actives liées a une surfaces de Si. Différents états stables de charge sont donc utilisés pour le stockage de l'information. Afin de mieux comprendre le design des systèmes moléculaires hybrides, le processus de l'opération écriture/effacement des mémoires flash est décrit figure.1.

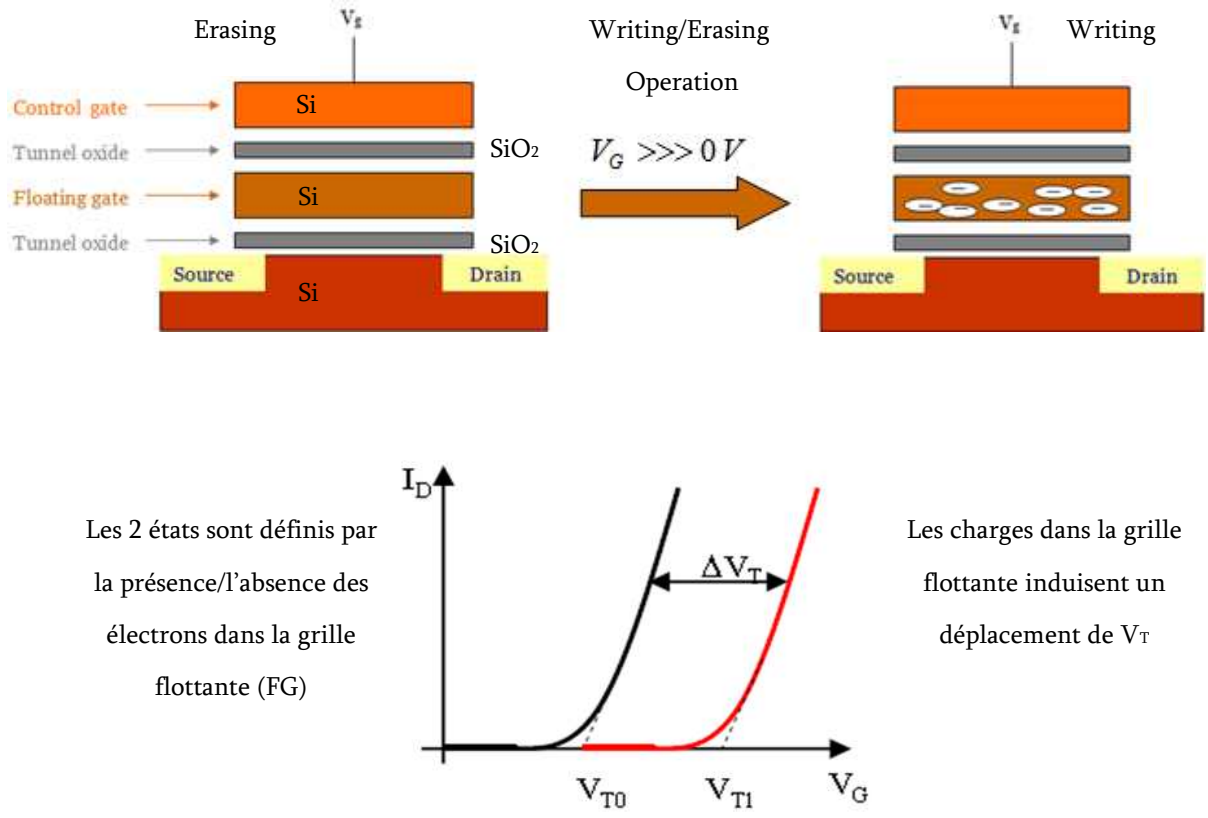

Figure 1. Schéma d'écriture/effacement des mémoires FLASH

Le dispositif de mémoire à grille flottante (figure.1) stocke les informations en gardant la charge électrique dans la grille flottante. Si on ajoute ou on éloigne une charge de la grille flottante, on obtient une variation du voltage V_T entre une limite inférieure et une limite

supérieure. Les 2 cas correspondent à deux états, 0 ou 1, et ils définissent si la cellule mémoire a été programmée ou effacée.

Nos systèmes de mémoires hybrides ont été inspirés par ces dispositifs et sont représentés en figure 2. Pour ce système, la couche redox-active joue le rôle de grille flottante. En appliquant un voltage qui correspond à un processus redox de la molécule, on devrait pouvoir transférer des électrons entre la molécule et le fil de Si. En général, une couche moléculaire permettant le stockage est constituée par un groupement rédox actif et un lien immobilisant de façon covalente la molécule à une surface semiconductrice.

Dans notre projet, nous avons choisi des molécules redox qui peuvent exhiber un ou plusieurs états redox distincts, comme le ferrocene, les porphyrines et les polyoxometallates (voir figure 2 pour des exemples).

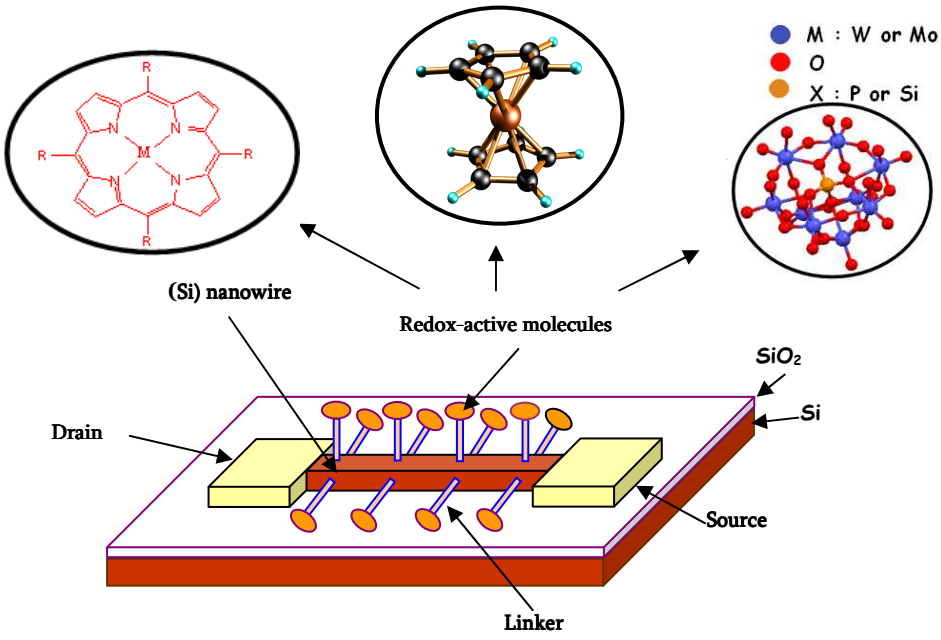

Figure 2. Représentation schématique de mémoires moléculaires hybrides/Si.

L'objectif général du projet CEA (INAC et Leti) sur les mémoires moléculaires est donc la compréhension (expérimentale et théorique) des mécanismes qui régulent l'échange d'électrons entre le semi-conducteur Si et la molécule redox.

Dans ce contexte, une étude théorique du transfert électronique des systèmes hybrides a été réalisée. Mon travail de thèse s'est développé autour de deux axes :

1) La première partie a été dédiée à la modélisation des molécules isolées qui montrent une bistabilité redox, comme les dérivées du ferrocene ou plusieurs porphyrines métalliques. La présence d'une bistabilité redox est une condition nécessaire afin de concevoir des dispositifs capables de stabiliser un état de charge sur un intervalle important de potentiel électrique. Des études préliminaires ont montré que des changements conformationnels pourraient induire ce type de bistabilité.
2) La deuxième partie est dédiée à l'étude de molécules redox greffées sur la surface de Si. L'idée est donc de reproduire et interpréter grâce au méthodes théoriques l'influence de différents paramètres (molécule, métal central, lien covalent) sur les propriétés électriques (localisation de la charge, potentiel redox, caractéristique du dispositif).

Pour les molécules greffés sur la surface de Si (1 0 0), et en raison de la nature hybride des systèmes à décrire, nous avons décidé de comparer deux approches théoriques différentes. D'un coté nous avons utilisé une description moléculaire pour l'ensemble. Dans ce cas la surface de Si a été modélisée comme un agrégat et des méthodes DFT moléculaires nous ont permis de décrire les écarts HOMO-LUMO, la localisation de la charge et les propriétés de liaison chimique. Néanmoins, si cette approche décrit bien la molécule, elle n'est pas très bien adaptée à la description de la surface infinie de Si. Pour cette raison, nous avons développé une étude basée sur la physique de l'état condensé et sur des calculs périodiques. Afin d'éviter des problèmes lié à la description du gap (confinement de surface*)*, nous avons commencé cette étude par la reconstruction de la surface de Si. Ensuite, nous avons développé des simulations de molécules choisies greffées sur la surface infinie. Ces calculs nous ont permis de calculer la densité projetée d'états (PDOS). Enfin, nous avons comparé les résultats obtenus avec les données expérimentales.

Pour résumer, les objectifs principaux de ce travail sont les suivants :

- Modéliser et caractériser des molécules redox qui sont intéressantes pour des applications dans des dispositifs électroniques
- Analyser la stabilité de ces molécules liées (directement ou indirectement) de façon covalent à la surface de Si
- Analyser et décrire les propriétés électroniques des systèmes hybrides molécules/Si
- Analyser l'influence du lien sur le phénomène de transfert de charge
- Proposer une méthode théorique efficace, en termes de ressources informatiques et temps CPU, pour la description de ces systèmes.
- Déterminer des propriétés électriques de matériaux hybrides adaptées aux dispositifs électroniques nano.

Ces objectifs sont donc de deux types, méthodologiques d'un coté, de compréhension chimique des systèmes hybrides de l'autre.

L'objectif à long terme serait d'utiliser les propriétés électroniques calculées pour développer des modèles de transport quantique et pour la simulation des mémoires moléculaires.

Chapitre I

Le premier chapitre décrit l'état de l'art dans le domaine des mémoires moléculaires en s'intéressant surtout aux mémoires de type DRAM et Flash. Plusieurs exemples de systèmes expérimentaux sont montrés. Le rôle important de la bistabilité rédox est également souligné, en se basant sur des exemples de la littérature. Dans ces exemples, nous décrivons les différents matériaux moléculaires utilisés, les procédés d'ancrage de ces systèmes sur le substrat, ainsi que les techniques expérimentales de caractérisation. Ce chapitre permet donc de situer le contexte général du travail de thèse.

Chapitre II

Un rappel des bases des méthodes théoriques standard utilisées dans ce travail est donné dans ce chapitre. Les systèmes moléculaires hybrides que nous avons étudiés pendant la thèse ont nécessité l'utilisation de deux approches théoriques : la Théorie de la Fonctionnelle de la Densité (DFT) et le formalisme de la physique de l'état solide décrivant les systèmes périodiques.

Chapitre III

Modélisation des propriétés moléculaires pour le stockage d'information.

Dans le but de rechercher de nouvelles molécules capables de stockage d'informations et qui utilisent des états de charge, il est nécessaire de se focaliser et étudier les propriétés suivantes :

- Les propriétés redox : états et potentiels redox stables
- Propriétés structurales
- Corrélation entre les propriétés redox et paramètres structuraux (pour la recherche de molécules bistables)

Par conséquent, notre premier objectif était donc d'être capable de reproduire les propriétés moléculaires (comme par exemples les paramètres géométriques, et les comportements énergétiques). En effet, la compréhension du phénomène de bistabilité nécessite une bonne reproduction des propriétés structurales en fonction de paramètres moléculaires comme les groupes fonctionnels, la nature du centre métallique, et l'état redox de la molécule. Cette dernière partie est principalement dédiée à l'étude des porphyrines bridées développées dans notre laboratoire.

Cette partie du travail est organisée en quatre parties. En premier lieu, nous étudions des espèces moléculaires simples qui sont des précurseurs des systèmes hybrides plus complexes. Dans ce cadre nous avons estimé les potentiels redox et les paramètres géométriques de simples porphyrines et des dérivés du ferrocene (figure 3).

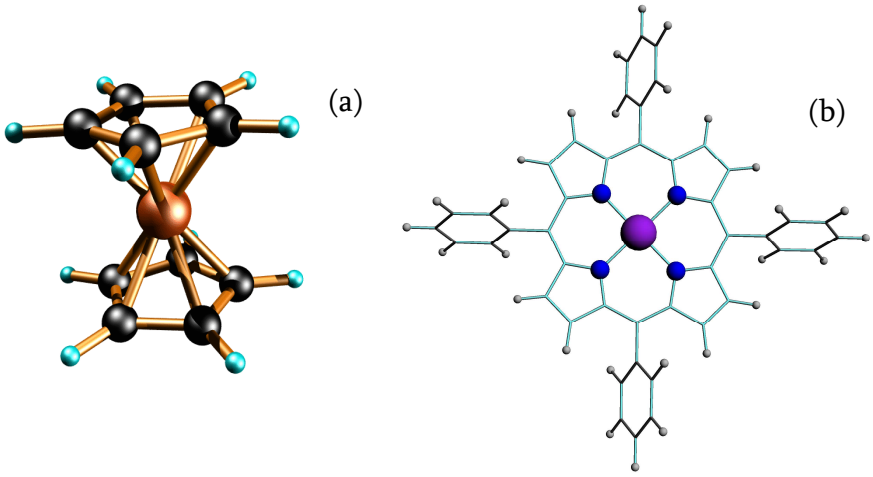

Figure 3. a) Structure du Ferrocene ; b) tetraphenylporphyrine de Zn (ZnTPP)

Ensuite, nous avons porté notre attention sur des porphyrines plus complexes, toujours précurseurs de stockage de charge. Nous avons inclus dans cette étude l'analyse conformationelle de porphyrines meso-substituées en fonction du groupe méso et de la nature du métal (figure 4).

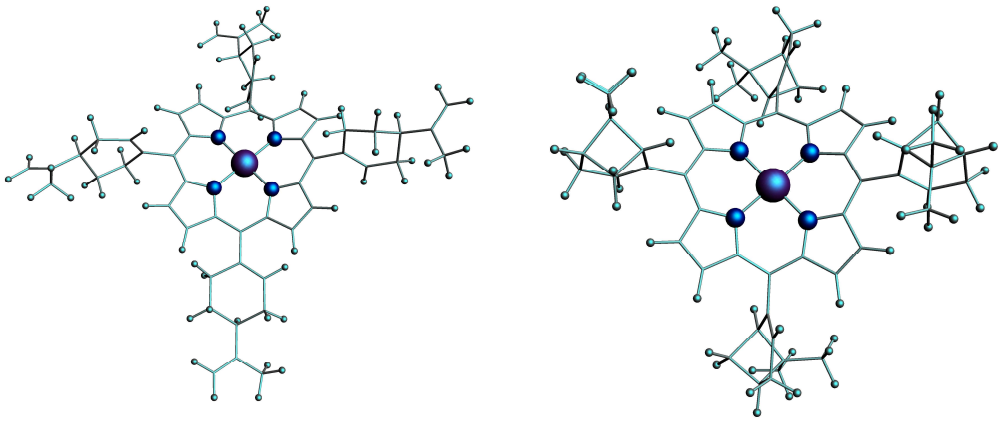

Figure 4. Porphyrine issue du Perilaldehyde (gauche); Porphyrine du Myrtenal (droite).

Enfin, nous nous sommes concentrés sur les propriétés structurales obtenues sur des porphyrines bridées (notées MBCP-8) qui contiennent un métal non redox (fig 5, 6) et précurseurs d'un comportement bistable.

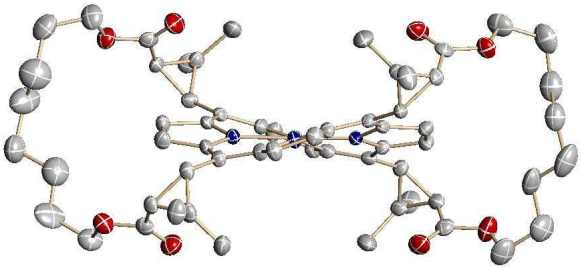

Figure 5. Structure de NiBCP-8

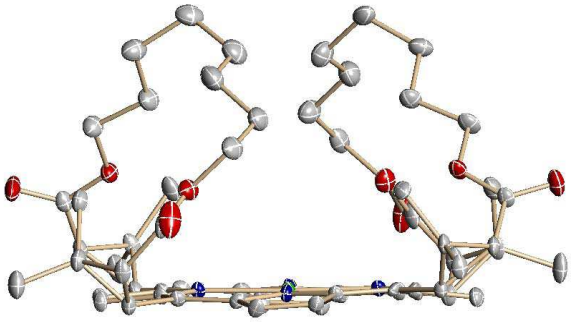

Figure 6. Structure de ZnBCP-8

Enfin, nous décrirons quelques résultats préliminaires obtenus sur les porphyrines de MnII ou III.

Chaque partie de cette étude est basée sur les données expérimentales disponibles et qui seront discuté en parallèle de notre analyse des résultats théoriques. Les calculs ont été réalisés par des méthodes de chimie quantique basées sur la DFT. Nous avons obtenu dans tous les cas un très bon accord avec les données expérimentales, qu'elles soient structurales ou thermodynamiques.

Chapitre IV

Modélisation des systèmes hybrides molécule – Si

Dans notre travail, la structure générique d'un système hybride consiste en un groupe redox actif (la molécule en elle-même), une molécule liante et la surface semi-conductrice.

Afin de décrire et de comprendre le transfert d'électrons correspondant et de le corréler avec les données expérimentales, nous avons besoin d'étudier une des propriétés clef de la structure électronique : l'alignement et la position relative des orbitales frontières de la molécule relativement au gap du substrat silicium. Nous avons ainsi besoin de décrire correctement les facteurs d'origine moléculaire qui influe sur cet alignement, et de les corréler avec les données expérimentales.

La difficulté principale avec de tels systèmes est leur nature hybride, étant construits à partir de molécules qui sont essentiellement des espèces localisées qui interagissent avec un système infini. La méthode que nous choisirons pour décrire le gap de tels systèmes représente une option décisive. Cette difficulté a déjà été identifiée et discutée dans la littérature. Dans notre contexte, nous avons utilisé deux approches théoriques pour comparaison. L'une est basée sur une description moléculaire, en remplaçant la surface par un petit agrégat de silicium, conduisant à une approche en orbitales moléculaires des caractéristiques suivantes : gaps Homo-Lumo, localisation de la charge, propriétés structurelles (figure 7).

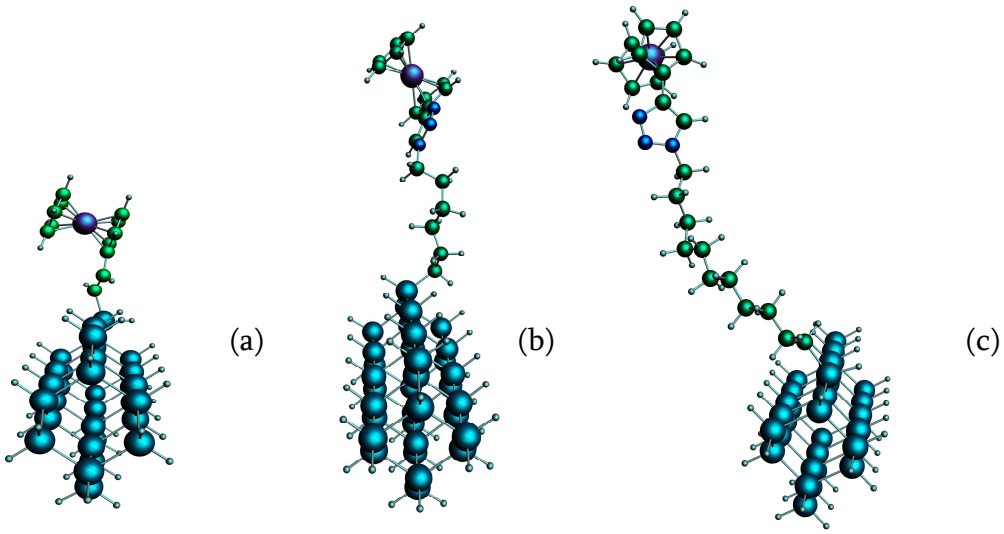

Figure 7. Structure géométrique de : (a) Ferrocene lié directement (b) Fc-N3(CH2)6, (c) Fc-N3(CH2)11 en liaison indirecte.

L'autre approche s'est concentrée sur des calculs de structures périodiques, avec des molécules accrochées sur une surface infinie (Figures 8 et 9). Les densités d'états issues de ces calculs ont été comparées avec les résultats moléculaires, et analysées à la lumière des résultats de mesures électriques.

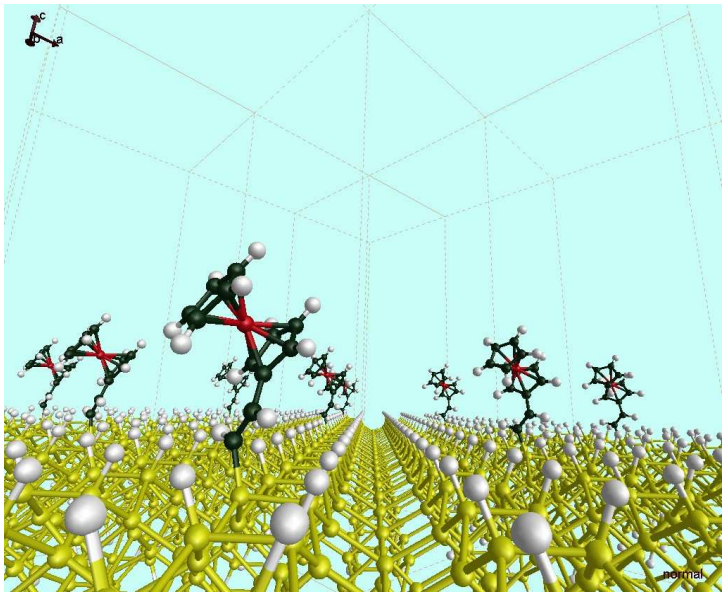

Figure 8. Structure optimisée de Fc en liaison directe sur Si (1 0 0).

L'approche utilisant la DFT moléculaire conduit à une description des niveaux HOMO et LUMO de la molécule et du Si qui permettent parfaitement de comprendre le comportement expérimental en terme de transfer de charge, même si le gap HOMO-LUMO est trop grand. Les calculs périodiques montrent que globalement l'ordre des niveaux moléculaires est le même que dans les calculs DFT standard, et qu'il n'y a aucun couplage avec les états du silicium.

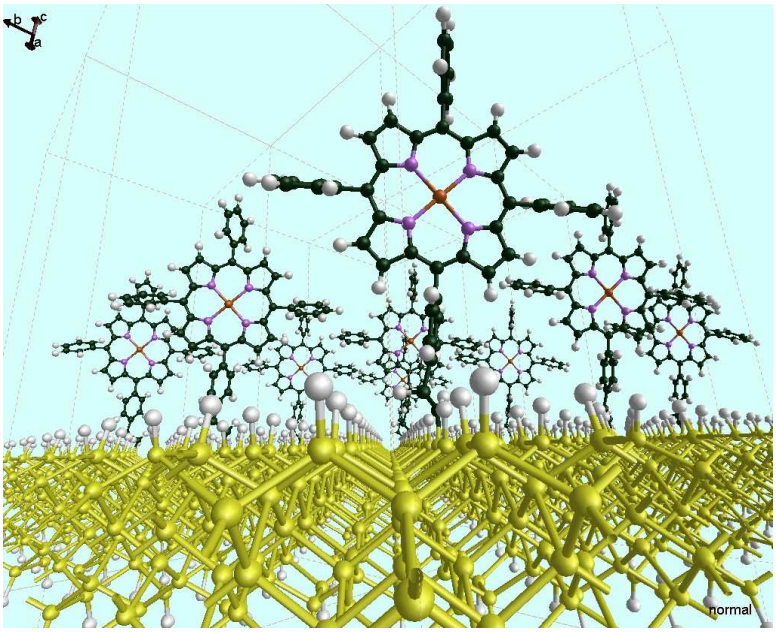

Figure 9. Structure optimisée de ZnTPP en liaison directe sur SI (1 0 0)

Chapitre V

La stabilité et la résistance des molécules organiques envisagées sont cruciales pour transposer cette technologie depuis la recherche jusqu'au développement et à la production. Les ferrocènes et les porphyrines sont des molécules d'une grande stabilité à température ambiante dans des conditions standard. Cependant, lorsqu'ils sont immobilisés sur une surface de Si, ce qui est important est la stabilité et le comportement

du système entier, qui consiste en la molécule rédox, le lien covalent, et la solution d'électrolyte. Pour cela, nous avons réalisé des calculs de dynamique moléculaire quantique à partir du ferrocène greffé, à l'état neutre et oxydé.

Les deux systèmes présentent une stabilité thermique à température ambiante à une échelle de temps court. Bien que préliminaires, ces résultats montrent en particulier que la molécule ne se dépose pas sur la surface de silicium. Des atomes d'hydrogène semblent réagir en premier, et nous attendons qu'une augmentation de température entraine une désorption de l'hydrogène de la surface, comme cela est bien connu en microélectronique, pour des températures entre 600 et 1300K. Ces calculs sont très lourds et ces premiers résultats devraient donc être poursuivis avec des systèmes avec les espaceurs plus longs ainsi que avec les porphyrines.

Résultats Principaux et conclusions

Dans la première partie, sur les propriétés moléculaires des dérivés de ferrocène et de métallo-porphyrines, nous avons montré que les calculs en DFT standard des potentiels redox sont en bon accord avec les mesures expérimentales à condition de tenir compte correctement du solvant (via la méthode PCM), et bien que nous négligions certains paramètres thermodynamiques comme l'énergie de point zéro (ZPE) et les variations d'entropie. Nous avons reproduit également de façon remarquable l'ensemble des propriétés structurales de complexes de Zn et Ni à partir de porphyrines bridées, y compris dans différents solvants. Pour autant, les porphyrines à base de manganèse (II) nécessitent de pousser plus loin notre étude, car la description correcte de leur structure électronique reste un défi pour la DFT, sachant que grâce à l'approche ab initio de type CAS nous devrions être capable de résoudre ce point.

La deuxième partie, dédiée à la description des molécules greffées sur une surface de silicium, a donc été réalisée en deux volets. La première méthode utilisée décrit la surface de silicium comme un petit agrégat : cela donne des niveaux moléculaires localisés et

précis et permet de traiter un environnement tel que le solvant. La contrepartie est un gap du silicium faux, avec une énergie trop élevée pour le niveau Lumo (bas de la bande de conduction du silicium). Néanmoins, l'augmentation de la taille du cluster permet de décroitre le gap en faisant baisser le niveau Lumo. A vrai dire, les niveaux Homo et de la bande de valence du silicium sont très proches de ceux obtenus avec un calcul périodique. Nous avons aussi obtenus en calculs moléculaires, de bons potentiels redox (comparés aux mesures expérimentales). Nous avons observé également une forte localisation de la charge sur les molécules greffées. De plus nous avons pu quantifier certaines différences dans l'alignement des gaps (molécule et surface de Si) en fonction du type de greffage (direct ou indirect), qui sont bien corrélées aux données expérimentales de voltammétrie cyclique. Par exemple, les résultats d'alignements des niveaux moléculaires et du gap du Si sont représentés pour le ferrocène figure 10.

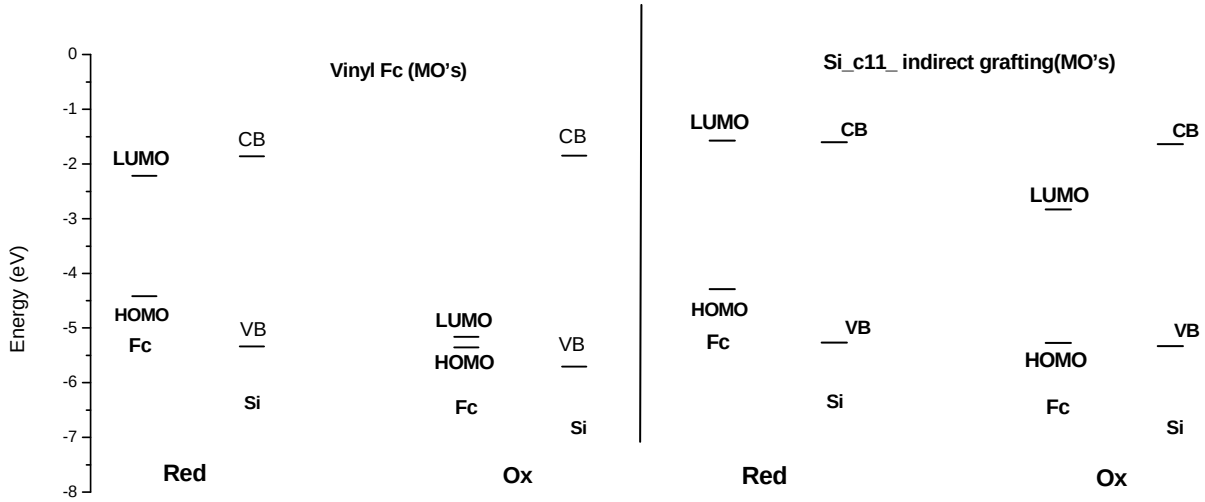

Figure 10. Comparison de l'alignement des niveaux HOMO-LUMO et gap Si. Gauche: lien direct; droite: lien indirect (C11).

La figure 10 (gauche) montre que les gaps HOMO-VB pour l'espèce réduite et LUMO-VB de l'espèce oxydée sont très proches en énergie. Cela est cohérent avec des valeurs similaires de potentiel d'oxydation et de réduction ($V_{ox} \approx V_{red}$). Ceci est en accord avec la

voltammétrie cyclique spécialement à faible vitesse de balayage où la vitesse de transfert électronique n'est pas limité par la vitesse de balayage en potentiel.

Pour le greffage indirect, avec Fc-$N_3(CH_2)_6$ et Fc-$N_3(CH_2)_{11}$, le transfert électronique n'est pas réversible au même potentiel et |Vox|>|Vred|. Ceci corrobore les voltammétries cycliques où on observe un écart plus important entre les potentiels d'oxydation et de réduction. Ainsi, ces modèles semblent bien reproduire les données expérimentales et permettent de mettre en évidence des corrélations entre les calculs moléculaires, et l'électrochimie ainsi que les mesures de capacitance. Des résultats analogues ont été trouvés pour les porphyrines de Zn greffées par un lien direct ou indirect.

La seconde méthode, par des calculs périodiques, est a priori moins précise dans la description des niveaux moléculaires et n'est pas capable d'évaluer les potentiels redox, mais elle permet d'obtenir une meilleure description de l'alignement des niveaux d'énergie. Sur la figure 11 est représenté un exemple de PDOS calculé sur une espèce Fc greffée de façon directe.

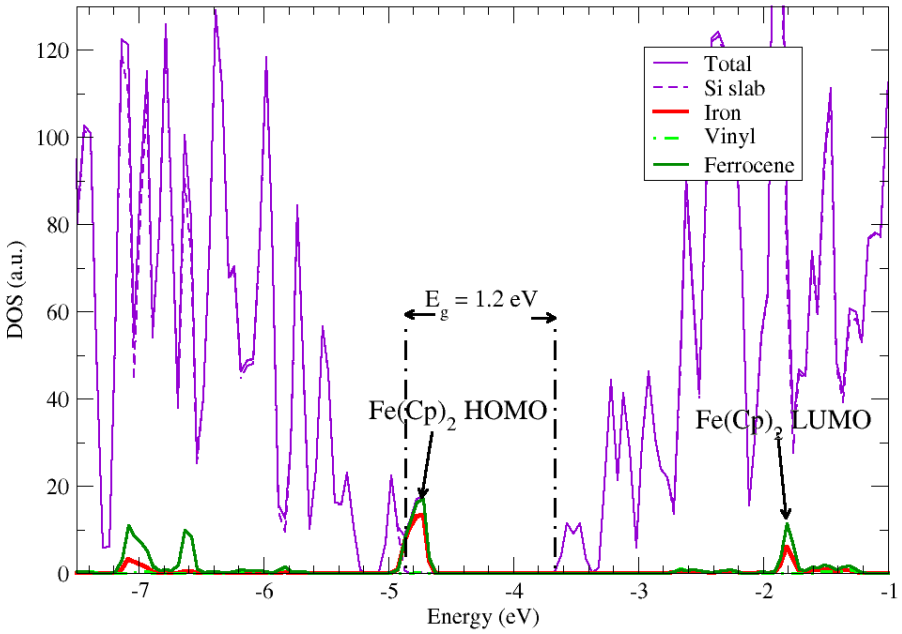

Figure 11. PDOS de Fc greffé directement.

Nous retrouvons un alignement des gaps proche de ce qui était obtenu en calculs moléculaires. Ainsi cela permet de calibrer les calculs moléculaires et d'identifier les problèmes dus à la mauvaise description du gap. Dans notre cas, les deux méthodes (moléculaire et périodique) donnent les mêmes résultats concernant les différentes énergies mises en jeu dans le transfert d'électron dû aux processus d'oxydation et de réduction. Cela est principalement dû au fait que nous n'avons pas besoin de prendre en compte la bande de conduction, dont la position est pourtant clairement incorrecte en description moléculaire. En effet, dans les expériences, le Si est dopé p, donc tous les transferts électroniques ont lieu avec la bande de valence (VB). Aussi, un autre effet sous-jacent, qui a certainement joué en notre faveur est que les différents groupes de niveaux d'énergie (molécule, lien covalent, Si) ne sont pas en interaction mutuelle ou en tous cas pas directement couplés. Ainsi, nous pouvons décrire le système total comme une superposition de deux sous-systèmes, la molécule et la surface de silicium, faiblement couplés. En réalité, un dipôle électrostatique d'interface d'origine moléculaire a pu être identifié.

Finalement, connaissant les avantages et inconvénients de chaque méthode, les conclusions de cette partie nous permettront de définir à l'avenir des simulations plus efficaces de tels systèmes hybrides. Ainsi d'autres systèmes hybrides pourront être étudiés par exemple en impliquant d'autres types de transferts de charge. Et pour aller plus loin, les propriétés de transports pourraient être évaluées en partant de nos résultats de calculs ab initio qui serviraient de données d'entrée pour des calculs de transport quantique.

Table of contents

Introduction

1.1. Overview of Hybrid electronics

The beginning of molecular electronics is generally believed to have occurred in 1974 when Aviram and Ratner [1] have proposed a model that was probably the first comprehensive theoretical example of unimolecular quantum transport. In particular, they have been inspired by the first studies on charge and energy transfer in molecules of Robert Mulliken and Albert Szent-Gyorgyi in the 1940's, on the so-called donor-acceptor systems [2]. Charge transfer was made tangible by the proposal of Aviram and Ratner to use a Mulliken-like electron donor-acceptor molecule, separated by a sigma-bonded tunnelling bridge. They theoretically calculated and demonstrated that the current-voltage characteristics of such a system behaved like a rectifying diode similar to a semiconductor p-n junction [1]. Their work was pioneering thanks to their first considerations of using single molecules as the active elements in hybrid electronic structures.

Nowadays, molecular electronics is envisioned as a promising candidate for the nanoelectronics of the future. More than a possible answer to the ultimate miniaturization problem in nanoelectronics, molecular electronics is foreseen as a possible and reasonable way to assemble a large numbers of nanoscale objects (molecules, nanoparticles, nanotubes and nanowires) to form new devices and circuit architectures.

1.1.1. CMOS scaling: Challenges and Strategies

According to Intel co-founder Gordon Moore, the number of transistors per square centimeter of silicon doubles every 18 to 24 months [3]. This performance increase has been obtained mainly by decreasing the size of circuit dimensions obtained by optimization and improvement of existing technology. If plotted on a logarithmic scale (figure 0.1), the decrease in size of micro-electronic components versus the year gives a straight line. In few decades to come, the dimensions of the components should approach the size of about one nanometer.

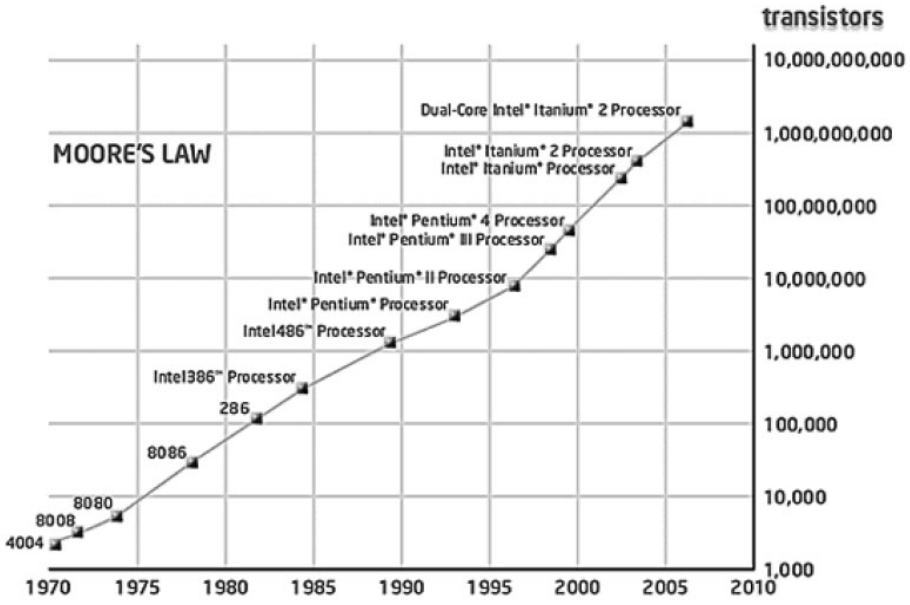

Figure 0.1. Plot of transistor densities against dates of introduction [4].

The curve shows counts doubling every two years.

With the continuous increase in the density of silicon-based devices, the process scaling in semiconductor technology will soon reach physical and technical limits. Other concerns, such as gate oxide thickness, power consumption, and fabrication costs, also highlight the difficulty of scaling standard electronics materials to molecular dimensions [5].

In this context, there is thus a revival of efforts to build devices with molecular-scale components. At device areas of a few tens of square nanometers, molecules have an inherent attractiveness because: 1) of their size; 2) they represent the ultimate goal in terms of atomic control over physical properties; 3) of various properties that can be achieved through such control.

In this light, the semiconductor industry through the Semiconductor Industry Association (SIA) proposed a Microelectronics Roadmap on the future of CMOS (Complementary Metal Oxide Semiconductor) technology. They provided data predominantly on the scaling of dynamic random access memory (DRAM), microprocessing units (MPU) and applications specific integrated circuits (ASICs) manufacture. The major research and development inside the main semiconductor manufacturers is in line with the SIA roadmap predictions [6]. The roadmap predicts a steady reduction in the feature size (figure 0.2) combined with a steady rise in density (figure 0.3) until the year 2012.

The minimum feature size is fast approaching 10 nm in the next decade with switching charges containing 1000 or less electrons. There are still a number of technological challenges required to be solved if CMOS is to reach the 19 nm and 10^{10} transistors per cm^2 in 2012 [6-9].

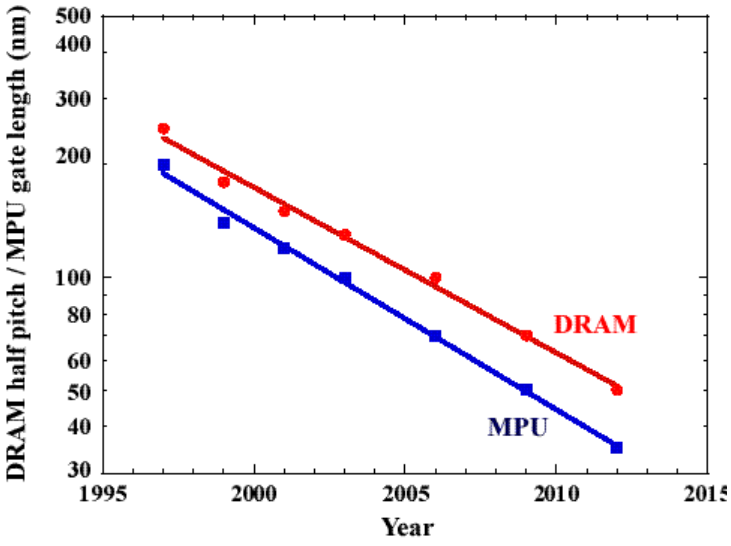

Figure 0.2. The minimum feature size plotted against year from the 1997 SIA Roadmap

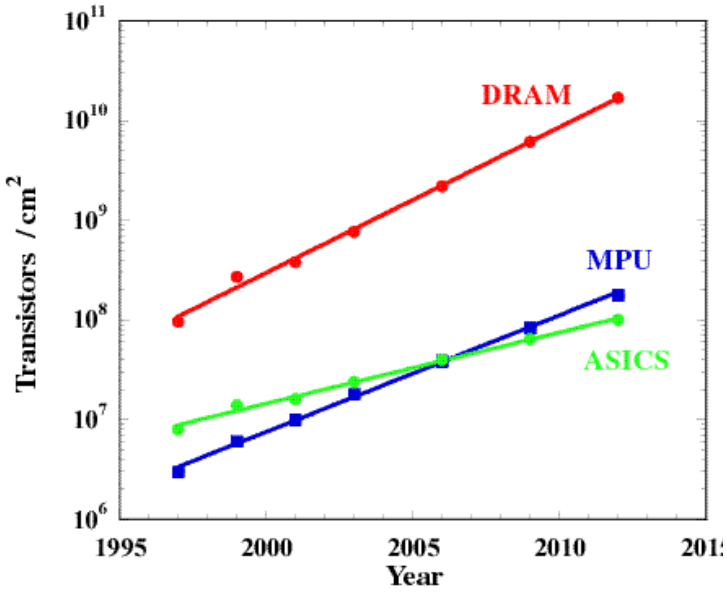

Figure 0.3. Number of transistors per cm^2 plotted against the year of first manufacture (green - application-specific integrated circuit ASICs, blue – microprocessor unit MPU, red - dynamic random access memory DRAM)

Physical limits (quantum effects and non-deterministic behaviour of small currents) and technological limits (such as power dissipation, design complexity and tunnelling currents) may hinder the further progress of microelectronics on the basis of conventional circuit scaling. They are frequently cited as the reason Moore's Law is "broken", or why CMOS scaling is coming to an end.

At this moment the industrial and academic communities are searching for solutions to meet these challenges with: (1) non-classical CMOS to extend the life of CMOS technology and (2) fundamentally new technologies which rely on electronics at the level of individual atoms and molecules.

Several emerging technology vectors based on nanomaterials and nanostructures have been well identified by the International Technology Roadmap for Semiconductors (ITRS) [10]. Figure I.4 shows the ITRS emerging technology sequence for various technology vectors listing the different technologies in the order of their risk factors. We then describe below the emerging routes toward memory devices.

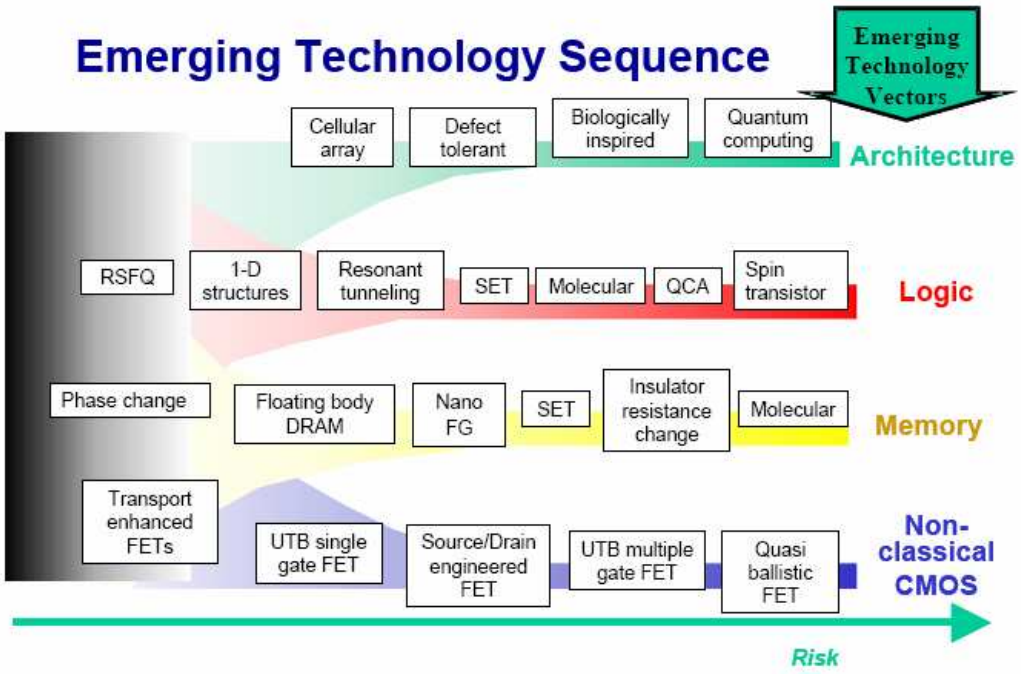

Figure 0.4 ITRS emerging technology sequence

There are six emerging research memory areas beyond traditional RAM and FLASH devices, that include phase change memory, floating body DRAM, nano floating gate memory, single electron memory, insulator resistance change memory, and molecular memory, which are also positively reviewed in [11 -13]:

- Phase Change Memory (PCM) [14], is a type of non-volatile computer memory that uses the unique behaviour of chalcogenide glass, which can be "switched" between two states, crystalline and amorphous, with the application of heat. Recent versions can achieve two additional distinct states, effectively doubling its storage capacity. PCM can offer much higher performance in applications where writing quickly is important, both because the memory element can be switched more quickly, and also because single bits may be changed to either 1 or 0 without needing to first erase an entire block of cells.
- Floating body DRAM and nano-floating gate memory are the other technologies which may come into the memory market in the next few years. The former is a one-transistor (1T) DRAM architecture, which stores data by charging the floating

body of the transistor, thereby enabling very high density [15-18]. The latter is a slight modification of conventional floating gate memory used in FLASH memory, where data is now stored in nanocrystals instead of a continuous film [19]. This can significantly improve the endurance and retention of the memory cells.

- A single electron tunnelling (SET) transistor device is a three terminal device based on the Coulomb blockade. It consists of two tunnel junctions sharing one common electrode with a low self-capacitance, known as the island. The electrical potential of the island can be tuned by a third electrode (the gate), capacitively coupled to the island [20]. Although the current varies periodically with gate voltage, in contrast to the threshold behaviour of the field-effect transistor a SET could still form a compact and efficient memory device.
- Another approach to memory that is still in its early research stage is the Insulator Resistance Change Memory [21], where a metal-insulator-metal structure is used. The change in (higher and lower) resistance states of the insulator occur under applied voltages. Owing to their very long retention time, these compounds are interesting candidates for non-volatile memory applications. The main challenge in this technology is in the development of new materials and integration.
- Molecular memory is a term for data storage technologies that use molecular species as the data storage element, rather than circuits, magnetics, inorganic materials or physical shapes [22].

Although these new technologies that can be considered alternative to CMOS may not involve bulk Si, it would still be preferable for them to be compatible with CMOS, which has been the pole of the electronics industry for more than 30 years.

1.1.2. Molecular electronics technology for further electronic applications

Molecular electronics [23] seeks to replace current electronics technology by implementing one or a few molecules to function as switches, connections, and other

logic or memory devices [24-29]. Molecules are self -assembled into devices, thus creating conductive and strong interconnects.

In the conventional "top-down" approach used by microelectronics industry, silicon nanostructures are patterned in bulk materials by a combination of lithography, etching and deposition to form functional devices [30]. The "bottom-up" approach [31], on the other hand, implies the construction of functionality, electron storage, using small building units such as molecules, with the opportunity to have the molecules further self – assembled into the higher ordered structural units such as transistors. Self–assembly [32, 33] is a thermodynamically favourable process, where entities interact to form some organized aggregate structure. This approach could lead to enormous advances in future manufacturing for electronics [34].

Until now, miniaturization in electronics has been achieved by the top-down approach thanks to the improvement of the lithographic step. However, the current trend is not further sustainable using this strategy. Technological and economical limitations related to the growing difficulties in fabricating smaller and smaller devices complete this picture. Gaining the nanometer scale and/or further enhancing computational capabilities requires a turning point, a change in architecture and the development of conceptually new devices to overcome the physical and technological limitations of the top-down approach.

In the following, we will focus on the emerging routes toward molecular memories, and in particular on the non-volatile memories.

1.1.3. Emerging Molecular Memories

In order to meet technology scaling in the field of solid-state memory and data storage, the mainstream transistor-based flash technologies will start evolving to incorporate material and structural innovations. In figure 0.5 are shown schematically the directions for the future developments of the non-volatile flash memories. Starting from the current technology, are proposed two distinct ways.

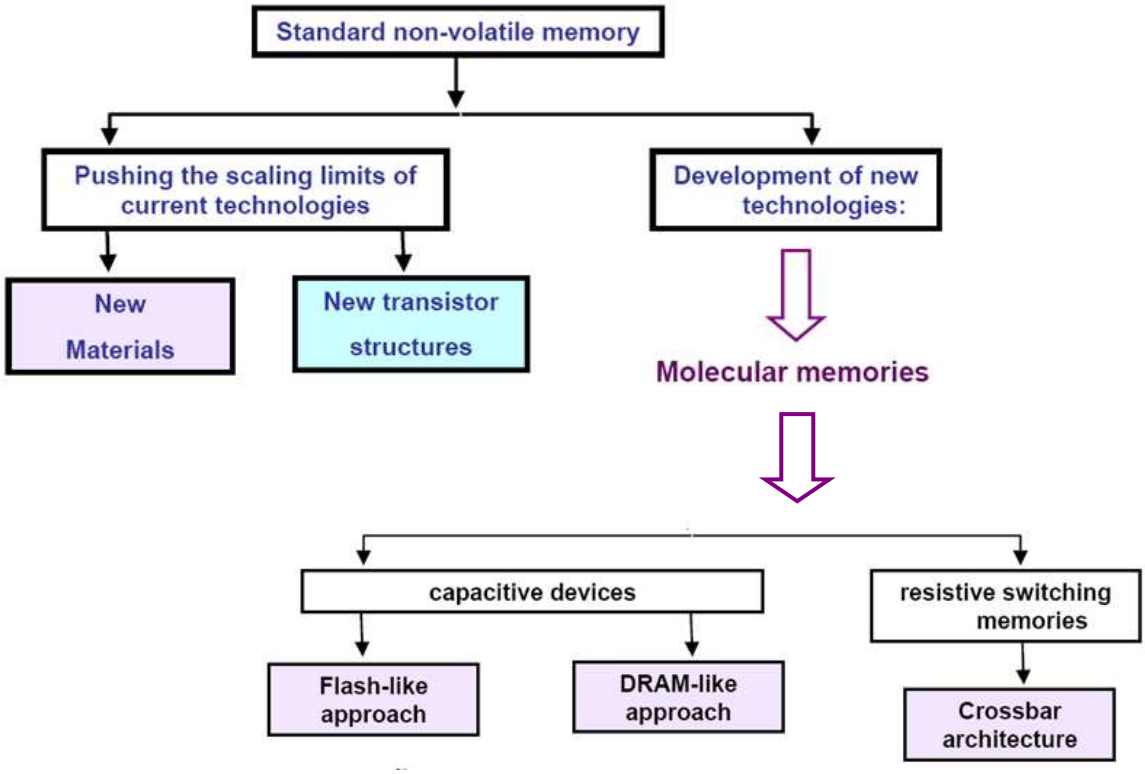

Figure 0.5 Emerging routes for non-volatile memories

The first one is pushing the scaling limits by developing new materials and new transistor structures, while the latter one is based on the development of new technologies, which rely on electronics at the level of individual atoms and molecules. These technologies are essentially based on molecular memories, that could be capacitive devices including Flash or DRAM –like approach or resistive switching memories using crossbar architectures. In this project, we are concentrating on developing hybrid molecular "capacitive devices" containing redox –molecules as the active component for charge-storage medium.

Hybrid silicon/molecular approach refer to the incorporation of organic molecules on the semiconductor Si platform to create a new class of memory devices. It has been the subject of a growing interest in the recent years as they offer possible options to overcome the current limitations (increasing processing costs, reliability, and variability) of standard silicon technology [35-40]. Some of the key advantages of this technology are listed below:

1. Easy integration with existing fabrication process - the number of additional steps involved in incorporating organic molecules on a silicon platform may be minimal. The size of molecules is between 1 and 100 nm, a scale that permits functional nanostructures with accompanying advantages in cost, efficiency, and power dissipation.

2. Assembly and recognition - molecular monolayers can be easily self-assembled on a variety of different substrates, including silicon, dielectrics and metal, by functionalizing them with appropriate linkers [41, 42]. Molecular recognition can be used to modify electronic behaviour, providing both switching and sensing capabilities on the single-molecule scale.

3. Synthetic tailorability of molecules – organic molecules with up to 8 multiple stable redox states have been already synthesized [43], and can provide multiple bits in a single memory cell. The latter possibility represents a significant advantage of molecular devices over conventional semiconductor and other memory technologies. Furthermore, the write/erase voltages and retention times can be tailored by varying for example the tethers attached to the end of the molecules or the spacers between the molecules and surface. By choice of composition and geometry, one can extensively vary transport, binding, optical, and structural properties of the molecules.

4. Dynamical behaviour: many molecules have multiple distinct stable geometric/ electronic structures, thus molecular switches between two stable structures can be obtained.

5. Discrete energy levels – the discrete nature of the MOs are preserved in a monolayer of molecules, resulting in discrete electronic states. Hence, the amount of charge stored will only depend on the number of molecules and not on the applied voltage.

6. Engineering the substrate and surface – the write/erase voltages and retention times can also be tuned. This can also lead to novel functionalities [44].

The main challenges in this field are:

1. Stability of molecules – organic molecules need to be stable at elevated temperatures of at least 400^0C in order to be able to integrate with the existing CMOS technology. The porphyrin molecules have shown thermal stability behaviour even after being exposed to

450^{0}C [45], so there are reasons to believe that this challenge can be overcome. The stability of linkers that covalently bond molecules to substrates and the role of contaminants, are some other stability issues that need to be addressed.

2. Reliability and endurance under electrical stress – this is an unknown quantity in this field. Reported data have not yet established direct links between device behaviour and molecular properties. Until now, just the group of Bocian from University of California has demonstrated the molecular stability of the porphyrin molecules after millions of writing/erasing cycles [45].

3. Contact engineering – although there have been demonstrations of metal evaporation directly on molecules, it is still unclear whether the inherent molecular properties are retained after metal deposition.

4. Characterization techniques – there is need to identify efficient techniques or develop new techniques to characterize hybrid silicon-molecular devices.

Moreover, for the next memory device to be considered as a silver bullet solution it is necessary to possess the following attributes: 1) fast access time, 2) non-volatility, 3) infinite read/write cycles, 4) low power, and 5) a wide operating temperature range.

From a manufacturing perspective, additional attributes are also required such as 6) scalability, 7) low cost, 8) manufacturability, 9) variability (of nanodevice feature size), and 10) integration ability with the Si platform.

In order to overcome all the challenges and to benefit of all the advantages that this field offers, it is essential to study, characterize and understand the physics of these devices.

1.2. Molecular Memories Project

1.2.1. General framework

Considering the aims and challenges above mentioned, one strategy has been developed in the last ten years to design electronic devices based on charge storage of redox-active molecules for memory applications [46, 47].

One such approach is developed in our project, where monolayers of redox-active molecules are formed on the semiconductor Si surface and the multiple stable charged states of the molecules are used to store information.

In order to better understand the design of such hybrid molecular devices, we show firstly on figure 0.6 the principle of writing/erasing operation in flash memories.

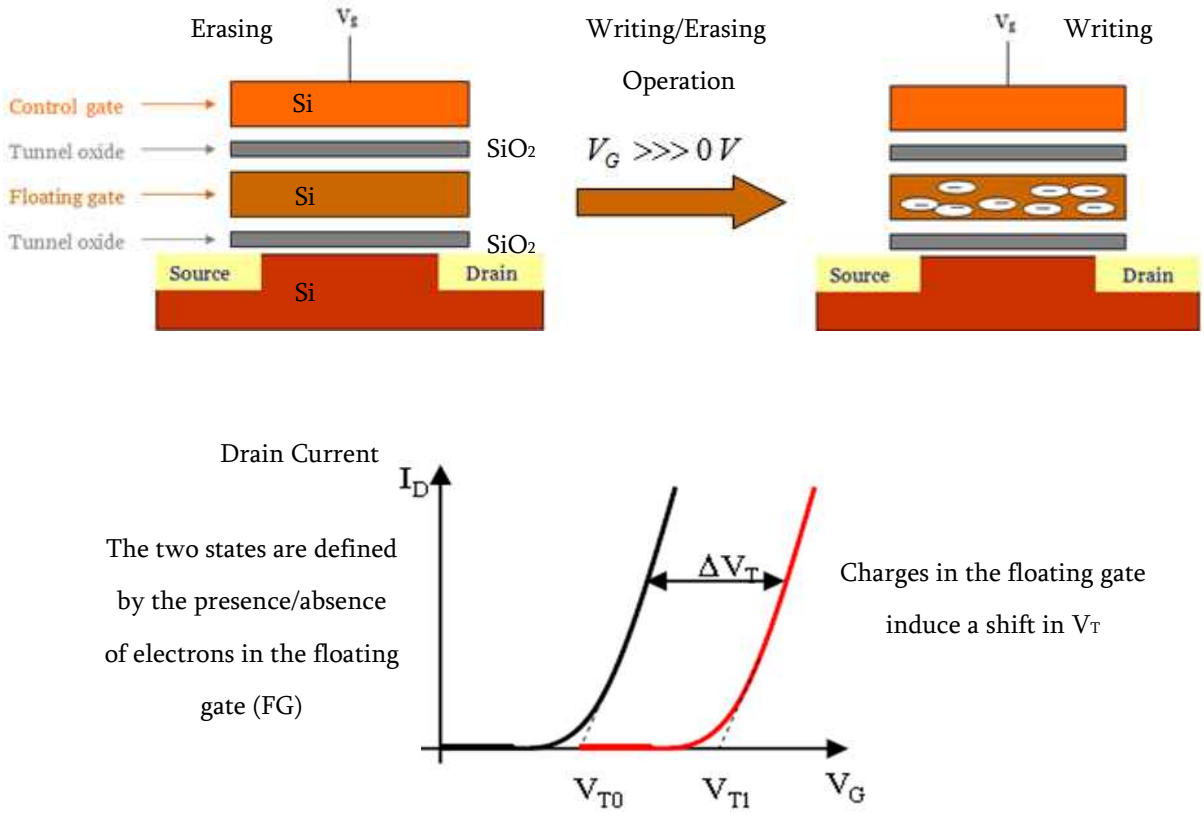

Figure 0.6. Writing/Erasing Scheme of FLASH memory

The floating gate memory device *(*figure 0.6, top*)* stores information by holding electrical charge within the floating gate. Adding or removing charge from the floating gate, changes the threshold voltage V_T of the cell between a low and a high value to represent logic 0 and 1, respectively (figure 0.6, bottom), thereby defining whether the memory cell is in a programmed or erased state. Inspired from this design, molecular hybrid systems currently under investigation are represented on figure 0.7. In such a hybrid device, the redox-active monolayer plays the role of the floating gate. Application of a voltage corresponding to a redox process of the molecule should cause the redox-active monolayer

to transfer electrons between the molecule and the Si nanowire. Typically, a redox-active compound consists of a charge storage group, a tether that may or may not be an insulating barrier, and a linker for covalent attachment to different electroactive surfaces. In our project, molecules have been chosen because they can exhibit one or several redox processes at distinct voltages such as ferrocene, porphyrins and polyoxometalates (POMs).

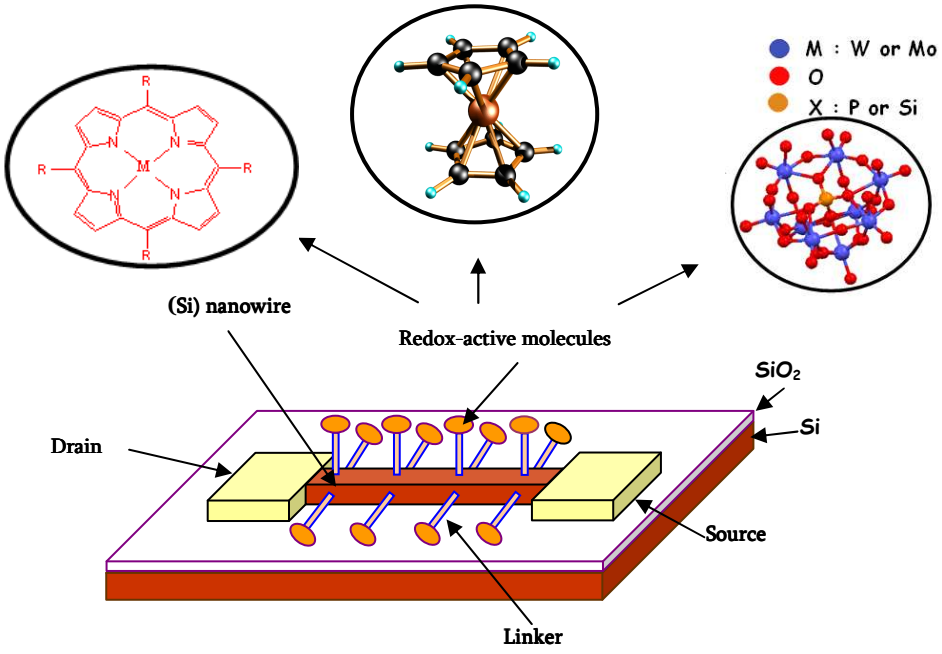

Figure 0.7 Schematic representation of the molecular hybrid Si memory

In order to study such systems, a strong knowledge of the molecules involved for the information storage, and on the resulting hybrid molecules/silicon structures *(*figure 3*)* are required. The general objective of the whole molecular memories project lead at the CEA (INAC and LETI) is thus to understand (experimentally and theoretically) the main mechanisms which govern the exchanges of electrons between semiconductor Si surface and redox molecules in such systems.

To achieve this, the whole project contains several steps: 1) the study of redox-molecules (ferrocene, porphyrins, or polyoxometallates POMs), 2) surface functionalization and electrochemical analysis of hybrid structures; 3) electrical measurements and device

fabrication. This work implies collaborations between laboratories with different expertises. Two experimentalist teams are involved: 1) team of the CEA/SCIB/ Reconnaissance Ionique et Chimie de Coordination which is focused on the investigations of new molecules (porphyrins, polyoxometallates) and on the development of grafting techniques and electrochemical analysis; 2) two applied research laboratories of CEA/LETI which are focused on the surface functionalization, electrical measurements and the design of new devices.

1.2.2. Theoretical approach and objectives

Apart from the experimental investigation of the molecules and hybrid devices, a theoretical description of the electronic transfers in hybrid systems was needed. The main objective of the present thesis work has been to develop such theoretical approaches using quantum chemistry. Two other major roles that quantum chemistry would play in molecular device area: 1) quantum chemistry tools are the natural simulation tools to investigate and to screen molecules and 2) other simulation approaches are unable to correctly take into account molecular levels and geometries, so quantum chemistry will furnish the right parameters to more global and sophisticated analytical models needed for molecular electronics – they don't exist yet.

The present manuscript describes these approaches, and in this context, my thesis work has been organised along two main axes. The first one was dedicated to the modeling of the isolated molecules like ferrocene derivatives or several metalic porphyrins that could exhibit some redox bistability. This latter property is important in order to stabilize a particular charge state over a large range of electrical potential. Some preliminary experimental conclusions indicated that conformational changes may induce such bistable effects.

The second part was devoted to the study of redox-active molecules grafted on Si surface. The intention was to reproduce and interpretate theoretically by quantum chemistry the influence of parameters (molecule, linker) on electrical properties (charge localization,

redox potentials, device characteristics) for molecular systems grafted on a semiconductor Si (1 0 0) surface.

To be in direct connection with experimental investigations, we have studied grafted systems with ferrocene (Fc) and Zn TPP (Tetra Phenyl Porphyrin), shown schematically in figure 0.8.

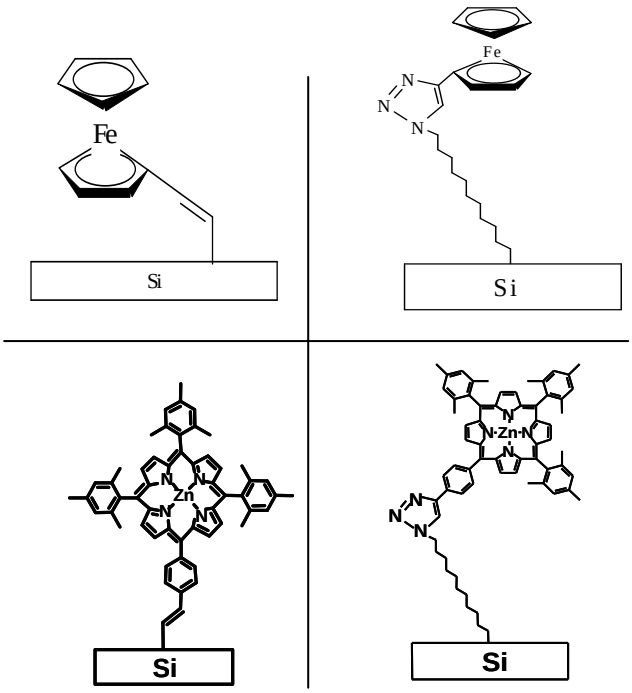

Figure 0.8. Ferrocene and ZnTPP grafted on Si surface. 1) Fc-direct covalent bond 2) Fc -covalent bond with $N_3(CH_2)_{11}$1inker 3) ZnTPP –direct covalent bond 4) ZnTPP- covalent bond with $N_3(CH_2)_{11}$1inker

Due to the hybrid nature of the systems, two approaches were developed. One was based on a molecular description of the whole system, where the Si surface was modelled by a Si aggregate. We used quantum chemistry through DFT methods, leading to a MO (molecular orbital) description of the hybrid systems which give important informations about Homo-Lumo gaps, charge localization or bonding properties. Neverthless, a MO description is very accurate especially for isolated molecules, but not well adapted for the description of infinite surfaces.

The other approach was thus based on solid state physics (collaboration with Philippe Blaise, CEA/ LETI), and the last part of my thesis was thus focused on periodical calculations. We have started with the reconstruction of the semiconductor Si surface in order to avoid the gap problem (surface confinement) [48]. Then simulations of chosen molecules grafted on 'infinite' Si surface were carried out in order to obtain projected density of states (DOS) of periodical calculations. We thus confronted the MO results with the periodical ones and with experimental data.

Some issues that were addressed in this thesis were: is a MO model made up with an aggregate able or not to describe the main features of such hybrid systems? Which molecules exhibit electronic functionalities? What is the influence of the linker? Which is the interaction between the molecules grafted (if it is)? How the energy levels of the molecules penetrate the valence band of Si semiconductor surface?

Both theoretical approaches that were used in this thesis, can offer some answers to these questions. The resulting relevant electronic properties certainly can contribute to a better understanding in analyzing the electronic transport properties of new hybrid silicon/molecular devices.

To summarize, the main objectives of this thesis were the following:

- to model and characterize individually the redox molecules who are interesting for molecular electronic devices;
- to analyze and describe the electronic properties of the hybrid molecular/silicon systems;
- to investigate the influence on the charge transfer of molecular structures, of the linker, or even the substrate itself;
- to investigate the stability of redox molecules (linked directly and indirect) that covalently bond to Si substrates;
- to propose the optimum strategies for theoretical investigation of such molecular systems from the computational resources and CPU time perspectives;

- to determine the electrical properties of hybrid electronic materials suitable for nanomolecular based electronic devices;

As can be seen, these objectives were of two types, methodology on one side, and chemical understanding of the hybrid systems on the other side.

The long-term objective is to further use the calculated electronic properties to develop quantum transport models for the simulation of molecular memories.

1.3. Presentation of work

This thesis is divided into five chapters as follows:

The first chapter describe the current status of molecular memories focusing on Flash and DRAMs memories. A series of existing experimental systems that are proposed as molecular memories are shown. The importance of bistability for redox molecules is shown here, including some examples. Molecular materials and attachment procedures that were used in this study were presented. The experimental procedures and characterization techniques employed in this research are also described here. This chapter brings the work of this thesis into context with the current state of the art of molecular-scale electronics.

In Chapter 2, a basic outline of the standard theoretical methods used in this work is given. Two approaches were been developed for the description of hybrid molecular systems, the Density functional theory (DFT) within the Kohn-Sham scheme, and solid state physics formalism.

Chapter 3 provides the structural and electronic properties of the molecules under investigation. This chapter was dedicated to the modeling of redox processes of molecules such as metalloporphyrins with bistability properties. It explores also the strategies to obtain multiple redox states for information storage.

Chapter 4 is dedicated to device modeling that try to furnish some physical and electrical explanations of hybrid molecular systems. The theoretical study of electron transport through ferrocene and Zn porphyrin based molecules using several attachment

groups were discussed in the light of small aggregate or band structure calculations. A comparison between the MO's of molecular approach and the DOS of band structure calculations was made and discussed in the light of experimental data on electrical properties.

In chapter 5 classical molecular dynamics calculations were performed in order to study the stability of ferrocene molecule in silicon based structure.

We will end this thesis with some conclusions over the thesis results.

Bibliography

[1] A. Aviram, M. A. Ratner, *Chem. Phys. Lett*. 1974, *29*, 277

[2] A. S. Gyorgyi, *Science* 1941, *93*, 609

[3] G. E. Moore, *Electronics* 1965, *38*, 114

[4] www.isgtw.org/?pid=1000693/index.jsp?&pName=sscs_level1_article&TheCat=6010& path = sscs/06Sept&file=Halfhill.xml

[5] P. Packan, *Science* 1999, *24*, 2079

[6] ftp://ftp.cordis.europa.eu/pub/esprit/docs/melnarm.pdf

[7] http://www.hardware.info/en-US/news/ymicl5qVwpuacJY/Intel_shows_roadmap_ of_ up_ to_4nm_in_2022/

[8] http://www.eetindia.co.in/ART_8800451715_1800009_NT_59998f26.HTM

[9] http://electronics.ihs.com/news/sematech-planar-finfet.htm?wbc_purpose =http%3A & WBCMODE=Pre

[10] http://www.itrs.net/links/2005itrs/ERD2005.pdf

[11] J. E. Brewer, V. V. Zhirnov, J. A. Hutchby, *IEEE Circuits Devices Mag*. 2005, *21*, *13*

[12] H. B. Akkerman, P. W. Blom, D. M. De Leeuw, B. De Boer, *Nature* 2006, *441*, 69

[13] http://www.itrs.net/links/2003SummerMtg/Conference/Presentations/ERD.pdf

[14] K. Greene, *A Memory Breakthrough*, Technology Review, 2008

[15] http://www.freshpatents.com/-dt20090611ptan20090147580.php?type=claims

[16] S. Okhonin, M. Nagoga, J. M. Sallese, P. Fazan, *IEEE Electron Device Letters* 2002, *23*, 85

[17] T. Ohsawa, K. Fujita, T. Higashi, Y. Iwata, T. Kajiyama, Y. Asao, K. Sunouchi, *IEEE Journal of Solid-State Circuits* 2002, *37*, 1510

[18] C. Kuo, T. J. King, C. M. Hu, *IEEE Electron Device Letters* 2002, *23*, 345

[19] S. Tiwari, F. Rana, H. Hanafi, A. Hartstein, E. F. Crabbe, K. Chan, *Applied Physics Letters* 1996, *68*, 1377

[20] http://physicsworld.com/cws/article/print/1420

[21] A. Beck, J. G. Bednorz, C. Gerber, C. Rossel, D. Widmer, *Applied Physics Letters* 2000, *77*, 139

[22] E. Katz, I. Willner, *Structure and Bonding* 2001, *99*, 237

[23] M. C. Petty, *Molecular Electronics: From Principles to Practice*, Wiley, 2007

[24] L. M. Adleman, *Science* 1994, *266*, 1021

[25] R. S. Braich, N. Chelyapov, C. Johnson, P. W. K. Rothemund, L. M. Adleman, *Science* 2002, *296*, 499

[26] S. A. Wolf, D. D. Awschalom, R. A. Buhrman, J. M. Daughton, S. von Molnar, M. L. Roukes, A. Y. Chtchelkanova, D. M. Treger, *Science* 2001, *294*, 1488

[27] F. De Martini, V. Buzek, F. Sciarrino, C. Sias, *Nature* 2003, *419*, 815

[28] A. Nitzan, *Annu. Rev. Phys. Chem.* 2001, *52*, 681

[29] C. Joachim, J. K. Gimzewski, A. Aviram, *Nature* 2000, *408*, 541

[30] V. Kumar, *Nanosilicon*, Elsevier, 2008

[31] V. Balzani, M. Venturi, A. Credi, *Molecular Devices and Machines – A Journey into the Nano World*, Wiley-VCH, 2002

[32] E. Kim, G. M. Whitesides, *Chem. Mat.* 1995, *7*, 1257

[33] E. Kim, Y. Xia, G. M. Whitesides, *Nature* 1995, *376*, 581

[34] J. R. Heat, M. A. Ratner, *Physics Today* 2003, 43

[35] http://www.itrs.net/reports.html

[36] Q. L. Li, G. Mathur, S. Gowda, S. Surthi, Q. Zhao, L. H. Yu, J. S. Lindsey, D. F. Bocian, V. Misra, *Advanced Materials* 2004, *16*, 133

[37] Q. L. Li, G. Mathur, M. Homsi, S. Surthi, V. Misra, V. Malinovskii, K. H. Schweikart, L. H. Yu, J. S. Lindsey, Z. M. Liu, R. B. Dabke, A. Yasseri, D. F. Bocian, W. G. Kuhr, *Appl. Phys. Lett.* 2002, *81*, 1494

[38] G. Mathur, S. Gowda, Q. L. Li, S. Surthi, Q. Zhao, V. Misra, *Ieee Transactions on Nanotechnology* 2005, *4*, 278

[39] R. Zanoni, F. Cattaruzza, C. Coluzza, E. A. Dalchiele, F. Decker, G. Di Santo, A. Flamini, L.Funari, A. G. Marrani, *Surf. Science* 2005, *575*, 260

[40] J. M. Buriak, *Chemical Reviews* 2002, *102*, 1271

[41] C. M. Carcel, J. K. Laha, R. S. Loewe, P. Thamyongkit, K. H. Schweikart, V. Misra, D. F.Bocian, J. S. Lindsey, *J. of Org. Chem*. 2004, *69*, 6739

[42] R. S. Loewe, A. Ambroise, K. Muthukumaran, K. Padmaja, A. B. Lysenko, G. Mathur, Q. L. Li, D. F. Bocian, V. Misra, J. S. Lindsey, *J. of Org. Chem*. 2004, *69*, 1453

[43] D. Gryko, J. Z. Li, J. R. Diers, K. M. Roth, D. F. Bocian, W. G. Kuhr, J. S. Lindsey, *J. of Mat .Chem*. 2001, *11*, 1162

[44] C. Yan, M. Zharnikov, A. Golzhauser, M. Grunze, *Langmuir* 2000, *16*, 6208

[45] Z. M. Liu, A. A. Yasseri, J. S. Lindsey, D. F. Bocian, *Science* 2003, *302*, 1543

[46] J. Jiao, I. Schmidt, M. Taniguchi, J. S. Lindsey, D. F. Bocian, *Langmuir* 2008, *24*, 12047

[47]C. Li, J. Ly, Bo Lei, W. Fan, D. Zhang, J. Han, M. Meyyappan, M. Thompson, C. Zhou, *J. Phys. Chem. B* 2004, *108,* 9646

[48] Y. M. Niquet, C. Delerue, G. Allan, M. Lannoo*, Physical Review B* 2000*, 62,* 8, 5109

Chapter I
State of the art-Molecular Memories: literature, laboratory investigations

I.1 Current memory devices

We will present in this chapter the main current developments that appear in the literature on molecular memories [1–12]. Then we will focus on the main achievements of our molecular memories project. Particular attention will be paid to capacitive devices: FLASH or DRAM-like approach) or resistive switching memories (crossbar architecture) that incorporate redox – molecules.

I.1.1 Volatile vs Non-Volatile Memories

Among the various existing semiconductor memories, it is necessary to distinguish first, the so-called volatile memories and non-volatile memories (figure I.1).

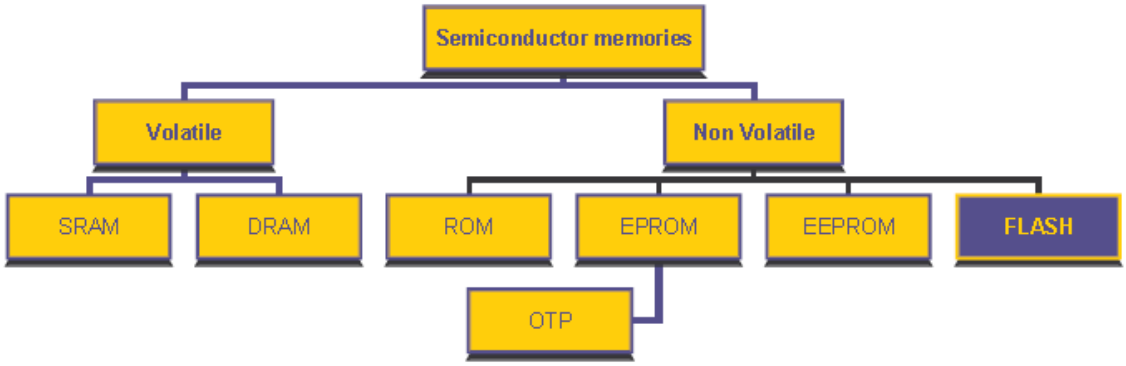

Figure I.1 Schematic classification of semiconductor memories [13]

Volatile memory, also known as volatile storage or primary storage device, loses any data as soon as the system is turned off; it requires constant power to remain viable. Most types of random access memory (RAM) fall into this category. From the point of view of the data storage mechanism, RAM are divided into two main groups [14]:

– **Static RAM**, where data is retained as long as there is power supply on.

– **Dynamic RAM**, where data is stored on capacitors and requires periodic refreshment.

Non-volatile memory (NVM) [15-18], also known as Read-Only Memory (ROM), does not lose its data when the system or device is turned off, thus retains its contents indefinitely. With respect to the data storage mechanism, NVM are divided into the following groups:

– **Mask programmed ROM**. The required contents of the memory are programmed during fabrication. Classic mask-programmed ROM chips are integrated circuits that physically encode the data to be stored, and thus it is impossible to change their contents after fabrication. Other types of non-volatile solid-state memory permit some degree of modification:

– **Erasable Programmable ROM (EPROM)**. Data is stored as a charge on an isolated gate capacitor (“floating gate”). Data is removed by exposing the PROM to the ultraviolet light.

– **One Time Programmable (OTP)**. It is electrically an EPROM. It can be written to or programmed via a special device called a PROM programmer. Typically, this device uses high voltages to permanently destroy or create internal links (fuses or antifuses) within the chip. Consequently, a PROM can only be programmed once.

– **Electrically Erasable PROM (EEPROM)** also known as Flash Memory. It is based on the concept of the floating gate. The contents can be re-programmed by applying suitable voltages to the EEPROM pins.

– **Flash memory** (sometimes called "flash RAM") [19, 20] is a mix of EPROM and EEPROM technologies. The term “flash” was chosen because a large part of memory could be erased at one time. The name, therefore, distinguishes flash devices from EEPROMs, where each byte is erased individually. Nowadays, the flash memory technology has become a strong competitor to EPROMs and EEPROMs memories, and to some DRAM

applications. Because non-volatile flash memories are the most related with our project, we will describe below the characteristics of this technology.

I.1.2. Non-Volatile Flash Memory

A flash memory device is a non standard MOS (metal–oxide–semiconductor) Field Effect Transistor (MOSFET) that has a source, a drain, an access or a control gate, and a floating gate (FG). Such device has been already described above (see figure 0.6, top left of introduction section). It is structurally different from a standard MOSFET in its floating gate, which is electrically isolated. This means that any electrons placed on it are trapped there and, under normal conditions, will not discharge. Kahng and Sze proposed the first floating gate device in 1967 [21].

Nowadays, flash memory has become a powerful and cost-effective solid-state storage technology widely used in mobile electronics devices and other consumer applications. Embedded applications can take advantage of flash memory by both storing application data in it and by allowing modifications or upgrades of the application code itself. Two major forms of flash memory, NAND Flash and NOR Flash [22], have emerged as the dominant varieties of non-volatile semiconductor memories utilized in portable electronics devices (figure I.2).

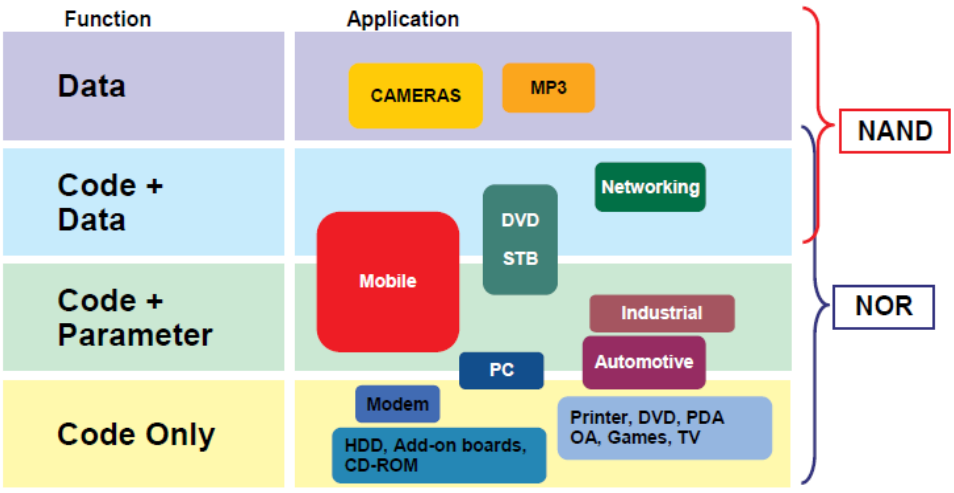

Figure 1.2. Flash Applications [13]

NAND flash was designed with a very small cell size to enable a low cost-per-bit of stored data and has been used primarily as a high-density data storage medium, while NOR flash has typically been used for code storage and direct execution in portable electronics devices. However, the distinction between the two types of flash memory has become less clear. Designers of memory subsystems in portable electronics are now using NAND in some traditional NOR-based applications.

Driven by an increasing demand for devices adapted to nomadism usage, the market for non-volatile memories is rapidly growing. Today the majority of non-volatile memories are based on charge storage and are fabricated by materials available in CMOS processes, as can be seen in the next paragraph.

I.2. The Future of Non-Volatile Memories

The vast majority of non-volatile memories available on the market today are based on charge storage and are fabricated by materials available in CMOS processes [23, 24]. Two possibilities to store charges are commonly used, namely floating gates and charge trapping [25] layers. The dominant devices today are floating gate memories. These devices have some general shortcomings like slow programming (from microseconds up to milliseconds), limited endurance (typically 10^5 – 10^6 write/erase cycles) as well as the need for high voltages (10-20V) during programming and erase [26, 27]. These shortcomings imply some severe restrictions on the system design side.

A memory that works like a random access memory (similar to DRAM or SRAM) and is also non-volatile would therefore greatly simplify the system design. Moreover, much higher data densities than the present ones will be required (for example, for storing multimedia data like videos). This calls for a memory with an extremely small bit cell size. To achieve these goals, novel materials showing new switching mechanisms have to be introduced into the CMOS process flow. Figure I.3 shows the hierarchy of possible CMOS memory material extensions [28].

The vast majority of non-volatile memories available on the market today are based on charge storage and are fabricated by materials available in CMOS processes [23, 24]. Two possibilities to store charges are commonly used, namely floating gates and charge trapping [25] layers. The dominant devices today are floating gate memories. These devices have some general shortcomings like slow programming (from microseconds up to milliseconds), limited endurance (typically 10^5 – 10^6 write/erase cycles) as well as the need for high voltages (10-20V) during programming and erase [26, 27]. These shortcomings imply some severe restrictions on the system design side.

A memory that works like a random access memory (similar to DRAM or SRAM) and is also non-volatile would therefore greatly simplify the system design. Moreover, much higher data densities than the present ones will be required (for example, for storing multimedia data like videos). This calls for a memory with an extremely small bit cell size. To achieve these goals, novel materials showing new switching mechanisms have to be introduced into the CMOS process flow. Figure I.3 shows the hierarchy of possible CMOS memory material extensions [28].

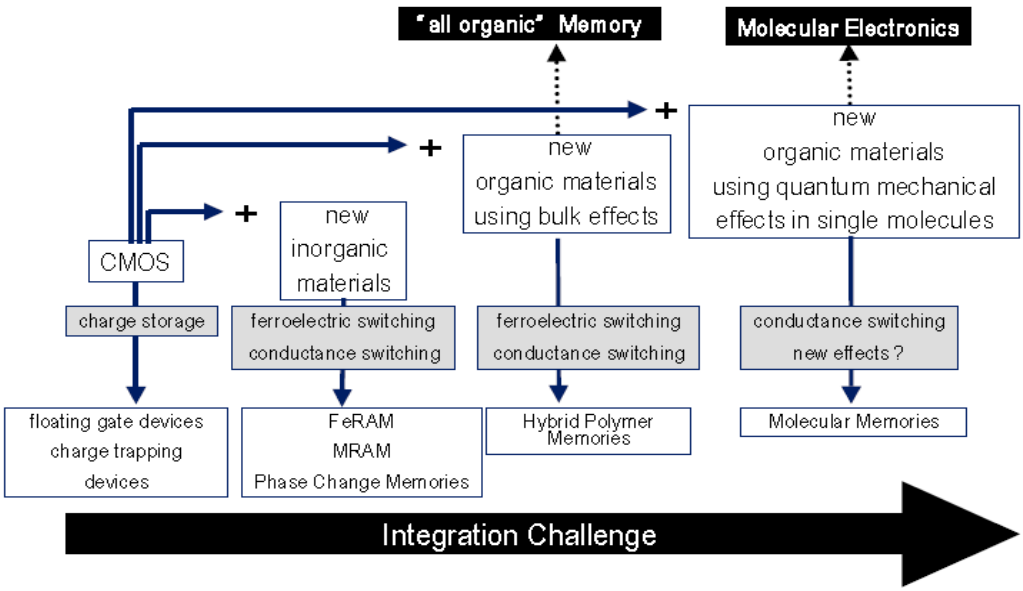

Figure I.3 Non-Volatile Memories emerging evolution [28]

Three main routes emerge, based on inorganic materials, organic bulk polymers and finally molecular species. Starting with a review of current non-volatile memories, advantages and drawbacks of the above mentioned emerging memory concepts are discussed below.

I.2.1. Non-Volatile Memories based on inorganic materials

A lot of experimental research effort and modeling has been spent on new memory technologies based on inorganic materials [29, 30]. These memory mechanisms include the use of ferroelectric, magnetic and material phase change to store bit information. The ferroelectric memory technology [31, 32] is based on the electric dipole switching of a certain class of materials. These crystalline ferroelectric materials can be programmed in two different states by simply applying an electrical bias to the films. The individual unit cells of the crystal interact with their neighbouring cells to form ferroelectric domains in the material. A typical memory element is shown in figure I.4.

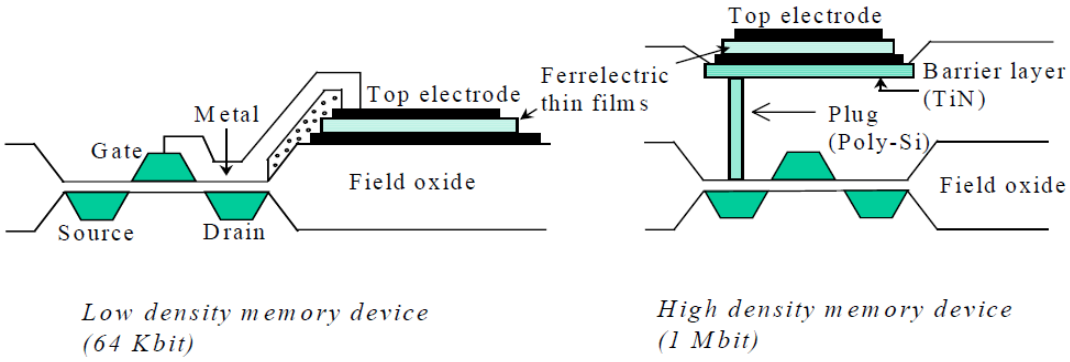

Figure I.4 Examples of ferroelectric memories: low density device (left) and high density memory device [31]

These modules may be realized as switchable capacitors or resistors with different reading and writing schemes. In order to implement highest memory density, passive crossbar arrays instead of active transistor cells can be generated, having the advantage of a lower

cell size but requiring a read out by a complex periphery thus compromising memory performance.

Most of these memory options are expected to merge into a CMOS technology platform and they are generally thought to be converted to competitive products in the next few years [31].

I.2.2. Organic Memories using bulk switching effects

Polymer memories use the bulk properties of inorganic materials which can be either resistance switching or ferroelectric switching. The advantage of organic materials lies in the fact that their properties can easily be tailored by chemical design. The main drawback is that usually the stability, especially the temperature stability is limited. In figure I.5, the principal arrangement of a three dimensional (3D) stacked organic hybrid memory is shown.

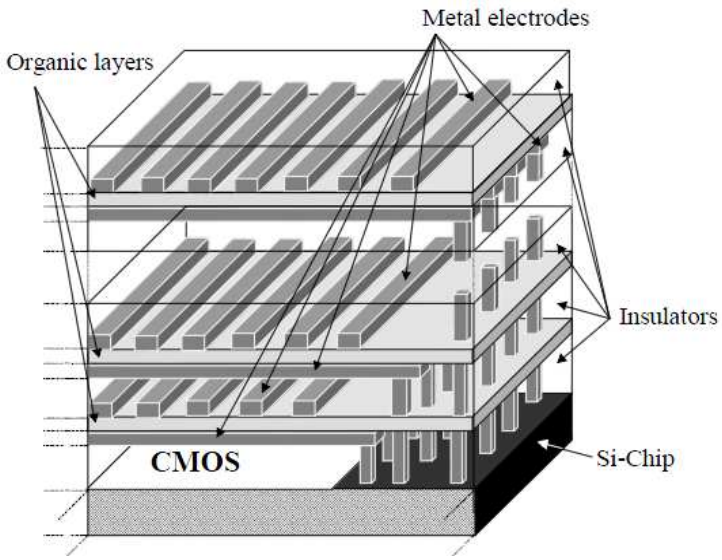

Figure I.5. Principal arrangement of 3D stacked organic memory [33]

The Si chip includes all the CMOS circuits necessary to operate the array. These can be placed under the array resulting in a very high cell efficiency. The organic memory layers are stacked on top of each other separated by insulators. Every electrode showed in the

diagram is used for one memory layer only. Depending on the switching effect used, electrodes may also be shared among different memory layers reducing the processing steps for the memory array [34].

A number of different concepts have been published. Krieger et al. have proposed the use of structural electronic instability in one dimensional molecular system [35]. Fast switching, 10^8 cycles, retention of 1.5 months as well as a multilevel cell storing 4 different resistance values were demonstrated [36, 37]. Potember et al., proposed an electrical induced phase transition in charge transfer complexes like silver and copper tetracyanoquinodimethane (TCNQ) salts as another class of material showing promising switching behaviour [38].

A large number of other materials showing resistance switching effects have been reported in the literature [39-41]. In most cases further work will be required to achieve stability and switching properties that are suitable for memory applications.

I.2.3. Molecular Memory Emerging routes

Molecular memory encompasses individual molecules as building blocks of memory cells in which one or more bits of information are stored within the molecule. The term molecular memory should be interpreted in such a way, that these memory elements make use of physical effects which occur in a single molecule involving quantum mechanical effects.

Two main challenges in this area of molecular devices are to be underlined. The first one is related to the choice of molecules: how to take advantage of a particular interesting molecular property for information storage? The second one is on the device design: how to integrate the molecules in a CMOS-type device in order to exploit their property?

This paragraph summarizes the current developments in this field of molecular memories. Some of the most important ones that are related to our project are discussed here. We propose to classify them in three principal categories: 1) resistive switching memories; 2) capacitive memories; 3) floating gate memories.

I.2.3.1. Resistive switching memories

Resistance switching behaviour has been first observed and studied in amorphous silicon (a-Si) devices since the 1980s [42-46]. Such a memory is based on a switching mechanism controlled in current and/or voltage, between two distinct resistive states depending upon the material nature integrated in the memory element. The switching element is a metal/molecule/metal sandwich junction where molecules are placed at the cross section of two nanoscale metal wires. This sandwich molecular device has two stable, highly-retentive and reversible states: high resistance state and low-resistance state [46, 47].

One first example for molecular memories is the rapid reversible conductance switching of molecules attached between two electrodes which can be controlled by the applied voltage. Using this approach, rotaxane molecules (figure I.6) were investigated by Collier et al. [48].

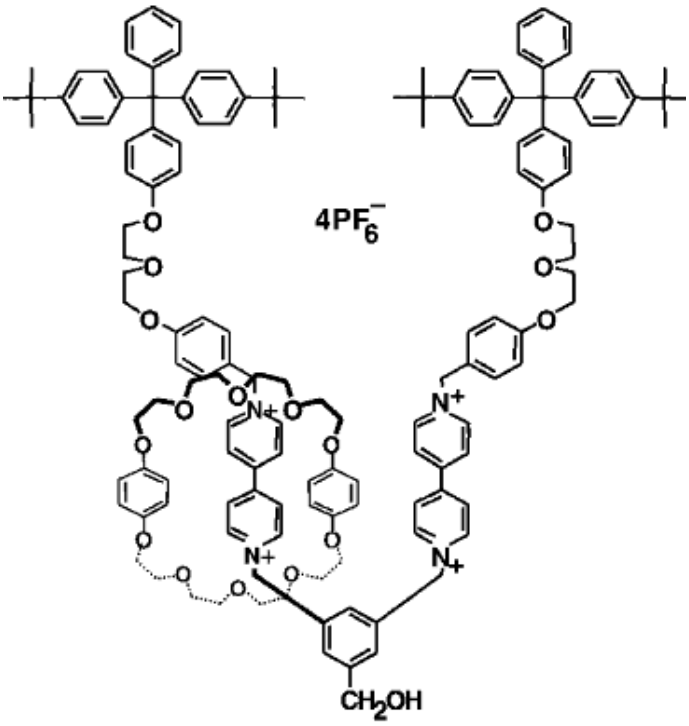

Figure I.6 Schematic R(1) rotaxane molecule used by Collier et al. [48]

Rotaxanes consist of two or more components mechanically interlocked with one another: one of the components is dumbbell-shaped, and the remaining components are rings that become trapped on the dumbbell component, encircling part of the dumbbell. In the class of rotaxanes used here, the dumbbell component contained two bipyridinium units and one encircling ring. Because the ring is not covalently bound to the rod, it can move freely between the stoppers. The functionality and polarity of the end groups, ring, and rod can be altered allowing control over this movement thus the ring's position could be controlled.

By using rotaxane molecules, they developed an electronically (singly) configurable junction that consists of a molecular monolayer and a tunnelling barrier sandwiched between lithographically fabricated metal wires (figure I.7).

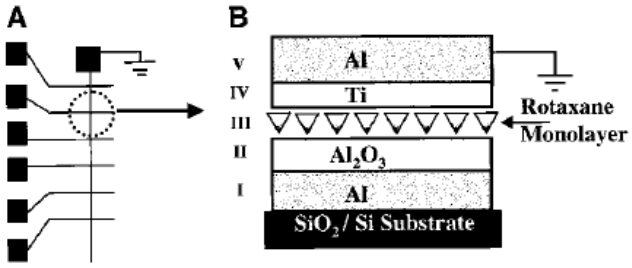

Figure I.7 (A) Top view of a linear array of six devices, shown approximately to scale. (B) Side view cross section of a single device junction [48].

The wires were a few microns in diameter, and each pad was a few hundred microns across to facilitate making an electrical connection to the device. The switches were read by monitoring current flow at reducing voltages. In the "closed" state, current flow was dominated by resonant tunnelling through the electronic states of the molecules. The switches were irreversibly opened by applying an oxidizing voltage across the device. This voltage change the ring's preference thus the molecule behaved as a switch. The current-voltage measurements are shown in figure I.8.A.

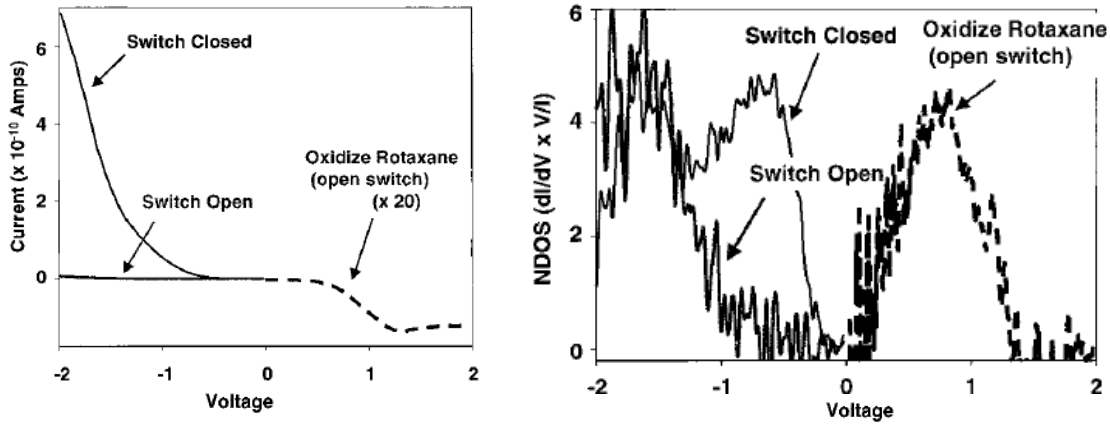

Figure I. 8. (A) Current-voltage traces that show the operation of the devices,(B) The same data as presented in (A), but plotted as the NDOS [48].

The molecular switches are "closed", and the status of the devices is probed by applying a negative voltage to the bottom electrode. The switches are "opened" by oxidizing the molecules at voltages greater than +0.7 V. Finally, the open switches are again interrogated at negative bias.

In figure I.8 (B), when the closed switch is read, two distinct features are recorded in the NDOS (normalized density of states). Oxidation at around + 0.7 to + 0.9 V irreversibly changes the molecules, so the NDOS falls to 0 as the resonant tunnelling process is quenched. When the oxidized devices are interrogated at negative voltage, the electronic states that were observed between 0 and 1 V for a "switch closed" device are now absent.

They have demonstrated that this junction can be used as a switch, and that several devices, fabricated in a linear array structure, could be used as electronically configurable wired-logic gates. Because these switches are only singly configurable, they cannot be used for random access memory (RAM) applications, although programmable read only memory (PROM) applications are possible. Nevertheless, the redox properties of these molecular compounds, do translate surprisingly well into solid-state device properties.

However, by introducing redox centers to molecules, Reed and Tour showed that it is possible to produce a large reversible switching behaviour [49, 50].

Another example of resistive switching memory was recently shown by the Hewlett Packard Research group. They proposed nanoscale circuits based on configurable crossbar

architecture to connect molecular switches in a two-dimensional grid (as shown schematically in figure I.9 (a). This example consisted of an 8×8 crossbar circuit [51]. In particular, they have integrated rotaxane molecules (developed by Heath and Stoddart) into crossbar architecture of Pt / Ti nanowires.

By using imprint lithography, a monolayer of rotaxane (green) is sandwiched between two crossed arrays of Pt/Ti nanowires (gold, on figure I.9.a). Before the fabrication of the top nanowires, the entire molecular monolayer is covered with a Ti protective layer (blue, on figure I.9.a.), which is etched away anisotropically by using the top nanowires as an etch mask.

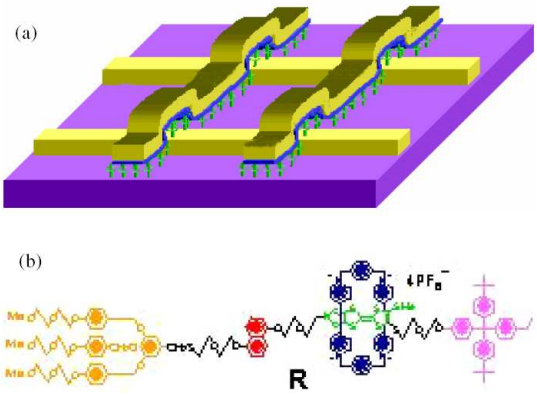

Figure I.9. (a) Schematic representation of the crossbar circuit structure. (b) Molecular structure of the bistable rotaxane R, [51]

The obtained SEM image and an image of the AFM crossbar are shown in figure I.10.

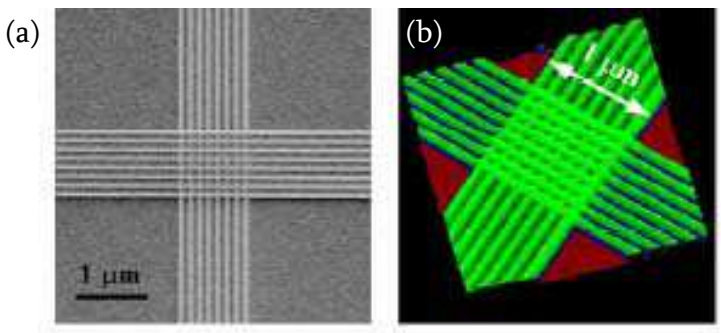

Figure I.10. (a) SEM image showing that the two sets of nanowires cross each other in the central area; (b) a 3D AFM image of the crossbar [51]

This memory has the advantage of architectural simplicity and potential of high density via fabrication of highly dense nanowires. Each intersection is a nanocircuit that can be addressed individually to store information. Figure I.11 shows a schematic diagram of a configuration test, set by applying a potential for every intersection.

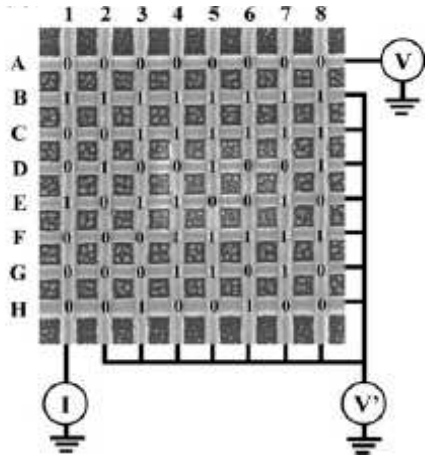

Figure I.11. 64 bits crossbar molecular memory of Hewlett Packard [51]

From these molecules the authors have designed nanocircuits addressable individually, and thus demonstrated that they can store a data set. However, that the effect of hysteresis in devices is actually due to the bistable conformation has not yet been fully demonstrated. This approach has two major disadvantages including high rate of defective switching elements and the difficulty in controlling metal/molecule interface. Nevertheless, a defect-tolerant architecture using this crossbar circuit has been developed [52]. However, as shown in their recent publications [53], the earlier results on electron transport phenomena in metal/molecule/metal junction may not be truly molecular but instead be dominated by electrode reactions with molecules. Another relevant example is given by the R. J. Luyken and F. Hofmann from Infineon Technologies [54].

Recent advances in crossbar architecture showing high storage densities can be seen in the resistive memory developed by Green and coll. [55]. They proposed a molecular memory circuit, which required the integration of molecular switches with large numbers of semiconductor and metal nanowires. The assembled crossbar memory (figure. I.12)

consisted of 400 Si bottom-nanowire electrodes (16nm wide, 33nm pitch) crossed by 400 Ti top-nanowire electrodes (16 nm wide, 33nm pitch), sandwiching a monolayer of bistable [2]rotaxanes (figure I.13). Each bit corresponds to an individual molecular switch tunnel junction (MSTJ) defined by a Si bottom nanowire and Ti top nanowire and contained approximately 100 [2]rotaxane molecules. Electrical contacts were established to several bottom and top nanowires to allow us to test up to 180 effective bits ('ebits') from the central region of the crossbar, but only 128 were actually tested, owing to measurement constraints.

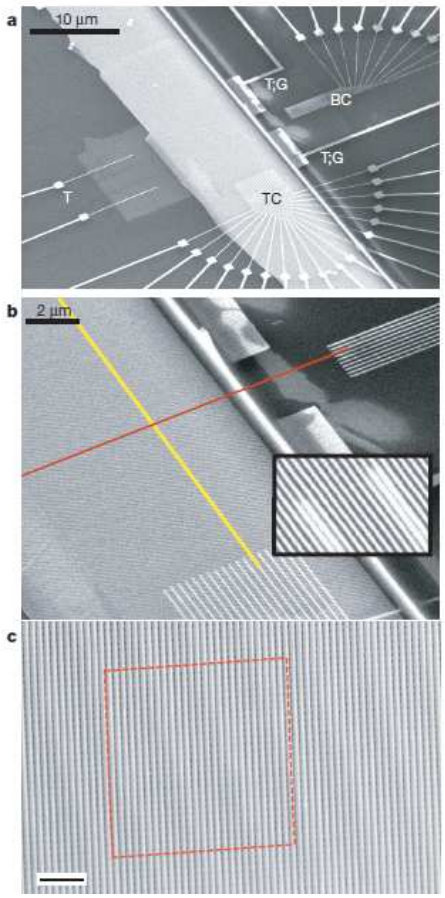

Figure I.12. SEMs of the nanowire crossbar memory. a, Image of the entire circuit. b, An SEM image showing the cross-point of top- (red) and bottom - (yellow) nanowire electrodes. c, High-resolution SEM of approximately 2,500 junctions out of a 160,000-junction nanowire crossbar circuit, scale bar: 200 nm [55]

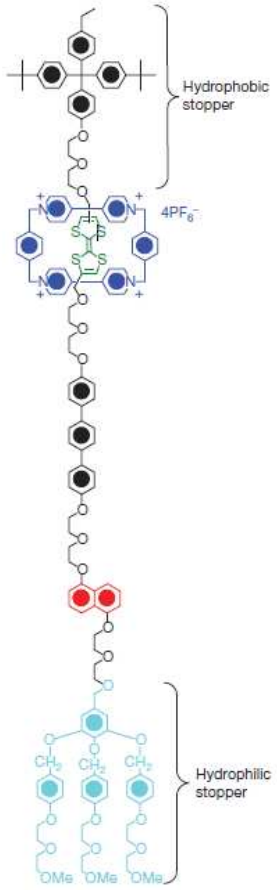

Figure I.14. Structural formula of the bistable [2]rotaxane used in the crossbar memory [55]

In figure I.12 a, the array of 400 Si bottom nanowires is seen as the light grey rectangular patch (labelled TC). In figure I.12b, each cross-point corresponds to an ebit in memory testing. The electron-beam-lithography defined contacts bridged two to four nanowires each (inset). By scanning electron microscopy (SEM), the crossbar appeared to be structurally defect-free (figure. I.12 c), the red square highlights an area of the memory that is equivalent to the number of bits that were tested.

In figure I.13, the ground-state conformation is shown and corresponds to the low-conductance, or '0' co-conformation. The molecule is oriented with the hydrophilic stopper in contact with the Si bottom-nanowire electrodes. The switching mechanism involves oxidation of the (green) tetrathiafulvalene (TTF) site to the TTF^{+1} or TTF^{+2} oxidation state, followed by translation of the blue ring from the TTF^{+} site to the dioxynapthalene site. The TTF^{+} is reduced back to the TTF^{0} oxidation state to form the metastable state co-conformer, which is the high-conductance, or '1' state. The metastable state relaxes back to the ground state with a half-life of about an hour.

An important result was that the good and bad bits were randomly dispersed, implying that the crossbar junctions are operationally independent of one another. About 48% of all bits tested were non switching (bad bits). From a device perspective, this represents the volatility, or memory retention time, of the bits. With respect to the bistable [2]rotaxane switching cycle, this represents a measurement of the rate-limiting kinetic step within the switching cycle. This device proposed by Green and coll. may serve as a fully functional random access memory circuit for storing and retrieving information.

The last example concerns the nanoelectromechanical nanotube memories that are a crossbar arrangement of carbon nanotubes [56]. The proposed memory array consists of single walled nanotubes arranged in parallel rows lying on an insulating substrate (figure I.14). The substrate consists of a conducting layer [highly doped silicon (dark gray)] covered by a thin dielectric layer [SiO2 (light gray)]. The lower nanotubes are supported directly on the dielectric film, whereas the upper nanotubes are suspended by periodic inorganic or organic pillars (gray blocks). Each nanotube is contacted by a metal electrode (yellow blocks).

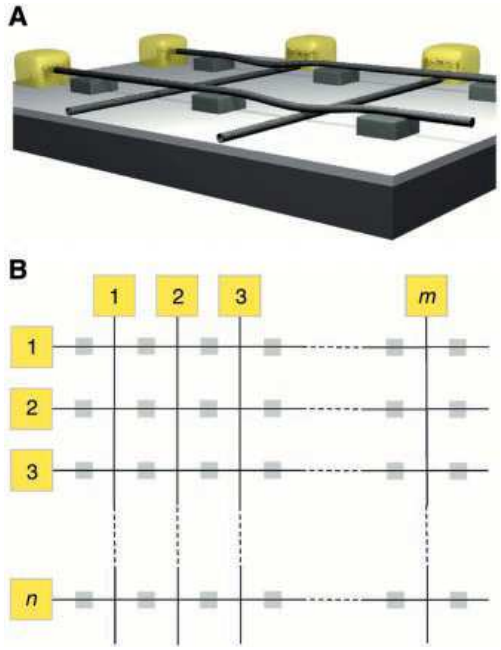

Figure I.14 (A) Three-dimensional view of a suspended crossbar array showing four junctions with two elements in the ON (contact) state and two elements in the OFF (separated) state. (B) Top view of an n by m device array [56].

In figure I.14 (B), the nanotubes are represented by black crossing lines, and the support blocks for the suspended SWNTs (single-walled nanotubes) are indicated by light gray squares. Memory functionality is based on the electrostatic forces which act in between transiently charged nanotubes: attractive or repulsive electrostatic forces can bring the nanotubes in contact or separate them. The resistance at a matrix crosspoint is by some orders of magnitude lower if the two nanotubes are in contact. Current-voltage (I-V) measurements are shown in figure I.15.

The inset on figure I.15 shows a dark-field optical micrograph of the nanotube crossing (scale bar, 4 mm). As can be measured from I-V curves in (A), the two-terminal resistances are 11 and 58 kilohms, respectively.

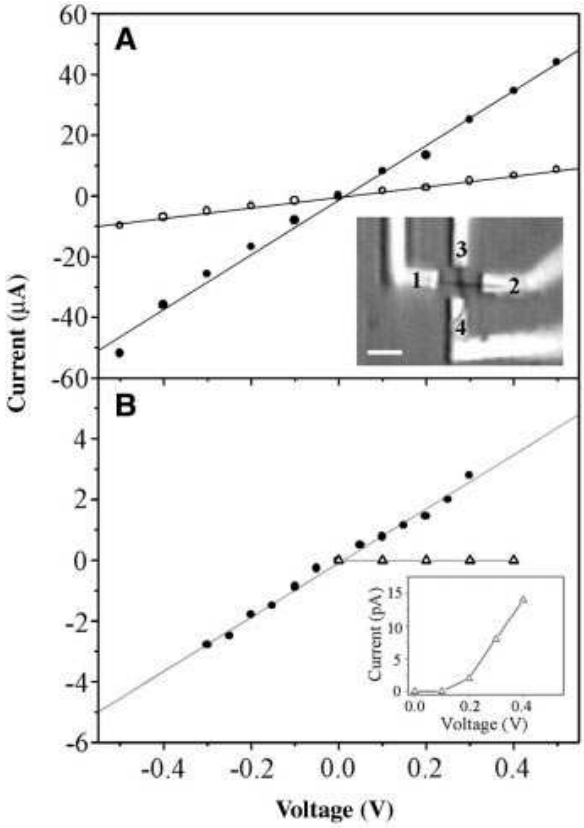

Figure I.15 Carbon nanotube devices. (A) I-V curves for the lower (electrodes 1 and 2, solid circles) and upper nanotubes (electrodes 3 and 4, open circles). (B) I-V curves of the nanotube junction [56].

In figure I.15 (B) is shown the I-V curve of the junction in OFF (open triangles) and ON (solid circles) states measured between electrodes 2 and 3. The junction was switched from OFF to ON at 2.5 V. The ON resistance, 112 kilohms, is ~10^5 times lower than the OFF resistance. The inset shows the OFF state *I-V* on an expanded current scale.

This type of memory should lead to ultrahigh density of 10^{12} elements per square centimetre and to very high operation frequencies [56]. It is expected that such reversible nanotube device elements could be used both as non-volatile RAM and as configurable logic tables and thus could serve as the key building blocks for a molecular-scale computer.

I.2.3.2. Capacitive Molecular Memories

The approach, based on charge storage, is similar to what is in use today and is compatible with conventional CMOS processing. The difference is that the charge is stored at a molecular level instead of a bulk level. In this type of memory, the redox-states of molecules are used to store charges.

An example of multibit memory using self-assembly of mixed ferrocene/porphyrin monolayers on silicon was presented by Bocian et al. [57]. They demonstrated that self assembled monolayers (SAMs) of redox active molecules on silicon could be used for hybrid memory device [58, 59]. The SAMs were prepared using either a benzyl alcohol-tethered ferrocene (4 – ferrocenylbenzyl alcohol, Fc – BzOH) or a benzyl alcohol-tethered porphyrin (5-(4-hydroxymethylphenyl)-10, 15, 20 trimesitylporphinatozinc, Por –BzOH). In order to achieve multibit functionality, they mixed the redox active molecules whose potentials are well separated. The structures of the two molecules, Fc – BzOH and Por – BzOH are shown in figure I.16 (A),(B), respectively. The test structure of the electrolyte – molecule-silicon (EMS) capacitor and its simplified equivalent circuit are shown in figure I.16 (C).

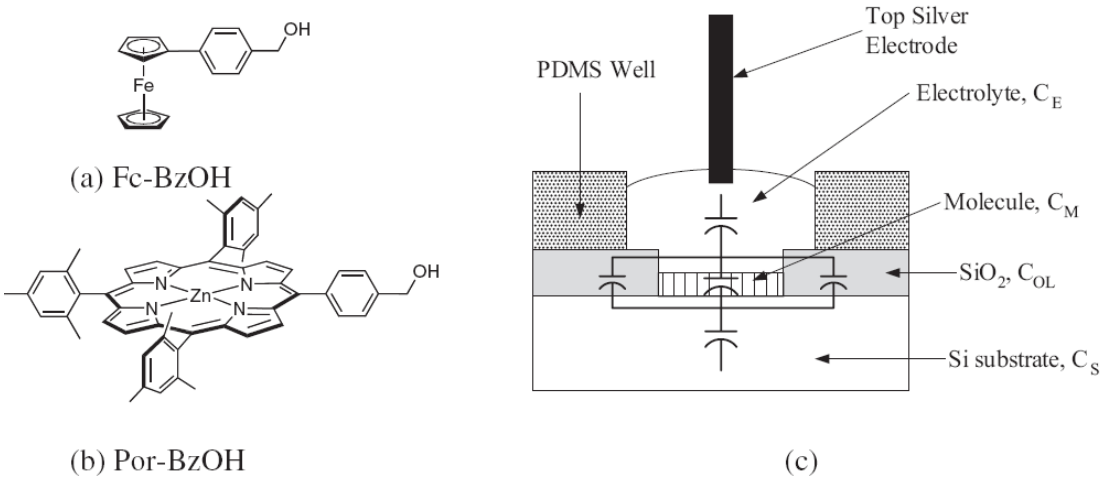

Figure I.16 Molecular structure of (a) Fc-BzOH and (b) Por-BzOH. (c) Schematic of the EMS capacitor with a simplified equivalent circuit [57].

The cyclic voltammetry (CV) of the SAMs of pure Fc-BzOH, pure Por-BzOH, and three mixtures of these molecules with varying ratios are shown in figure I.17.

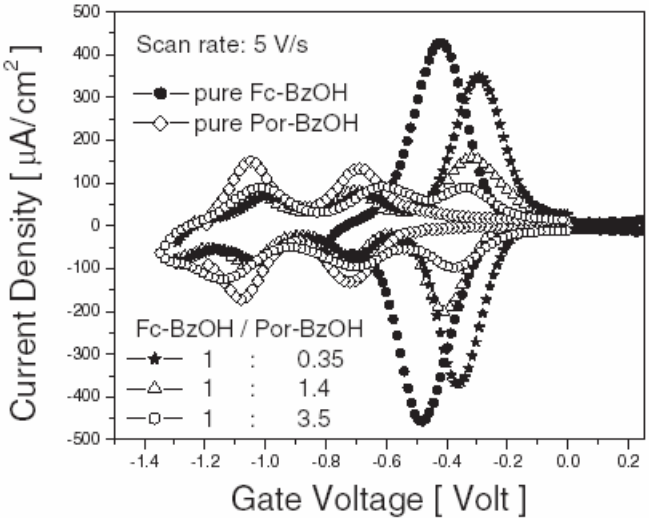

Figure I.17 (CV) of the SAMs of pure Fc-BzOH, pure Por-BzOH, and three mixtures of the molecules [57]

The bottom curves represent oxidation processes and the top curves represent reduction processes. Application of an oxidizing potential causes transfer of electrons from the molecular SAM into the silicon substrate, resulting in storage of positive charges in the SAM. Application of a reducing potential causes transfer of electrons back into the molecular layer, thereby erasing the stored charge.

Conventional capacitance-voltage (C-V) and conductance voltage (G-V) measurements were performed to characterize the monolayers, either made of a pure compound or with a mixture in different molar ratios of FC-BzOH/Por-BzOH (1:0.35, 1:1.4 and 1:3.5) and shown in figure I.18.

The (C-V) and (G-V) curves resemble those of a MOS capacitor except that multiple peaks are present related to the redox processes of the molecules. Each of the mixed SAMs shows three peaks corresponding to the charging behaviour of the two different redox species. Each of the mixed SAMs shows three peaks corresponding to the charging behaviour of the two different redox species.

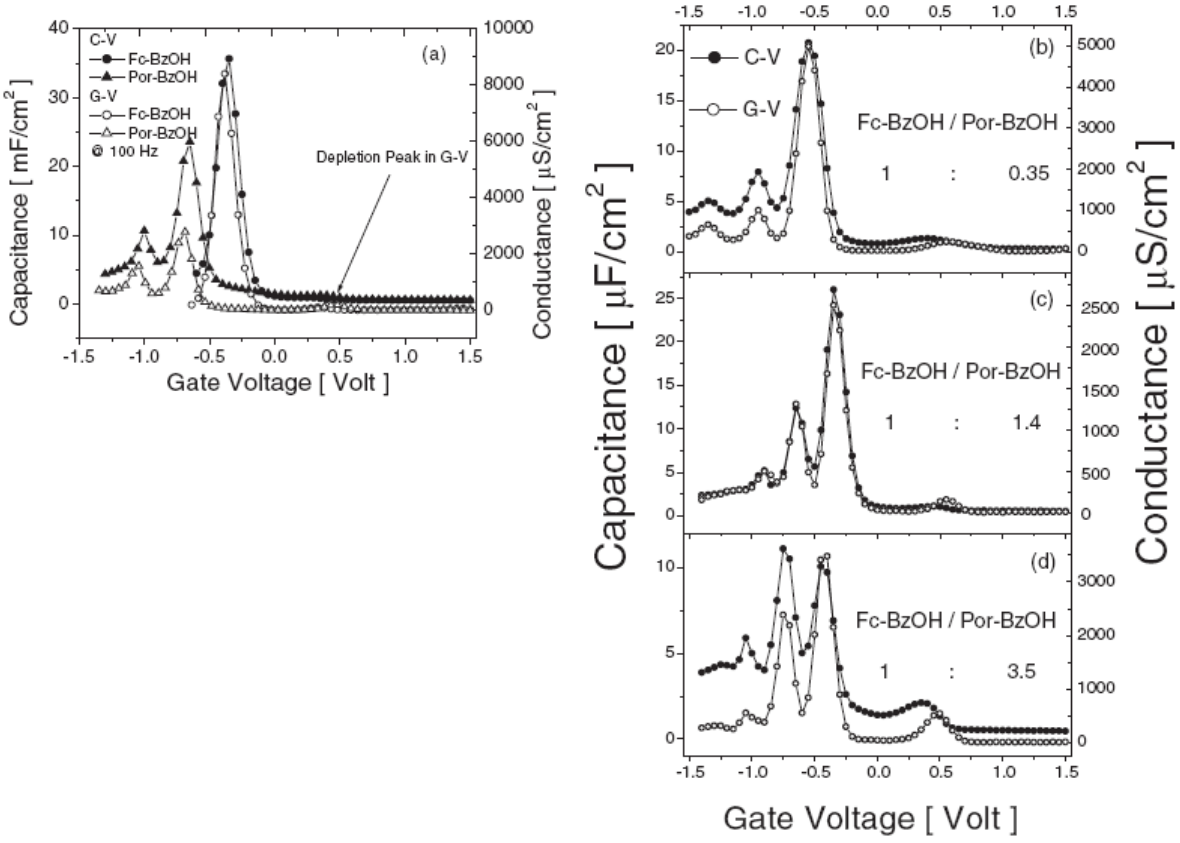

Figure I.18 Capacitance-voltage and conductance voltage characteristics with a) SAMs of pure Fc-BzOH / Por-BzOH and b),c),d), mixed SAMs formed by solutions of Fc-BzOH/ Por –BzOH in the molar ratios indicated [57].

The reversible, stable, and distinct charging and discharging peaks of the SAM make this structure attractive as a multibit memory device. The low applied voltage when in operation is a further advantage of the device and suggests possible applications in both random access and FLASH memory [57].

Another example of capacitive memories is due to the ZettaCore Company [60-62]. ZettaCore is developing ultra-dense, low-power molecular memory chips based on technology from the University of California and North Carolina State University. It uses a conventional DRAM architecture except that the conventional capacitor is replaced with a new molecular capacitor (figure I.19).

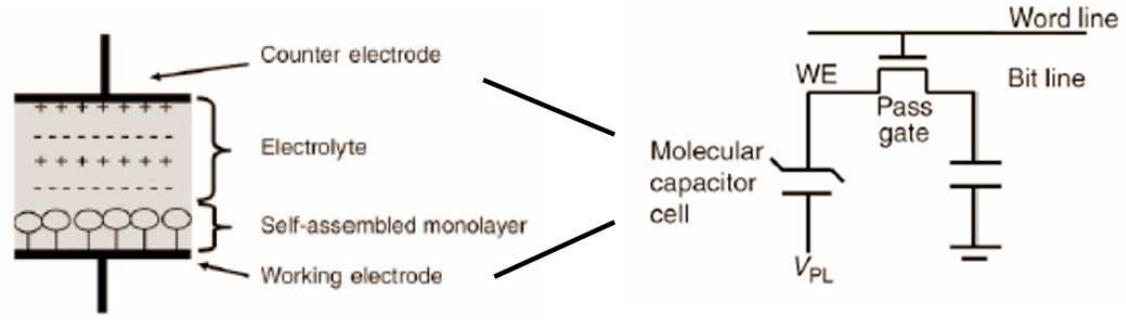

Figure I.19 Molecular capacitor developed by ZettaCore [61]

The molecular capacitor has a discrete threshold voltage, above which all molecules are charged and below which all molecules are discharged. Thus, while voltage still controls charging/discharging, the fixed charge deposited on the molecular capacitor is voltage-independent. The chosen molecules were functionalized porpyrins, (from Bocian and coll.). In figure I.20 are shown the cyclic voltammetry measurements of several porphyrins that were used by ZettaCore and the coverage density on the surface.

Structure	CV	Coverage (mol/cm^2) **Charge Density (μC/cm^2)**
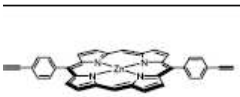	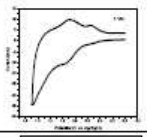	N/A
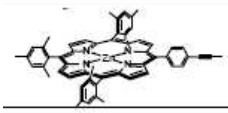	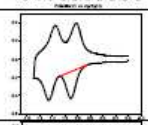	5.29×10^{-11} **5.1**
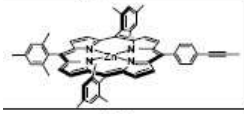	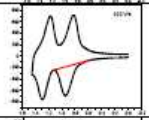	9.75×10^{-11} **9.4**
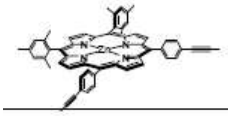	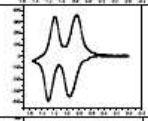	5.6×10^{-9} **540**
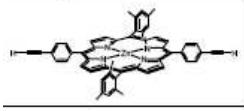	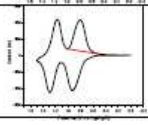	7.52×10^{-9} **725**

Figure 1.20 Cyclic voltammetry of various porphyrins and coverage density of these molecules on the surface [61]

ZettaCore have designed molecules with up to eight oxidation states, meaning that it is possible to remove up to eight electrons and detect the resulting state of the molecules using distinct, discrete voltages. Thus, they can in principle reliably store more than one bit of information in a single memory location. The diagram below shows the basic concepts of ZettaCore molecular memory.

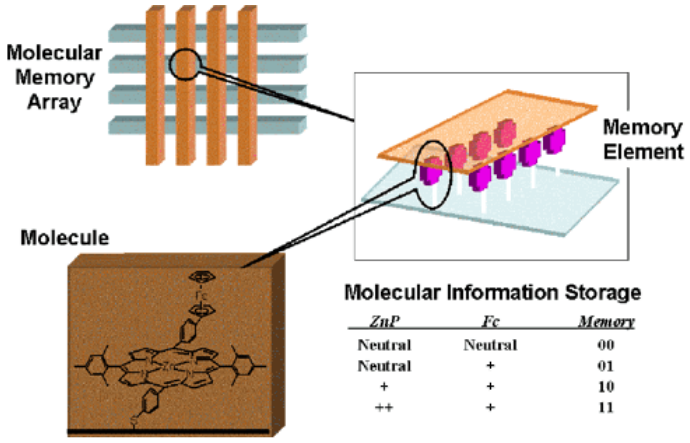

Figure I.21 Simplified diagram of ZettaCore molecules in a memory array [60]

An individual molecule is shown in the lower left corner. This molecule has four states, so it stores two bits of information. At each location in the array there may be between a few thousand and a million molecules.

The writing time was estimated at between 10^{-3} and 10^{-5} second. The retention time of loads is 100 to 200 seconds and the charge density could reach a few hundred of µC per cm^2 [61].

I.2.3.3. Floating Gate Memories

Lieber et al. have proposed another design which integrates redox molecules [63]. They have explored the combination of bistable nanoscale switches assembled using semiconductor NWs (nanowires) and redox active molecules as building blocks.

The nanodevice consists of nanowire field-effect transistors (NW-FET) functionalized with cobalt phthalocyanines (CoPc), where the redox species can store charges and thereby maintain the NW- FETs in either a logic "*on*" or "*off*" state with high or low channel conductance, respectively. The overall configuration and operating principle of NW devices are illustrated in figure I.22.

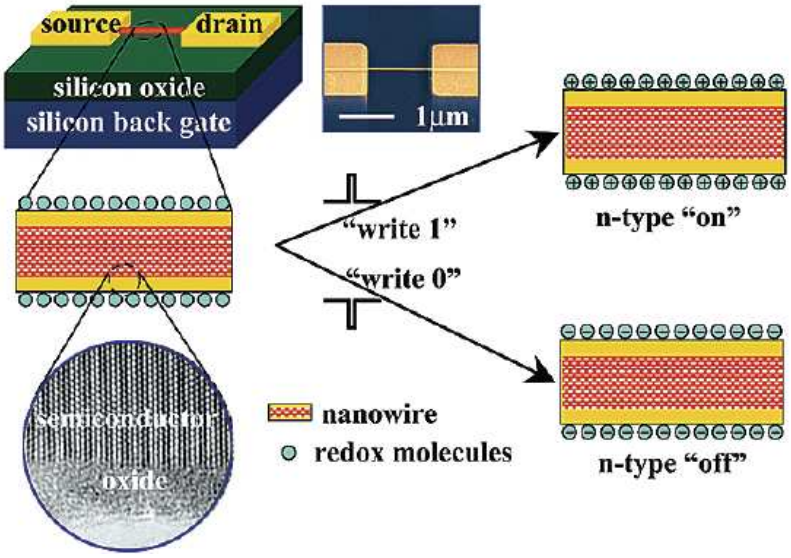

Figure I.22 Schematic architecture proposed by Lieber [63]

The top-middle inset shows an SEM image of a device, and the lower circular inset shows a TEM image of an InP NW highlighting the crystalline core and surface oxide. An applied gate voltage *(Vg)* or source-drain voltage *(Vsd)* pulse injects net positive or negative charges on the molecular layer. The oxide layer on the NW surface, which can be controlled synthetically, serves as a barrier to reduce charge leakage between the molecules and NW. Several different redox active molecules were examined including ferrocene, zinc tetrabenzoporphine, and cobalt phthalocyanine (CoPc). Typical conductance before and after modification with a CoPc layer is shown in figure I.23 (a). Before addition of the CoPc layer, the response is characteristic of an n-type FET (green curve); that means, little or no hysteresis is observed in *G-Vg* for positive/negative

variations in *Vg*. Significantly, a large hysteresis in *G- Vg* is reproducibly observed after the NW surface is modified with CoPc (red curve, figure I.23 (a)).

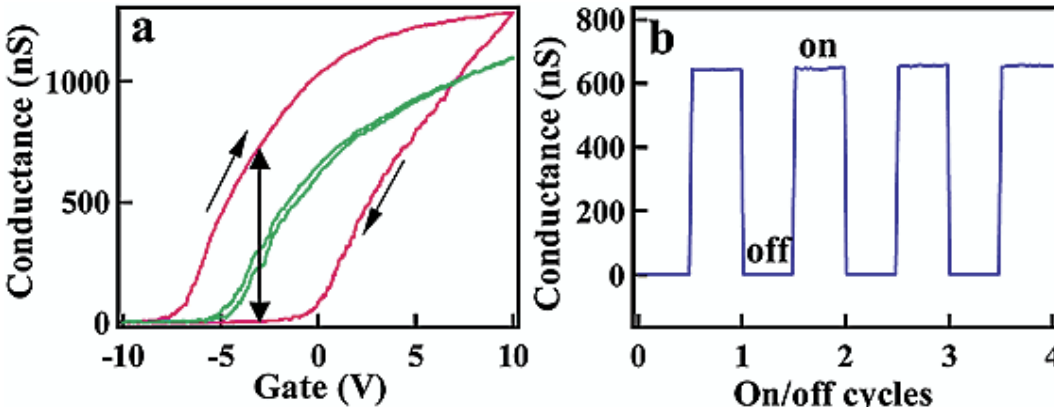

Figure I.23 (a) G vs Vg for an n-InP NW-FET before (green) and after (red) surface modification with CoPc recorded with Vsd =0.1 V. (b) Reversible on and off switching [63].

Starting from the neutral form of CoPc, the nanowire presents a zero conductance between -10 and 0 V, then going to high positive potentials, the molecule is charged and the nanowire acquires a non-zero conductance. When applying again a strong negative potential, the molecule returns to its original state. The effect of hysteresis observed defines the two stable states: 0 (off - low conductance) and 1 (on - high conductance) of the device. Such system shows reversible switching (figure I.23(b)) over many cycles between the "*on*" and "*off*" states. The resulted hysteresis defines the two states of a bistable system and has been exploited to configure a three-terminal switch or memory device. These properties (long retention time and large on/off ratio) make them attractive for non-volatile molecular memories and for programmable logic arrays [63].

The second example of a molecular memory floating gate architecture is due to Zhou et al. and it was developed in 2004 [64-68]. In this device (figure I.24), cobalt and nonmetalated porphyrins were anchored on an indium oxide nanowire between two indium sources and drain plots.

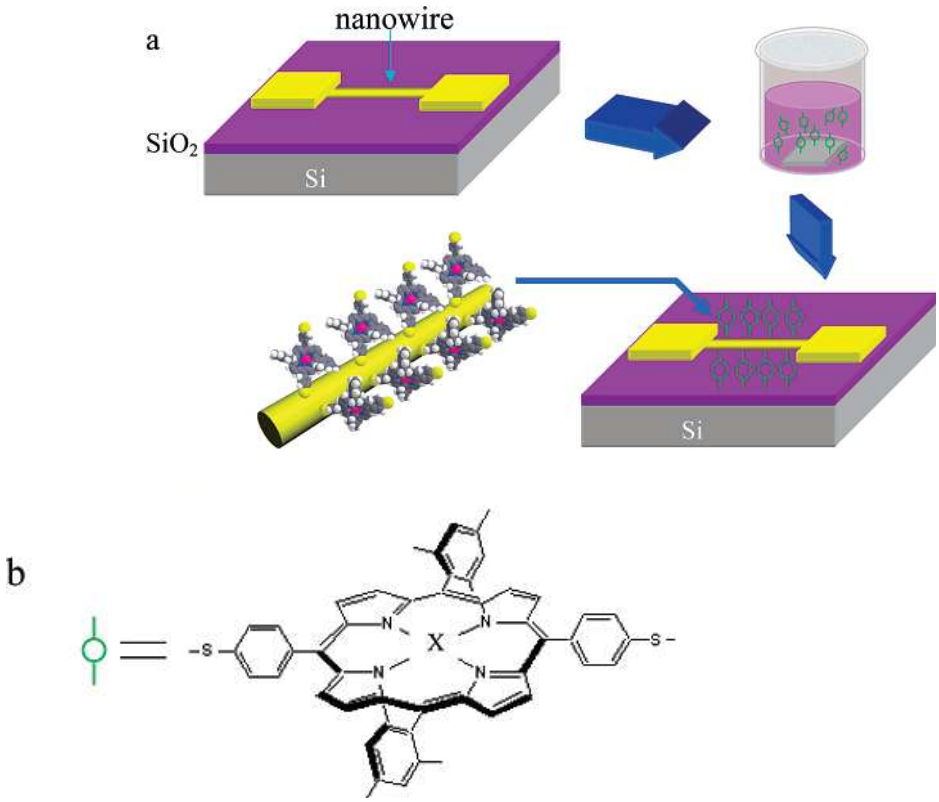

Figure 1.24 (a) Fabrication process of the memory device. (b) Molecule structure of the porphyrins (X = H_2 or Co^{2+}) [68].

The porphyrins used here as molecular gates are illustrated schematically in figure I.24 (b). Figure I.25 shows the typical memory operations of an In_2O_3 nanowire field effect transistor functionalized with a self assembled monolayer of Co-porphyrin molecules in comparison with the free base (X = H_2).

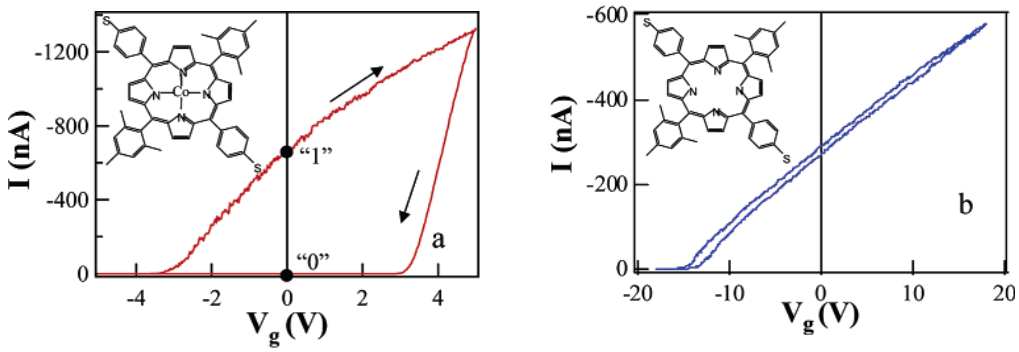

Figure I.25 I-Vg characteristics of In_2O_3 nanowire devices with self assembled Co-porphyrin (top) and protio porphyrin (below) [68].

The memory effect was only observed for samples with Co-metalated porphyrins, and no memory effect was obtained with free base porphyrins. In this device, the hysteresis effect is put forward, but the relation between the hysteresis effect and the oxidation of the metal depending on the applied voltage has not been clearly characterized [66 -68].

Note that the experimental devices based on molecules that we described here, shows a retention time of information between a few seconds and a few hours. Moreover, retention of information depends on the power supply. Without voltage at the terminals, these devices do not keep written information (volatile) in contrast with current floating gate memories that are non volatile.

I.3. Molecular Memories and bistable molecules

A condition to improve retention times is that the molecule is bistable, i. e. exhibits stability at two different redox states over a large range of voltage [69 - 71]. The general idea is to associate the redox process with a structural change, as described in so-called square scheme known to describe non reversible redox behaviour in electrochemistry. Figure I.26 shows the simple version of such a pattern.

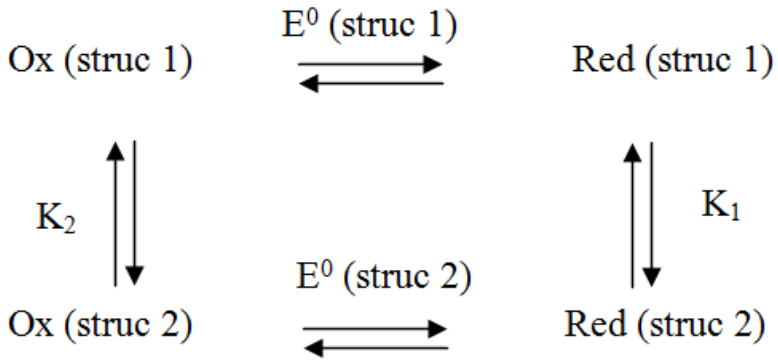

Figure 1.26 Square schemes for a redox-induced structural change. E^0 (struc i) is the standard redox potential of the molecule in its structure i (i = 1 or 2)

The structural equilibrium constants and the redox potentials are related by equation (1) derived from the well-known relationship between the standard Gibbs free energy change ($\Delta G°$) and the equilibrium constant (K) or the standard potential, $\Delta G°=-RT\ln K=-nFE°$, and by taking into consideration that $\Delta G°=0$ for the thermochemical cycle:

$$\frac{K_2}{K_1}=\exp\left[\frac{F}{RT}\left\{E^0(struc1)-E^0(struc2)\right\}\right] \quad (1)$$

Therefore a non reversible system exhibits a shift between its two redox states as a function of the voltage related to the ratio between structural constants. The use of such effect in coordination compounds with the purpose to store discrete charges has been explored for a few years and some examples are given below.

In a review on the isomerism in octahedral coordination complexes controlled by transfer electrons by Pombeiro and coll. [72], several carbonyl complexes of general formula $ML_2L'_y$ (M = Cr, Mo or W, L = CO, L' = phosphine ligand) were described. The structural change was observed as "cis" and "trans" forms (with respect to both CO ligands) depending of the redox state of M. In such complexes, the 18-electron configuration is more stable in the *cis* form while the oxidized 17-electron state is more stable in the *trans* form, the conversion of the former into the latter can occur upon its oxidation ($cis^+ \rightarrow trans^+$) whereas the reverse isomerisation can result upon reduction of $trans^+$.

Another example of redox-bistable complexes is given by a family of ruthenium complexes developed by Sano et al. [73], using an ambidentate ligand, DMSO. The redox process and isomerism are described on figure I.27. When the S-bonded isomer is oxidized at 1.0 V, linkage isomerisation occurs to the more stable O-bond form. This behaviour is a nice illustration of the HSAB (hard and soft acids and bases) concept: Ru^{2+} being a soft acid is more stable with the S-bonded DMSO, whereas Ru3+ being hard is more stable with O-bonded DMSO.

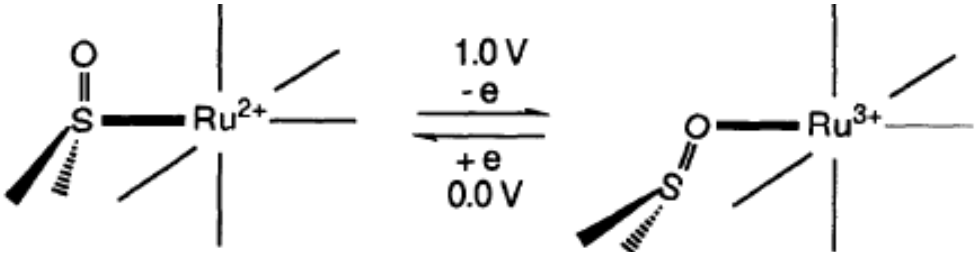

Figure I.27 Complexes $[Ru(NH_3)_5(dimethylsulfoxyde)]^{2+/3+}$ [73]

They extended the study of this type of isomerisation using a ruthenium binuclear complex for which there are two possible forms of the mixed valence Ru^{2+}… Ru^{3+} complex derived from monoelectronic oxidation or reduction of resp. Ru^{2+}… Ru^{2+} or Ru^{3+}… Ru^{3+}. The whole process is summarized on figure I.28. Following the mechanism described by Taube [74], they observed that the mixed-valence state exists in two forms, A' and B', the species A' accessible only by oxidation of the stable fully reduced form, and the species B', only by reduction of the stable fully oxidized form. The species of A' and B', have the same composition, are different from one another, and are said to show 'bistability'.

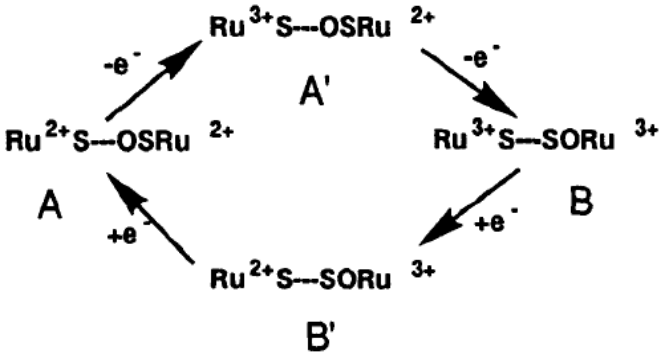

Figure I.28 Schematic redox reactions in the binuclear complex [73]

The structure of A' is similar to that of A, and B' is also to B, hence, A' and B' species can be said to memorize their former structures. These molecules may be interesting for the memory type applications, because of the multiple redox reactions which occur in the binuclear complex.

Another example of bistable redox molecules were developed by Bucher et al. [75]. They described a molecular switch based on the copper complexes (figure I.29) of a bis(ferrocenyl)cyclam ligand, 1,8-dimethylferrocene-4,11-dimethyl-1,4,8,11-tetraazacyclo tetradecane (L), capable of redox-triggered fast and reversible motion, in homogeneous solution and, still better, in the solid state. The X-ray structures of complexes of copper (I) and copper (II) are shown in figure I.29.

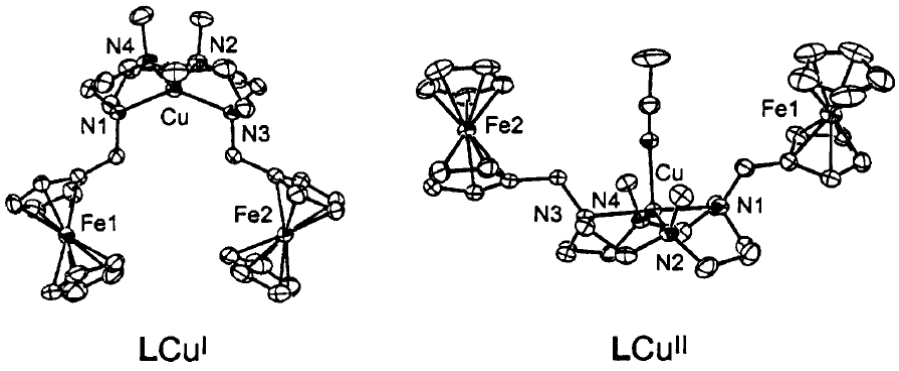

Figure I.29 X –ray structures of 1,8-diferrocenylmethyl-4,11-dimethyl-1,4,8,11-tetraazacyclotetradecane (L) of Cu(I) and Cu(II) [75].

These complexes can adopt two stable geometries that differ from one another mainly by the position of ferrocene substituents which are above or below the cyclamic plane. The movement of the substituents is reversible upon the redox process which occurs on the copper. The ability to trigger a movement in LCu by a heterogeneous electron transfer was probed by cyclic voltammetry experiments showing a non reversible system. These results show that a chemical reaction, a reversible type I to type V rearrangement, follows the electron transfer. The overall electrochemically driven process could be modelled as a classic square scheme (figure I.30).

The authors showed that this change in geometry occurs also in the solid phase using a cavity microelectrode (CME). Since the chemical coupled reaction was observed at the same CV time scale in solution and in the solid state they anticipated that in both cases

the kinetics of the redox-induced movement is of the same order of magnitude for these first-order reactions.

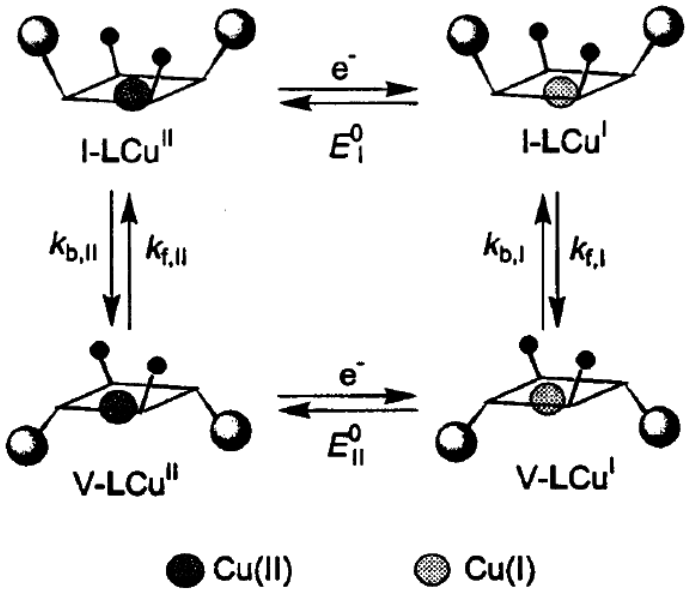

Figure I.30 Redox-induced motion in LCu complexes

The system based on copper cyclamic could change conformation under the influence of electron transfer, so that reversible and reproducible. Such systems, capable of controlled and readable movement at the molecular level, could indeed be considered as molecular switches, finding potential applications in the area of molecular electronics.

The third example in the literature of bistable redox molecules that we have chosen to describe in this chapter is the family of catenanes and rotaxanes shown in figure I.31. These molecules have been extensively described by Heath, Stoddart et al. [76-78]. They consist of two parts: one fixed with two "stations" red and green, and the other mobile (ring blue). Both sides are said interconnected.

Note that, while the starting states of the catenane and rotaxane II, shown in (a) and (d) respectively, exist as one co-conformation (where the blue ring encircles only the green site) in solution, the pseudorotaxane and the rotaxane I, shown in (b) and (c) respectively, exist as approximately 1:1 mixtures of both co-conformations (where the green and red sites are encircled more or less equally by the blue ring).

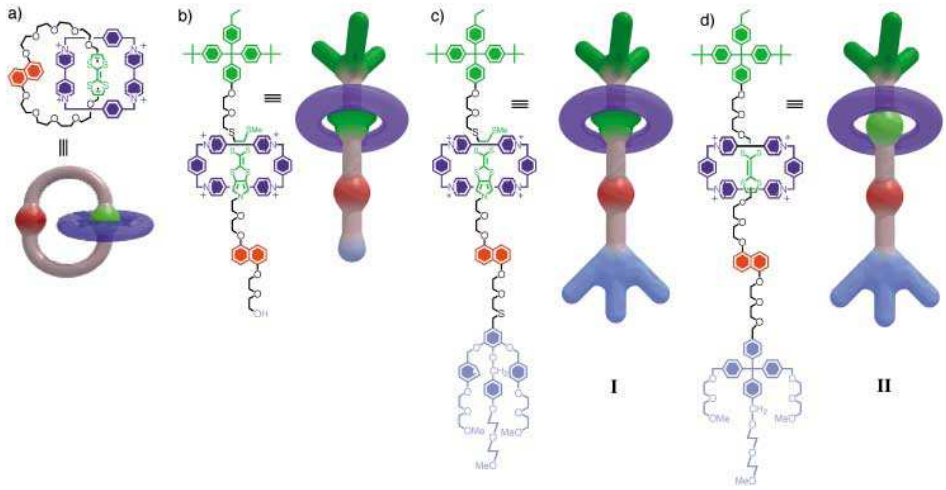

Figure I.31 a) Bistable catenane b) an amphiphilic, bistable pseudorotaxane, c, d) the I and II versions of amphiphilic, bistable rotaxanes.

Their use in cross-bar architectures has been already mentioned above. In figure I.32 is shown as a square scheme the mechanical movement for rotaxanes.

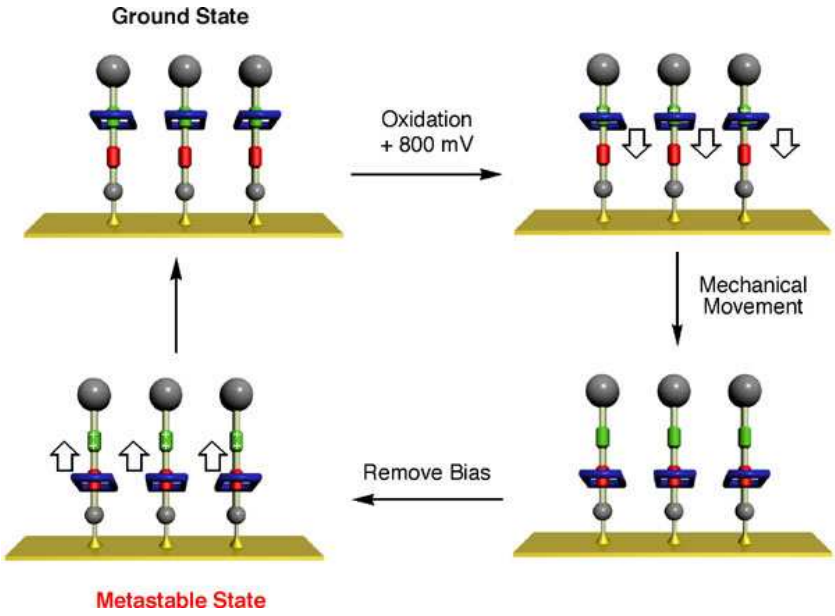

Figure I.32 Molecular motion of rotaxanes

Devices based on rotaxanes and catenanes show a current tension characteristic current tension with a hysteresis effect.

After this review of the various works described in the literature on bistability associated to a redox process, we will focus now on the current studies lead in our laboratory.

I.3.1 Molecular memories at CEA

Since 1998, our laboratory has been involved in the development of families of bistable bridled chiroporphyrins. The first member of these molecules [79] is presented in figure I.33. The adjacent meso substituents are linked by a bridge of 'n' methylene groups which are chiral biocartol groups.

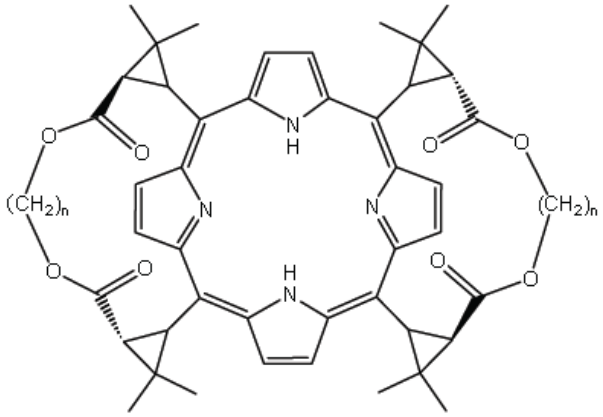

Figure I.33 Bridled chiroporhyrins [79]

The length of bridled 'n' from 8 to 16 carbon atoms and these porphyrins have been complexed with various transition metals (Ni, Zn, Cu, Mn, Fe, Co, etc ...) [79]. The bridled porphyrin with n=8 (called H_2BCP-8) present a distinguished conformational flexibility as shown on figure 1.34. Depending on the size of the metal atom, different atropoisomers were observed. The free base and the Zn^{2+} complex exhibit a preferential 4α conformation in solution as shown by NMR studies. The structure of Zn porphyrin was also obtained by the X-Ray diffraction (see figure 1.34 (b)). For the Ni^{2+} analogue, the atropisomer is 100 % αβαβ in solution and its crystal structure (see figure I.34 (a)) confirm this behaviour. The objective was thus to use this conformational switch to stabilize distinct states of a redox

active metal porphyrins. We have investigated also the case Mn II/III species. More details are in chapter 3.

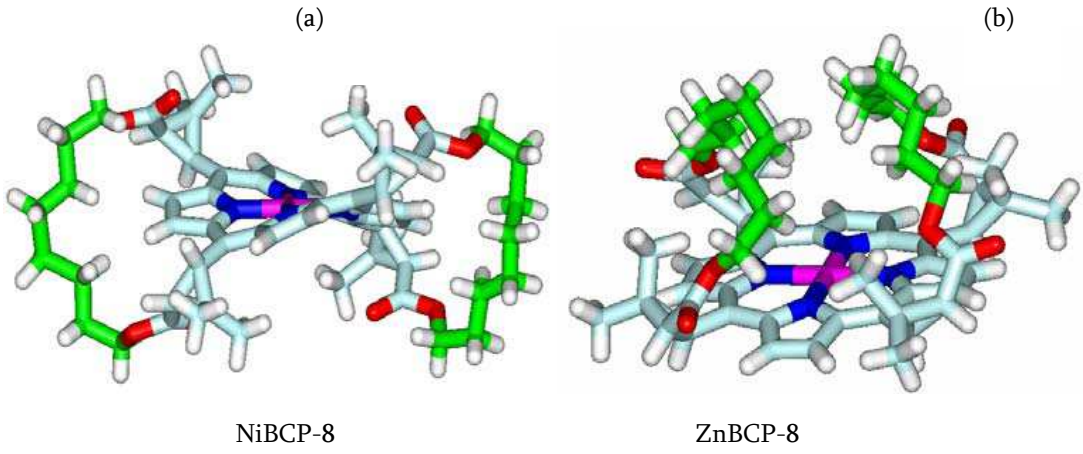

Figure I.34 X-ray structures of NiBCP-8 and ZnBCP-8: open and closed conformations

In this paragraph, we have presented a perspective over the non-volatile memories, followed by few examples from the literature of different ways to design devices based on molecules with a memory effect. In resistive, capacitive or floating grid molecular memories, it appears that information may be retained if the device is powered. Without voltage at the terminals of these devices do not keep written information (volatile).

Devices based on bistable molecules that show hysteresis effect, on the other hand offer access to non-volatile memory, to store information even if no written voltage is applied and this is occurring because of the bistability of molecules. The prospect of using these types of molecules as elements in electronic circuits is an exciting challenge for chemists and physicists. Some relevant examples were exposed here.

We will continue this chapter with a brief description of molecular materials, attachment groups and the experimental tools that were used for the characterization of the hybrid systems in this work.

I.4. Molecular Materials, Attachment Methods, Characterization Techniques

The description and understanding of experimental work are essential having in view that our theoretical models are strongly correlated with the experimental data. Thus this chapter gathers the compounds used in this study along with their main chemical properties. The attachment procedures, the fabrication of test structures and their electrical characterization techniques are also discussed.

I.4.1 Molecular Materials and Properties

The materials used in our project are redox-active nanoscaled metal complexes. By their nature, these molecules can exhibit two or multiple redox states. The two basic classes of molecules chosen in this study are ferrocenes and metalloporphyrins. The compounds are functionalized with tethers and linkers for attachment to silicon and silicon dioxide surfaces via covalent bonds.

I.4.1.1. Ferrocene molecule

The most commonly complex used in this study is ferrocene [80, 81]. Ferrocene, $Fe(C_5H_5)_2$, is an organometallic compound consisting of two cyclopentadienyl rings bound on opposite sides to a central iron(II) center (figure I.35). Such organometallic compounds are also known as sandwich complexes [82].

The iron atom in ferrocene is normally assigned to the +2 oxidation state. Each cyclopentadienyl (Cp) ring is then allocated a single negative charge, bringing the number of π-electrons on each ring to six, and thus making them aromatic. These twelve electrons (six from each ring) are then shared with the metal via covalent bonding, which, when combined with the six *3d*-electrons on Fe^{2+}, results in the complex having a 18-electron configuration.

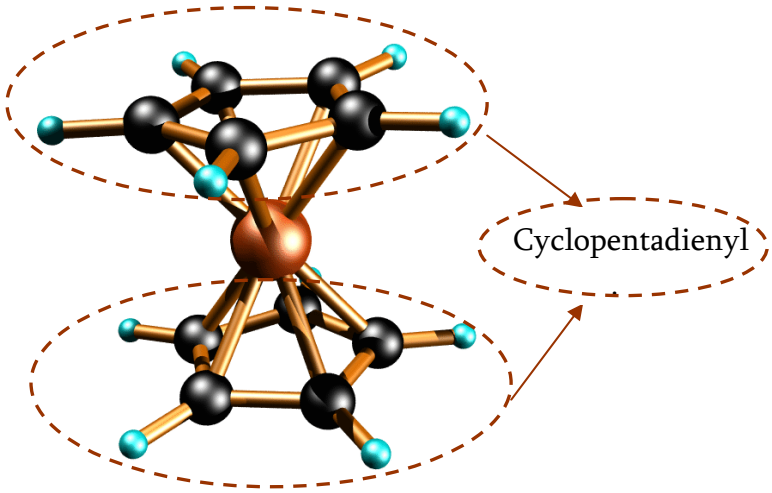

Figure I.35 Ferrocene structure

Ferrocene demonstrates reversible one-electron redox behaviour, thus exhibiting two redox states. In the field of molecular electronics, the two states of the molecule can be associated to a bit of information. Both ferrocene (neutral) and ferrocenium ion (formed by oxidation of ferrocene) are very stable in air. A substitution group can be introduced to the cyclopentadienyl rings, which are very reactive, enabling the attachment of ferrocenes to different surfaces via covalent bonds [83]. As expected for a symmetric and uncharged species, ferrocene is soluble in normal organic solvents, but is insoluble in water. It is stable to temperatures as high as 175°C [84].

The stable redox property of ferrocenes and the ability to attach them to different surfaces make these molecules very attractive for investigating molecule-based memory devices.

I.4.1.2. Porphyrin family (two or more redox potentials)

One goal for designing more complex redox-active components is to increase the number of available redox states, thereby increasing the storage density. A molecule that has more than one single redox potential and implying multiple states is porphyrin.

The porphyrin structure (figure I.36), consists of a conjugated ring of four pyrrole subunits linked together by single carbon bridges. The molecule is stabilized by the aromatic

character which extends over its entire structure. The four nitrogen atoms facing the center may stabilize a metal ion in the middle (after deprotonation of the two hydrogens of the free base.

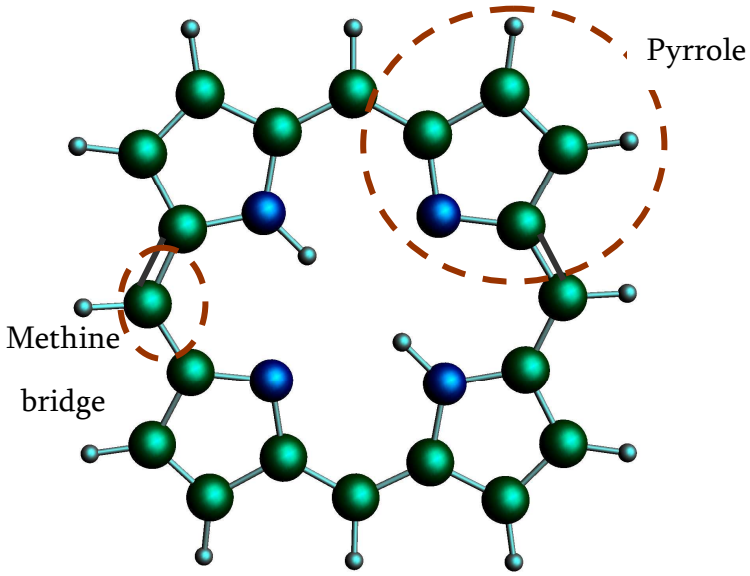

Figure I.36 Structure of porphyrin

Porphyrins combine readily with metal ions (Zn, Co, Cu etc.), coordinating them in the central "hole" to form metalloporphyrins. Generally, porphyrin molecules have multiple stable states. Redox processes occur primarily on the conjugated core, leading easily to mono radical or diradical cationic species and are dynamically reversible. Other redox activity may be brought by the metal ion if it is a redox ion (Mn, Fe, Co…). Generally, the redox potentials depend on their molecular properties, such as their basicity, their substituents, or the central metal ion and the possible presence of axial ligands [85-94].

In our work we have used used metalloporphyrin ZnTPP that exhibit two oxidation states (figure I.37). The behaviour of ZnTPP is well described by quantum chemistry and electrochemical analysis and impedance spectroscopy (ZnAB3P has almost the same structure) in the chapter 3.

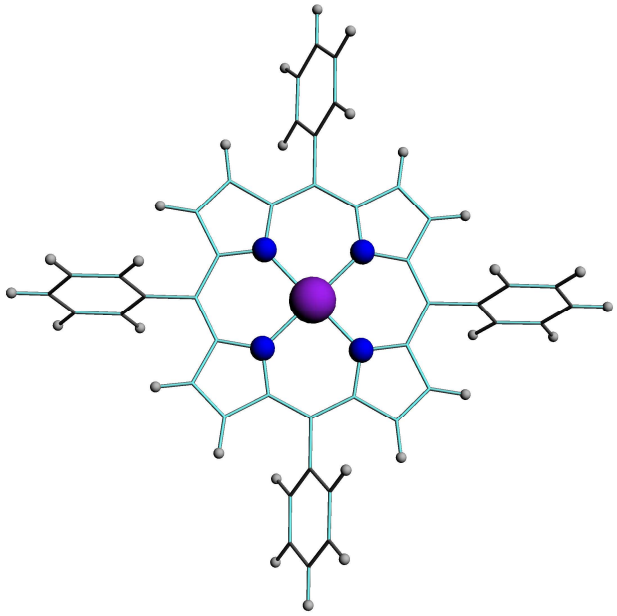

Figure I.37 ZnTPP porphyrin

Then, bridled porphyrins were been investigated. In these molecules, transition metal complexes of chiroporphyrins, in which two adjacent meso substituents are linked by a strap of 8 methylene groups, MBCP-8, can exist as either an *αααα (closed)* or *αβαβ (open)* atropisomer depending on the nature of the coordinated metal cation. We already described above which are the studied bridled porphyrins in this work and the advantages of using these types of molecules for further molecular memories. Also a deep theoretical investigation of Zn, Ni and MnBCP-8 is presented in chapter 3.

To summarize, porphyrins were chosen as the information storage medium because they exhibit a number of key properties [86-94], such as multiple cationic states that are accessible at relatively low potentials, affording multibit information storage with low power consumption. As candidates for emerging applications, they have been shown to be able to storing charge for extended periods, up to tens of minutes, in the absence of applied potential, further diminishing power consumption and significantly attenuating the refresh rates required in a memory device. In a well controlled and inert environment, the switching properties of molecules can endure up to 10^{10} cycles [95], which also indicate that the molecules are intrinsically stable during the redox processes.

Porphyrins are extremely suitable as building blocks and, like ferrocenes, can be easily functionalized with various tethers and linkers for attachment to different surfaces.

I.4.2 Attachment Methods

Functionalization of molecules on Silicon

The redox-active molecules are functionalized with tethers and linkers for stable attachment to different surfaces via formation of covalent bonds between the molecules and the substrate [96]. This approach is called functionalization and is employed for surface modification by using functional groups onto the surface.

The three commonly used tether/linkers are: (a) the vinyl tether for so-called direct grafting (b) $N_3(CH_2)_6$ linker and (c) $N_3(CH_2)_{11}$ linker for indirect grating to silicon surface. The linkers $N_3(CH_2)_6$ and $N_3(CH_2)_{11}$ are composed by an alkyl chain of 6 carbon atoms and 11 carbon atoms respectively. The N3 group (triazole) is the chemical function that forms a bond with the molecules.

Figure I.38 shows the tether/linkers that have been synthesized and theoretically investigated for grafting ferrocene and ZnAB3P (ZnTPP) on Si.

For both molecules, the direct grafting was obtained by hydrosilylation [97, 98] technique, while the indirect grafting that involved the two chemical linkers, $N_3(CH_2)_6$ (designated C_6) and $N_3(CH_2)_{11}$ (designated C_{11}) a particular technique, called "click chemistry" [99, 100] due to its self –assembling nature.

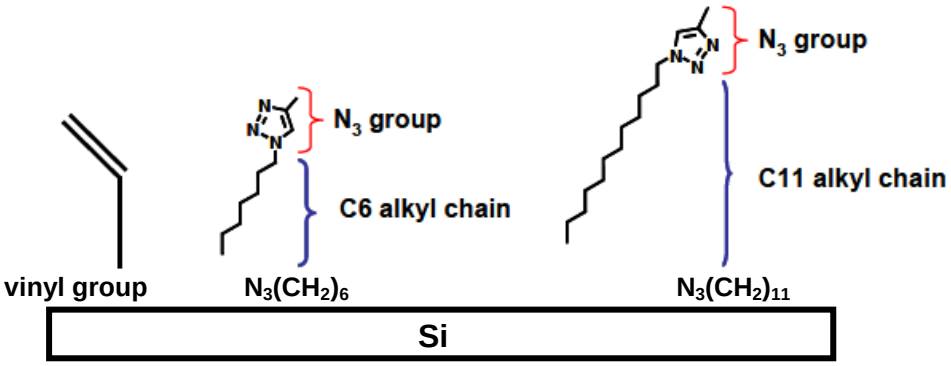

Figure I.38 Chemical structures of linkers and tethers: (a) vinyl tether, (b) $N_3(CH_2)_6$ linker, (c) $N_3(CH_2)_{11}$ linker

Both vinyl groups and C_6/C_{11} linkers imply a covalent Si-C bond. In figure I.39, are shown the directly grafted ferrocene using a vinyl group, and the C_6 and C_{11} linkers for the indirect grafting.

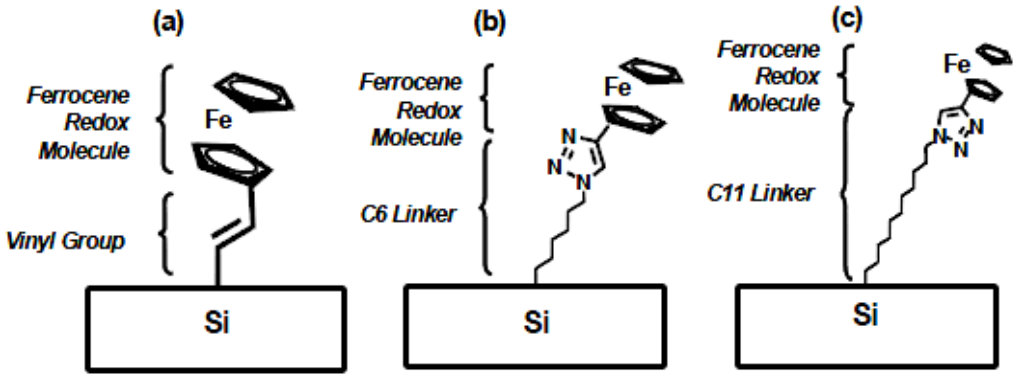

Figure I.39 Structures of linkers: (a) vinyl group; (b) C6 linker; (c) C11linker

The choice of the linker/tether is expected to provide flexibility in tuning the electrical behaviour of the device. It is expected that the charge transfer properties from/to the redox-active monolayer can be tuned by the use of a molecular linker. The chemical linker is expected to play the role of an insulating layer between the redox molecule and the silicon substrate and the insulating properties of the tunnel barrier should increase with the length of the linker.

I.4.3. Surface Characterization

The molecular layers were characterized mainly with X-ray photoelectron spectroscopy (XPS) and Atomic Force Microscopy (AFM). Cyclic voltammetry, capacitance and conductance voltage measurements were also performed on capacitor cells in order to characterize the charge transfer between the redox molecules and the Si and the effect of an organic linker on its rate.

II.3.1. X-ray Photoemission Spectroscopy (XPS)

X-ray Photoelectron Spectroscopy (XPS) [101, 102] is a surface chemical analysis technique based on the photoelectric effect. By monitoring the energy of X-ray excitation photons and measuring the kinetic energy of the expelled photoelectron, the energy associated with the bonding electrons from the elements in the surface of the sample can be determined. The energy of the photoelectrons leaving the sample gives a spectrum with a series of photoelectron peaks. The binding energies given by these peaks, which correspond to core electrons, are characteristic of each element, and of its hybridization. The peak areas can be used to determine the composition and ratio of different elements of the materials surface.

XPS measurements were performed in CEA/LETI. At every step of the silicon surface functionalization, the chemical composition was checked by XPS. As an illustration, in figure I.40 are shown some results of XPS measurements at the end of the grafting procedure for ferrocene direct grafted and indirect grafted including the C_6 and C_{11} long linkers.

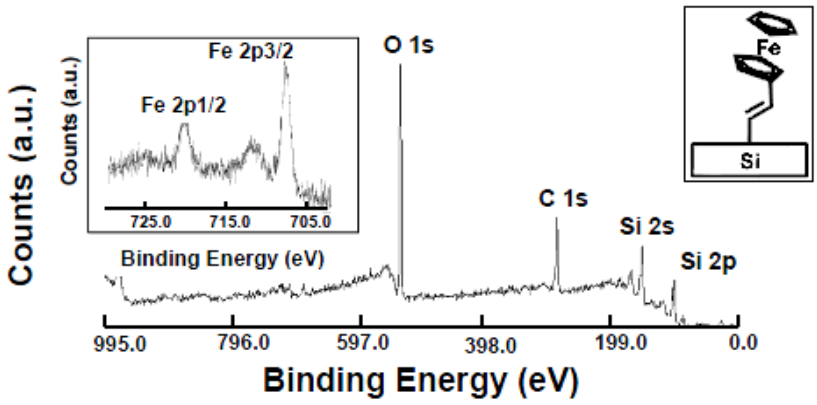

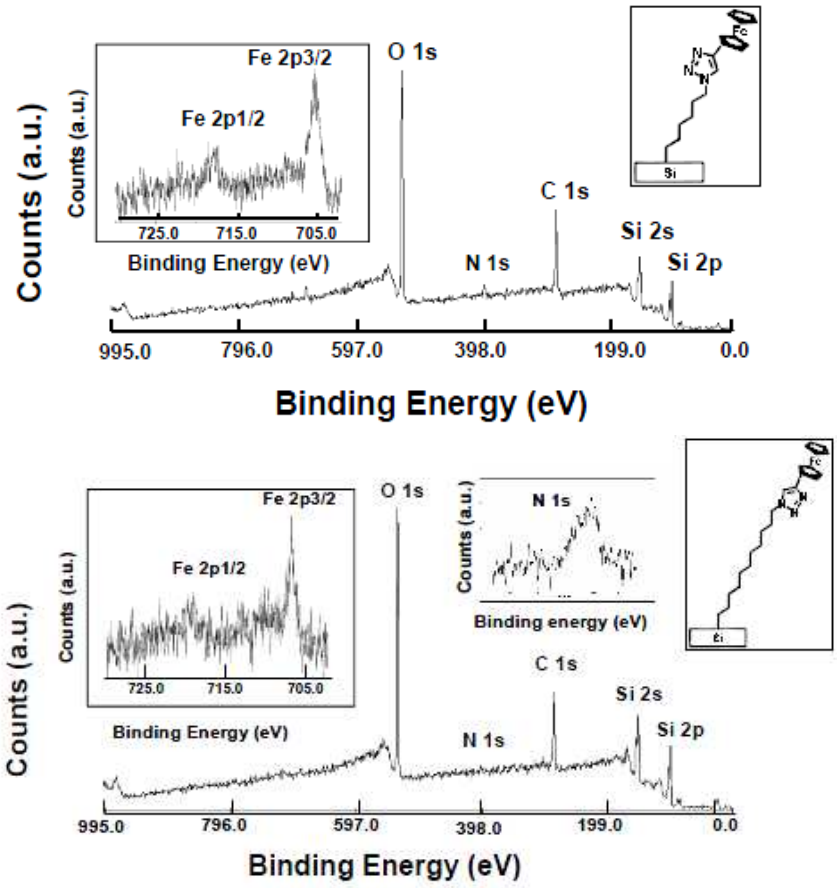

Figure I.40 XPS and HP-XPS spectra of ferrocene direct grafted and indirect grafted

The resulting spectra of Fc-Si reveal the presence of Si from the substrate, and also the presence of carbon, coming from the cyclopentadienyl rings of ferrocene. In the inset, a high-resolution XPS (HRXPS) spectrum shows the existence of Fe, coming from the central atom of the ferrocene molecules. In addition, for the two long linkers Fc-$N_3(CH_2)_6$-Si and Fc-$N_3(CH_2)_{11}$-Si, the XPS spectrum reveals the presence of nitrogen, coming from the triple-nitrogen group of the linker.

I.4.3.2. Atomic Force Microscopy (AFM)

AFM [103, 104] is one of the foremost tools for imaging, measuring, and manipulating matter at the nanoscale. The materials being investigating include thin and thick film

coatings, ceramics, composites, glass, synthetic and biological membranes, metals, polymer and semiconductors.

It is a method of measuring surface topography on a scale from angstroms to 100 microns. The technique involves imaging a sample through the use of a probe, or tip, with a radius of 20 nm. The tip is held several nanometers above the surface using a feedback Mechanism that measures surface–tip interactions on the scale of nano Newtons. Variations in tip height are recorded while the tip is scanned repeatedly across the sample, producing a topographic image of the surface.

Measurements were performed in CEA-LETI. The figure I.41 shows an example of the 3D AFM image of Fc directly grafted on Si.

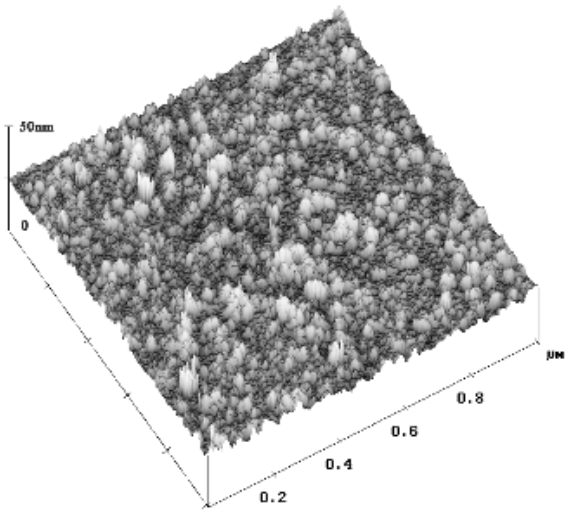

Figure I.41 3D AFM image of Fc directly grafted.

The diagram demonstrates the uniform distribution of ferrocene aggregates on the Si surface. Also, it was calculated the surface root mean square (RMS) roughness in the same case of ferrocene directly grafted (figure I.42).

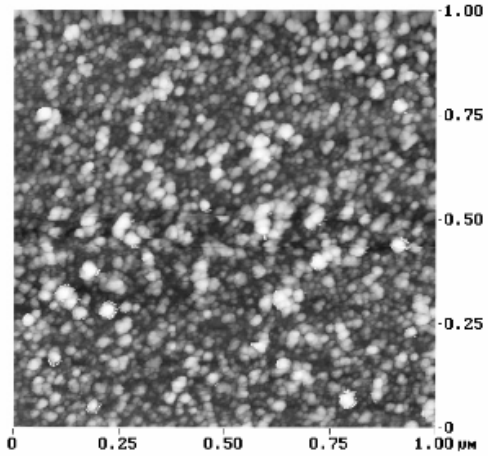

Figure I.42 AFM of Fc directly grafted

The RMS value calculated in the surface is of 3.3 nm. It was observed that the aggregate size was less than 10 nm.

I.4.3.3. Cyclic Voltammetry (CyV)

Cyclic voltammetry [105, 106] is the most widely used technique for acquiring qualitative information about electrochemical reactions. It is able to rapidly provide considerable information on the thermodynamics of redox processes and the kinetics of heterogeneous electron-transfer reactions, and on coupled chemical reactions or adsorption processes. The figure I.43 is shown the setup for typical cyclic voltammetry measurements. The solution component to be oxidized or reduced is in contact with an electrode surface on which is applied a voltage scan. When the surface becomes sufficiently negative or positive, a solution species may gain electrons from the surface or transfer electrons to the surface. This results in a measurable current in the electrode circuitry. When the voltage cycle is reversed, it is often the case that electron transfer between electrode and chemical species will also be reversed, leading to an “inverse” current peak. The system is then said to be reversible.

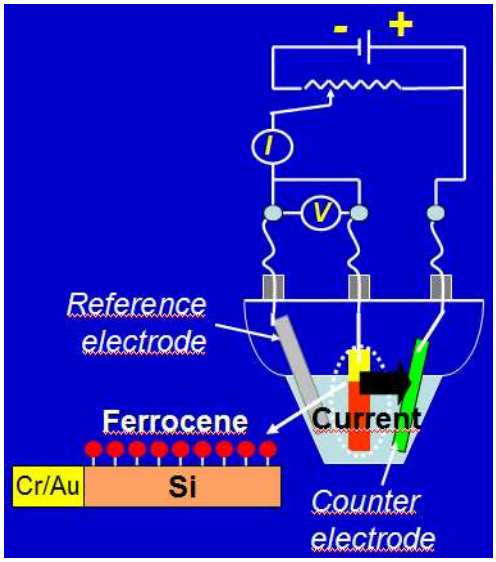

Figure I.43 Schematic of characterization setup for cyclic voltammetry

Figure I.44 shows a typical voltage sweep (a) and the resulting current-voltage characteristics (b) for a reversible redox species.

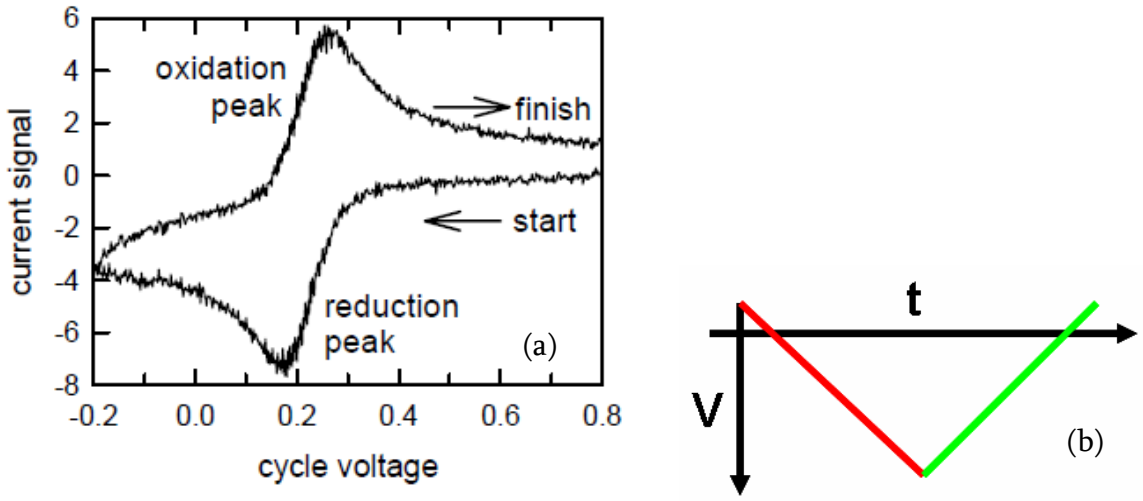

Figure I.44 (a) Example of Voltage scan vs. time during cyclic voltammetry; (b) Cyclic voltammetry (CyV) characteristics

Key parameters involved in this technique are the starting voltage, scan rate and the voltage range. Informations given by this technique on our grafted systems are firstly on

the fundamental redox properties of the redox molecules and also on the electronic behaviour of the grafted surface:

1. Oxidation and reduction peak voltages: these give the write and erase voltages that need to be applied to a memory cell.

2. Area under the oxidation and reduction peaks: it quantifies the density of molecules in the monolayer.

3. Peak separation: it depicts the speed of electron-transfer to and from the molecules. This also portrays the read window available for a non-destructive read of the memory cell when employed as a Flash device. The separation between the charging and discharging peaks increase with increasing scan rates, indicating that input scan rate is becoming comparable to the electron-transfer rate. Peak separation can also arise due to series resistance present in the system.

4. Scan rate dependence: a linear dependence of the peak current on the scan rate indicates that the molecules are strongly adsorbed to the underlying substrate. It gives also an estimate of the molecular coverage density, which was estimated in our samples to be *ca* 10^{13} molecules/cm^2. The area under the peaks vs. scan rate can also give a picture of the speed of electron-transfer.

CyV measurements were performed in CEA/LETI/DTBS on functionalized surfaces to prove molecule redox activity on Si. A solution of tetrabutylammonium hexafluoro phosphate in propylene carbonate (Bu_4N, PF_6/PC, 1.0 M) was used as supporting electrolyte, with Platinum as counter electrode and Saturate Calomel Electrode (SCE) as reference electrode. The functionalized Si surface played the role of the working electrode.

I.4.4. Capacitance -Voltage (CV) and Conductance-Voltage (GV) characterization

Electrical properties of molecules/Si systems were studied through capacitance-voltage (*C–V)* and conductance–voltage (*G–V*) measurements [107]. These are useful tools

to study semiconductor interfaces and charge trap mechanism as well as the charge storage behaviour in nanostructures.

The experiments were performed by the CEA/LETI. In figure I.45 is shown the electrochemical capacitor that was used for measurements. In order to contact the molecules, a gate made of a liquid electrolyte solution (propylene carbonate) was used in which was plunged a silver electrode. The gate voltage was thus applied on this silver tip.

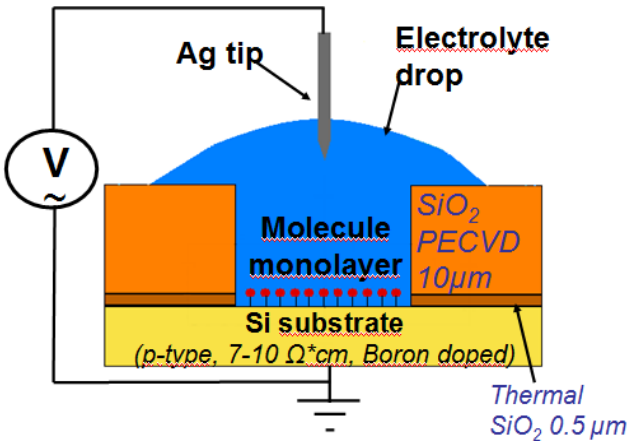

Figure I.45. Schematic electrochemical capacitors

Capacitance-voltage (C-V) and conductance-voltage (G-V) plots can be extracted similar to conventional semiconductor C-V and G-V measurements [108]. Typically, at a given frequency, these plots will exhibit peaks, both in capacitance and conductance, associated with redox property of the molecules (figure I.46).

In figure II.12, we observe one peak in the case of capacitance measurements, which intensity decreases for higher frequencies while in the case of conductance measurements the peak intensity increases for higher frequencies. Even at low frequency, the capacitance and conductance are such that the quality factor of the whole system is large enough to provide reasonable accuracy in the measurements.

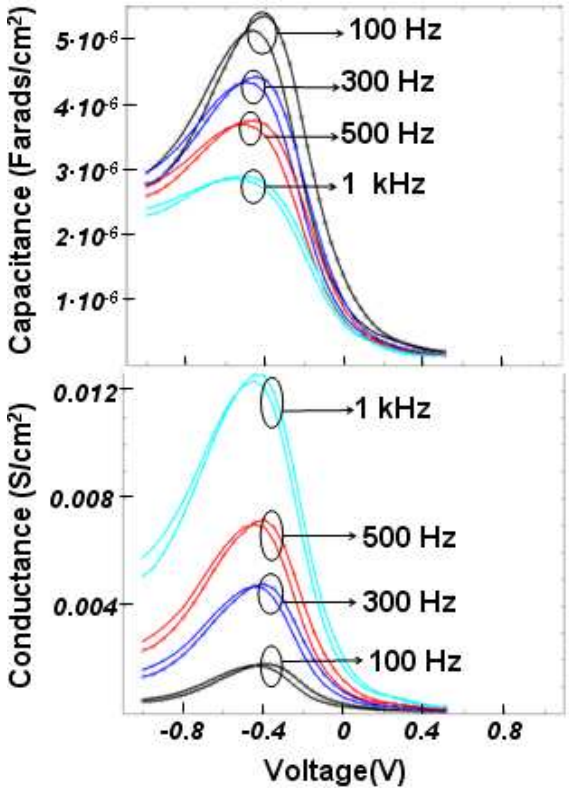

Figure I.46. Capacitance and conductance voltage measurements of ferrocene directly grafted

In figure I.46, we observe one peak in the case of capacitance measurements, which intensity decreases for higher frequencies while in the case of conductance measurements the peak intensity increases for higher frequencies. Even at low frequency, the capacitance and conductance are such that the quality factor of the whole system is large enough to provide reasonable accuracy in the measurements.

C-V and G-V were been used to characterize capacitor structures formed using these monolayers. Distinct capacitance and conductance peaks have been observed, which confirm the processes of charging and discharging of the molecules.

I.4.5. Electrical model

An original electrical model has been developed by the team of CEA/LETI, where the oxidation/reduction of the molecules grafted on Si is regarded as the filling/emptying process of traps at the Si interface (considered in a Shockley–Read–Hall approach [109], usually used for Si surface state modeling). This hypothesis was adopted in order to ease the elaboration of a physical model of molecules on the Si surface; the frequency behaviour observed experimentally suggests this approach. The associated equivalent electrical circuit is shown in figure I.47 showing a capacitor with a molecule layer directly grafted on the Si surface.

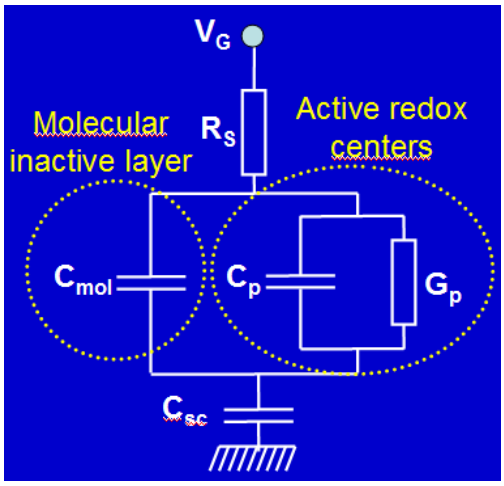

Figure I.47 Electrical model of hybrid molecule/Si electrochemical capacitors

In this circuit, *Rs* represents series resistance, C_{SC} the capacitance associated to the p-type semiconductor depletion region, and *Vg* the voltage signal. The capacitance related to the SiO_2 walls of the capacitor is not considered as the thickness of the dielectric (10.5 μm) makes its value negligible. The capacitance associated to the Si depletion region is calculated as follows:

$$C_{SC} = \frac{dQ_{SC}}{d\psi_S} \quad (2)$$

where $Q_{sc}(\psi_s)$ is the space charge per unit area, associated to the depletion region as a function of the Si surface potential ψ_s.

The molecules are modelled with two impedances in parallel: one related to the molecular layer not considering the redox centers *(C_{mol})* and the other one corresponding to the redox centers themselves *(Cp, Gp).* C_{mol} represents the capacitance of the organic layer, considered as a dielectric layer:

$$C_{mol} = \frac{\varepsilon_{mol}}{d_{mol}} \quad (3)$$

where ε_{mol} represents the dielectric constant of the molecular layer and d_{mol} is its thickness expressed as:

$$d_{mol} = d_{fc} + d_{linker} \quad (4)$$

where d_{fc} represents the diameter of the molecules, which has been set equal to 1 nm, while d_{linker} is the length of the linker. C_{redox} is the capacitance associated to the charged molecules/traps, and it corresponds to the variation of the total charge captured by the traps, Q_{redox}, depending on the variation of ψ_s.

$$C_{redox} = \frac{dQ_{redox}}{d\psi_s} \quad (5)$$

From the Shockley–Read–Hall theory [18], the dependence of total charge Q_{redox} over ψ_S is described by a Fermi function:

$$Q_{redox}(\psi_s) = qN_{mol}\frac{1}{1+\exp(-qE_{mol}(\psi_s)/kT)} \quad (6)$$

where N_{mol} is the molecule surface density in square centimeters, and k and T the Boltzmann constant and temperature, respectively. E_{mol} is the level energy of the trap from E_F and is defined as follows:

$$E_{mol}(\psi_s) = E_{mol-FB} + \frac{Q_{SC}(\psi_S)}{\varepsilon_{mol}}(d_{mol} - d_{redox}) - \psi_s \quad (7)$$

where $E_{mol\text{-}FB}$ is the energy level associated to the molecule redox center. d_{redox} is the distance of the redox center with respect to the Si surface. When the Fermi level of the system (E_F) approaches the redox energy of the molecule E_{mol}, a charge transfer occurs between the molecule and the Si. Equation (6) can thus be viewed as the energetic distance between E_F and the energy of the redox site $E_{mol\text{-}FB}$ in the presence of a specific surface potential and a dielectric layer between the redox site and the Si surface.

Thus an electrical model that could give qualitative trends of the energetic potential which allows an electron/hole transfer was developed. In figure I.48 are shown the diagrams which describe the electronic transfer mechanism in the oxidation/reduction states of the molecules.

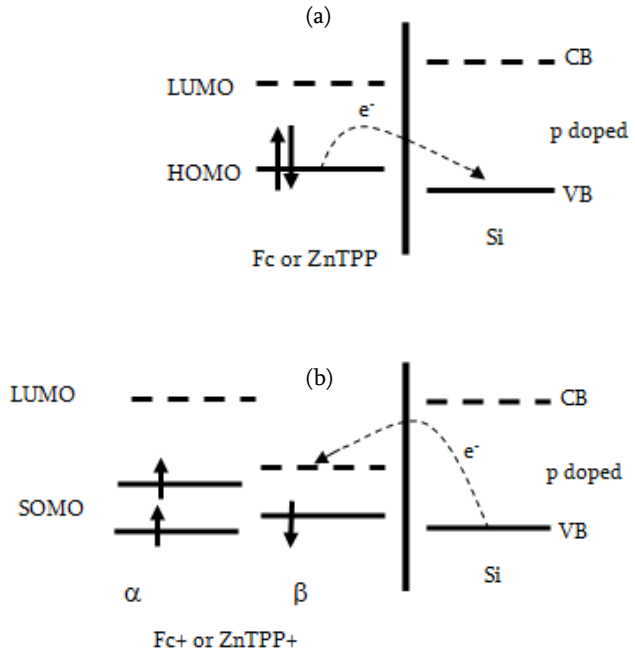

Figure I.14 Electron transfer from molecule to Si in the neutral (a) or charged species (b)

Starting from this model, we have interpreted this model in the framework of quantum chemistry DFT approach. In the resulting molecular diagrams of the molecule grafted on Si cluster, are given the energy levels of the HOMO and LUMO of the Si part compared to

the HOMO and LUMO of the molecular part (in neutral, or oxidized or reduced form). In figure I.48 a is shown the electron transfer in the neutral (reduced) state of the system. In this case the highest occupied molecular orbital (HOMO) is fully occupied and the paired electrons share the same spatial orbital and an electron transfer between this level and VB of the Si surface (if the surface is considered p doped) could take place. In figure I.48 b is shown the electron transfer in the charged (oxidized) state of the system. The situation is different now, due to the unpaired electron that appears in the system after charging. In this case are used two completely separate sets of orbitals for the α and β electrons (unrestricted Hartree-Fock). Because α orbital levels are fully occupied, the transfer of electron from the surface should occupy the unpaired β orbital levels of the molecules as shown in figure (I.48 b).

DFT molecular approach is able to reproduce such arrangement (in energy levels) and can describe the electronic transfer that occurs in our hybrid systems. The modeling capacitor could be useful in understanding the obtained electrical results and can furnish some physical and electrical explanations.

Bibliography

[1] Z. M. Liu, A. A. Yasseri, J. S. Lindsey, D. F. Bocian, *Science* 2003, *302*, 1543

[2] A. R. Pease, J. O. Jeppesen, J. F. Stoddart, Y. Luo, C. P. Collier, J. R. Heath, *Accounts Chem. Res.* 2001, *34*, 433

[3] C. P. Collier, E. W. Wong, M. Belohradsky, F. M. Raymo, J. F. Stoddart, P. J. Kuekes, R. S. Williams, J. R. Heath, *Science* 1999, *285*, 391

[4] J. M. Tour, W. L.Van Zandt, C. P. Husband, S. M. Husband, L. S.Wilson, P. D. Franzon, D. P. Nackashi, *IEEE Trans. Nanotechnol.* 2002, *1*, 2, 100

[5] J. R. Heath, M. A. Ratner, *Phys. Today* 2003, *56*, 43

[6] Y. Luo, V. Misra, *Nanotech*. 2006, *17*, 4909

[8] C. P. Collier, J. O. Jeppesen, Y. Luo, J. Perkins, E. W. Wong, J. R. Heath, J. F. Stoddart, *J. Am. Chem. Soc.* 2001, *123*, 12632

[9] Y. Huang, X. Duan, Y. Cui, L. J. Lauhon, K. H. Kim, C. M. Lieber, *Science* 2001, *294*, 1313

[10] X. Duan, Y. Huang, C. M. Lieber, *Nano Lett.* 2002, *2,* 487

[11] J. Chen, M. A. Reed, *Chem. Phys.* 2002, *281*, 127

[12] C. M. Carcel, J. K. Laha, R.S. Loewe, P. Thamyongkit, K. H. Schweikart, V. Misra, D.F. Bocian, J.S. Lindsey, *J. of Org. Chem*. 2004, *69*, 6739

[13] L. Selmi, Flash Memories, DIEGM- University of Udine, International Ph.D. Programme, 2005

[14] http://www.buzzle.com/articles/what-is-computer-ram-random-access-memory.html

[15] J. J. Makwana, D. K. Schroder, *A Nonvolatile Memory Overview*, A. P. Lawrence, 2004

[16] http://en.kioskea.net/contents/pc/rom.php3

[17] http://www.electronics-manufacturers.com/products/computer-hardware/computer-memory/eprom/

[18] J. C. Whitaker, *The electronics Handbook*, CRC Press, 1996

[19] S. Mueller, *Upgrading and Repairing PCs*, Pearson Education, 2003

[20] S. Vassiliadis, M. Berekovic, T. D. Hamalainen, *Embedded Computer Systems: Architectures, Modeling, and Simulation*, Springer Verlag, 2007

[21] S. M. Sze, K. K. Ng, *Physics of Semiconductor Devices,* Wiley, John & Sons, 2006

[22] L. Null, J. Lobur, *The essentials of computer organization and architecture*, Jones & Bartlett Publishers, 2006

[23] W.D. Brown, J. E. Brewer*, Nonvolatile Semiconductor Memory Technology*, IEEE Press, New York, 1998

[24] S. Mori, M. Sato, Y. Mikata, T. Yanase, K. Yoshikawa, *IEEE Trans. on El. Dev.*, 1991 *38*, 386

[25] http://www.imec.be/wwwinter/mediacenter/en/SR2005/html/142290.html

[26] G. Campardo, R. Micheloni, D. Novosel, *VLSI-Design of Non-Volatile Memories*, Springer-Verlag, 2005

[27] P. Pavan, L. Larcher, A. Marmiroli, *Floating Gate Devices,* Springer-Verlag, 2008

[28] http://klabs.org/richcontent/MemoryContent/nvmt_symp/nvmts_2002/ docs/02/02_ mikolajic_a.pdf

[29] B. Prince, *Emerging Memories, Technologies and Trends*, Kluwer Academic Publishers, 2002

[30] J. Hutchby et al., *Extending the Road Beyond CMOS*, IEEE Circuits & Devices Magazine, 28, 2002

[31] http://scholar.lib.vt.edu/theses/available/etd-050699-154541/unrestricted /Chapter1.pdf

[32] T. Mikolajick, C. Dehm, W. Hartner, I. Kasko, M. J. Kastner, N. Nagel, M. Moert, C. Mazure, *Microelec. Rel.* 2001, *41*, 947

[33] http://klabs.org/richcontent/MemoryContent/nvmt_symp/nvmts_2002/docs/02/ 02_mikolajic_a.pdf

[34] S. Lai, *Future Trends in Non-Volatile Memory Technology*, Intel Developer Forum, 2002

[35] Ju. H. Krieger, *Struct. Chem*. 1999, *40*, 594

[36] Ju. H. Krieger, S. V. Trubin, S. B. Vaschenko, N. F. Yudanov, *Synt. Met.* 2001, *122*, 199

[37] Ju. H. Krieger, N. F. Yudanov, I. K. Igumenov S. B. Vaschenko, *J. Struct. Chem.* 1993, *34*, 966

[38] R. S. Potember, T. O. Poehler, D. O. Cowan, *Appl. Phys. Lett*. 1979, *34*, 405

[39] D. Ma, M. Aguire, J. A. Freire, I. A. Huemmelgen, *Adv. Mater.* 2000, *12*, 106

[40] K. Sakai, H. Kawada, K. Eguchi, T. Nakagiri, *Appl. Phys. Lett.* 1988, *53*, 1274

[41] H. K. Henisch, J. A. Meyers, *Thin Solid Films* 1978, *51*, 265

[42] W. den Boer, *Appl. Phys. Lett*. 1982, *40*, 812

[43] A. E. Owen, P. G. Lecomber, J. Hajto, M. J. Rose, A. Snell., *Int. J. Elect.* 1992, *73,* 89

[44] M. Jafar, D. Haneman, *Phys. Re*v. *B* 1994*, 49,* 13611

[45] A. Avila, R. Asomoza, *Solid-State Electron,* 2000, *44*, 17

[46] J. Hu, H. M. Branz, R. S. Crandall, S. Ward, Q. Wang, *Thin Solid Films* 2003**,** *430*, 249

[47] Y. Chen, D. Ohlberg, X. Li, D. Stewart, R. Williams, J. Jeppesen, K. Nielsen, J. Stoddart, D. Olynick, E. Anderson, *Appl. Phys. Lett*. 2003, *82,* 1610

[48] C. Collier, E. Wong, M. Belohradsky, F. Raymo, J. Stoddart, P. Kuekes, R. Williams, J. Heath, *Science* 1999, *285*, 391

[49] M. A. Reed, J. Chen, A. M. Rawlett, D. W. Price, J. M. Tour, *Appl. Phys. Lett*. 2001, *78*, 3735

[50] M. A. Reed, D.W. Bennett, J. Chen, D. S. Grubisha, L. Jones, A. M. Rawlett, J. M. Tour, *IEDM Techn. Digest* 1999, 227

[51] Y. Chen, G. Jung, D. Ohlberg, X. Li, D. Stewart, J. Jeppesen, K. Nielsen, J. Stoddart, R. Williams, *Nanotech.* 2003, *14*, 462

[52] J. Heath, P. Kuekes, G. Snider, R. Williams, *Science* 1998, *280*, 1716

[53] D. Stewart, D. Ohlberg, P. Beck, Y. Chen, R. Williams, J. Jeppesen, K. Nielsen, J. Stoddart, *Nano Lett.* 2004, *4*, 133

[54] R. J. Luyken, F. Hofmann, *Nanotech.* 2003*, 14*, 273

[55] J. E. Green, J. W. Choi, A. Boukai, Y. Bunimovich, E. J. Halperin, E. DeIonno, Yi Luo, B. A. Sheriff, Ke Xu, Y. S. Shin, H.R. Tseng, J. F. Stoddart, J. R. Heath, *Nature* 2007, *445*, 415

[56] T. Rueckes, K. Kim, E. Joselevich, G. Y. Tseng, C. L. Cheung, C. M. Lieber , *Science* 2000, *289*, 94

[57] Q. Li, G. Mathur, S. Gowda, S. Surthi, Q. Zhao, L. Yu, J. S. Lindsey, D. F. Bocian, V. Misra , *Adv. Mater*. 2004, *16,* 2

[58] Z. Liu, A. A. Yasseri, J. S. Lindsey, D. F. Bocian, *Science* 2003, *302*, 28

[59] G. Mathur, S. Gowda, Q. Li, S. Surthi, Q. Zhao, V. Misra, *IEEE Transactions on Nanotech.* 2005, *4*, 2

[60] http://www.zettacore.com

[61] http://www.stanford.edu/class/ee380/Abstracts/Zettacore.pdf

[62] R. K. Venkatesan, A. S. Al-Zawawi, K. Sivasubramanian, Eric Rotenberg, IEEE Trans. on Comp., 2007, *56*, 147

[63] X. Duan, Y. Huang, C. M. Lieber, *Nano Lett.* 2002, *2*, 487

[64] C. Li, D. Zhang, S. Han, X. Liu, T. Tang, C. Zhou, *Adv. Mater*. 2003, *15*, 143

[65] D. Zhang, C. Li, S. Han, X. Liu, T. Tang, W. Jin, C. Zhou, *Appl. Phys. Lett*. 2003, *82*, 112

[66] C. Li, W. Fan, B. Lei, D. Zhang, S. Han, X. Liu, Z. Liu, S. Asano, M.Meyyappan, J. Han, C. Zhou, *Appl. Phys. Lett.* 2004, *84*, 1949

[67] C. Li, W. Fan, D. A. Straus, B. Lei, S. Asano, D. Zhang, J. Han, M. Meyyappan, C. Zhou, *J. Am. Chem. Soc.* 2004, *126*, 7750

[68] C. Li, J. Ly, B. Lei, W. Fan, D. Zhang, J. Han, M. Meyyappan, M. Thompson, C. Zhou, *J. Phys. Chem. B* 2004*, 108*, 9646

[69] D. X. Shi, Y. L. Song, H. X. Zhang, P. Jiang, S. T. He, S. S. Xie, S. J. Pang , H. J. Gao, *Appl. Phys. Lett.* 2000, *77*, 3203

[70] D. X. Shi, Y. L. Song, D. B. Zhu, H. X. Zhang, P. Jiang, S. S. Xie, S. J. Pang, H. J. Gao, *Adv. Mater*. 2001, *13*, 1103

[71] M. Feng, X. F. Guo, X. Lin, X. B. He, W. Ji, S. X. Du, D. Q. Zhang, D. B. Zhu, H. J. Gao, *J. Am. Chem. Soc.* 2005, *127*, 15338

[72] A. J. L. Pombeiro, M. F. C. Guedes da Silva, M. A. N. D.A Lemos, *Coord. Chem. Rev.* 2001, *219*, 53

[73] M. Sano, *Adv. in Coll. and Int. Science* 1997, *71-72*, 93

[74] A. Yeh, N. Scott, H. Taube, *Inorg. Chem.* 1982, *21,* 2543

[75] C. Bucher, J. C. Moutet, J. Pécaut, G. Royal, E. Saint-Aman, F. Thomas, *Inorg. Chem.* 2004, *43*, 3777

[76] H. Kim, W. A. Goddard III, S. S. Jang, W. R. Dichtel, J. R. Heath, J. F. Stoddart, *J. Phys. Chem.* 2009, *113,* 2136

[77] Yi Luo, C. P. Collier, J. O. Jeppesen, K. A. Nielsen, E. DeIonno, G. Ho, J. Perkins, H. R. Tseng, T. Yamamoto, J. F. Stoddart, J. R. Heath, *ChemPhysChem* 2002, *3,* 519

[78] V. Balzani, A. Credi, F. M. Raymo, J. F. Stoddart, *Angew. Chem. Int. Ed*. 2000, *39*, 3348

[79] S.Gazeau, J. Pécaut, R. Haddad, J. A. Shelnutt, J-C. Marchon, *Eur. J. Inorg. Chem.* 2002*, 11*, 2956

[80] T. J. Kealy, P. L. Pauson, *Nature* 1951*, 168*, 1039

[81] G. Wilkinson, M. Rosenblum, M. C. Whiting, R. B. Woodward, *J. Am. Chem. Soc.* 1952, *74*, 2125

[82] R. Dagani, *Chem. & Eng. News* 2001, *79* (49), 37

[83] C. E. D. Chidsey, *Science* 1991, *251*, 919

[84] T. W. G. Solomons, C. B. Fryhle, Organic Chemistry. 9th ed. USA: John Wiley & Sons, Inc., 2006.

[85] K. M. Kadish, E. Van Caemelbecke, J. Sol. St. Electro. 2003, *7*, 5, 254

[86] K. M. Roth, N. Dontha, R. B. Dabke, D. T. Gryko, C. Clausen, J. S. Lindsey, D.F. Bocian, W. G. Kuhr, *J. Vac. Sci. Technol. B* 2000, 1*8*, 2359

[87] K. M. Roth, R. B. Dabke, Z. Liu, A. A. Yasseri, D. T. Gryko, C. Clausen, J. S. Lindsey, D. F. Bocian, W. G. Kuhr, *ACS Symp. Series,* Oxford University Press*,* 2002*,* 844

[88] D. Gryko, J. Li, J. R. Diers, K. M. Roth, D. F. Bocian, W. G. Kuhr, J. S. Lindsey, *J. Mater. Chem.* 2001, *11,* 1162

[89] K. M. Roth, J. S. Lindsey, D. F. Bocian, W. G. Kuhr, *Langmuir* 2002, *18*, 4030

[90] D.T. Gryko, C. Clausen, K. M. Roth, N. Dontha, D. F. Bocian, W. G. Kuhr, J. S. Lindsey, *J. Org. Chem.* 2000, *65*, 7345

[91] D. T. Gryko, F. Zhao, A. A. Yasseri, K. M. Roth, D. F. Bocian, W. G. Kuhr, J. S. Lindsey, *J. Org. Chem.* 2000, *65*, 7356

[92] C. Clausen, D. T. Gryko, R. B. Dabke, N. Dontha, D. F. Bocian, W. G. Kuhr, J. S. Lindsey, *J. Org. Chem.* 2000, *65*, 7363

[93] C. Clausen, D. T. Gryko, A. A. Yasseri, J. R. Diers, D. F. Bocian, W. G. Kuhr, J. S. Lindsey, *J. Org. Chem.* 2000, *65*, 7371

[94] J. Li, D. Gryko, R. B. Dabke, J. R. Diers, D. F. Bocian, W. G. Kuhr, J. S. Lindsey, *J. Org. Chem.* 2000, *65*, 7379

[95] Z. Liu, A. Yasseri, J. Lindsey, D. Bocian, *Science* 2003, *302*, 1543

[96] D. T. Gryko, C. Clausen, K.M. Roth, N. Dontha, et al, *J. Org. Chem*. 2000, 65, *22*, 7345

[97] M. R. Linford, P. Fenter, P. M. Eisenberger, C. E. D. Chidsey, J. Am. Chem. Soc. 1995, *117*, 3145

[98] B. Marciniec, *Hydrosilylation*, Springer-Verlag New York, 2008

[99] H. C. Kolb, M. G. Finn, K. B. Sharpless, *Angewandte Chem. Int. Edition* 2001*, 40* (11), 2004

[100] W. H. Zhan, W. J. Wu, J. L. Hua, Y. H. Jing, F. S. Meng, H. Tian, *Tetrahedron Lett.* 2007, 48, 2461

[101] B. G. Yacobi, D. B. Holt, L. L. Kazmerski, *Microanalysis of Solids*, Springer-Verlag New York, 1995

[102] F. de Groot, A. Kotani, *Core Level Spectroscopy of Solids*, Taylor & Francis*, 2008*

[103] S. H. Cohen, M. L. Lightbody, *Atomic Force Microscopy/Scanning Tunneling Microscopy 3*, Springer-Verlag, 1999

[104] Z. L.L. Wang, Yi Liu, Ze Zhang, *Handbook of Nanophase and Nanostructured Materials: Characterization,* Springer-Verlag New York, 2002

[105] http://www.veeco.com/

[106] A. J. Bard, L. R. Faulkner, *Electrochemical methods: fundamentals and applications*, 2 ed., John Wiley & Sons, 2001

[107] A. M. Bond, *Broadening Electrochemical Horizons: Principles and Illustration of Voltammetric and Related Techniques*: Oxford University Press, 2002

[108] A. Jacubowski, *Diagnostic Measurements in LSI and VLSI Integrated Circuits Production*, World Scientific Publishing Company, 1991

[109] J. R. Brews, E. H. Nicollian, *MOS (Metal Oxide Semiconductor) Physics and Technology*, Wiley, 2002

Chapter II
Theory and Methodology

Introduction

The Schrödinger picture of quantum mechanics [1, 2] remains the most used, principally because it has proven to be the simplest to use in practical calculations. Solutions of the Schrödinger wave equation give in principle a complete understanding of the properties of matter at the atomic scale. The time-independent Schrödinger equation has the form:

$$\hat{\mathrm{H}}\psi_i(\vec{x}_1,\vec{x}_2...,\vec{x}_N,\vec{y}_1,\vec{y}_2,...,\vec{y}_M) = E_i\psi_i(\vec{x}_1,\vec{x}_2...,\vec{x}_N,\vec{y}_1,\vec{y}_2,...,\vec{y}_M) \quad (1.1)$$

where $\hat{\mathrm{H}}$ is the Hamiltonian operator for a molecular system consisting of M nuclei (position vector y_i) and N electrons (position vector x_i) in the absence of magnetic or electric field. The wave function ψ is a function of the electron and nuclear positions. $\hat{\mathrm{H}}$ is a differential operator representing the total energy which has the form (in atomic units):

$$\hat{\mathrm{H}} = -\frac{1}{2}\sum_{i=1}^{N}\nabla_i^2 - \frac{1}{2}\sum_{A=1}^{N}\frac{1}{\mathrm{M}_A}\nabla_A^2 - \sum_{i=1}^{N}\sum_{A=1}^{M}\frac{Z_A}{r_{iA}} + \sum_{i=1}^{N}\sum_{j>i}^{N}\frac{1}{r_{ij}} + \sum_{A=1}^{M}\sum_{B>A}^{M}\frac{Z_A Z_B}{r_{AB}} \quad (1.2)$$

In equation (1.2), A and B run over the M nuclei while i and j indicate the N electrons in the system. The first two terms express the kinetic energy of the electrons and nuclei respectively, with $\mathrm{M_A}$ being the mass of nucleus A. The last three terms define the

potential energy part of the Hamiltonian and represent the attractive electrostatic interaction between the nuclei and the electrons and the repulsive potential due to the electron-electron and nucleus-nucleus interactions, respectively.

But the Schrödinger equation can be further simplified if we take advantage of the significant difference between the masses of nuclei and electrons. The nuclei move much slower than the electrons, thus it is possible to separate the nuclear and electron motions. This is called the Born-Oppenheimer (B-O) approximation [3]. With the nuclei fixed in space, the nuclear-nuclear repulsion potential is a constant and the nuclear kinetic energy is of course, zero. The Hamiltonian for a molecule in the B-O approximation is:

$$\hat{\mathrm{H}}_{elec} = -\frac{1}{2}\sum_{i=1}^{N}\nabla_i^2 - \sum_{i=1}^{N}\sum_{A=1}^{M}\frac{Z_A}{r_{iA}} + \sum_{i=1}^{N}\sum_{j>i}^{N}\frac{1}{r_{ij}} \quad (1.3)$$

The first term in this equation is the kinetic energy of the electrons. The second term is the attraction of electrons to nuclei with charge Z_A. The last term represents the repulsion between electrons. The repulsion between nuclei is added onto the energy at the end of the calculation. The motion of nuclei can be described by considering this entire formulation to be a potential energy surface on which nuclei move. The total energy E_{tot} is given by the sum of electron energy and the constant nuclear repulsion term:

$$\mathrm{E}_{tot} = E_{elec} + E_{nuc} \quad (1.4)$$

The probability of finding the N electrons anywhere in space must be exactly:

$$\int\ldots\int\left|\psi(\vec{x}_1,\vec{x}_2,\ldots\vec{x}_N)\right|^2 d\vec{x}_1, d\vec{x}_2,\ldots, d\vec{x}_N = 1 \quad (1.5)$$

A wave function which satisfies this equation is considered to be normalized. In the following parts, we will exclusively work with normalized wave functions.

II.1. Hartree – Fock Theory

II.1.1. The variational principle

By definition, the ground state has the lowest energy, and therefore any trial wave function will have energy greater than or equal to the ground state energy [4]. The expectation energy given by Hamiltonian for any trial wave function must be greater or equal to the actual ground state energy. In other words:

$$\left\langle \psi_{trial} \left| \hat{\mathrm{H}} \right| \psi_{trial} \right\rangle = E_{trial} \geq E_{ground} = \left\langle \psi_{ground} \left| \hat{\mathrm{H}} \right| \psi_{ground} \right\rangle \quad (1.6)$$

Thus, by varying the guessed ψ_{trial} until the expectation value of E_{trial} is minimized we can obtain an approximation to the wave function and energy of the ground-state. The strategy for finding the ground state energy and wave function is based on minimization of the functional $\left\langle \psi_{trial} \left| \hat{\mathrm{H}} \right| \psi_{trial} \right\rangle$ by searching through all acceptable N-electron wave functions. While such a search over all eligible functions is not possible, may restrict the search to some subsets of all possible functions:

$$E_{ground} \cong \min_{\psi \to N} E[\psi] = \min_{\psi \to N} \left\langle \psi \left| \hat{T} + \hat{V}_{Ne} + \hat{V}_{ee} \right| \psi \right\rangle \quad (1.7)$$

The result will be the best approximation to the exact wave function that can be obtained from this particular subset. It is important to realize that by restricting the search to a subset, the exact wave function itself cannot be identified. In the following discussions we will treat the Hartree-Fock approximation where the subset consists of all antisymmetric products (Slater determinants) composed of N spin orbitals.

Despite its apparent simplicity, this principle is extremely powerful and forms the basis for the vast majority of large scale quantum calculations carried out in current research.

II.1.2. Hartree-Fock approximation. Slater determinant.

As discussed above, it is impossible to solve equation (1.7) by searching through all acceptable N-electron wave functions. One simple way to approximate the wave function of a many-particle system is to take the product of properly chosen wave functions of the individual particles:

$$\psi(x_1, x_2 ... x_N) = \chi_1(x_1)\chi_2(x_2)\cdots\chi_N(x_N) \quad (1.8)$$

The one electron functions $\chi_i(\vec{x}_i)$ are called spin orbitals and consist of a product of one spatial orbital $\phi_i(\vec{r})$ and one of the two spin functions α or β. The spin independent wave function ψ is thus equal with:

$$\Psi(r_1, r_{2,\cdots,} r_N) = \phi_1(r_1)\phi_2(r_2)...\phi_N(r_N) \quad (1.9)$$

This expression is used in the Hartree method for the many-particle wave function and is known as a Hartree product. However, it is not satisfactory for fermions, such as electrons, because the wave function is not antisymmetric with respect to the exchange of two electrons. Therefore the Hartree product does not satisfies the Pauli principle. This problem was fixed by the introduction of Slater determinants.

Slater determinants

We can describe the wave function with a Slater determinant [5]:

$$\Psi \approx \Phi_{SD} = \frac{1}{\sqrt{N!}} \begin{vmatrix} \chi_1(x_1) & \chi_2(x_1) & \cdots & \chi_N(x_1) \\ \chi_1(x_2) & \chi_2(x_2) & \cdots & \chi_N(x_2) \\ \vdots & \vdots & \ddots & \vdots \\ \chi_1(x_N) & \chi_2(x_N) & \cdots & \chi_N(x_N) \end{vmatrix} \quad (1.10)$$

The $\frac{1}{\sqrt{N!}}$ pre-factor ensures that Φ_{SD} fulfils the normalization condition. An interesting consequence of this functional form is that the electrons are all indistinguishable, consistent with the results of quantum mechanics. This method breaks the many-electron Schrödinger equation into simpler one-electron equations. Each one-electron equation is solved to yield a single-electron wave function, called an orbital, and an energy, called an orbital energy.

The one-electron functions $\chi_i(\vec{x}_i)$ are called spin orbitals, and are composed of a spatial orbital $\phi_i(\vec{r})$ and one of the two spin functions, $\alpha(s)$ or $\beta(s)$:

$$\chi(\vec{x}) = \phi(\vec{r})\sigma(s) \quad \sigma = \alpha, \beta \quad (1.11)$$

The spin functions are orthonormal, $\langle\alpha|\alpha\rangle = \langle\beta|\beta\rangle = 1$ and $\langle\alpha|\beta\rangle = \langle\beta|\alpha\rangle = 0$

Usually, the spin orbitals themselves are chosen to be orthonormal and have the form:

$$\int \chi_i^*(\vec{x})\ \chi_i(\vec{x})d\vec{x} = \langle\chi_i|\chi_j\rangle = \delta_{ij} \quad (1.12)$$

where δ_{ij} is the Kronecker delta symbol and equals 1 for i = j and 0 otherwise. If the form of the wave function is known, the next step is to use the variational principle in order to find the best Slater determinant Φ_{SD} that yields the lowest energy.

II.1.3. Energy expression

We consider that Hartree-Fock wave function has the form of a Slater determinant, and the energy will be given by the usual quantum mechanical expression:

$$E_{elec} = \langle\psi|\hat{H}|\psi\rangle \quad (1.13)$$

The only flexibility in a Slater determinant is provided by the spin orbitals. They are varied under the constraint to remain orthonormal and that the energy obtained from the corresponding Slater determinant is minimal:

$$E_{HF} = \min_{\Phi_{SD} \to N} E[\Phi_{SD}] \qquad (1.14)$$

The Hartree -Fock energy will be:

$$E_{HF} = \langle \Phi_{SD} | \hat{H} | \Phi_{SD} \rangle = \sum_{i}^{N} (i|\hat{h}|i\rangle + \frac{1}{2} \sum_{i}^{N} \sum_{j}^{N} (ii \mid jj) - (ij \mid ji) \qquad (1.15)$$

where the term:

$$\langle i|\hat{h}|i\rangle = \int \chi_i^*(\vec{x}_1) \left\{ -\frac{1}{2}\nabla^2 - \sum_{A}^{M} \frac{Z_A}{r_{1A}} \right\} \chi_i(\vec{x}_1) d\vec{x}_1 \qquad (1.16)$$

is monoelectronic, and represents the kinetic energy and electron-nucleus attraction and:

$$\begin{aligned} (ii \mid jj) &= \int\int |\chi_i(\vec{x}_1)|^2 \frac{1}{r_{12}} |\chi_j(\vec{x}_2)|^2 d\vec{x}_1 d\vec{x}_2 \\ (ij \mid ji) &= \int\int \chi_i(\vec{x}_1) \chi_j^*(\vec{x}_1) \frac{1}{r_{12}} \chi_j(\vec{x}_2) \chi_i^*(\vec{x}_2) d\vec{x}_1 d\vec{x}_2 \end{aligned} \qquad (1.17)$$

give the so-called Coulomb and exchange bielectronic integrals, respectively.

II.1.4. Hartree-Fock equations

Hartree-Fock energy expression should be minimized with respect to the changes in orbitals. In addition, the constraint that the $\{\chi_i\}$ set remains orthonormal must be satisfied throughout the minimization, and that introduces the Lagrangian multipliers in the resulting equations. For achieving this, the Hartree-Fock equations [6, 7] are expressed as:

$$\hat{f}\chi_i = \varepsilon_i \chi_i \text{, where } i = 1, 2, \ldots N \qquad (1.18)$$

The equations (1.18) represent the Hartree - Fock equations, which determine the 'best' spin orbitals. The Lagrangian multipliers yield N eigenvectors being the monoelectron orbitals, and eigenvalues ε_i being the corresponding orbital energies. The Fock operator $\hat{f}$ appears like a one electron operator:

$$\hat{f}_i = -\frac{1}{2}\nabla_i^2 - \sum_A^M \frac{Z_A}{r_{iA}} + V_{HF}(i) \quad (1.19)$$

The first two terms in equation (1.19) represent the kinetic energy and the potential energy due to the electron nucleus attraction. $V_{HF}(i)$ represents the Hartree-Fock potential. Thus, the complicated two-electron repulsion operator is replaced by a sum of simple one electron operators $V_{HF}(i)$ where the electron-electron repulsion is taken into account only in an average way. V_{HF} potential has the following two components:

$$V_{HF}(\vec{x}_1) = \sum_j^N [\hat{J}_j(\vec{x}_1) - \hat{K}_j(x_1)] \quad (1.20)$$

where the Coulomb operator $\hat{J}$ is:

$$\hat{J}_j(\vec{x}_1) = \int |\chi_j(\vec{x}_2)|^2 \frac{1}{r_{1,2}} d\vec{x}_2 \quad (1.21)$$

and represents the potential seen by an electron 1 due to the average charge distribution of electron 2 in spin orbital χ_j. This interaction is integrated over all space and spin coordinates. Because the results of $\hat{J}_j(\vec{x}_1)$ on a spin orbital $\chi_i(\vec{x}_1)$ depend only on the value of χ_i at position $\vec{x}_1$, this operator and the corresponding potential are called local.

The second term in equation (1.20) is the exchange contribution to the Hartree-Fock potential where the exchange operator $\hat{K}$ can be defined through its effect when operating on a spin orbital:

$$\hat{K}_j(x_1)\chi_n(x_1) = \int \chi_j^*(x_2)\frac{1}{r_{1,2}}\chi_n(\vec{x}_2)d\vec{x}_2\chi_j(\vec{x}_1) \qquad (1.22)$$

This operator and the corresponding exchange potential are called non-local.

Hartree-Fock theory is fundamental to electronic structure theory. It is the basis of molecular orbital (MO) theory, which implies that each electron's motion can be described by a single-particle function (orbital) which does not depend explicitly on the instantaneous motions of the other electrons.

The major problem in Hartree – Fock approximation comes from the fact that it doesn't take into account the electron correlation which can lead to large deviations from experimental results. A number of approaches to this weakness, collectively called post Hartree–Fock methods, have been devised to include electron correlation to the multi-electron wave function. (See II.1.7).

II.1.5. Restricted and Unrestricted Hartree-Fock models

A variation on the Hartree-Fock procedure is the way that orbitals are constructed to exhibit paired or unpaired electrons [8]. If the molecule is closed -shell, then the same orbital spatial function can be used for both 'α' and 'β' spin electrons in each pair. This is called the restricted Hartree - Fock method (RHF). Every electron feels the Coulomb repulsion from every other electron, while the exchange interaction only occurs between electrons with the same spin.

There are two techniques for constructing HF wave functions of molecules with unpaired electrons. One technique is to use two completely separate sets of orbitals for the 'α' and 'β' electrons. This is called unrestricted Hartree - Fock theory (UHF). This means that paired electrons will not have the same spatial distribution and may introduce an error into the calculation due to spin contamination. UHF calculations are popular

because they are easy to implement and run fairly efficiently. It is the most common molecular orbital method for open shell molecules.

Another way of constructing wave functions for open-shell molecules is the restricted open shell Hartree-Fock method (ROHF). In this method, the paired electrons share the same spatial orbital. Thus, there is no spin contamination. The ROHF technique is more difficult to implement than UHF and may require slightly more CPU time to execute. ROHF is primarily used for cases where spin contamination is large using UHF model.

II.1.6. The Roothan-Hall equations

Molecular orbitals can be obtained numerically using integration over a grid, or (much more commonly) as a linear combination of a set of given basis functions so-called ''atomic orbital'' basis functions (LCAO). These basic functions are generally centered on the nucleus of different atoms of the molecule. Thus, the molecular orbitals can be written as:

$$\chi_i = \sum_{\mu=1}^{K} C_{\mu_i} \tilde{\chi}_\mu \qquad \text{where } \chi_\mu \text{ are atomic orbitals} \quad (1.23)$$

The calculation of molecular orbitals is limited now on the determination of coefficients C_{μ_i}. This leads to equations of Roothaan and Hall [9, 10], that introduced a basis set which transforms the Hartree –Fock equations (1.18) into so-called Roothaan equations:

$$\sum_{\upsilon=1}^{K} (F_{\mu\upsilon} - \varepsilon_i S_{\mu\upsilon}) C_{\upsilon i} = 0 \quad (1.24)$$

where the terms $F_{\mu\upsilon}$ and $S_{\mu\upsilon}$ are defined as :

$$F_{\mu\upsilon} = \int dx_1 \tilde{\chi}_\mu^*(x_1) f(x_1) \tilde{\chi}_\nu(x_1) \quad (1.25)$$

$$S_{\mu\upsilon} = \int dx_1 \tilde{\chi}_\mu^*(x_1) \tilde{\chi}_\nu(x_1) \quad (1.26)$$

Now the Hartree-Fock-Roothaan equations (1.24) can be written in a simple matrix form as:

$$FC = SC\varepsilon \quad (1.27)$$

where F is the so-called Fock matrix, C is the matrix of coefficients $C_{\mu i}$, S is the overlap matrix of the basis functions, and ε is the matrix of orbital energies. Since F depends on its own solution through the orbitals, the process must be done iteratively. This is why the solution of the Hartree-Fock-Roothaan equations is often called the self-consistent field procedure.

II.1.7. Electron Correlation

Dynamic and Non-Dynamic (static) Electron Correlation Effects [11]

One of the outstanding problems of computational quantum chemistry is the understanding of electron correlation. The correlation energy is defined as the difference between the Hartree–Fock energy and the exact (non-relativistic) energy of the molecule [12].

$$E_{correlation}^{HF} = E_{exact} - E_{HF} \quad (1.28)$$

It is often separated into two parts, a short range effect due to the reduction in probability as two electrons come together, and a long range effect which is often responsible for electrons proceeding correctly to their atoms as the molecule dissociates.

The first part is called "dynamic correlation", and is often associated with the necessity of including the interelectronic distance r_{ij} in accurate wavefunctions.

The second part is called "left–right correlation" by reference to the dissociation issue, as above mentioned, but it is equally called "static correlation" or "near-degeneracy correlation" or "non-dynamic correlation". Static correlation is important for molecules where the ground state cannot be described with only one Slater determinant and when several electronic states lie close in energy. Such degeneracy occurs in numerous cases as transition metal complexes, radicals, and excited states. For these systems, determinants with electron configurations corresponding to all low-lying states must be included in the wave function.

Nowadays, a number of methods including the correlation are used: Møller-Plesset perturbation theory, multi configurational self–consistent field MCSCF), configuration interaction (CI) or the coupled cluster theory (CC). We will very briefly recall their main features below.

II.1.7.1. Møller-Plesset Perturbation Theory [13]

This method is based on quantum mechanics perturbation theory. The perturbation in that case represents the difference between the "real" Hamiltonian and the zero-order Hamiltonian calculated from the Fock operator $\hat{f}$ where:

$$\hat{\Phi} = \hat{H} - \hat{f} \quad (1.29)$$

is the fluctuation potential and represents the difference between the true two electron Coulomb potential $\hat{g}$ of the Hamiltonian operator and the effective one-electron Fock potential $\hat{V}$ of the Fock operator:

$$\hat{\Phi} = \hat{g} - \hat{V} \quad (1.30)$$

Thus, correlation can be treated as a perturbation from the Hartree-Fock wavefunction. Applying the perturbation theory, we obtain the zero and the first order in perturbation in the spin orbital basis as:

$$E_{MP}^{(0)} = \langle HF | \hat{f} | HF \rangle = \sum_I \varepsilon_I$$
$$E_{MP}^{(1)} = \langle HF | \hat{\Phi} | HF \rangle \quad (1.31)$$

Thus, the Hartree-Fock energy is equal to the sum of the zero and first order corrections:

$$E_{HF} = E_{MP}^{(0)} + E_{MP}^{(1)} = \langle HF | \hat{\mathrm{H}} | HF \rangle \quad (1.32)$$

The second-order Møller-Plesset correction is:

$$E_{MP}^{(2)} = -\sum_{A>B,I>J} \frac{|g_{AIBJ} - g_{AJBI}|^2}{\varepsilon_A + \varepsilon_B - \varepsilon_I - \varepsilon_J} \quad (1.33)$$

The energy of the system up to the second order is thus:

$$E_{MP2} = E_{MP}^{(0)} + E_{MP}^{(1)} + E_{MP}^{(2)} + h_{nuc} = E_{HF} - \sum_{A>B,I>J} \frac{|g_{AIBJ} - g_{AJBI}|^2}{\varepsilon_A + \varepsilon_B - \varepsilon_I - \varepsilon_J} \quad (1.34)$$

Third-order (MP3) and fourth-order (MP4) calculations are also common. MP5 and higher calculations are seldom done due to the high computational cost (N^{10} CPU time scaling). The MP2 method represents a very successful approach to the correlation problem providing an accurate, size-extensive correction at low computational costs (CPU time scales as N^3 to N^5). This method is adapted to correct effects from dynamic electron correlation.

II.1.7.2. Configuration Interaction (CI)

A configuration interaction [14] wavefunction is a multiple-determinant wave function. It is based on the variational principle, analogous to the HF method. The trial wave function is written as a linear combination of determinants with the expansion coefficients determined by requiring that the energy should be a minimum (or at least

stationary). The MOs used for building the excited Slater determinants are taken from a Hartree-Fock calculation and held fixed. This is constructed by starting with the Hartree-Fock wave function and making new determinants by promoting electrons from the occupied to unoccupied orbitals. Hence CI calculations usually only include determinants close to the Hartree-Fock ground state determinant.

The CI is classified by the number of excitations used to make each determinant. If only one electron has been moved for each determinant, it is called a configuration interaction single-excitation (CIS) calculation. CIS calculations give an approximation to the excited states of the molecule, but do not change the ground-state energy. Single-and double excitation (CISD) calculations yield a ground-state energy that has been corrected for correlation. Triple-excitation (CISDT) and quadruple-excitation (CISDTQ) calculations are done only when very high accuracy results are desired. If we subscript S, D, T, etc. the determinants which are respectively singly, doubly, triply, etc. excited relative to the HF configuration it is obtained:

$$\psi_{CI} = a_0\phi_{SCF} + \sum_S a_S\phi_S + \sum_D a_D\phi_D + \sum_T a_T\phi_T \ldots = \sum_{i=0} a_i\phi_i \quad (1.35)$$

This is an example of constrained optimization; the energy should be minimized under the constraint that the total CI wave function is normalized. However it can provide highly accurate results for small systems. Configuration interaction calculations can be very accurate, but the cost in CPU time is very high (N^8 time complexity or worse). This method is adapted to correct effects from dynamic electron correlation or to calculate excitation energies, provided that truncation effects are correctly handled. An extension of this method is to use several reference determinants to generate the excitations, called MRCI (multiple reference Configuration Interaction). This is preferred when the ground state is nearly degenerate and thus the single determinant issued for the HF calculation is wrong.

II.1.7.3. Multi-Configurational Self Consisted Field (MCSCF)

Compared to CI, an MCSCF calculation [15] gives more of the correlation energy with fewer configurations. The orbital relaxation usually does not recover much electron correlation, and it is more efficient to include additional determinants and keep the MOs fixed (like CI) if the interest is just in obtaining a large fraction of the correlation energy. The major problem with MCSCF methods is selecting the necessary configurations to include for the property of interest. One of the most popular approaches is the Complete Active Space Self-consistent Field (CASSCF) method in which all combinations of the active space orbitals are included. Here the selection of configurations is done by partitioning the MOs into active and inactive spaces. The active MOs will typically be some of the highest occupied and some of the lowest unoccupied MOs from a RHF calculation. The inactive MOs either have 2 or 0 electrons, always doubly occupied or empty. Within the active MOs, a full CI is performed and all the proper symmetry adapted configurations are included in the MCSCF optimization.

The variational principle is applied, by varying both the weight of Slater determinant but also the coefficient of molecular orbitals (MOs). In order to add the dynamic correlation, the perturbative theory is often used, through the CASPT2 method. Similarly to the MP2 correction method, the CASPT2 method [16] use as reference function the CASSCF wave function and applies the corrections to second order on this function.

MCSCF is a method used in quantum chemistry for generating qualitatively correct reference states of molecules in cases where Hartree-Fock and density functional theory are not adequate (for molecular ground states which are quasi-degenerate with low lying excited states or in bond breaking situations), when it is useful to recover most of the static correlation.

II.1.7.4. Coupled Cluster (CC)

Coupled cluster [17] calculations are similar to configuration interaction calculations in that the wave function is a linear combination of many determinants [18]. Like CI, there are various orders of the CC expansion, called CCSD, CCSDT, and so on. Coupled cluster calculations give variational energies as long as the excitations are included successively. The idea is to include all corrections of a given type to infinite order. The coupled cluster wave function is written as:

$$\psi_{CC} = e^{T}\phi_0 \qquad (1.36)$$

$$e^{T} = 1 + T + \frac{1}{2}T^2 + \frac{1}{6}T^3 + \cdots = \sum_{k=0}^{\infty}\frac{1}{k!}T^k$$

and the cluster operator T is given by:

$$T = T_1 + T_2 + T_3 \cdots + T_N \qquad (1.37)$$

where T_1 is the operator of all single excitations, T_2 is the operator of all double excitations and so on. The cost in CPU time of the CC methods is very high, around N^7 time complexity.

The Post-Hartree-Fock methods described above are a set of methods which were developed to improve the Hartree-Fock (HF), or self-consistent field (SCF) method. They add electron correlations more accurately than in the Hartree-Fock method where repulsions are only averaged. More explanations about HF approach and electron correlation methods are available in the references [18 -21].

Bibliography

[1] D. D. Fitts, *Principles of Quantum Mechanics,* Cambridge University Press, 2002

[2] W. Koch, M. C.Holthausen, *A Chemist's Guide to Density Functional Theory*, 2e. ed., Wiley, 2001

[3] M. Born, J. R. Oppenheimer, *Ann. Phys.*1927, *84*, 457

[4] http://farside.ph.utexas.edu/teaching/qmech/lectures/node127.html

[5] J. C. Slater, *Phys. Rev*. 1951, *81*, 3

[6] C. D. Sherrill, An Introduction to Hartree-Fock Molecular Orbital Theory, School of chemistry and Biochemistry, Georgia Institute of Technology, 2000

[7] http://www.lct.jussieu.fr/local/PDF/SilviM524.pdf

[8] P.Carsky, I. Hubac, Theor. Chim. Acta 1991, *80*, 4-5, 407

[9] J. C. C. Roothaan, *Rev. Mod. Phys*. 1951, *23*, 69

[10] G. G. Hall, *Proc. of the Royal Soc.* 1951 *A205*, 541

[11] http://www.rsc.org/ej/CP/2004/B402989P/#cit1

[12] P. O. Lowdin, *Phys. Rev.* 1955, *97*, 1474

[13] C. Moeller, M.S. Plesset, *Phys. Rev.* 1934*, 46,* 618

[14] http://www.psicode.org/doc/userman_sectioned/node37.html

[15] F. Jensen, *Computational chemistry*, John Wiley & Sons, 1999

[16] K. Andersson, P.A. Malmqvist, B. O. Roos. *J. Chem. Phys.* 1992, *96*, 1218

[17] http://www.ccc.uga.edu/lec_top/rltvt/node16.html

[18] J. Cizek, Ch*em. Phys*. 1966, *45*, 4256

[19] C. J. Cramer, *Essentials of Computational Chemistry*, Wiley, 2e ed., 2004

[20] D. C. Young, *Computational Chemistry: A practical Guide for Applying Techniques to Real World Problems*, Wiley, 2001

[21] R. Parr, W. Yang, *Density Functional Theory of Atoms and Molecules,* Oxford University Press, 1989

II.2. Density Functional Theory (DFT)

Introduction

The original density functional approach of quantum systems is the method of Thomas and Fermi [1-3] proposed in 1927. The approach is based on the quantum statistical model of electrons which can be used to approximate the distribution of electrons in an atom. It is a remarkable theory that allows replacing the complicated N-electron wave function $\psi(x_1, x_2 \ldots x_N)$ and the associated Schrödinger equation by the much simpler electron density ρ(r). The Thomas-Fermi expression for the energy of an atom is:

$$E_{TF}[\rho(\vec{r})] = \frac{3}{10}(3\pi)^{2/3}\int \rho^{5/3}(\vec{r})d\vec{r} - Z\int \frac{\rho(\vec{r})}{r}d\vec{r} + \frac{1}{2}\iint \frac{\rho(\vec{r}_1)\rho(\vec{r}_2)}{r_{12}}d\vec{r}_1 d\vec{r}_2 \qquad (2.1)$$

In 1951, Slater using an approximation [4] to the non-local exchange contribution of Hartree-Fock has introduced another example where the electron density is exploited as the central quantity. The exchange contribution is expressed now like:

$$E_X[\rho] \cong C_x \int \rho(\vec{r}_1)^{4/3} d\vec{r}_1 \qquad (2.2)$$

If the exchange contributions of equation (2.2) are combined with the Thomas-Fermi energy given by expression *(2.1),* we end up with an approximation which is known today as the Thomas-Fermi-Dirac model [5, 6]. This model includes the kinetic and classical Coulomb contributions as well as the quantum mechanical exchange effects. All parts are expressed as pure functionals of the density.

However, the Thomas-Fermi-Dirac theory remains rather inaccurate for most applications. The largest source of errors was in the representation of the kinetic energy, followed by the errors in the exchange energy, and the complete neglect of electron

correlation. Hohenberg, Kohn and Sham will bring important improvements in the development of density functional theory as can be seen in the next discussions.

II.2.1. Hohenberg - Kohn Theory

II.2.1.1. The first theorem

In 1964, Hohenberg and Kohn [7] expressed the first theorem stating that the external potential $V_{ext}(\vec{r})$ is represented as a unique functional of the ground state electron density $\rho_0(\vec{r})$ of a many electron system.

Thus the ground state electron density is sufficient to construct the full Hamiltonian operator and hence to calculate in principle any ground state property of the system without the knowledge of the many electron wavefunctions. Alternatively formulated, this means that any ground state property can be expressed in terms of the ground state electron density $\rho_0(\vec{r})$ as:

$$E_0[\rho_0] = \int \rho_0(\vec{r}) V_{Ne} d\vec{r} + T[\rho_0] + E_{ee}[\rho_0] \qquad (2.3)$$

The first term in equation (2.3) is due to the nuclei-electron attraction. The last two terms are collected into a new quantity, called Hohenberg-Kohn functional $\mathrm{F_{HF}}[\rho_0]$, thus the ground state energy may be expressed as:

$$E_0[\rho_0] = \int \rho_0(\vec{r}) V_{Ne} d\vec{r} + F_{HK}[\rho_0] \qquad (2.4)$$

II.2.1.2. The second Hohenberg -Kohn theorem

The groundstate energy can be obtained variationally: the density that minimises the total energy is the exact groundstate density.

$$E_0 \le E[\tilde{\rho}] = T[\tilde{\rho}] + E_{Ne}[\tilde{\rho}] + E_{ee}[\tilde{\rho}] \qquad (2.5)$$

For any trial $\tilde{\rho}(\vec{r})$ which satisfies the boundary conditions ($\tilde{\rho}(\vec{r}) \ge 0; \int \tilde{\rho}(\vec{r})d\vec{r} = N$) the energy given in (2.4) represents an upper bound to the true ground state energy E_0. If any trial density $\tilde{\rho}(\vec{r})$ defines its own Hamiltonian $\hat{\mathrm{H}}$ and own wavefunction $\tilde{\psi}$, then we can consider this wave function as the trial wave function for the Hamiltonian generated from the true external potential V_{ext}:

$$\langle \tilde{\psi} | \hat{\mathrm{H}} | \tilde{\psi} \rangle = T[\tilde{\rho}] + V_{ee}[\tilde{\rho}] + \int \tilde{\rho}(\vec{r}) V_{ext} d\vec{r} = E[\tilde{\rho}] \ge E_0[\rho_0] = \langle \psi_0 | \hat{\mathrm{H}} | \psi_0 \rangle \qquad (2.6)$$

The properties of a system that are defined by an external potential V_{ext} are determined by the ground state density. In this case, the ground state energy associated with a density ρ will be available through the functional $\int \rho(\vec{r}) V_{Ne} d\vec{r} + F_{HF}[\rho]$. The minimum of this functional is obtained with respect to all allowed densities if the input density is the true ground state density for $\tilde{\rho}(\vec{r}) \equiv \rho_0(\vec{r})$.

This theorem enables the ground state electron density to be calculated variationally; it holds only for electron densities for which the associated Schrödinger equation yields an antisymmetric wave function.

Although these theorems are extremely powerful, they do not offer a way of computing the ground-state density of a system in practice. Indeed one year after the seminal DFT paper by Hohenberg and Kohn, Kohn and Sham devised a simple method for carrying-out DFT calculations. This method is described in the next paragraph.

II.2.2. Kohn –Sham approach

Density Functional theory has become the most widely used method today for electronic structure calculations because of the approach proposed by Kohn and Sham in 1965 [8-10], which replaced the original many-body problem by an auxiliary

independent-particle problem. The auxiliary system can be solved more easily by assuming that the ground state density of the original interacting system is equal to that of some chosen non-interacting system. This leads to independent particle equations for the non interacting system that can be considered exactly soluble (in practice by numerical means) with all the difficult many body terms incorporated into an exchange – correlation functional of the density. A non interacting reference system was set up with a new Hamiltonian which contains a local potential $V_S(\vec{r})$:

$$\hat{\mathrm{H}}_S = -\frac{1}{2}\sum_i^N \nabla_i^2 + \sum_i^N V_S(\vec{r}_i) \qquad (2.7)$$

Because this Hamiltonian doesn't contain any electron–electron interactions, it could be interpreted like a non – interacting system. Its ground state wave function is represented by a Slater determinant which has the form:

$$\Phi_{SD} = \frac{1}{\sqrt{N!}}\begin{vmatrix} \varphi_1(\vec{x}_1) & \varphi_2(\vec{x}_1) & \cdots & \varphi_N(\vec{x}_1) \\ \varphi_1(\vec{x}_2) & \varphi_2(\vec{x}_2) & \cdots & \varphi_N(\vec{x}_2) \\ \vdots & \vdots & \vdots & \vdots \\ \varphi_1(\vec{x}_N) & \varphi_2(\vec{x}_N) & \cdots & \varphi_N(\vec{x}_N) \end{vmatrix} \qquad (2.8)$$

where the spin orbitals are determined by :

$$\hat{f}^{KS}\varphi_i = \varepsilon_i\varphi_i \qquad (2.9)$$

and the one-electron Kohn-Sham operator $\hat{f}^{KS}$ defined as:

$$\hat{f}^{KS}\varphi_i = -\frac{1}{2}\nabla^2 + V_S(\vec{r}) \qquad (2.10)$$

In order to distinguish these orbitals from their Hartree-Fock counterparts, they are usually termed Kohn-Sham (K-S) orbitals. The effective potential V_S of equation (2.10)

establishes the connection between the artificial system and the one we are really interested in such that the density resulting from the summation of the module of the squared orbitals $\{\varphi_i\}$ exactly equals the ground state density of our target system of interacting electrons:

$$\rho_S(\vec{r}) = \sum_i^N \sum_s \left|\varphi_i(\vec{r}, s)\right|^2 = \rho_0(\vec{r}) \qquad (2.11)$$

II.2.2.1. Kohn –Sham equations

The clever idea of Kohn and Sham was to realize that they are not able to accurately determine the kinetic energy through an explicit functional, so they concentrated on computing as much as possible the true kinetic energy exactly. They proposed to use the Hartree-Fock kinetic energy term:

$$T_{HF} = -\frac{1}{2}\sum_i^N \langle \chi_i | \nabla^2 | \chi_i \rangle \qquad (2.12)$$

Hence, they suggested using expression (2.12), to obtain the exact kinetic energy of the non-interacting reference system with the same density as the real, interacting one:

$$T_S = -\frac{1}{2}\sum_i^N \langle \varphi_i | \nabla^2 | \varphi_i \rangle \qquad (2.13)$$

The K-S orbitals from the equation (2.10) allow the determination of the non interacting kinetic energy T_s, but which is not equal to the exact kinetic energy. Kohn and Sham accounted for that by introducing a partition of functional $F[\rho]$:

$$F[\rho(\vec{r})] = T_S[\rho(\vec{r})] + J[\rho(\vec{r})] + E_{XC}[\rho(\vec{r})] \qquad (2.14)$$

where the exchange correlation energy is defined as:

$$E_{XC}[\rho] \equiv (T[\rho] - T_S[\rho]) + (E_{ee}[\rho] - J[\rho]) = T_C[\rho] + E_{nucl}[\rho] \qquad (2.15)$$

The residual part of the true kinetic energy T_C is added to the non classical electrostatic contributions. In that case, the E_{XC} is the functional which contains everything that is unknown, not only the non classical effects of self interaction correction, exchange and correlation, which are contributions to the potential energy of the system, but also a portion corresponding to the kinetic energy. The energy is separated into kinetic energy T_S of the non interacting system, E_{Ne} which includes terms describing the potential energy of electron-nucleus attraction and repulsion between nuclei, the classical electron-electron repulsion *J* and the E_{XC} term:

$$E[\rho(\vec{r})] = T_S[\rho] + J[\rho] + E_{XC}[\rho] + E_{Ne}[\rho] \qquad (2.16)$$

$$= T_S[\rho] + \frac{1}{2}\iint \frac{\rho(\vec{r}_1)\rho(\vec{r}_2)}{r_{12}} d\vec{r}_1 d\vec{r}_2 + E_{XC}[\rho] + \int V_{Ne}\rho(\vec{r}) d\vec{r} \qquad (2.17)$$

$$= -\frac{1}{2}\sum_i^N \langle \varphi_i | \nabla^2 | \varphi_i \rangle + \frac{1}{2}\sum_i^N \sum_j^N \iint |\varphi_i(\vec{r}_1)|^2 \frac{1}{r_{12}} |\varphi_j(\vec{r}_2)|^2 d\vec{r}_1 d\vec{r}_2 + E_{XC}[\rho(\vec{r})] - \sum_i^N \int \sum_A^M \frac{Z_A}{r_{1A}} | \qquad (2.18)$$

The variational principle is applied in the same way in Hartree-Fock theory. The orbitals $\{\varphi_i\}$under the constraint $\langle \varphi_i | \varphi_j \rangle = \rho_{ij}$ are used in order to minimize the energy expression. Equations *(2.19)* are called the Kohn-Sham equations:

$$[-\frac{1}{2}\nabla^2 + V_{eff}(\vec{r}_1)]\varphi_i = \varepsilon_i \varphi_i \qquad (2.19)$$

If we compare this equation with the one-particle equation from the non-interacting reference system it can be observed that the expression in square brackets of V_{eff} is identical to V_S of equation (2.10):

$$V_S(\vec{r}) \equiv V_{eff}(\vec{r}) = \int \frac{\rho(\vec{r}_2)}{r_{12}} d\vec{r}_2 + V_{XC}(\vec{r}_1) - \sum_A^M \frac{Z_A}{r_{1A}} \qquad (2.20)$$

The potential V_{XC} of equation (2.20) is due to the exchange correlation energy E_{XC}. This potential is simply defined as the functional derivative of E_{XC}:

$$V_{XC} \equiv \frac{\delta E_{XC}}{\delta \rho} \qquad (2.21)$$

If the exact forms of E_{XC} and V_{XC} were known, the Kohn –Sham strategy would lead to the exact energy and we would obtain a correct eigenvalue of the Hamiltonian of the Schrödinger equation. The Kohn-Sham one electron equations (2.19) just like the Hartree-Fock equations have to be solved iteratively.

II.2.3. Exchange-correlation functionals

Density-functional theory reduces the quantum mechanical many-electron ground-state problem to self-consistent one electron form, through the Kohn-Sham equations. In this formally exact theory, the many-electron exchange and correlation effects are described by the exchange-correlation functional.

The early implementation of DFT is the local density-functional approximation (LDA), which is derived from the case of a homogeneous electron gas. Because atoms and molecules are inhomogeneous systems, generalized gradient approximation (GGA) corrections were developed and have been shown to improve the calculated results, especially for molecular bond energies and electronic spectra. Further progress in DFT is given by the introduction of a fraction of the HF exchange. These functionals are called hybrid.

Since the HF exchange considerably increases the computing efforts, some attempts have recently been made to replace the HF-exchange part of hybrid DFTs with a pure density

functional part. A new approximate XC form has recently been developed by including the electron kinetic energy density and/or the Laplacian of the electron density. Such a form is called meta-GGA, which does not contain HF exchange.

II.2.3.1. Local Density Approximation (LDA)

In the local density approximation (LDA) [11], E_{XC} have the form:

$$E_{XC} = \int \rho(r)\varepsilon_{XC}[\rho(r)]dr \quad (2.22)$$

where $\varepsilon_{XC}[\rho(r)]$ is the exchange-correlation energy per electron in a homogeneous electron gas of constant density. In a hypothetical homogeneous electron gas, an infinite number of electrons travel throughout a space of infinite volume in which there is a uniform and continuous distribution of positive charge to retain electro-neutrality. This expression for the exchange-correlation energy is clearly an approximation. The quantity $\varepsilon_{XC}[\rho(r)]$ can be divided into exchange and correlation contributions:

$$\varepsilon_{XC}[\rho(\vec{r})] = \varepsilon_X[\rho(\vec{r})] + \varepsilon_C[\rho(\vec{r})] \quad (2.23)$$

The exchange part ε_X was derived by Bloch and Dirac [12] and has the form:

$$\varepsilon_X = -\frac{3}{4}\sqrt[3]{\frac{3\rho(\vec{r})}{\pi}} \quad (2.24)$$

The most accurate expression of ε_C is given now by the Vosko, Wilk, and Nusair (VWN) [13] and most recently by Perdew and Wang [14].

LDA approximation gives very good trends in gas phase because of exchange-correlation hole of the uniform electron gas which is used as a model for the exact hole. It provides a realistic description of the atomic structure for a wide range of systems. But it is not enough reliable to describe the energetics of chemical reactions, such as reaction

enthalpies and activation energy barriers. In particular, it leads to binding energies of molecules and solids which are overestimated. But LDA is a good basis, for the construction of more sophisticated approximations to the exchange-correlation energy, such as generalized gradient approximations or hybrid functionals.

II.2.3.2. Generalized Gradient Approximation (GGA)

As stated above, the LDA uses the exchange-correlation energy for the uniform electron gas at every point in the system regardless of the homogeneity of the real charge density. For non uniform charge densities the exchange-correlation energy can deviate significantly from the uniform result. This is the case for instance in valence region of molecular species. This deviation can be expressed in terms of the gradient and higher spatial derivatives of the total charge density. Indeed, the GGA use not only the information about the density $\rho(\vec{r})$ at a particular point $\vec{r}$ but also the gradient of the charge density $\nabla\rho(\vec{r})$ in order to account for the non homogeneity of the true electron density [16]. Thus, we arrive at:

$$E_{XC}(\rho) = \int \varepsilon_{XC}(\rho(\vec{r}), \nabla\rho(\vec{r}))d\vec{r} \qquad (2.25)$$

The first widely popular GGA exchange functional was developed by Becke [17]. This functional adopts a mathematical form that has correct asymptotic behaviour at long range for the energy density.

$$F^{B88} = \frac{\beta s_\sigma^2}{1 + 6\beta s_\sigma \sinh^{-1} s_\sigma} \qquad (2.26)$$

where β incorporates an empirical parameter the value of which was optimized by fitting to the exactly known exchange energies of the six noble gas atoms He through Rn and s_σ is the reduced density gradient for the σ spin, which is interpreted as a parameter of non- homogeneity.

We will give a qualitative description of the most known correlation functionals. For example, the correlation functional Perdew, P86 [18] uses a single semi-empirical parameter, adjusted for correlation energy of the neon atom. Another correlation functional widely used now was developed by Lee, Yang and Parr (1988) LYP [19] which, unlike the other functional, is not developed on the uniform electron gas but which has a single parameter semi-empirically adjusted to a precise calculation of the correlation energy of the helium atom. A few years later, Perdew and Wang have developed a formalism to arrive at a correlation functional PW91 [20] without parameter adjustment. Another more recent functional inspired from PW91 is the PBE (Perdew, Burke, Ernzerhof) [21], which is not based on semi empirical parameters. Finally a recent exchange functional by Handy et al (OPTX) has been developed, which is quite efficient for systems with spin states [22].

The current GGAs seem to give reliable results for all main types of chemical bonds (covalent, ionic, metallic and hydrogen bond). For Van der Waals interactions, however, common GGAs and LDAs fail. For describing these very weak interactions several more specialized approaches have been developed within DFT [23-27].

Both in physics and in chemistry the widespread use of GGAs has lead to major improvements as compared to LDA. A useful collection of explicit expressions for some GGAs can be found in the appendix of Ref. [28], and a detailed discussion of some selected GGAs and their performance is given in reference [29].

II.2.3.3. Hybrid Functionals

Hybrid functionals are a class of approximations to the exchange-correlation energy functional, that incorporate a portion of exact exchange from Hartree-Fock theory within conventional GGAs. The parameters determining the weight of each individual functional may be fitting the functional predictions to experimental or accurately calculated thermo-chemical data such as B3LYP. Some other hybrid functionals are built ab initio (such as PBE0) using the adiabatic connection method [30].

II.2.3.3.1. The Adiabatic Connection

The principle of the adiabatic connection is a switch that would smoothly convert the non interacting K-S reference system to the real interacting system [30]. The two systems of K-S scheme are connected by gradually increasing the coupling strength parameter λ:

$$\hat{\mathrm{H}}_{\lambda} = \hat{T} + V_{ext}^{\lambda} + \lambda \sum_{i}^{N} \sum_{j>i}^{N} \frac{1}{r_{ij}} \quad (2.27)$$

The equation (2.27) is called the adiabatic connection. For each λ, the effective external potential V_{ext}^{λ} is adapted such that the density always equals the density of the fully interacting system. For $\lambda = 0$, the Hamiltonian operator is due to the non interacting reference system and for $\lambda = 1$ the Hamiltonian represents the regular expression for the real system.

The hybrid approach to constructing density functional approximations was introduced by Axel Becke in 1993 [30]. The exact exchange energy functional is expressed in terms of the Kohn-Sham orbitals rather than the density and is expressed as:

$$E_{XC}^{hybrid} = \alpha(E_X^{HF} - E_X^{GGA}) + E_{XC}^{GGA} \quad (2.28)$$

where E_X^{HF} represent the Hartree-Fock exchange expression, except that Kohn-Sham rather than Hartree-Fock orbitals are used.

Perhaps the most popular functional in quantum chemistry is B3LYP functional. This is a combination of the LYP GGA for correlation, and Becke's three-parameter hybrid functional B3 for exchange. The B3LYP exchange-correlation functional has the form:

$$E_{XC}^{B3LYP} = E_{XC}^{LDA} + a_0(E_X^{HF} - E_X^{LDA}) + a_X(E_X^{GGA} - E_X^{LDA}) + a_C(E_C^{GGA} - E_C^{LDA}) \quad (2.29)$$

where $a_0 = 0.20$, $a_X = 0.72$, and $a_C = 0.81$ are the three empirical parameters determined by fitting the predicted values to a set of atomization energies, ionization potentials, proton affinities, and total atomic energies [31]. E_X^{GGA} and E_C^{GGA} are generalized gradient approximations: the Becke 88 [17] exchange functional and the correlation functional of Lee, Yang , Parr, [19]; E_C^{LDA} is the VWN local-density approximation to the correlation functional. The parameters, that Becke fitted to dissociation energies of neutral molecules at fixed geometries, also improved predicted structures and vibrational frequencies as compared to pure GGAs and also worked well for ionization potentials and electron affinities. Another well known example of a hybrid functional is PBE0 [32]. In this case, no fitting parameters were used and the percentage of exact exchange is fixed at 25%. Perdew, Ernzerhof and Burke have used the coupling constant integration approach to generate PBE0 hybrid functionals:

$$E_{XC} = E_{XC}^{LDA} + \frac{1}{4}(E_X^{HF} - E_{XC}^{GGA}) \quad (2.30)$$

Another recent beyond-GGA development is the emergence of so-called Meta-GGAs [33, 34]. The meta-GGA is essentially an extension of the GGA which depend, in addition to the density and its derivatives, also on the Kohn-Sham kinetic-energy density $T_{KS}(r)$:

$$T_{KS} = \frac{1}{2}\sum_{i=1}^{N}\left|\vec{\nabla}\varphi_i(r)\right|^2 \quad (2.31)$$

The additional degree of freedom provided by T_{ks} is used to satisfy additional constraints on E_{XC}, such as a self-interaction-corrected correlation functional, recovery of the fourth-order gradient expansion for exchange in the limit of slowly varying densities, and a finite exchange potential at the nucleus.

The Kohn –Sham approach of DFT and exchange correlation functionals are described in detail in the references [35 -41].

II.2.4. Basis Sets

Slater and Gaussian Type Orbitals

One of the approximations inherent in all ab-initio methods for quantum chemistry is the introduction of a basis set [41]. In chemistry, a basis set represents a set of functions that is used to create molecular orbitals, which are expanded as a linear combination of such functions with the weights or coefficients to be determined.

Quantum chemical calculations are typically performed within a finite set of basis functions. In these cases, increasing the size of basis set may lead close to the infinite basis set limits.

Chemical basis functions [42] are usually atomic orbitals centered on each atom. They are classified with respect to their behaviour as a function of the radial coordinate into Slater type orbitals (STOs), which corresponded to a set of functions which decayed exponentially with distance from the nuclei, and Gaussian type orbitals (GTOs), which have a gaussian behaviour. These are the most common methods for solving the Kohn-Sham equations in quantum chemistry. Slater orbitals [43] have the functional form:

$$\chi_{\zeta,n,l,m}(r,\theta,\varphi) = NY_{l,m}(\theta,\varphi)r^{n-1}e^{-\zeta r} \qquad (2.32)$$

where N represents the normalization constant and $Y_{l,m}$ are the usual spherical harmonic functions. The exponential dependence ensures a fairly rapid convergence with increasing the number of functions. Gaussian type orbitals [43] can be written in terms of polar or cartesian coordinates:

$$\chi_{\zeta,n,l,m}(r,\theta,\varphi) = NY_{l,m}(\theta,\varphi)r^{(2n-2-l)}e^{-\zeta r^2} \qquad (2.33)$$

where l is the orbital momentum which determines the type of orbital and n is the principal quantum number; The difference between Slater and Gaussian orbitals is the

power of r in the exponent. The r^2 dependence in the exponent in the GTOs is a poorer representation than that of the STOs. GTOs also have a zero slope at the nucleus ($r = 0$) whereas STOs have a cusp. GTOs fall off more rapidly with distance than STOs. These factors suggest that more GTOs are needed to form a suitable basis set than STOs for achieving the same accuracy.

Nevertheless one strong advantage of GTOs is to handle easily products of functions on different centers, which is more difficult with STOs.

Bibliography

[1] E. H. Lieb, *Rev. of Mod. Phys*. 1981, *53*, 4

[2] J. Schwinger, *Phy. Rev. A* 1980, *22*, 5

[3] J. Schwinger, *Phy. Rev. A* 1981, *24*, 5

[4] J. C. Slater, Phys. Rev.1951, *81*, 3

[5] P.A. M. Dirac, *The principles of quantum mechanics*, 4ed, Oxford University Press, 27, 1989

[6] F. A. Reuse, *Electrodynamique et optique quatiques*, Presses polytechniques et universitaires romandes, 2007

[7] P. Hohenberg, W. Kohn, *Phys. Rev*. 1964, *136*, B864

[8] http://dft.uci.edu/book/gamma/g1.pdf

[9] R. G. Parr, W. Yang, *Density Functional Theory of Atoms and Molecules*, Oxford University Press, New York, 1989

[10] W. Kohn, A. D. Becke, R. G. Parr, *J. Chem. Phys.* 1996, *100*, 12 974

[11] R. O. Jones, O. Gunnarsson, *Rev. Mod. Phys*. 1989, *61*, 689

[12] P. Blanchard, G. Dell'Antonio, *Multiscale Methods in Quantum Mechanics*, Birkhauser, 2004

[13] S. Vosko, L. Wilk, M. Nusair, *Can. J. Phys.* 1980, *58*, 1200

[14] J. P. Perdew, Y. Wang, *Phys. Rev. B* 1992, *45*, 13244

[15] M. Ernzerhof, J. P. Perdew, K. Burke, *Density functionals: Where do they come from, why do they work?* ,*Topics in Current Chemistry*, 180, Springer, Berlin, 1996

[16] G. B. Bachelet, D. R. Hamann, M. Schlüter, *Phys. Rev. B* 1982*, 26*, 4199

[17] A. D. Becke, *Phys. Rev. A* 1988, *38*, 3098

[18] J. P. Perdew, *Phys. Rev. B* 1986**,** *33*, 8822

[19] C. Lee, W. Yang, R. G. Parr, *Phys. Rev. B*. 1988, *37*, 785

[20] J. P. Perdew, Y. Wang, *Phys. Rev. B* 1992**,** *46*, 6671

[21] J. P. Perdew, K. Burke, M. Ernzerhof, *Phys. Rev. Lett.* 1996**,** *77*, 3865

[22] N. C. Handy, A. J. Cohen, *Mol. Phys.* 2001, *99*, 403.

[23] W. Kohn, Y. Meir, D. E. Makarov, *Phys. Rev. Lett*. 1998, *80*, 4153

[24] M. Lein, J. F. Dobson, E. K. U. Gross, *J. Comput. Chem*. 1999, *20*, 12

[25] J. F. Dobson, B. P. Dinte, *Phys. Rev. Lett.* 1996, *76*, 1780

[26] Y. Andersson, D. C. Langreth, B. I. Lundqvist, *Phys. Rev. Lett.* 1996, *76*, 102

[27] E. R. Johnson, A. D. Becke, *J. Chem. Phys*. 2005, *123*, 024101

[28] C. Filippi, C. J. Umrigar, M. Taut, *J. Chem. Phys*. 1994, *100*, 1290

[29] R. M. Martin, *Electronic Structure, Basic Theory and Practical Methods*, Cambridge University Press, 2004

[30] A. D. Becke, *J. Chem. Phys.* 1993*, 98*, 5648; A. D. Becke, J. P. Perdew, M. Ernzerhof, K. Burke, *J. Chem. Phys*. 1996, *105*, 9982

[31] A. D. Becke, *J. Chem. Phys*. 1998, *109*, 2092

[32] C. Adamo, V. J. Barone, *J. Chem Phys.* 1999, *110*, 6158

[33] J. Tao, J. P. Perdew, V. N. Staroverov , G. E. Scuseria, *Phys. Rev. Lett.* 2003*, 91*, 146401

[34] R. M. Dreizler, E. K. U. Gross, *Density Functional Theory*, Copyright Springer Verlag, 1990

[35] W. Koch, M. C.Holthausen, *A Chemist's Guide to Density Functional Theory*, 2e ed., Wiley, 2001

[36] C. J. Cramer, *Essentials of Computational Chemistry*, Wiley, 2e ed., 2004

[37] D. C. Young, *Computational Chemistry: A practical Guide for Applying Techniques to Real World Problems*, Wiley, 2001

[38] R. Parr, W. Yang, *Density Functional Theory of Atoms and Molecules,* Oxford University Press, 1989

[39] F.Jensen, *Computational chemistry*, John Wiley & Sons, 1999

[40] T. Helgaker, P. Jorgensen, J. Olsen, *Molecular Electronic Structure Theory*, Copyright John Wiley & Sons, 2000

[41] H. Eschrig, *The fundamentals of Density Functional Theory*, B. G. Verlagsgesellschaft, 1996

[42] A. Szabo, N. S. Ostlund, *Modern Quantum Chemistry,* McGraw-Hill, New York, 1989

[43] http://www.physik.unizh.ch/~sam/diss/node71.html

II.3. Solid State Physics Theory of Semiconductors

In solid-state physics [1, 2] many phenomena can be understood by resort to energy band structure which constitutes the allowed electronic energy levels in crystalline solids and which relate to the inter-atomic binding. Conductivity trends, photoemission spectra, and optical properties can all be understood by examining the quantum states or energy bands of solids. The diversity of applications can be readily understood with a basic understanding of the theory behind these materials.

II.3.1. Periodic systems and Bloch theorem

II.3.1.1. Periodic boundary condition

A periodic boundary is a clever trick to make a simulation that consists of only a few hundred atoms behave as if it was infinite in size. Since this is impossible to achieve computationally, a simulation cell (or box) must be employed. This cell being finite, it would appear that it must be bounded in some way. Thus, periodic boundary conditions [3-5] are typically employed for the simulations of bulk materials (either disordered, or crystalline, in which case the cell must be carefully chosen.)

In periodic boundary conditions, the cubical simulation box is replicated throughout space to form an infinite lattice. In the course of the simulation, when a molecule moves in the central box, its periodic image in every one of the other boxes moves with exactly the same orientation in exactly the same way. Thus, as a molecule or an atom leaves the central box, one of its images will enter through the opposite face. There are no walls at the boundary of the central box, and the system has no surface. The central box simply forms a convenient coordinate system for measuring locations of the N molecules. A two-dimensional version of such a periodic system is shown in figure II.1.

It is not necessary to store the coordinates of all images in a simulation (this would be an infinite number), just those of the molecules in the central box. When a molecule leaves

the box by crossing a boundary, attention may be switched to the identical molecule just entering from the opposite side.

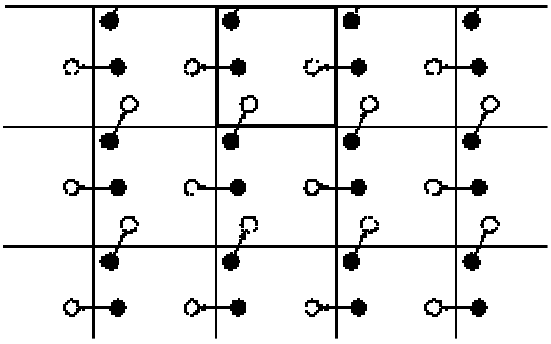

Figure II.1. Periodic boundary conditions. The central box is outlined by a thicker line.

Periodic boundary conditions are particularly useful for simulating a part of a bulk system with no surfaces present. Moreover, in simulations of planar surfaces, it is very often useful to simulate two dimensions (e.g. x and y) with periodic boundaries, while leaving the third (z) direction with different boundary conditions, such as remaining vacuum to infinity. This setup is known as slab boundary condition.

II.3.1.2. Born von Kárman periodic boundary condition

A real crystal always terminates with a surface. The single-particle wave function of a crystal must vanish at the boundaries (fixed plane boundary condition). Thus a real finite size crystal is characterized by the presence of propagating waves as well as standing waves. It is suitable for dealing with surface and interface states, but requires that the single particle wave vector k to be considered as complex.

Some improvements on periodic boundary conditions were made by Born von Kárman [6] which imposes the restriction that a wave function must be periodic on a certain Bravais lattice. This condition is often applied in solid state physics to model an ideal crystal.

$$\psi_k(r + N_i a_i) = \psi_k(r) \quad i = 1, 2, 3 \qquad (3.1)$$

where N_i are integers representing the number of cells in i directions, a_i are the primitive translation vectors, $N_0 = N_1 N_2 N_3$ is the total number of primitive unit cell in the crystal.
The Born von Kárman boundary condition is important in solid state physics for analyzing the band gap. Modeling the potential of a crystal as a periodic function with the Born von Kárman boundary condition and plugging in Schroedinger's equation results in a proof of Bloch's theorem, which is particularly important in understanding the band structure of crystals.

II.3.1.3. Bloch's theorem and Bloch waves

Essentially, there are two difficulties to overcome in a infinite solid: a wave function has to be calculated for each of the infinite number of electrons which will extend over the entire space of the solid, and the basis set in which the wave function will be expressed will be infinite. Bloch's theorem [7, 8] allows expressing the wave function of the infinite crystal in terms of wave functions at reciprocal space vectors of a Bravais lattice.
The translational periodicity of a crystal is determined by its lattice pattern, and the crystal potential can be expressed as:

$$U(r+T) = U(r) \qquad (3.2)$$

where T is a general direct Bravais translation vector of the periodic potential. If the wave function is expressed in the form of a modulated plane wave, Bloch's theorem can be expressed as:

$$\psi_k(r) = e^{ikr} u_k(r) \quad (3.3)$$

where k is a vector of Brillouin zone. The factor e^{ikr} represents a plane wave, and it is modulated by the function $u_k(r)$, which represents a function with the periodicity of the underlying Bravais lattice called cell periodic part:

$$u_k(r+T) = u_k(r) \quad (3.4)$$

The arbitrary vector k labels thus different eigenvalues and eigenstates of translation operators. Furthermore, the above function is also eigenvector of all possible translation operators of the lattice. The infinite sum is now reduced to a discrete (still infinite) sum over the reciprocal lattice vectors, and that is a great simplification of the problem.

More generally, a Bloch-wave [9, 10] description applies to any wave-like phenomenon in a periodic medium. The plane-wave wavevector (or Bloch wavevector) k is unique only up to a reciprocal lattice vector, so one only needs to consider the wavevectors inside the first Brillouin zone. For a given wavevector and potential, there are a number of solutions to Schrödinger's equation for a Bloch electron. These solutions, called bands, are separated in energy by a finite spacing at each k. If there is a separation that extends over all wavevectors, it is called a band gap. The band structure is the collection of energy eigenstates within the first Brillouin zone. The states in the band and their dependence on energy are described by the density of states.

All the properties of electrons in a periodic potential can be calculated from this band structure and the associated wave functions, at least within the independent electron approximation. A corollary of this result is that the Bloch wavevector k is a conserved quantity in a crystalline system, and hence the group velocity of the wave is conserved.

Bloch has resolved one of the key problems in the Pauli –Sommerfeld theory of conductivity of metals, by considering the wave function in a perfect crystal an eigenvector of crystal momentum [11]. It has proven to be a very valuable approximation, without which most solid-state physics analysis would be intractable.

Monkhorst and Pack [12] have proposed a method for generating a set of k points in the Brillouin zone (the Wigner-Seitz cell of the reciprocal lattice) which provides an efficient means of integrating periodic functions of the wave vector. The integration can be over the entire Brillouin zone or over specified portions.

II.3.2. The pseudopotential or effective potential

A plane wave basis set is usually very poorly suited to expanding the electronic wave functions because a very large number are required to accurately describe the rapidly oscillating wave functions of electrons in the core region. It is well known that most physical properties of solids are dependent on the valence electrons to a much greater degree than that of the tightly bound core electrons. For this reason the pseudopotential approximation [13-21] has been introduced. This approximation allows describing the core electrons and the strong nuclear potential and replaces them with a weaker pseudopotential which acts on a set of pseudo wave functions rather than the true valence wave functions.

Following the orthogonalised plane-waves approach of Phillips and Kleinman [22], we consider an atom with Hamiltonian $\hat{\mathrm{H}}$, core states $\{|\chi_n\rangle\}$ and core energy eigenvalues $\{E_n\}$ and focus on one valence state $|\psi\rangle$ with energy eigenvalue E. From these states, we attempt to construct a smoother pseudo-state $|\varphi\rangle$ defined by:

$$|\psi\rangle = |\varphi\rangle + \sum_{n}^{core} a_n |\chi_n\rangle \quad (3.5)$$

The valence state must be orthogonal to all of the core states which fix the expansion coefficients $\{a_n\}$:

$$|\psi\rangle = |\varphi\rangle - \sum_{n}^{core} |\chi_n\rangle\langle\chi_n|\varphi\rangle \quad (3.6)$$

Substituting the expression (3.6) in the Schrödinger equation $\hat{\mathrm{H}}|\psi\rangle = E|\psi\rangle$ we obtain:

$$\hat{\mathrm{H}}|\varphi\rangle + \sum_{n}^{core} (E - E_n)|\chi_n\rangle\langle\chi_n|\varphi\rangle = E|\varphi\rangle \quad (3.7)$$

The smooth pseudo-state obeys a Schrödinger equation with an extra energy-dependent non-local potential $\hat{V}_n$:

$$\left[\hat{\mathrm{H}} + \hat{V}_n\right]\left|\varphi\right\rangle = E\left|\varphi\right\rangle \qquad (3.8)$$

$$\hat{V}_n = \sum_n^{core} (E - E_n)\left|\chi_n\right\rangle\left\langle\chi_n\right| \qquad (3.9)$$

The energy of the smooth state described by the pseudo wave function is the same as that of the original valence state. The additional potential V_n, whose effect is localised in the core, is repulsive and will cancel a part of the strong Coulomb potential, so that the resulting sum is a weaker pseudo-potential.

An enormous number of plane waves are required to expand the tightly bound core wave functions or the valence wave functions in the core region. This is an obstacle to increase the computational efficiency. For this reason, the plane wave basis formalism is not suitable for all electron calculations (frozen cores).

II.3.2.1. Norm conserving pseudopotential. Troullier-Martins method

In the norm conserving pseudopotential approach, outside of a cutoff-radius, the pseudo-wave- functions are identical to the real all-electron wavefunction.

We have chosen to use those pseudopotentials generated by the method of Troullier and Martins [23]. The first step in generating Troullier-Martins (TM) pseudopotentials is to solve self consistently the radial Kohn-Sham equation for the given atomic configuration, with (*n, l*) as the principal and angular quantum numbers:

$$\left[\frac{-1}{2m}\frac{d^2}{dr^2} + \frac{l(l+1)}{2mr^2} + \upsilon^{AE}\right] rR_{nl}^{AE}(r) = \varepsilon r R_{nl}^{AE}(r) \qquad (3.10)$$

where $\upsilon^{AE} = \upsilon^{AE}[\rho; r]$ represent the screened all –electron (AE) potential and $R_{nl}^{AE}(r)$ is the radial wave function. The screened atomic pseudo-potential υ_l and the radial pseudo-wave-function $R_l^{ps}(r)$ are satisfying the equation with the same energy ε:

$$\left[\frac{-1}{2m}\frac{d^2}{dr^2} + \frac{l(l+1)}{2mr^2} + \upsilon_l^{atomic}\right] rR_l^{ps}(r) = \varepsilon rR_l^{ps}(r) \qquad (3.11)$$

Both the pseudo-wave-function and the screened pseudo-potential are analytic functions within the cutoff radius r_{cl}. Concerning the unscreened (ionic) pseudo-potential, it is obtained by subtracting from the screened (atomic) pseudo-potential the screening part:

$$\upsilon_l^{ionic}(r) = \upsilon_l^{atomic}(r) - \upsilon_H^{ps}(\rho; r) - \upsilon_{xc}^{ps}(\rho; r) \qquad (3.12)$$

This pseudo-potential is generally insensitive to reasonable variations in the electronic configuration of the atom.

To obtain the exchange-correlation energy accurately it is necessary that outside the core region, the real and pseudo-wave-functions be identical, so that both wave functions generate identical charge densities. With other words, in the norm conserving pseudopotential approach outside of a cutoff-radius, the pseudo-wave-functions are identical to the real all-electron wave functions.

II.3.3. 'Plane waves' basis sets

Additionally, basis sets composed of sets of plane waves [24, 25] down to a cutoff wavelength are often used, especially in calculations involving systems with periodic boundary conditions. Bloch's theorem uses the periodicity of a crystal to reduce the infinite number of one-electron wave functions to be calculated to simply the number of electrons in the unit cell of the crystal (or half that number if the electronic orbitals are

assumed to be doubly occupied - that is, spin degenerate). Thus, the wave function is written as the product of a cell periodic part and a wavelike part (see II.2.3.1.3).
The plane wave basis sets are often used in combination with an 'effective core potential' or pseudopotential, so that the plane waves are only used to describe the valence charge density. This is because core electrons tend to be concentrated very close to the atomic nuclei, resulting in large wave function and density gradients near the nuclei which are not easily described by a plane wave basis set, unless a very high energy cutoff, (and therefore small plane wavelength), is used.

II.4 Molecular Dynamics (MD)

The molecular dynamics method was first introduced by Alder and Wainwright in the late 1950's [26, 27] to study the interactions of hard spheres. Many important insights concerning the behaviour of simple liquids emerged from their studies. The next major advance was in 1964, when Rahman [28] carried out the first simulation using a realistic potential for liquid argon. The first molecular dynamics simulation of a realistic system was done by Rahman and Stillinger in their simulation of liquid water in 1974 [29].
Classical molecular dynamics is an atomistic simulation method where:

- each atom is treated as a point mass,
- simple force rules describe the interactions between atoms
- Newton's equations are integrated to advance the atomic positions and velocities
- thermodynamic statistics are extracted from the motion of the atoms.

Classical Molecular Dynamics

The molecular dynamics simulation method is based on Newton's second law or the equation of motion. From knowledge of the force on each atom, it is possible to determine the acceleration of each atom in the system. Integration of the equations of motion then yields a trajectory that describes the positions, velocities and accelerations of the particles

as they vary with time. From this trajectory, the average values of properties can be determined. The method is deterministic; once the positions and velocities of each atom are known, the state of the system can be predicted at any time in the future or the past.

The potential energy is a function of the atomic positions (3N) of all the atoms in the system. Due to the complicated nature of this function, there is no analytical solution to the equations of motion; they must be solved numerically. Numerous numerical algorithms have been developed for integrating the equations of motion. In choosing which algorithm to use, one should consider the following criteria: 1) the algorithm should conserve energy and momentum; 2) it should be computationally efficient and 3) it should permit a long time step for integration. We will discuss here just the case of Verlet algorithms and Verlet velocities.

II.4.1. Verlet Algorithm

The Verlet algorithm [30, 31] is widely used for optimizations because it requires a minimum amount of computer memory and CPU time. It uses the positions and accelerations of the atoms at the current time step and positions from the previous step in order to compute the positions for the next time step:

$$R_I(t+\Delta t) = R_I(t) + \mathrm{v}_1(t+\frac{\Delta t}{2})\Delta t \qquad (4.1)$$

At each time step t the position of each nucleus $R_I(t)$ is advanced to the next time step $t+\Delta t$ depending upon the forces due to the other nuclei at the present time step. The equations are only approximate for any finite Δt and the energy is conserved allowing long and stable runs for simulations.

A problem with this version of the Verlet algorithm is that velocities are not directly generated. The velocity Verlet algorithm uses positions, velocities, and accelerations at the current time step. This gives a more accurate integration than the simple Verlet algorithm. The Verlet and velocity Verlet algorithms often have a step in which the velocities are

rescaled in order to correct for minor errors in the integration, thus simulating a constant-temperature system:

$$\mathrm{v}_1(t+\frac{\Delta t}{2}) = \mathrm{v}_1(t-\frac{\Delta t}{2}) + \frac{\Delta t}{M_I} F_I[\{R_J(t)\}] \qquad (4.2)$$

where $\mathrm{v}_I(t+\frac{\Delta t}{2})$ represents the velocity at $(t+\frac{\Delta t}{2})$, $F_I[\{R_J(t)\}]$ is the force of J atoms acting on I atoms at the time t, and M_I is the mass of atom *I.* The temperature can be calculated from the velocities. Each step is usually on the order of femtoseconds.

II.4.2 Thermalization of the system

Thermodynamics dictates the energetic relationships between different chemical states, whereas the sequence of events that occur as molecules transform between their various possible states is described by kinetics:

$$\frac{3}{2} N k_B T = \frac{1}{2} \sum_I M_I \mathrm{v}_I^2 \qquad (4.3)$$

where N represents the number of particles in system, k_B is the Boltzmann, T is the system temperature. The rate and direction of motion (velocity) are governed by the forces that the atoms of the system exert on each other as described by Newton's equation. This is carried out by slowly "heating" the system (initially at absolute zero) and then allowing the energy to equilibrate among the constituent atoms. The heat causes the atoms to become unstuck from their initial positions (a local minimum of the internal energy) and wander randomly through states of higher energy; the slow cooling gives them more chances of finding configurations with lower internal energy than the initial one. This approach is called the annealing method.

II.4.3 Annealing method

Annealing method [32, 33] also is used for optimization of atomic structures. We suppose that a set of N particles has many possible equilibrium configurations. The energy of these configurations is in general different, and one of them will be the optimal one. Finding the optimal structure within an approach based on traditional minimization techniques (steepest descent method, conjugate gradient method, etc.) is tricky, as these methods do not normally overcome energy barriers and tend to fall into the nearest local minimum. Temperature in a molecular dynamics calculation provides a way to "fly over the barriers". States with energy E are visited with a probability $\exp(-E/k_B T)$. If T is sufficiently high, the system can explore the different minima present in the potential energy surface (PES) spending more time in the deeper ones. By decreasing slowly T to 0, there is a good chance that the system will be able to localize in one of the minima of PES. This consideration is the base of simulated annealing methods, where the system is equilibrated at a certain temperature and then slowly cooled down to T=0.

II.5 Computational Softwares

We will detail here some specific features of the softwares used through out this work. The used package softwares were Amsterdam Density Functional (ADF) and Spanish Initiative for Electronic Simulations with Thousands of Atoms (SIESTA).

II.5.1 Amsterdam Density Functional (ADF)

Amsterdam Density Functional [34-41], has been used for ab-initio electronic structure calculations of isolated organic molecules or on the grafting of molecules on a small aggregate of Si (1 0 0) surface.

One unique characteristic of ADF is the use of fragments approach. The poly-atomic system to be computed is conceptually built up from fragments, the molecular one-

electron orbitals are calculated as linear combinations of fragment orbitals, and final analyzes of the bonding energy are in terms of initial fragment properties. The principle of building molecular fragments is shown schematically in the following diagram.

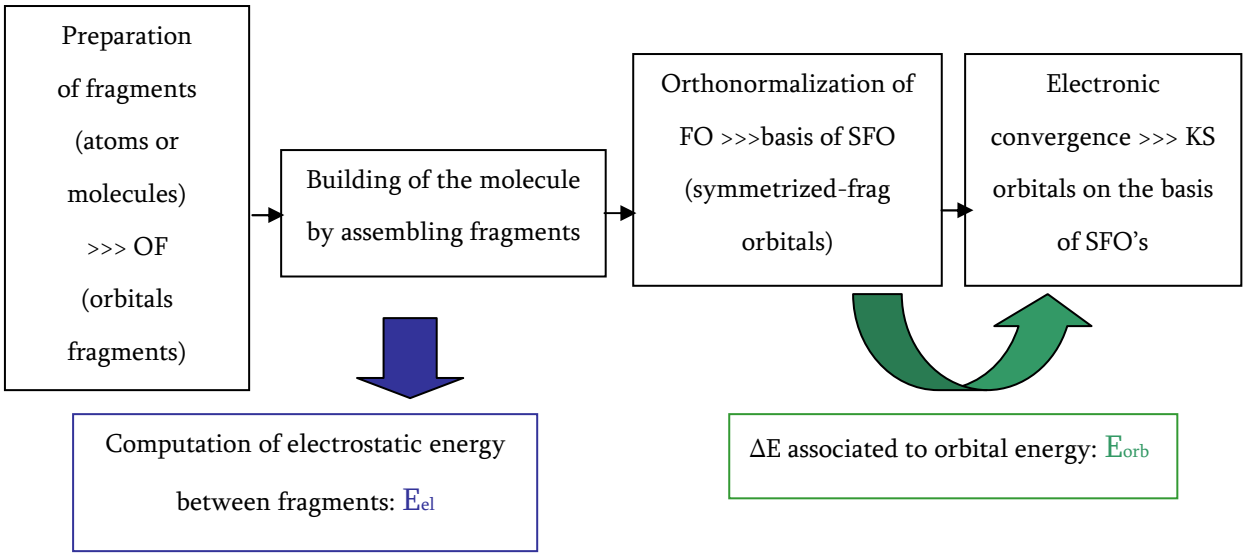

Figure II.2. Molecular fragments in ADF

Energetic analysis is made by using partitioning of the total bonding energy in terms of electrostatic, repulsion and bonding energy: $E_{tbe} = E_{el} + E_P + E_{orb}$. Then, the orbital analysis is done by decomposition of KS orbitals on the basis of SFO (Symmetrized Fragment Orbitals). It should be underlined that KS orbitals are not strictly speaking molecular orbitals, but it is now commonly admitted that they are very similar, and we will use the term molecular orbitals (MOs) to describe KS orbitals.

Basis sets are built with Slater-type orbital functions and range from minimal to triple-zeta-plus-double-polarization quality. A choice of density Functionals, both for the Local Density Approximation (LDA) [42], for the Generalized Gradient Approximation (GGA) [43], and also for hybrid ones (without gradient, thus only used for energy single points) are available. We have used in our calculations various functionals including Becke-Perdew, Becke [44] exchange with LYP [45] correlation, Perdew-Wang 1991 [46], Perdew, Burke, Ernzerhof [47] and several others.

Solvation effects are taken into account using the COSMO model that is a Polarizable Continuum Model.

An important aspect of ADF is the (optional) use of a frozen core to trim down the computational time by reducing the size of the variational basis set. With a frozen core calculation we can obtain the total charge density and potential in the valence and in the core region, neglecting the slight change in the deep-core orbitals upon formation of the chemical bond.

Molecular orbital diagrams and the optimized structures were visualized using the graphical interface of ADF.

II.5.2 SIESTA

SIESTA combines the quantum chemistry DFT with Solid State Physics Approach. This software package has been used for band structures calculations of hybrid Si/molecular systems.

SIESTA allow the simulation of molecules and systems with an increasing number of atoms N, using of so-called order –N algorithms [48, 49], in which the computer time and memory scales linearly with the simulated system size. It is based on self consistent density functional method [50] using standard norm-conserving pseudo potentials in their fully nonlocal form [51] and a flexible linear combination of atomic orbitals (LCAO) basis set, with essentially perfect order *(N)* scaling, which includes multiple-zeta and polarization bases [52-54]. There are no constraints either on the radial shape of these orbitals (which are treated numerically), or on the size of the basis, allowing for the full quantum-chemistry (QC). The cores are described now by norm-conserving pseudopotentials factorized in the Kleinman-Bylander form [55].

The Perdew, Ernzerhof and Burke (PBE) GGA functional was used, including spin polarization in our calculations. Hybrids are not generally used in solid state physics because of the difficulty of computing the exact-exchange part within a plane-wave basis set. The basis functions and the electron density are projected on a real-space grid, in

order to calculate the Hartree and exchange–correlation potentials and matrix elements, with a number of operations that scales linearly with the size of the system. Forces on the atoms and the stress tensor are obtained from the Hellmann-Feynman theorem (including Pulay corrections [56]), and can be used for structure relaxations or molecular dynamics simulations of different types.

Bibliography

[1] R. M. Martin, *Electronic Structure*, Cambridge University Press, 2004

[2] G. P. Srivastava, *Theoretical Modelling of Semiconductor Surfaces*, World Scientific Publishing, 1998

[3] http://www.fisica.uniud.it/~ercolessi/md/md/node17.html

[4] H. Smith, introduction to quantum mechanics, *World Scientific*, 1991

[5] K. B. Lipkowitz, D. B. Boyd, T. R. Cundari, R. Larter, *Reviews in Computational Chemistry*, Wiley, John & Sons, vol. 21, 2005

[6] S. L. Altmann, *Band Theory of Solids: An Introduction from the point of view of symmetry*, Oxford University Press, 1994

[7] S. Fujita, K. Ito, *Quantum theory of Conducting Matter*, Springer, 2007

[8] J. M. Ziman*, Principles of the theory of Solids*, Cambridge University Press, 1979

[9] C. Kittel, *Introduction to Solid State Physics*, Wiley, 1996

[10] N. W. Ashcroft, N. D. Mermin, *Solid State Physics*, 1976

[11] G. Joos, *Theoretical Physics*, Dover Publications, 1987

[12] H. J. Monkhorst, J. D. Pack, *Phys. Rev. B* 1976, *13*, 5188

[13] J.C. Phillips, *Phys. Rev*. 1958, *112*, 685

[14] J.C. Phillips, L. Kleinman, *Phys. Rev*. 1958, *116,* 287

[15] V. Heine, *Solid State Physics*, Academic Press, 1970

[16] W.E.Pickett, *Comp. Phys. Rep.* 1989*, 9*, 115

[17] A. Redondo, W.A.Godard, T. C. McGill, *Phys. Rev. B* 1977, *15*, 5038

[18] D. R. Hamann, M. Schlüter, C. Chiang, *Phys. Rev. Lett.* 1979, *43*, 1494

[19] A. Zunger, M. L. Cohen, *Phys. Rev. B* 1979, *20*, 4082

[20] G. P. Kerker, *J. Phys.C* 1980, *13*, L189,

[21] G. B. Bachelet, D. R. Hamann, M. Schlüter. *Phys. Rev. B* 1982, *26*, 4199

[22] J. C. Phillips, L. Kleinman, *Phys. Rev*. 1959, *116*, 287

[23] N. Troullier, J. L. Martins, *Phys. Rev. B* 1991, *43*, 1993

[24] http://cmt.dur.ac.uk/sjc/thesis_dlc/node33.html

[25] www.pci.uzh.ch/gruppe.hutter/e/information/lyon_lect2.pdf

[26] B. J. Alder, T. E. Wainwright, *J. Chem. Phys.* 1957, *27*, 1208

[27] B. J. Alder, T. E. Wainwright, *J. Chem. Phys.* 1959, *31*, 459

[28] A. Rahman, *Phys. Rev.* 1964, *A136*, 405

[29] F. H. Stillinger, A. J. Rahman, A. *J. Chem. Phys.* 1974, *60*, 1545

[30] L. Verlet, *Phys. Rev*. 1967, *159*, 98

[31] J. P. Hansen, L. Verlet, *Phys. Rev*. 1969, *184*, 151

[32] S. Kirkpatrick, C. D. Gelatt, M. P. Vecchi, *Science* 1983, *220*, 671

[33] V. Cerny, *J. of Opt. Theory and Appl*. 1985, *45*, 41

[34] G. Te Velde, F. M. Bickelhaupt, E. J. Baerends, C. F. Guerra, S. J. A. Van Gisbergen, J. G. Snijders, T. Ziegler, *J. of Comp. Chem*. 2001, *22*, 931

[35] E. J. Baerends, D. E. Ellis, P. Ros, *Chem. Phys.* 1973, *2*, 41

[36] P. M. Boerrigter, G. te Velde, E. J. Baerends, *Int. J. Quantum Chem*, 1988, *33,* 87

[37] G. te Velde, E. J. Baerends, *J. Comput. Phys*. 1992, *99*, 84

[38] G. te Velde, E. J. Baerends, *Phys Rev B* 1991, *44*, 7888

[39] L. Versluis, T. Ziegler, *J. Chem. Phys*. 1988, *322,* 88

[40] L. Fan, T. Ziegler, *J. Chem. Phys.* 1922, *96*, 9005

[41] http://www.scm.com/

[42] R. O. Jones, O. Gunnarsson, *Rev. Mod. Phys*. 1989, *61*, 689

[43] M. Ernzerhof, J. P. Perdew, K. Burke, *Density functionals: Where do they come from, why do they work? Topics in Current Chemistry*, Springer, Berlin, 1996

[44] A. D. Becke, *J. Chem. Phys.* 1986, *84*, 4524

[45] C. Lee, W. Yang, R. G. Parr, *Phys. Rev. B,* 1988**,** *37*, 785

[46] J. P. Perdew, Y. Wang, *Phys. Rev. B,* 1986**,** *33*, 8800

[47] J. P. Perdew, K. Burke, M. Ernzerhof, *Phys. Rev. Lett.* 1996**,** *77*, 3865

[48] L. Greengard, *Science* 1994*, 265***,** 909

[49] R. W. Hockney, J. W. Eastwood, *Computer Simulation Using Particles,* Bristol: Institute of Physics, 1988

[50] M. C. Payne, M. P. Teter, D. C. Allan, T. A. Arias, J. D. Joannopoulos, *Rev. Mod. Phys.* 1992, *64***,** 1045

[51] L. Kleinman, D. M. Bylander, *Phys. Rev. Lett.* 1982*, 48*, 1425

[52] P. Ordejon, E. Artacho, J. M. Soler,1996 *Phys. Rev.* B 1996, *53*, 441

[53] D. Sanchez-Portal, P. Ordejon, E. Artacho, J. M . Soler, *Int. J. Q. Chem.,* 1997, *65***,** 453

[54] http://www.uam.es/siesta

[55] S. G. Louie, S. Froyen, M. L. Cohen, *Phys. Rev. B* 1982, *26*, 1738

[56] P. Pulay, *Molec. Phys.* 1969*, 19*, 197

Chapter III

Modeling of molecular properties for information storage

Introduction

The main relevant properties for the design of molecules for storage information based on charge states that deserve to be studied are:

- redox properties: stable redox states and redox potentials
- their structural properties
- correlation between redox properties and structural features for the purpose of bistable systems.

Our objectives in this chapter will thus be firstly to be able to reproduce these molecular properties, i. e. to estimate geometrical and energetic features for stable states of the redox molecules. Secondly, the understanding of potential bistability phenomenon necessitates to reproduce the structural changes of large switchable molecular systems such as the bridled porphyrins, depending on molecular parameters such as the functional groups, the metal atom and the redox state of the molecule. This latter part was based mainly on the bridled porphyrins developed in the laboratory and that we mentioned previously in the 1st chapter.

The chapter will thus be organized in four parts. We will describe firstly the modeling of structural and redox properties of simple molecular species, precursors for the more complex hybrid systems. This includes ferrocene derivatives and simple porphyrins, for which we estimated geometrical and redox potential values. Then we will turn our attention towards more complex porphyrins, still precursors for switchable systems, including meso substituted porphyrins for which we studied the conformational properties depending on the meso group and the central metal ion. Then we will present the results obtained on the bridled porphyrins with non redox metal center with aim the aim to focus on structural properties. Finally, we will describe our results on Mn porphyrins. In all these parts, we will rely on available experimental data that will be given along with our theoretical results.

III.1 Computation of simple redox molecular species

As above mentioned we will focus on ferrocene derivatives and a simple functionalized porphyrin in order to check the computations of redox potentials against experimental and/or other published results.

III. 1.1. Theoretical approach

In this first part, we will remind the main modeling approach used to calculate redox potentials. We have fully optimized the molecular geometries of reduced and oxidized forms, using a solvent PCM model. Once the total energies for both forms have been computed, we have used the following equation to obtain the redox potential of a ox/red species, using the convention:

$$Ox + 1\ e \longrightarrow Red \quad (1.1)$$

Expressing the redox potential versus the Normal Hydrogen Electrode (NHE) and with energy terms in eV, the relation between the potential and the Gibbs energy terms is thus:

$$V_{ox/red} - V_{NHE} = [(\Delta G_{red} - \Delta G_{ox}) - \Delta G_{H+/H2}] \approx -[(\Delta H_{red} - \Delta H_{ox}) - \Delta G_{H+/H2}] \quad (1.2)$$

if we neglect the entropy term. Finally if we neglect the zero-point energy (ZPE), we can approximate the redox potential vs NHE reference as:

$$V_{ox/red} - V_{NHE} \approx -[(E_{red} - E_{ox}) - \Delta G_{H+/H2}] \quad (1.3)$$

Then with the value $\Delta G_{H+/H2} = 4.44eV$ we can calculate the redox potential in volts versus NHE with the following equation [1]:

$$V - V_{NHE} = -[(E_{red} - E_{ox}) - 4.44] \quad (1.4)$$

where $E_{red/ox}$ represents total bonding energies in eV of the ox and red species calculated in the PCM solvent environment [1, 2]. The main approximations in that case lie on the neglect of the entropy and ZPE terms between oxidized and reduced forms.

Acetonitrile solvent *(ε = 37,5)* was taken into account through a Polarizable Continuum Model within ADF using default parameters of the program [3]. In this method, the solute is accommodated in a cavity, formed by spheres centered on the solute atoms, and the solvent reaction field is described in terms of apparent charges on the cavity walls. Starting from a widely used compilation of atomic radii [4] optimized for aqueous solutions, we have optimized the ferrocene and ferrocenium in acetonitrile and we calculated the redox-potential.

III.1.2. Ferrocene species

Ferrocene (Fc) shown below in its two stable conformations on figure 3.1, and several ferrocene derivatives (figure 3.2), precursors for the grafting steps on Si were studied.

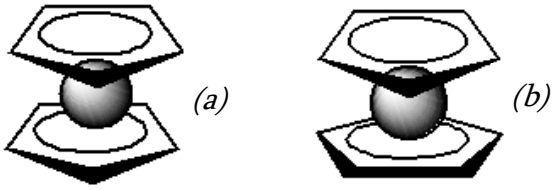

Figure III.1 (a) ferrocene eclipsed, (b) ferrocene staggered

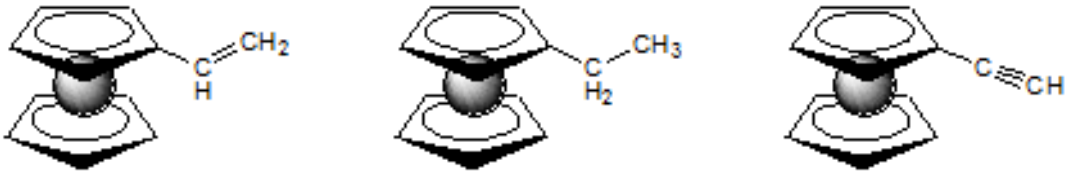

Figure III.2 (a) vinyl –Fc; (b) ethyl- (EtFC); ethinyl-Fc (EFC)

All calculations have been carried out in the Kohn-Sham formalism within the Density Functional Theory framework, using Amsterdam Density Functional (ADF) 2006 [3, 5, 6]. The basis sets were made of Slater-type orbital double-zeta functions including one polarization function for H and C. Frozen cores were used for C (1s) and (1s–2p) for Fe. The exchange and correlation potentials were, respectively, the Becke 88 and Perdew 86 [7, 8] functionals.

Having in view that these molecules were used for grafting, we checked first which is the most stable conformation. In table 1 are shown the resulting ground state energies for neutral ferrocene and the oxidized species (ferrocenium) in both conformations.

Table 1. Ferrocene total bonding energies

Ferrocene	**Total bonding Energies (eV)**	**Ferrocenium**	**Total bonding Energies (eV)**
Eclipsed	ΔE= -133.03	Eclipsed	ΔE= -126.21
Staggered	ΔE=- -132.99	Staggered	ΔE= -126.20

The resulting energies, either for eclipsed or staggered conformation are very close, as already known for ferrocene. This means that for grafting we can use either eclipsed or staggered conformation.

In table 2 are shown the resulting energies and the energy difference between neutral and oxidized systems in gas phase and solvent.

Table 2. Total bonding energies in gas phase and solvent and ferrocene/ferrocenium energy difference

	Gas Phase			**Acetonitrile**		
R	$RFeCp_2$ eV	$RFeCP_2^+$ eV	$\Delta E_{red/ox}$ eV	$RFeCp_2$ eV	$RFeCp_2^+$ eV	$\Delta E_{red/ox}$ eV
Ferrocene	-132.16	-125.02	7.14	-132.26	126.95	5.31
Ethyl-Fc	-164.72	-157.78	6.94	-164.90	-159.74	5.15
Vinyl -Fc	-156.59	-149.57	7.02	-156.80	-151.57	5.22
Ethynyl-Fc	-147.82	-140.61	7.21	148.06	-142.63	5.43

Thus, we can calculate the redox potentials using equation (1.4). The entropy changes have not been evaluated, as we assume that the changes in entropy between two conformers are negligible. In figure III.3 are shown the computed redox potential (volts, referred to NHE) for Fc derivatives in acetonitrile.

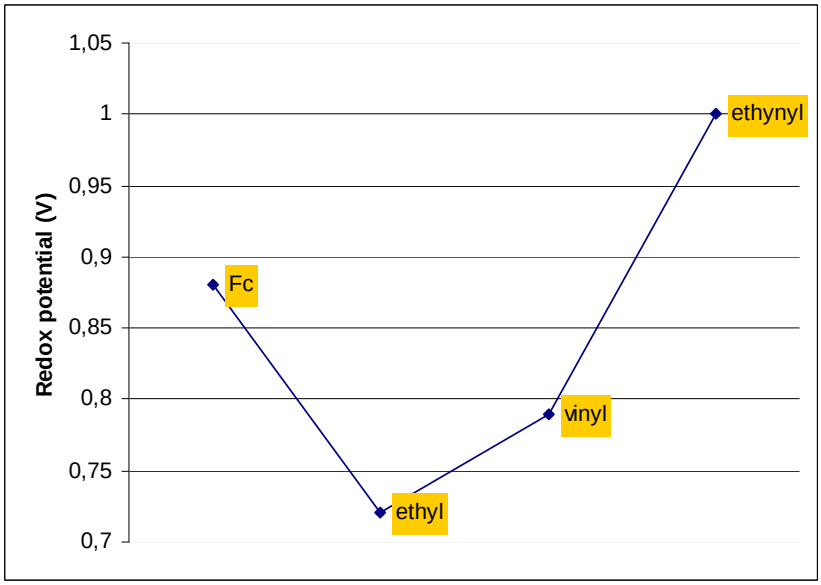

Figure III.3 Computed redox potential (volts, referred to NHE) for Fc derivatives in acetonitrile

These results are quite in good agreement with previously reported experimental and theoretical data by Cossi et al. [9] shown on figure III.4.

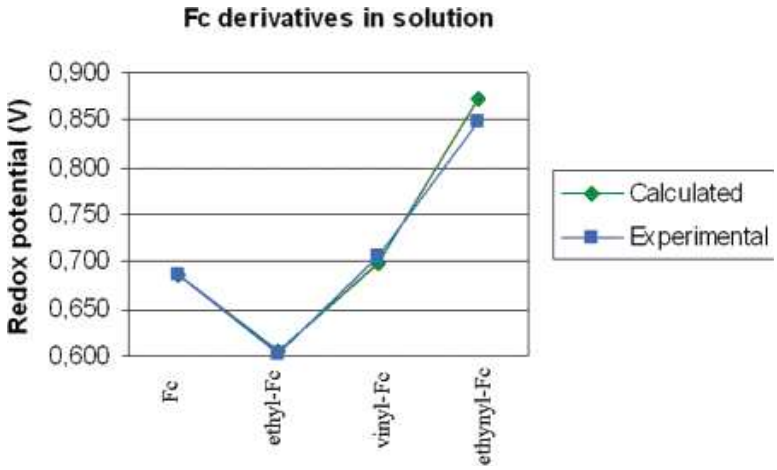

FigureIII.4 Computed and experimental redox potential (volts, referred to NHE) for Fc derivatives in acetonitrile (from [9]).

It should be mentioned that they used a B3LYP functional instead of a GGA like ours. But the most important difference is that their atomic radii of atoms were adjusted in order to match exactly the experimental redox potential for Fc.

We can observe that our results, obtained with standard parameters, are for all Fc derivatives within an error range of 200 mV which is commonly observed when calculating redox potential [1].

III.1.3. Zn porphyrins

Zn tetraphenyl porphyrin (ZnTPP) is the precursor of the redox porphyrins that have been used for studies of the electrical properties of Si-hybrid devices. Indeed, the zinc (4-ethynylphenyl) 5, 15, 20- (mesityl) porphyrin noted $ZnAB_3P$ below (represented on figure III.5) has been functionalized with an ethynyl group for further grafting. Its cyclic voltammetry (CyV) [10] is shown on figure. III.5 with a saturated calomel electrode (ECS) as reference. It undergoes two reversible redox reactions, very similarly to ZnTPP [11, 12].

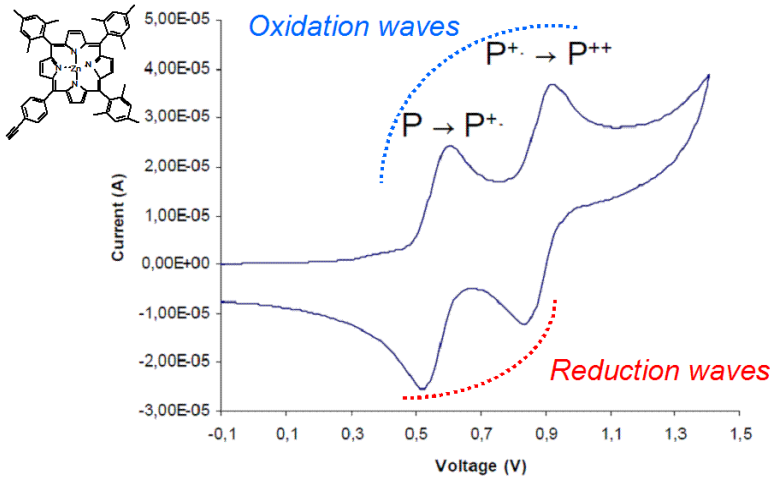

Figure III.5 Cyclic Cyclic Voltammetry test $ZnAB_3P$ in solution [10, 13]

As for ZnTPP, two monoelectronic oxidation processes can be observed, the first wave (at 0.55 V) corresponding to oxidation to a radical cation and the second to the formation of

the bication (at 0.88 V). In order to use the NHE reference, we add +0.24 V to these values, to get 0.79 V /NHE and 1.12 V/NHE resp. for the 1st and 2nd oxidation steps.

They are very close to the ZnTPP redox potentials obtained in the literature, some of them being noted on table 3.

All calculations have been carried out using Amsterdam Density Functional (ADF) 2007 code. The basis sets were made of Slater-type orbital double-zeta functions including one polarization function for H, C and N and a triple-zeta for Zn. Small frozen cores were used ([He] for light atoms, [Ne] for Zn). The exchange and correlation potential was described by the Perdew Burke and Ernzerhof (PBE) functional [14]. Metal ion Zn^{2+} has a singlet ground state and thus the system is closed shell. Then, acetonitrile solvent was taken into account through a Polarizable Continuum Model within ADF using default parameters of the program [3]. The oxidized cation species being a radical, an unrestricted formalism was used imposing a doublet ground state. The structures have been fully optimized in solvent.

In table 3 are shown the resulting redox potentials (V versus NHE) computed in solvent for the two redox potentials of ZnTPP as well as experimental data from the literature [11, 12].

Table 3. Redox potentials (V vs NHE) for ZnTPP: computations and experimental data

	ZnTPP/ZnTPP^{+}	**ZnTPP^{+}/ZnTPP^{2+}**
Exp [11]	1.19	1.59
Exp [12]	0.90	1.19
Our work	1.02	1.50

It should be noted that data from the literature were obtained under different conditions of solvent in particular.

Finally, an analysis of the atomic orbital contributions in the HOMO and LUMO of our calculated structures of ZnTPP, $ZnTPP^{+}$ and $ZnTPP^{2+}$ shows clearly that the two redox

process occur on the conjugated plane of the porphyrin, the metal being not redox active and its d orbitals being much lower in energy. This was already shown by Liao et al. [15]. Clearly on these two families of redox active precursors, the computation of the redox potentials is in excellent agreement with experimental values, within the 200 mV error range.

III.2. Computational studies of chiral meso-(α,β-unsaturated)-porphyrins

In this part, we report the results on the chiral meso α,β-unsaturated porphyrins [16, 17] derived from (S)-(-)-perilaldehyde and myrtenal (noted PeriP and MyrtP, see figure III.6). They are functionalized on meso positions with chiral groups able to act as an anchor for further functionalization with "bridles" in order to favour large structural switches for bistability properties. The purpose here was to describe theoretically the dynamic conformational features of the free base, zinc(II) and nickel(II) complexes and to compare them with experimental results.

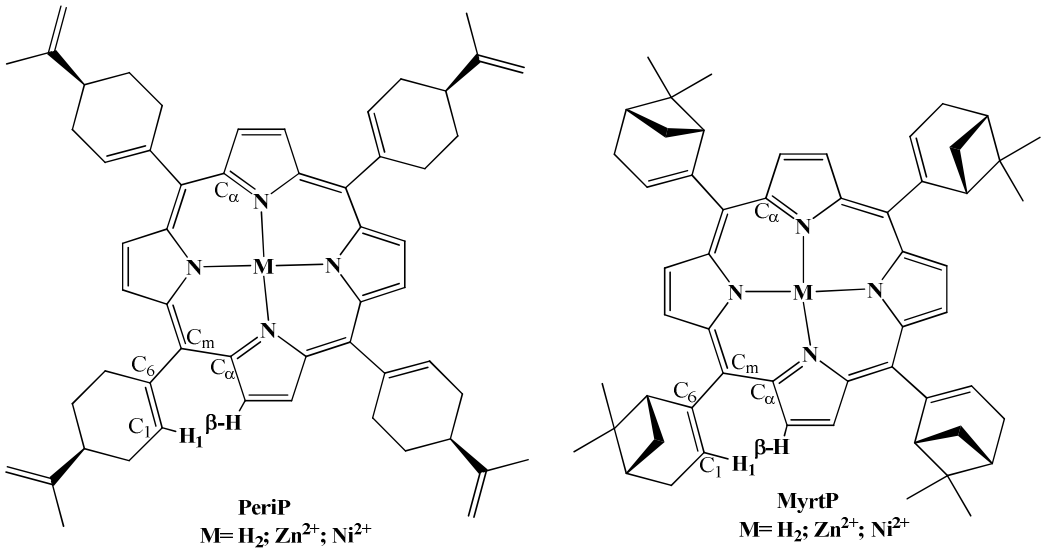

Figure III.6 Perilaldehyde Porphyrin (left) and Myrtenal Porphyrin (right)

III.2.1. Main experimental structural features

Before presenting our own results, we will summarize the main experimental features obtained on these porphyrins. Some experimental structures are known on these metal porphyrins [16, 17]. For instance the single-crystal X-ray diffraction studies of NiPeriP and NiMyrtP reveal that the porphyrinic plane is highly distorted, with a ruffle or saddle mode depending on the meso group [16]. This high deformation is quite general to Ni^{2+} meso substituted porphyrins [16]. NMR spectroscopy proved to be also very powerful to obtain many structural informations in solution. For instance, by examination of the chemical shifts of protons located on the pyrrole rings (i. e. in β positions), it is possible to give a trend of the deformation of the ring. Indeed, these shifts depend on the ring current intensity, which decreases when the porphyrinic core gets more distorted. Thus the NMR shifts give the following order for the deformation of the metal porphyrin core: NiPeriP>H_2PeriP>ZnPeriP. The same is obtained for MyrtP. Another important feature deduced from variable temperature NMR experiments is the coalescence temperatures of the β-proton signals, which help to characterize the dynamical processes linked with the meso substituents rotation. Such data are shown below on figure III.7.

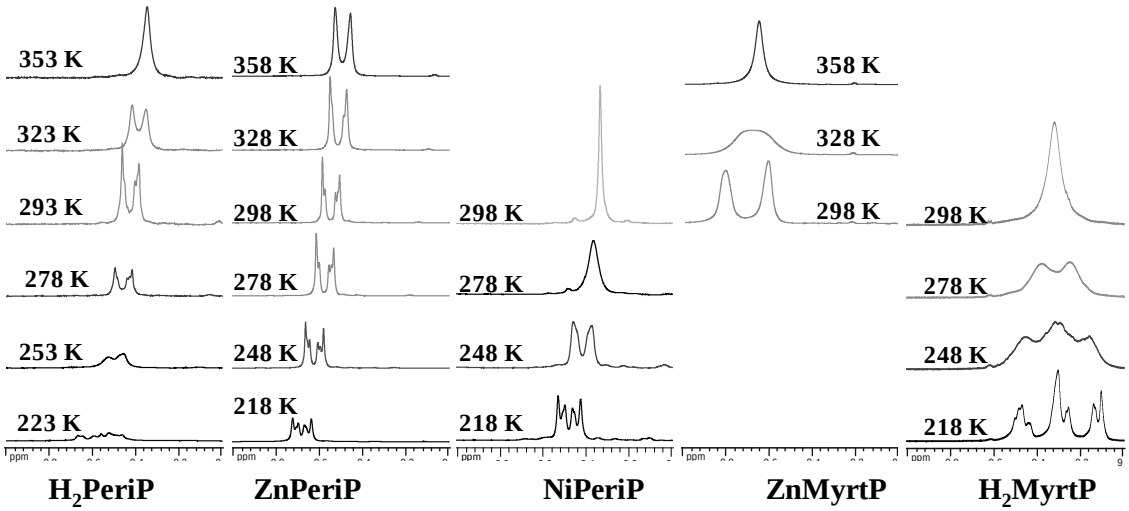

Figure III.7. Variable temperature ^{1}H NMR of the β-H region registered for all studied porphyrins (for NiMyrtP, see reference [17]).

The observed values of coalescence temperature are summarized in table 4.

Table 4. Coalescence temperature and thermodynamic data obtained from variable temperature NMR experiments. $\Delta G^{\neq}$ are experimental activation energies from coalescence temperatures, Ea are computed energy barriers

Porphyrin	Tc (K)	$\Delta G^{\neq}$(kJ.mol^{-1})	E_a (kJ.mol^{-1})
H_2PeriP	T_{c1}=343	72.3	B_1= 117.5
	T_{c2}=273	58.0	B_2= 80.1
H_2MyrtP	T_{c1}=288	58.0	B_1= 87.1
	T_{c2}=258	54.6	B_2=80.0
ZnPeriP	T_{c1} nd	nd	B_1= 95.6
	T_{c2}=338	73.7	B_2=93.3
ZnMyrtP	T_{c1}=333	67.3	B_1= 89.4
	T_{c2}=298	65.1	B_2=85.5
NiPeriP	T_{c1}=278	57.8	B_1= 96.2
	T_{c2}=298	53.3	B_2=67.0
			B_1= 103.1
			B_2=96.1
NiMyrtP	T_{c1}=213	43.0	B_1= 52.8
	T_{c2} nd	nd	B_2=52.3

From these temperatures, it is possible to extract activation energies (noted $\Delta G^{\neq}$ in table 4) for each rotational process. The main conclusions are that for a given metal, PeriP has a higher coalescence temperature than MyrtP and that for a family of porphyrins, the coalescence temperature follows the order Zn > free base > Ni. The values of the free energy of rotation range from 43.0 kJ.mol^{-1} to 73.7 kJ.mol^{-1}, the energy difference between the two rotational processes (T_{c1}, T_{c2}) varies from 2.2 kJ.mol^{-1} to 14.3 kJ.mol^{-1}.

III.2.2. Theoretical study

All calculations have been carried out using Amsterdam Density Functional (ADF) 2006 [3, 5, 6]. The basis sets were made of Slater-type orbital double-zeta functions including one polarization function for H, C and N. Frozen cores were used for C, N (1s) and 3d metal (1s–3p). The exchange and correlation potentials were, respectively, the Becke 88 and Perdew 86 [7, 8] functionals. Both metal ion (Zn^{2+} and Ni^{2+}) complexes with porphyrins have a singlet ground state and thus all systems were closed shell. Total bonding energies were calculated using the usual procedure from the generalized transition state from Ziegler [18].

The starting geometries were derived from crystallographic structures. The free base H_2PeriP came from a low resolution X-ray crystallographic structure obtained in the laboratory, and the Zn^{2+} complex was generated from this structure. The MyrtP analog was obtained by changing perillyl substituents into myrtenyl ones using the facilities of the Chem3D modeling software [19]. This procedure allowed thus to get the starting structures for PeriP and MyrtP free base and Zn species. The NiMyrtP was obtained from the X-ray crystallographic structure. For NiPeriP, two starting structures were used. One was derived from NiMyrtP by changing the peripheral groups using Chem3D software. The other one came directly from the X-ray structure obtained by us. All these starting structures were then fully optimized using ADF, using the default geometric convergence criteria [3].

It should be mentioned that the geometries resulting from the first full optimization are generally close to the starting ones. If the initial structure exhibits a particular distortion of the central core, the optimization process is able to find the equilibrium point which is closest to this distortion, and will not be able to explore other ones. In figure III.8 are shown the optimized structures of NiPeriP and NiMyrtP.

This is a general structural feature of porphyrinic cores: the potential energy surface versus deformation is generally very flat, so that the search for a global minimum is very difficult by common optimization procedures, even using tighter convergence criteria [20].

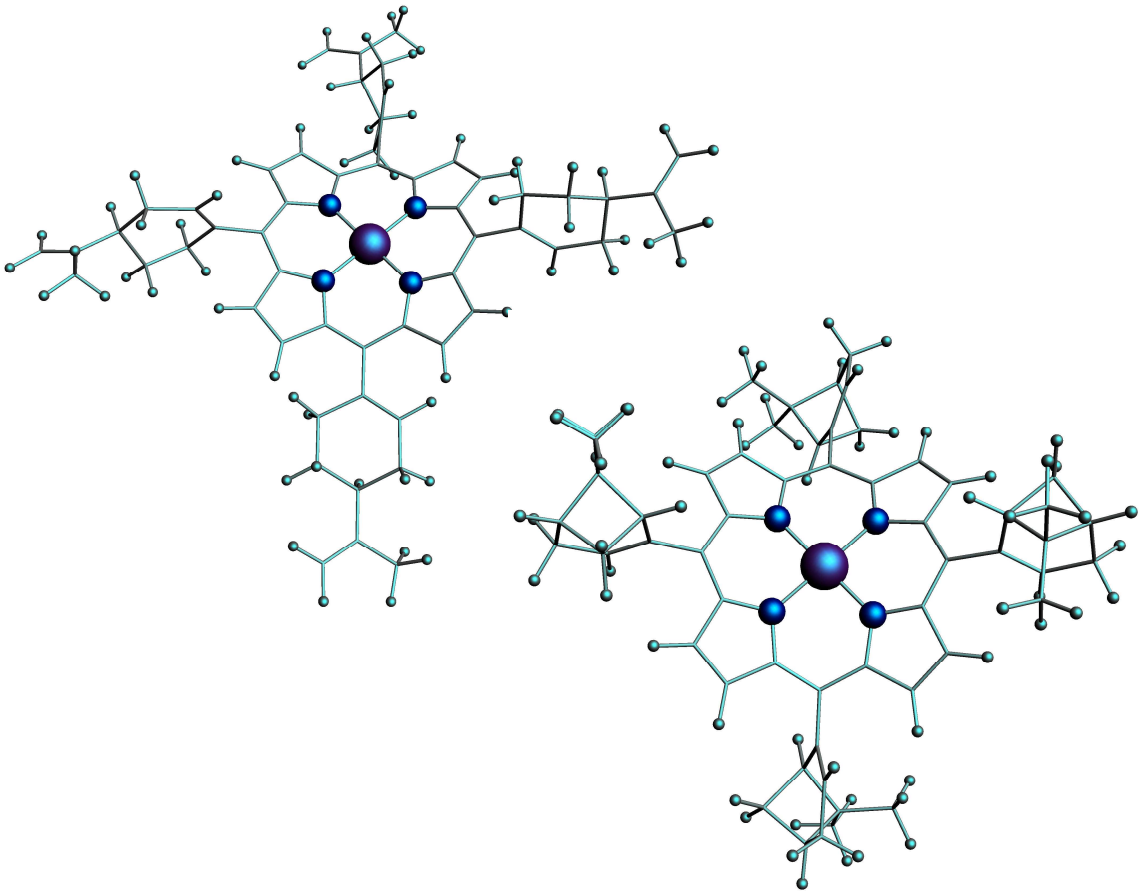

Figure III.8 Optimized structures of NiPeriP (left) and NiMyrtP (right)

Some structural data obtained from optimized geometries are summarized in table 5 showing the very good agreement with experimental data.

Table 5. Averaged metal-N distances (Å), compared to experimental data.

a. From ZnTPP [21]. b. From NiTPP [18]. c. [17]

	<dM-N> : Our work	<dM-N> : exp. Data
ZnPeriP	2.04	2.03[a]
NiPeriP	1.925	1.93[b]
ZnMyrtP	2.03	2.03[a]
NiMyrtP	1.91	1.90[c]

Another feature is the distortion of the porphyrinic ring. We observe that the core in ZnPeriP and ZnMyrt is almost flat, in comparison with the core of Ni porphyrins which are much more distorted. This is another commonly observed feature of Zn and Ni porphyrins.

Then we calculated the conformational barriers of all systems. Starting from the initially fully optimized structure, a fast scan of the energy curve was carried out by computing single points energies on geometries generated by rotating one of the peripheral group, by steps of 20^0 in a 360^0 range for the corresponding dihedral angle. The mechanism of rotation is shown schematically in figure III.9.

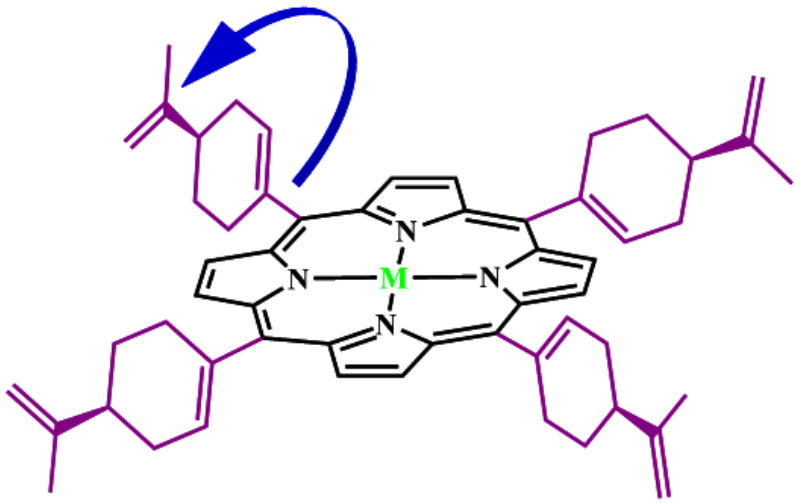

Figure III.9 Rotation of meso substituent

From these conformational profiles, we extracted structures around each minimum and maximum and submitted them to a full geometry optimization, except for the dihedral angle that was kept fixed. In figure III.10 is shown the energy evolution of the single point and optimized curves as a function of the dihedral angle Cα–Cmeso–Cx–Cx.

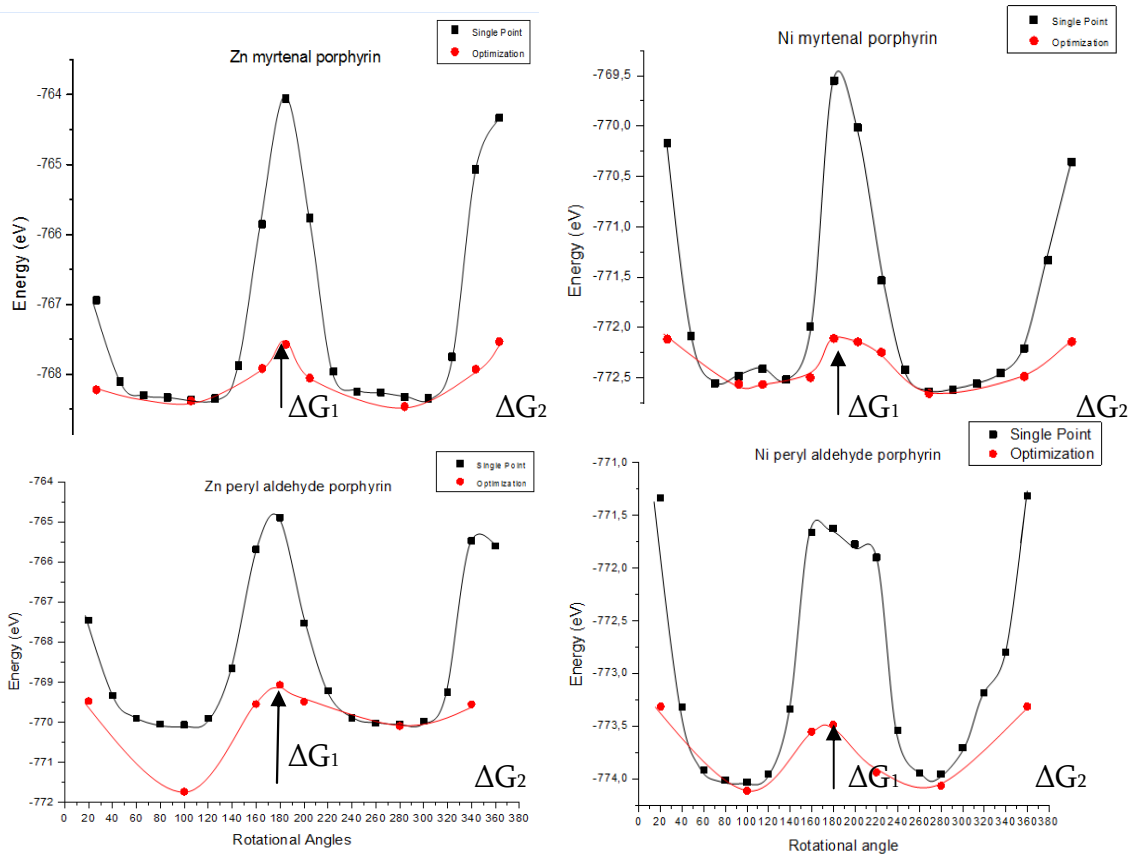

Figure III.10 Computing single points energies and geometry optimization on geometries generated by rotating one of the peripheral group, by steps of 20^0 in a 360^0:(a) Zn Myrtenal;(b) Ni Myrtenal; (c)Zn Perylaldehyde; (d) Ni Perylaldehyde

We thus calculated the energetic barriers between $\Delta G = \Delta G_1 - \Delta G_2$, maxima and minima from these structures. In table 6 are shown the calculated energies that were obtained for conformational barriers. These energies correspond to enthalpic terms (not corrected for zero-point energies). The entropy changes have not been evaluated, as we assume that the changes in entropy between two conformers are negligible. The solvent was not taken into account in our calculations. Indeed, one series of calculations was performed on the ZnPeriP species including toluene solvent through the Polarizable Continuum Model (COSMO in ADF).

Table 6. Calculated energies of conformational barriers

Porphyrin	Theoretical minimum energy (eV)	Theoretical maximum energy (eV)
H_2PeriP	-747.12	-745.92
	-747.14	-746.31
H_2MyrtP	-745.43	-744.52
	-770.17	-744.60
ZnPeriP	-770.17	-769.18
	-770.17	-769.21
ZnMyrtP	-768.38	-767.53
	-768.46	-767.57
NiPeriP	-774.14[b]	-773.16[b]
	-774.15[b]	773.46[b]
	-774.17[a]	-773.12[a]
	-774.19[a]	-773.19[a]
NiMyrtP	-772.57	-772.11
	-772.66	-772.11

We have not observed any change in the structures and energy barriers between the gas phase and solvent results. The comparison with the conformational barriers that were obtained experimentally is shown in figure III.11.

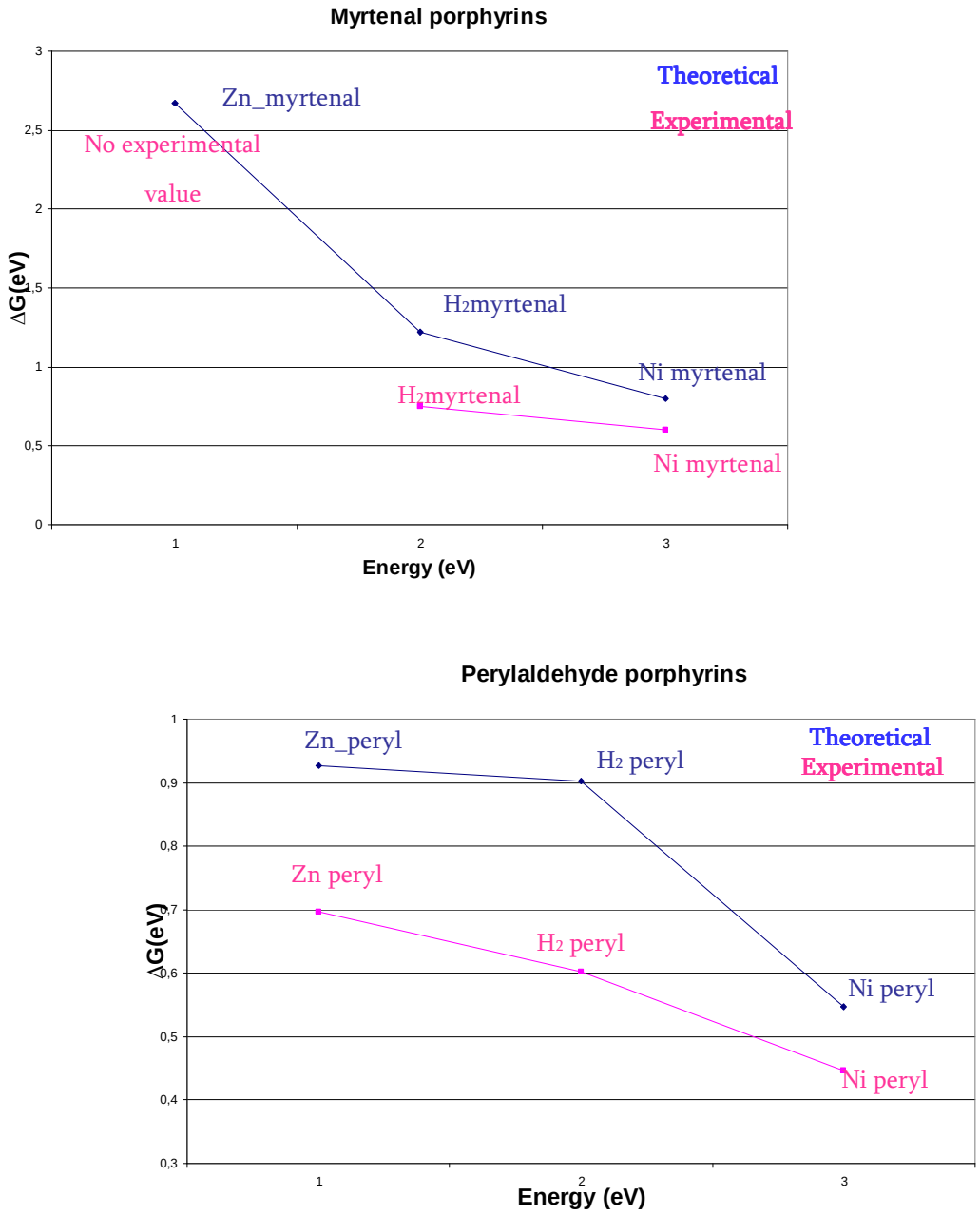

Figure III.11 Theoretical and experimental conformational barriers comparison

As can be seen in the above diagrams, the theoretical results can offer good trends in comparison with experimental data. Because of the temperature factor, no experimental data is available for ZnMyrtP. The conformational barriers for NiPeriP or NiMyrtP are lower in energies than for ZnPeriP or ZnMyrtP. We can explain that taking into account the planarity of the porphyrinic core. In the case of Zn (and free base), the porphyrinic

core is almost flat, while for Ni, it is very distorted. Distortion of the Ni porphyrin core can favour an easier rotation of meso substituent.

To go further into the analysis of the core distortion, were used (by Lionel Dubois in our laboratory) the NSD deconvolution program developed by Shelnutt [22]. A comparison between experimental and theoretical distortion of NiPeriP and NiMyrtP was made. The results obtained are given in figure III.12.

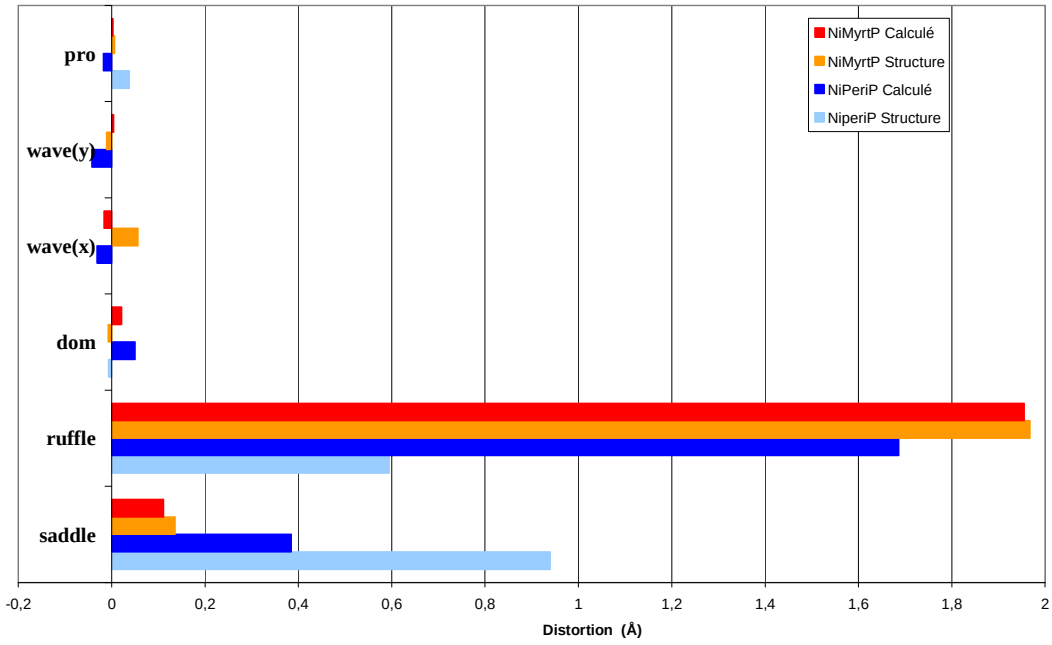

Figure III.12. Types of distortions in NiPeriP and NiMyrt

It can be seen a good agreement with calculated geometry optimization structures concerning the distortion of the two poprhyrins. The distortion of NiPeriP mainly occurs in the saddled mode with an important contribution of the ruffled mode, contrary to NiMyrtP, which is mostly twisted in the ruffled mode.

Theoretical calculations of the activation rotation energy for the meso substituent helped us to have a better understanding of the dynamic behaviour of these porphyrins. We also can conclude that we are able to compute energetic barriers for conformational changes that are in good agreement to experimental trends. This is an important conclusion for

further modeling studies, because energetic conformational barriers are important parameters for the possible switch between two stable structures.

III.3. Bridled porphyrins: towards possible bistable complexes

We have studied in a first part the Zn^{2+} and Ni^{2+} derivatives of BCP8 porphyrin family [23].The general formula of this porphyrin core is drawn on figure III.13

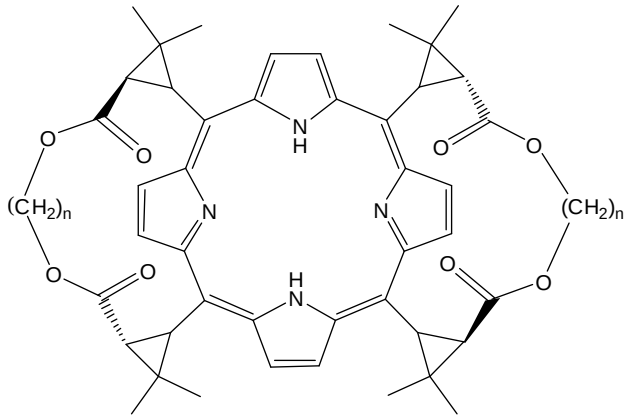

Figure III.13. H_2-BCP8 structure (n= 8).

The presence of the bridles leads to remarkable conformational features, which we mentioned rapidly in the 1st chapter, and we will know detail these characteristics that we have modelled in this work. These molecules may exist as either an *αααα (closed)* or *αβαβ (open)* atropisomer depending on the nature of the coordinated metal cation. We will describe below the main features of the Zn and Ni complexes [24].

III.3.1. Experimental characterizations

III.3.1.1 Solid-state behaviour:

The X-Ray structure of the Ni bridled porphyrin is shown in the figure III.14.

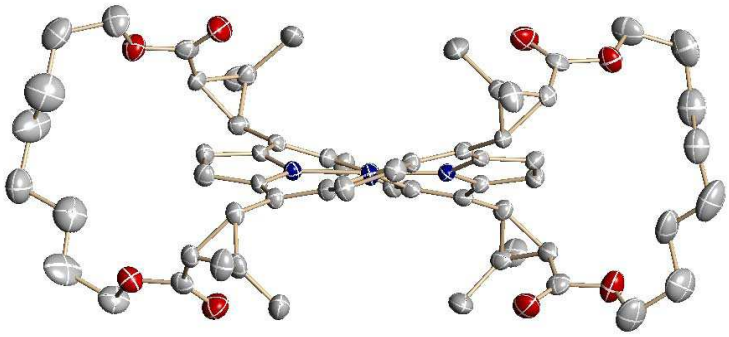

Figure III.14. X-Ray Structure of NiBCP-8

The resulting structure shows that the meso substituents are alternatively above and below of the porphyrin plane, giving an αβαβ conformation. The crystalline structure of ZnBCP-8 is presented in figure III.15.

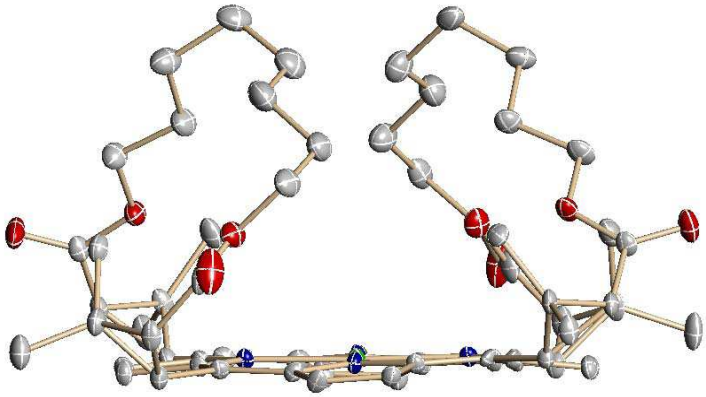

Figure III.15. X-Ray structure of ZnBCP-8

In this structure it is observed that the four meso-substituents are above the porphyrin mean plane, positioning the two 'bridges' on the same side of the macrocycle. The carbonyl groups appear outside of the porphyrin. The porphyrinic cycle is almost planar, with a slight deformation. In this zinc complex, the four anchors of the bridles are located on the same side of the porphyrinic core, leading a αααα atropoisomer. The latter is said to be in a "closed" conformation in contrast with the Ni porphyrin, said to be in an open form.

III.3.1.2 Solution behaviour

NMR spectroscopy was used to probe the structural properties in various solvents. For NiBCP8, only one atropoisomer is observed, whatever the solvent: the αβαβ (open) form. For the ZnBCP8 analogue, a equilibrium between αααα and *αβαβ* is observed, leading to a conformational distribution that depends heavily on solvent and concentration. The relative proportions of different atropoisomers of ZnBCP-8 are summarized in table 7.

Table 7. Distribution of ZnBCP-8 atropoisomers using different solvent at room temperature

Solvent	%αβαβ	%αααα	%(ααβα+ααββ)
Dichloromethane	18	54	28
Nitrobenzene	30	30	40

In contrast with the Ni porphyrin, an equilibrium exists between the two atropoisomers of ZnBCP8. Moreover, it has been shown that in dichloromethane (DCM), a dimerization equilibrium was observed. This property is reminiscent of the X-Ray structure which shows clearly that the porphyrins are associated in dimers, as shown in figure III.16.

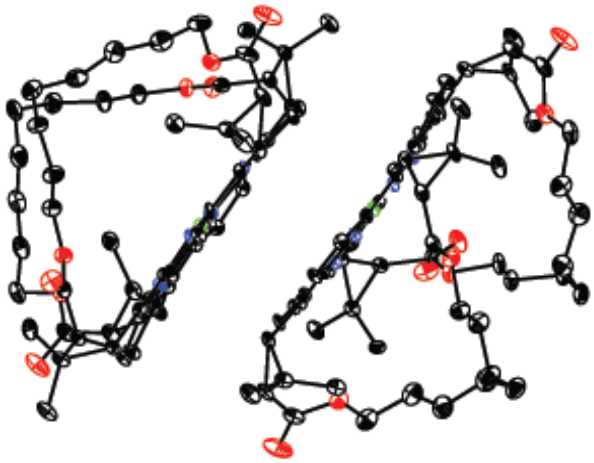

Figure III.16. Dimer structure observed in the crystal

In these dimers, the porphyrinic cores are almost parallel exhibiting interactions through their aromatic cores. Their centers are slightly shifted, so the protons located on the outskirts of one of the two monomers are found near the center of the second one. We can therefore also interpret this phenomenon in terms of monomer-dimer equilibrium as:

$$\alpha\alpha\alpha\alpha + \alpha\alpha\alpha\alpha \underset{}{\overset{K_1}{\rightleftharpoons}} (\alpha\alpha\alpha\alpha)_2 \qquad (1.5)$$

With the constant K_1 defined as follows:

$$K_1 = \frac{[(\alpha\alpha\alpha\alpha)_2]}{[\alpha\alpha\alpha\alpha]^2} \qquad (1.6)$$

By NMR temperature dependence in DCM, the equilibrium constant could be estimated to 95 L. mol^{-1}. No dimerization process exists in nitrobenzene that experimentalists tentatively explained by some π-stacking between the solvent and the porphyrinic core. [23]

III.3.2. Theoretical study

Our aim here was to reproduce the whole set of experimental features, indicating that our methods were able to catch all the main properties of these systems.

All calculations have been carried out using Amsterdam Density Functional (ADF) 2006 [3, 5, 6]. The basis sets were made of Slater-type orbital triple-zeta functions including one polarization function. Frozen cores were used for C, N (1s) and 3d metal (1s–3p). The exchange and correlation potentials were, respectively, the Perdew Burke and Ernzerhof (PBE) [14] functionals. Both metal ion (Zn^{2+} and Ni^{2+}) complexes with porphyrins have a singlet ground state and thus all systems were closed shell.

III.3.2.1. Computations of ZnBCP8 and NiBCP8

Using this approach, we have started to optimize first in gas phase the ZnBCP-8 and NiBCP-8, both in each atropoisomer (αααα and αβαβ). Apart from the Zn porphyrin in closed form and Ni in open form, the two others initial structures (i. e. Zn in open form and Ni in closed form) were generated by changing the metal ion in the X-Ray structures, and reutilizing the new geometries. In figure III.17 are shown the optimized structures.

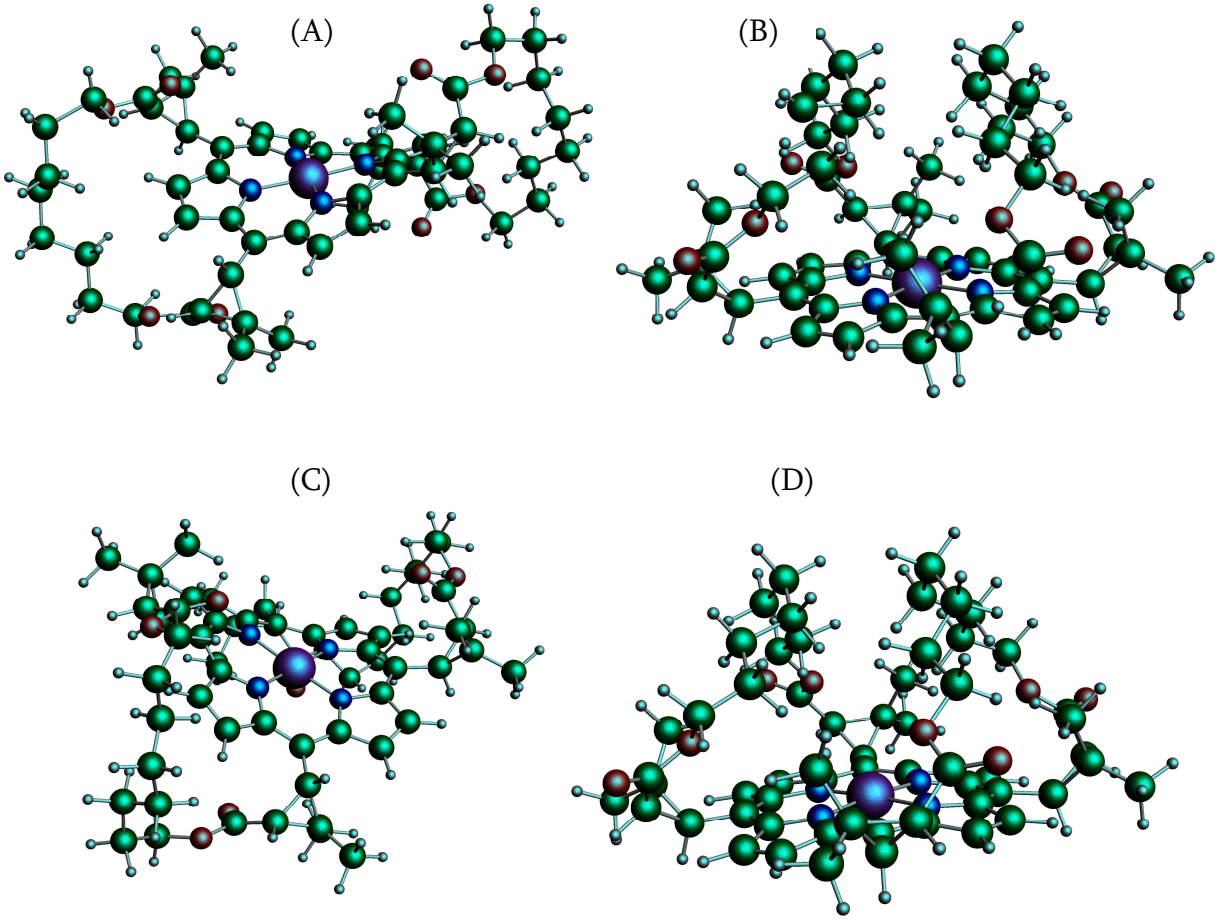

Figure III.17. Conformations of the optimized structures: (A) ZnBCP-8 (αβαβ); (B) ZnBCP-8 (αααα); (C) NiBCP-8 (αβαβ); (D) ZnBCP-8 (αααα);

In table 8 are summarized the total bonding energies that were obtained for these structures, together with the average computed M-N distances and experimental values.

Table 8. Ground state energies for ZnBCP-8 and NiBCP-8 in both conformations (open and closed) and averaged metal-N distances

Porphyrin	Total Bonding Energy (eV)	<M-N>distances (Å) Calc. / exp.
ZnBCP-8 (αβαβ)	-918.09 eV	2.06/2.03
ZnBCP-8 (αααα)	-918.15 eV	2.02
NiBCP-8 (αβαβ)	-922.395 eV	1.97
NiBCP-8 (αααα)	-922.132 eV	1.93/1.92

One point that deserves attention is that on a structural point of view, the open (*αβαβ*) conformation is obtained for a metal-N equilibrium distance higher than the closed (*αααα*) form. Also the deformation of the porphyrin ring is more pronounced in Ni species than in Zn ones. This was already the case for the MPeriP and MMyrtP porphyrins presented before. Also, experimental data can be found in reference [25]. This correlation between the metal ion size and the deformation of the porphyrinic core is a well-known phenomenon, well documented since the seventies [26]. Indeed, the Ni-N distances in tetracoordinated porphyrins are shorter (range 1.93-1.96 Å) than Zn-N distances (*ca* 2.04 Å) [23]. The short distances in Ni porphyrins are supposed to be responsible for the ruffling of the porphyrinic core, whereas the Zn^{2+} ion being larger, fits better in the cavity and does not impose any strong deformation. We will describe later on the case of Mn porphyrins.

As can be seen in table 8, the most stable atropoisomers are well reproduced in gas phase and are in agreement with crystal structure data. In the case of ZnBCP-8 the closed conformation is the most stable, while in the case of NiBCP-8 the open conformation is the most stable. The following scheme summarizes these results:

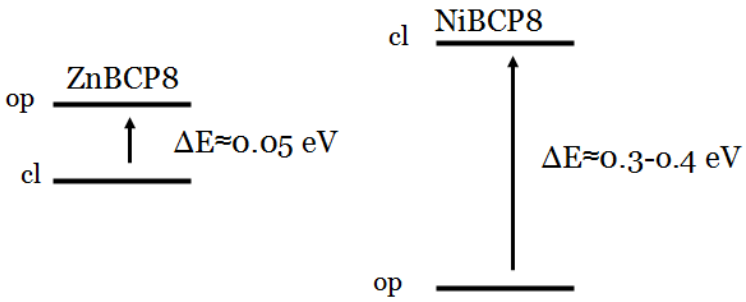

Scheme 1. Energy difference between open and closed conformations

One important point to notice is the difference in energy between open and closed conformations: in the case of zinc, it is quite small in gas phase, while for nickel the difference is larger.

We have then performed calculations in dichloromethane and nitrobenzene. We have optimized again all the structures in both solvents. In table 9 are shown the results obtained.

Table 9. Ground state energies for ZnBCP-8 and NiBCP-8 in dichloromethane and nitrobenzene, and averaged metal-N distances

Porphyrin	**E_{TBE} (eV) DCM**	**E_{TBE} (eV) Nitrobenzene**	**<M-N>distances (Å) Calc. / exp.**
ZnBCP-8 (αβαβ)	-919.610 eV	-919.623 eV	2.06/2.03
ZnBCP-8 (αααα)	-919.305 eV	-919.458 eV	2.02
NiBCP-8 (αβαβ)	-923.995 eV	-924.027 eV	1.97
NiBCP-8 (αααα)	-923.229 eV	-923.342 eV	1.93/1.92

In the following scheme are shown gaps in energies between open and closed conformations:

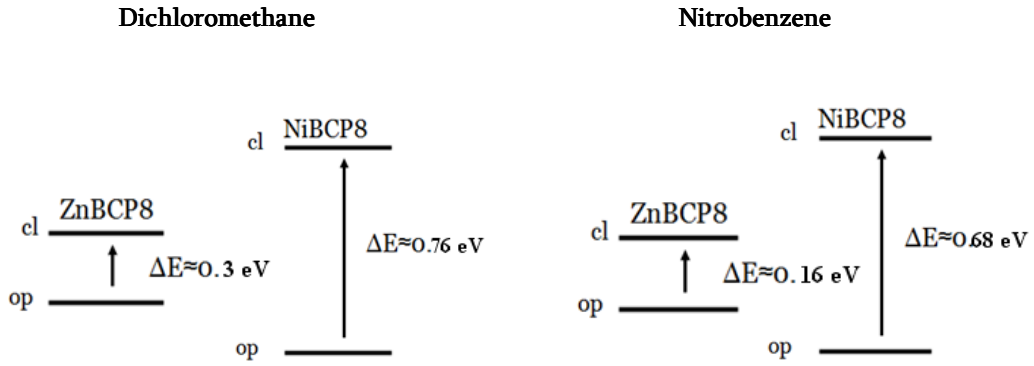

Scheme 2. Energy difference between open and closed conformations in dichloromethane and nitrobenzene solvents

For NiBCP-8 it is very clear that the open conformation (αβαβ) is the most stable (difference of ≈ 0.7 eV between open and closed forme). This reproduces very well the experimental NMR in solution, where either in dichloromethane or nitrobenzene, the αβαβ (open) atropoisomer is 100%.

In the case of ZnBCP-8 the main atropoisomer is changing. In comparison with the crystal data where the Zn closed conformation was the most stable one, in dichloromethane and nitrobenzene solutions we have a Zn open conformation (αβαβ) that is the most stable but in equilibrium with the closed conformation. This is reflected by the small energy gap between the two conformations (0.16 to 0.3 eV). Two reasons may explain why we do not reproduce completely the experimental results for this complex. One is that in solution in DCM, it is experimentally observed that porphyrins have tendency to form dimers, thus this should displaced the equilibrium between open and closed forms towards the closed form. The second is more methodological, as we have only calculated total bonding energies, that are approximations to enthalpies (neglecting the ZPE) and that do not take entropy terms into account. We have thus investigated these two reasons more into detail.

III.3.2.2. Formation of dimers

Figure III.18 illustrates the possible equilibrium existing between monomers and a dimeric form inspired from the arrangement observed in the crystal structure.

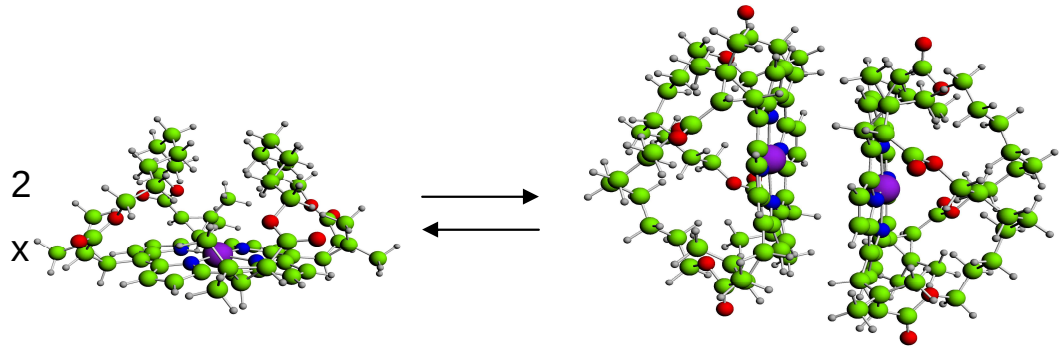

Figure III.18. Schematic equilibrium between monomeric and dimeric structures

The energy of formation of a ZnBCP-8 bimolecular complex could be obtained by the following procedure. We first optimized the structure of the dimer in gas phase. This gave a mean distance between the two porphyrinic planes of ca. 4.1 Å, very close to the value obtained in the X-ray structure of Zn-BCP8 (which presents such dimer association in the crystal). Then the energy for the interaction ΔE_{int} was calculated using the following equation:

$$\Delta E_{\text{int}} = \Delta E_{\text{dim}\,er} - 2\Delta E_{monomer} + 2\Delta E_{BSSE} \qquad (1.7)$$

ΔE_{BSSE} is the basis set superposition error (BSSE). This error is due to the fact that when calculating the dimer, the basis functions on each monomer gives an overstabilization of the energy of the other partner, by being involved in the description of its partner electronic structure. It is obvious that the BSSE is expected to be particularly significant when small, inadequate basis sets are used which do not provide an adequate representation of the electron distribution far from the nuclei, particular in the region where non – covalent interactions are the strongest. The usual way for estimating the BSSE [27] is expressed as follows:

$$\begin{aligned} &A + B \rightarrow AB \\ &\Delta E = E(AB) - \left[E(A + (B)\right] \end{aligned} \qquad (1.8)$$

The calculation of the energy of the individual species A is performed in the presence of "ghost atoms" on B, that is using atomic orbitals on B but without the nuclei or electrons of B. A similar calculation is performed for B using ghost atoms on A.

Following the approach described above, we have thus calculated the interaction energy first in gas phase. In table 10 are shown the energies obtained for the dimer, the two monomers and the BSSE energy.

Table 10. Calculated energies for dimer, the two monomers and BSSE

ZNBCP-8	**Energy (eV)**
dimer ZNBCP-8 (αααα)	ΔE = -1780.334 eV
monomer	ΔE = -890.122 eV
BSSE	ΔE = 0.034 eV

Please note that as mentioned above, our calculations were made with TZP basis sets, whereas a first trial with DZP (double-zeta) functions gave a very large BSSE (≈6 eV) as expected with too small basis sets. Inserting all the data in equation (1.7) gives a very weak stabilization of the dimer in gas phase: $\Delta E_{int} \approx$ -0.02eV. This is in agreement with the experimental data (crystal structure). Calculations in two solvents were then performed: dichloromethane (DCM) and nitrobenzene, chosen because the dimerization occurs in the former, not in the latter. The monomers and dimers were each optimized in the solvent, and table 11 shows the resulting energies.

Table 11. Calculated energies for the dimer, the monomer and BSSE in dichloromethane

ZnBCP-8 in dichloromethane	**Energy (eV)**
dimer ZnBCP-8 (αααα)	ΔE = -1781.991 eV
monomer	ΔE = -891.262 eV
BSSE	ΔE = 0.034 eV

It should be noted that the ghost atoms cannot be used in solvent PCM conditions, thus we used the BSSE energy from gas phase. Now, inserting all the data in equation (2), it can be observed that the dimer is strongly stabilized compared to the monomers: ΔE_{int} = -0.58 eV. The same calculations in nitrobenzene gave the results summarized in table 12, and in that case we obtained a positive ΔE_{int} = 1.01 eV, showing that no dimerization is expected from our calculation, as experimentally observed.

Table 12. Calculated energies for the dimerization process in nitrobenzene

ZnBCP-8 in nitrobenzene	**Energy (eV)**
dimer ZnBCP-8 (αααα)	ΔE = -1782.12 eV
monomer	ΔE = -891.6 eV
BSSE	ΔE = 0.034 eV

As one possible reason for the experimentally observed non dimerization was the interaction between one solvent molecule with the porphyrin plane, we also computed the interaction energy between the nitrobenzene molecule and ZnBCP-8. In figure III.19 is shown the resulting optimized structure (in nitrobenzene with PCM) of ZnBCP-8 interacting with the nitrobenzene molecule.

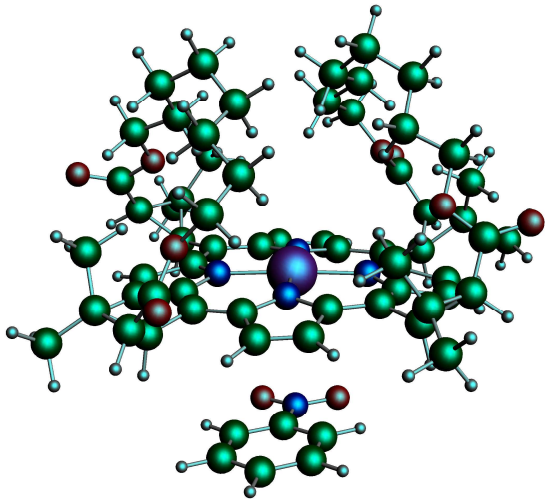

Figure III.19. ZnBCP-8 interacting with the nitrobenzene molecule

We thus obtained the resulting energies shown in table 13.

Table 13. Energies of optimized ZnBCP-8 interacting with the nitrobenzene molecule

ZnBCP-8 in nitrobenzene	**Energy (eV)**
ZnBCP-8 (αααα)+ Nitrobenzene molecule	ΔE = -982.619 eV
Nitrobenzene molecule	ΔE = -91.312 eV
ZNBCP-8 (αααα)	ΔE = -891.422 eV

The interaction energy is thus:

$$\Delta E_{\text{int}} = \Delta E_{ZnBCP8+nitro} - \Delta E_{ZnBCP8} - \Delta E_{nitro} + BSSE \qquad (1.9)$$

But it can be seen that $\Delta E_{ZnBCP8+nitro}$ is higher than $\Delta E_{ZnBCP8} + \Delta E_{nitro}$, so we can conclude directly without estimating the BSSE that the two individual partners, ZnBCP-8 and solvent molecule, are more stable than when they are interacting. Thus the nitrobenzene molecule doesn't seem to participate to stabilization of the closed form of Zn-BCP8. Of course, it should be reminded here that the energies are only approximations of enthalpic terms (as already mentioned before) as we did not perform a complete thermodynamic computation.

The dimerization occurring in DCM not in nitrobenzene could be due to some dipole effects. It should be noted first that the dielectric constant for DCM is 8.9 and for nitrobenzene is 34.8. The monomer, i. e. ZnBCP-8 has a dipole moment calculated in gas phase of 1.34 Debye, whereas it is null for the dimer. If we examine the energies of monomer and dimer in gas phase and solvents, as represented in table 14, we observe that the solvation effect stabilizes differently these two species.

Table 14. Energies obtained for ZnBCP-8 as monomer and dimer

	E (eV) / gas	E (eV) / DCM (ε = 8.9)	E (eV) / nitrobenzene (ε = 34.8)
Monomer ZnBCP-8	-890.12	-891.26	-891.6
Dimer	-1780.33	-1781.99	-1782.12

We observe that the stabilization due to solvation increases much more for the monomer (+ 30%) than for the dimer (+ 8%), which is quite in line with the differences in dipole moments of the monomer and the dimer.

This effect could be thus an explanation of the difference of behaviour observed for ZnBCP-8 by experimentalists depending of the solvent.

III.3.2.3. Estimation of thermodynamic parameters for the open/closed equilibriums in MBCP-8

As mentioned at the end of paragraph III.3.2.2 the discrepancy between our relative stabilisations of open and closed forms of ZnBCP-8 compared to experimental trends could come from our approximations in the estimations of stabilization energies. To be more accurate, we thus performed a more quantitative computation of ΔH and ΔS terms by analytical frequencies calculations. Because of the high computing demand, the studies were made in gas phase. We thus computed the thermodynamic parameters of the equilibrium:

$$\text{ZnBCP-8 } (\alpha\beta\alpha\beta) \rightleftharpoons \text{ZnBCP-8 } (\alpha\alpha\alpha\alpha) \quad (1.10)$$

In the following, the (αβαβ) form is noted “op” and the (αααα) is noted “cl”. Thus we have for the Gibbs energy (and also for the enthalpy and entropy parameters):

$$\Delta G = \Delta G_{cl} - \Delta G_{op} \quad (1.11)$$

The ΔH term is evaluated as ΔH = ΔE + ZPE where ΔE is the total bonding energy term given by the computation, and ZPE being the Zero point Energy. The latter corresponds to the difference between the minimum energy of the potential well and the "true" energy of the fundamental vibrational state. It is thus evaluated through a frequency calculation. The ΔS term is also extracted from the frequency calculation that estimates the partition function of the system.

In table 15 are shown the resulting values (calculated with usual conditions: TZP basis sets, small frozen cores and PBE functional). It should be stressed that all the frequencies were real, without any imaginary frequency in any of the species investigated here.

Table 15. Energies and thermodynamic parameters calculated in gas phase for the three MBCP-8 systems (M = Zn, Ni and H_2) at 298 K.

Porphyrins	**Energy (eV)**	**ZPE (eV)**	**Enthalpy (kJ/mol) ΔH**	**Entropy (J/mol/K) ΔS**	**Gibbs Energy (kJ/mol) ΔG**
ZNBCP-8 (αβαβ)	-857.94	32.169	-4.2	5.05	-5.7
ZNBCP-8 (αααα)	-857.90	32.194			
NiBCP-8 (αβαβ)	-895.53	32.237	-83.213	1521.5	
NiBCP-8 (αααα)					
H_2BCP-8 (αβαβ)	-895.24	32.745	-6.7	30.68	-15.86
H_2BCP-8 (αααα)	-895.33	32.767			

NiBCP-8 in closed form is still running. We can see that the ΔG for the open/closed equilibrium of ZnBCP-8 is slightly negative at room temperature, thus in favour of the closed conformation. But the value is rather low (-5.7 kJ/mol), so that we are at this temperature in a situation of equilibrium between the two forms as observed experimentally. For this complex, the equilibrium is mainly driven by the enthalpy term.
In the case of the free base, the Gibbs energy is close to that of the Zn system, and indeed experimentally, the free base has the same conformation features [23, 24]. But this comes from enthaly and entropy contributions which are both higher than for the Zn system. Especially the higher entropy term for $M=H_2$ may be due to a less rigid core as no metal atom is present.

To conclude on this theoretical study of bridled metal porphyrins, we have obtained by a careful use of various DFT approaches a very good agreement with experimental properties, either on structural data or on energy estimations (stabilizations energies, thermodynamic data, …). We have also been able to go further in the mechanisms that stabilize the species in solution. Based on this study we have thus investigated porphyrins that could be able to present a redox active center with Mn.

III.4. Mn (II) and Mn (III) porphyrins

In this study, the objective is to correlate if possible some structural properties with redox stabilization of Mn(II) and Mn(III) porphyrins. We have thus focused firstly on the theoretical investigation of the electron structure of d^5 manganese (II) and d^4 manganese (III) porphyrins. As a matter of fact, in these species, the manganese ion may be either high spin (HS) or intermediate spin (IS), i. e. for Mn(II): S = 5/2 or 3/2 and for Mn(III): S = 2 (HS) or S = 1 (IS).

III.3.4.1. Computation of spin states ordering in manganese (II) and (III) porphyrins

III.3.4.1.1. Literature data on simple Mn porphyrins

Experimental characterizations on Mn(II) and Mn(III) porphyrins have appeared between the 70's and to the 90's. With their Fe analogues, they have been particularly studied as models of heme active sites involved in many biological processes from photosynthesis to oxygen transport. Yet only few X-ray structures of Mn(II) porphyrins are available, among them MnTPP [28] and $[MnTPPCl]^-$ [29] (TPP = tetraphenylporphyrin). The main structural feature is that the Mn(II) tends to be out of the plane of the porphyrin due to the large size of this ion. The Mn-N distances are 2.08-2.09 Å for MnTPP and 2.16 Å for $[MnTPPCl]^-$ (here the Mn^{2+} ion is 0.64 Å above the mean plane of the four nitrogen atoms). It is also well documented that the Mn(II) ion is high spin in these systems [28].

For Mn(III), much more experimental data are available, with a wide range of structural characterizations with various axial ligands [26,30,31,32].The closest system to our own studies is the MnClTPP porphyrin which gives dMnN = 2.00 Å and a slight displacement of the MnIII from 0.16 Å out of the plane [cheng2]. As can be seen, the Mn(III)-N distance is much shorter that the Mn(II) one, consistent with the higher redox state. The Mn(III) porphyrins are also known to be high spin [26, 30, 31].

The recent computational studies published so far are mainly made with DFT methods [33-35]. They generally predict quite well structural features for Mn(II) and Mn(III) systems. The relative ordering of spin states for Mn(III) is correctly reproduced, i. e. HS is the ground state and IS is an excited state. In contrast, none is able to reproduce the HS nature of the ground state of Mn(II) porphyrins [33, 34].

The relatively long bonds in the high-spin Mn(II) porphyrins (*ca* 2.09 Å) are correlated with the HS state and with the singly occupied antibonding dx^2-y^2 orbital. In figure III.21 is shown the arrangement of the d orbitals in the two configurations of intermediate and

high spin states. This orbital is unoccupied in the high-spin Mn(III) and IS Mn(II) derivatives, which have relatively short Mn-N bond distances.

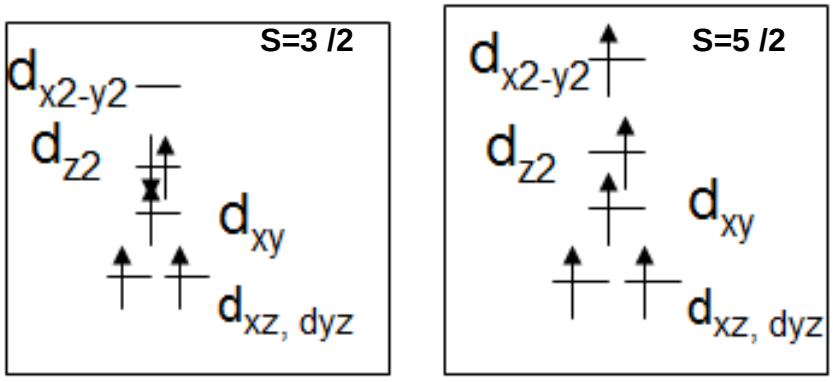

Scheme 3. Arrangement of d orbitals in intermediate and high spin configurations

Theoretically [33], for reproducing the high spin of Mn(II), were used hybrid B3LYP functionals or DFT+U calculations. GGA functionals namely PBE are not able to reproduce the high spin configuration of Mn^{2+} and shows a 3/2 configuration lower in energy.

III.3.4.1.2. Theoretical study on simple Mn porphyrins

We have started this study by performing geometry optimizations of the Mn (II) and Mn (III) high and intermediate spin, without any substituents in meso positions. We investigated thus MnP for Mn(II) and MnPCl for Mn(III) (see figure III.20).

All calculations were carried out using Amsterdam Density Functional (ADF) 2006 [3, 5, 6]. The basis sets were made of Slater-type orbital, double (DZP) and triple-zeta functions including one polarization function (TZP). Frozen cores were used for C, N and O (1s), and 3d metal (1s–2p) for Mn. A General Gradient Approximation (GGA) functional namely Becke-Perdew (BP) [7,8], hybrid functionals: B3LYP [7, 36], PBE0 [37], KMLYP [2] and BHandHLYP [2] were used for calculations of simple Mn porphyrins. In the case of bridled Mn porphyrins, PBE [14] and hybrid B3LYP functionals were used.

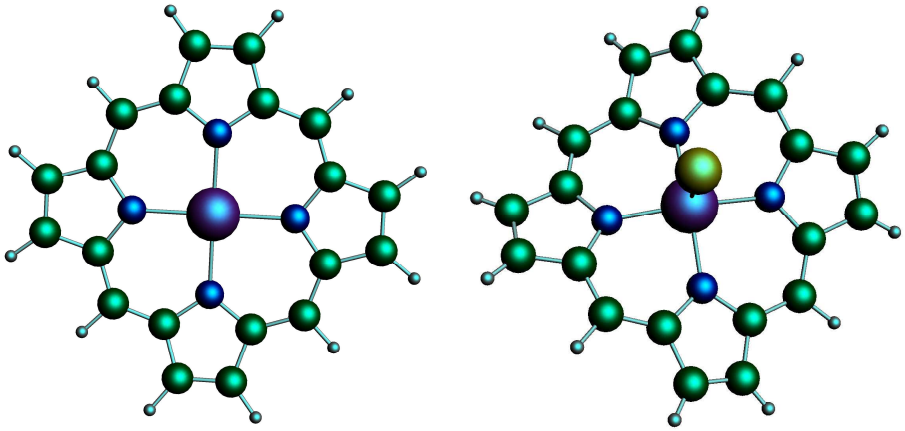

Figure III.22 Mn porphyrin: (a) Mn(II) and (b) Mn(III)Cl

Using GGA and BP exchange and correlation functionals, we have optimized the Mn^{2+} porphyrins for S=5/2 configuration and S=3/2 configuration and the Mn^{3+} porphyrin for S=2 and S=1 configurations. The total bonding energies for different spin states obtained with BP functional are gathered in table 16.

Table 16. Results of Mn^{2+} and Mn^{3+} porphyrins : energies (eV) and average Mn-ligand distances (Å) optimized.

Basis Set	**$Mn2^+$ porphyrin**		**$Mn3^+$ Cl porphyrin**	
	S= 3/2	**S=5/2**	**S= 1**	**S= 2**
DZP	-284.70	-284.32	-316.31	-316.65
TZP	-287.47	-286.79		

It can be seen that the BP exchange correlation functional fails to reproduce the high spin configuration for Mn^{2+}, either in DZP or TZP basis set. The 3/2 intermediate spin is lower in energy. We attribute this failure to the fact that the high-spin state is systematically favoured in Hartree–Fock-type theories, because Fermi correlation is included in the exact exchange, while Coulomb correlation is not. We thus expect that the admixture of

exact exchange to a given density functional will heavily influence the energy splitting between states of different multiplicity. This will be demonstrated in next paragraph, when we made calculations using various hybrid functionals with a high Hartree –Fock exchange contribution.

In the case of Mn^{3+}, this problem does not appear and the high spin is reproduced. The geometrical parameters obtained through geometry optimizations in the high spin state agree well with experiment. For instance we obtained dMn-N = 2.06 Å for MnP (exp. 2.08-2.09 Å) and dMn-N = 2.02 Å for MnClP (2.00 Å experimentally [32]. As the metal-N distances are an important parameter correlated to the spin state, it is necessary to be able to reproduce geometries in the correct spin state.

In this context, we will focus now on the study of Mn^{2+} porphyrin. It is now well established that most of the time, GGAs tend to overstabilize low-spin states, whereas hybrid functionals stabilize high spins [38]. We applied thus a series of hybrid functionals for intermediate and high spin of Mn^{2+} (collaboration with Valentina Vetere in the theoretical group of the laboratory). The obtained results are shown in table 17.

Table 17 Hybrid functionals results for MnP: spin states ordering (energies in eV).
All calculations are made with TZP basis sets.

Functionals	**ΔE ($Mn2^+$ porphyrin)**		**% HF exchange**	**ΔE (5/2 vs 3/2)**
	S = 3/2	**S = 5/2**		
B3LYP	-300.84 eV	-301.12 eV	20 %	0.28
PBE0	-324.88 eV	-325.47 eV	25 %	0.59
BHandHLYP	-371.62 eV	-372.52 eV	50 %	0.9
KMLYP	-400. 08 eV	-401.17 eV	55 %	1.09

For these hybrid functionals and using a TZP basis set, we have obtained a good reproduction of the 5/2 high spin configuration. If we compare the results of these hybrid

functionals, it seems that the larger is the Hartree-Fock exchange contribution, the larger is the gap. Especially in the case of Mn^{2+} porphyrins, it seems thus that a functional with high exact exchange contribution is necessary to reproduce the ordering.

In order to shed some light on this particular problem, we have collaborated with the group of Dr. V. Robert from ENS-Lyon for performing multiconfigurational calculations for MnP, especially through Complete Active Space (CAS) approaches (thesis Michael Képénékian). This method is often used in quantum chemistry for generating qualitatively correct reference states of molecules in cases where Hartree-Fock and DFT are not adequate.

The CASPT2 calculations have been performed starting from various X-ray structures from the literature, where the phenyl groups were replaced by hydrogen atoms. The potential energy surface of Mn porphyrin has been calculated by moving the Mn along the z axis while the geometry of porphyrin has been kept frozen.

A 15 electrons/ 14 orbitals active space has been used, containing all 3d orbitals of Mn, 8 π-type orbitals and a σ-type orbital of the porphyrin. In figure III.21 are shown examples of the π and σ orbital type in MnP.

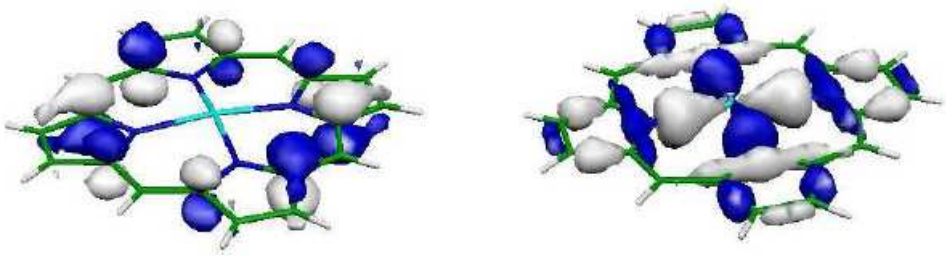

(a) π-type orbital (b) σ-type orbital

Figure III.21 Active orbitals for CAS

Using a large ANO basis set the following resulting potential energy at the CASPT level was obtained for the lowest lying states:

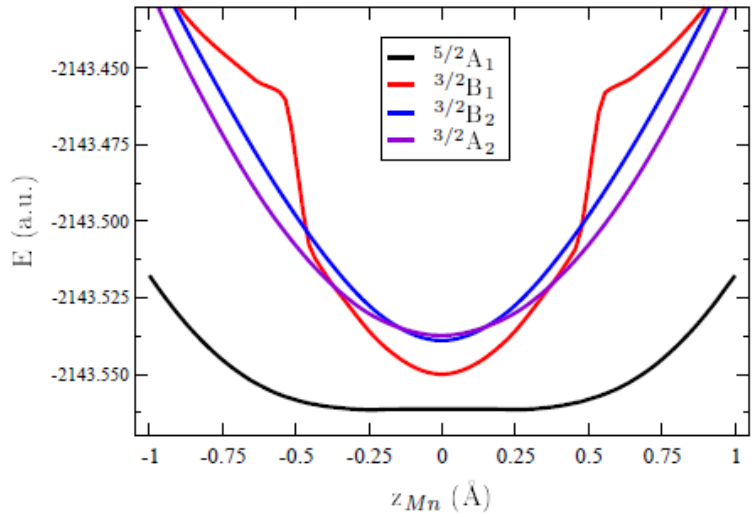

Figure III.22 CASPT2 Potential Energy Surface of MnP

As can be seen, the high spin configuration is lower in energy than the spin configuration, with an energy gap of 0.47 eV. Thus the CAS approach is now in good agreement with the spectroscopy of this system. Unfortunately, the computational costs for such methods preclude their use for large systems such as the bridled porphyrins. So we are currently checking the PES given by various hybrid functionals and by the OLYP or OPBE GGA functionals in order to reproduce the CASPT2 results.

III.3.4.2. Bridled Mn porphyrins

III.3.4.2.1. Literature data on bridled Mn porphyrins

Concerning the MnClBCP-8, no crystallographic structure is available, but the structure of MnClBCP-10 (with longer bridles) has been solved previously in our laboratory [23]. In figure III.23 are shown the X-Ray structures for open (αβαβ) and closed conformations (αααα) which remarkably coexist in the same crystal. The oxygen atoms are shown in red, nitrogen atoms in blue, chlorine atoms in green and carbon atoms in grey.

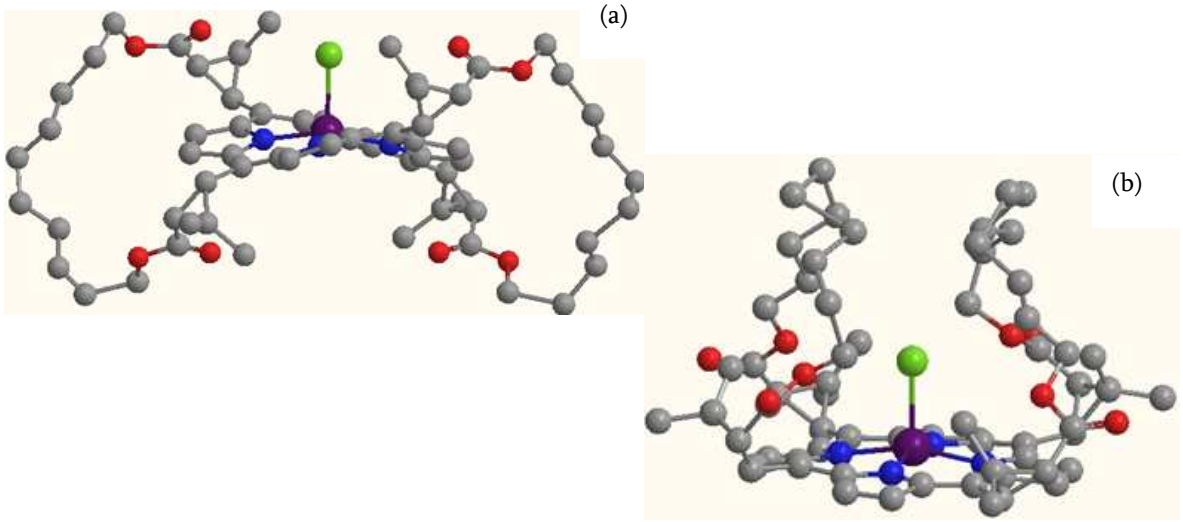

Figure 3.23. Crystallographic structure of MnClBCP-10: (a) open conformation (b) closed conformation

The main distances can be summarized in the next table.

Table 18. Crystallographic structural distances in open (αβαβ) and closed conformations (αααα) for MnClBCP-10

Form	dMn-N (Å)	dMn-Cl (Å)
(αβαβ)	1.98	2.37
(αααα)	2.03	2.37

This may enlights the fact that the two atropoisomers are almost at the same energy. Their behaviour in solution was more difficult to study than for Zn and Ni analogues, due to their paramagnetism that precludes NMR techniques. Thus experimentalists have used circular dichroïsm measures differences in the absorption of left-handed polarized light versus right-handed polarized light which arise due to structural asymmetry. It has been shown for these systems [23] that the MnClBCP-10 complex presents a mixture of the two signals and thus it is believed that the two atropoisomers, αααα and αβαβ are also present. A recent paper by Lawson-Daku et al. [39] on some Fe(III) and Mn(III) homologues of these porphyrins but without bridles reported that the Mn(III)-Cl porphyrin was more stable in the (αβαβ) form.

III.3.4.2.2. Computation of bridled manganese porphyrins

Despite the problem of the correct ordering of the spin state in Mn(II), we have undertaken some preliminary geometry optimizations of Mn(II) and Mn(III) porphyrins for high and intermediate spins. The initial structures came from the X-ray structures. We used the same methods as previously described in this chapter. In figure III.26 are shown the optimized geometries for the high spin state. Generally the intermediate spin geometries gave very similar structures with only a slight decrease of the Mn-ligand distances.

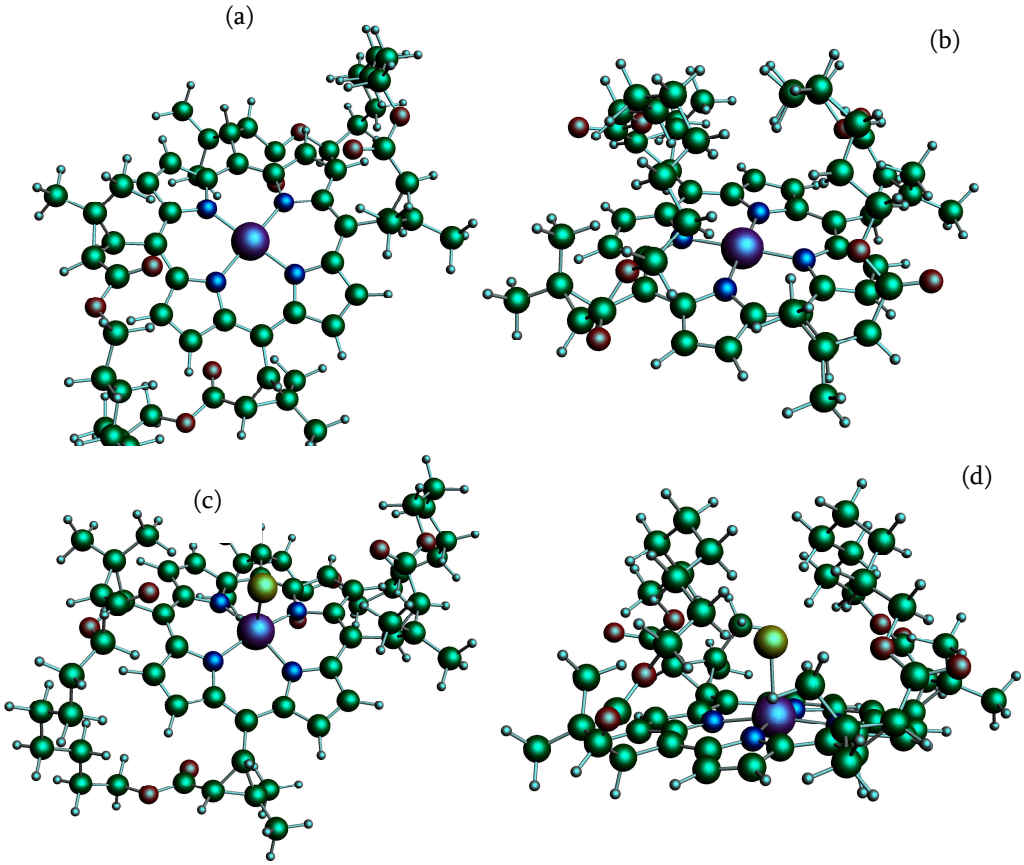

Figure III.24 Optimized structures of bridled Mn(II) and Mn(III) porphyrins: (a) Mn(II)open, (b) Mn(II)closed, (c) Mn(III) Cl open (d) Mn(III)Cl closed

The structural parameters (see table 19) are in very good agreement with experimental data (see table 18).

Table 19. Crystallographic structural distances (*Å*) in open (αβαβ) and closed conformations (αααα) for the high and low spin state of MnIIIClBCP-8 and MnIIBCP-8

Distance	**dMn-N Å**	**dMn-Cl Å**
Atropoisomer	**MnIIIClBCP-8 Spin 2**	
(αβαβ)	1.99	2.35
(αααα)	2.03	2.38
Atropoisomer	**MnIIIClBCP-8 Spin 1**	
(αβαβ)	1.98	2.3
(αααα)	2.0	2.31
Distance	dMn-N	
Atropoisomer	**MnIIBCP-8 Spin 3/2**	
(αβαβ)	1.97	1.97
(αααα)	2.0	2.0
Atropoisomer	**MnIIBCP-8 Spin 5/2**	
(αβαβ)	1.97	1.97
(αααα)	2.0	2.0

As already detailed before, for the Mn(II) system, the correct spin state is obtained with B3LYP (see table 20). In that case, it seems to indicate that the open (αβαβ) atropoisomer is more stable than the closed one. But this result comes from single points issued from geometry optimizations made at the GGA level (no geometry optimization possible in ADF with hybrids).

Table 20. Stabilization Energies (eV) of Mn(II) and Mn(III) bridled porphyrins (DZP basis sets).

Theoretical approaches	**Mn(II) porphyrin** (αβαβ)		**Mn(II) porphyrin** (αααα)	
Functional	**S=3/2**	**S=5/2**	**S= 3/2**	**S=5/2**
GGA PBE	-939.073 eV	-939.035 eV	-938.355	-938.375
Hybrid B3LYP	-1060.55 eV	-1060.15 eV	-1059.14	-1059.43
B3LYP	**Mn(III) porphyrin** (αβαβ)		**Mn(III) porphyrin** (αααα)	
Method	**S =1**	**S = 2**	**S = 1**	**S = 2**
GGA PBE	-954.57 eV	-954.74 eV	-955.23	-955.46

For the Mn(III) system, the closed conformation seems to be preferred. Nevertheless these very preliminary results should be confirmed by calculations in solvent.

Conclusions

These DFT investigations on several molecular systems, precursors or potential species for bistability redox properties, were performed firstly to check their reliability and secondly to understand better their behaviour. The relevant molecular properties that we studied are their structural behaviour depending on the metal ion, the environment (solvent) and the electronic state (redox, spin) and the redox potentials. Such properties are directly dependant on the ability to estimate energies (rotational energies, spin states, …). We have been able to show that we are able to reproduce such important features.

The Mn species deserve still a lot of work, in order to investigate their structures more into details with a hybrid functional. As a matter of fact, for Zn and Ni species, we are

able to reproduce some correlation between the M-N distances and the most stable atropoisomer could be found [23, 24] in line with some work made previously by Scheidt [26]: the Zn^{2+} ion being larger gives a more planar porphyrinic core favouring the *(αααα)* isomer whereas the Ni^{2+} being smaller gives the *(αβαβ)* preferentially with a more distorted core. Unfortunately, the extension of this correlation to $Mn^{2+/3+}$ species has not yet been clearly established neither experimentally nor theoretically.

Nevertheless we have now a very solid basis for further investigations on such bistable systems.

Bibliography

[1] Y. Fu, L. Liu, H-Z. Yu, Y-M. Wang, Q-X. Guo, *J. Am. Chem. Soc*. 2005, *127*, 7227

[2] L. E. Roy, E. Jakubikova, M. G. Guthrie, E. R. Batista, *J. Phys. Chem. A* 2009, *113,* 6745

[3] E. J. Baerends, ADF 2006.01. SCM, Theoretical Chemistry, Vrije Universiteit: Amsterdam, The Netherlands, http://www.scm.com.

[4] S. Miertus, E. Scrocco, J. Tomasi, *Chem. Phys.* 1981, *55*, 117

[5] C. F. Guerra, J. G. Snijders, G. t. Velde, E. J. Baerends, *Theor. Chem. Acc.* 1998, *99*, 391

[6] G.t. Velde, F. M. Bickelhaupt, S. J. A Gisbergen, C. F. Guerra, E. J. Baerends, J. G. Snijders, T. J. Ziegler, *Comput. Chem*. 2001, *22*, 931

[7] A. Becke, Phys. Rev. A 1988, *38*, 3098

[8] J. P. Perdew, Phys. Rev. B 1986, *33*, 8822

[9] M. Cossi, M. F. Iozzi, A. G. Marrani, T. Lavecchia, P. Galloni, R. Zanoni, F. Decker, *Phys. Chem. Lett. B* 2006*, 110*, 22961

[10] PhD thesis of Tiziana Pro, CEA/LETI, 2009

[11] M-C. Kuo, L-A. Li, W-N. Yen, S-S. Lo, C-W. Lee,C-Y. Yeh, *Dalton Trans.* 2007, 1433

[12] A. Wahab, M. Bhattacharya, S. Ghosh, A. G. Samuelson, P. K. Das, *J. Phys. Chem. B* 2008**,** *112,* 2842

[13] http://en.wikipedia.org/wiki/Saturated_calomel_electrode

[14] J. Perdew, K. Burke, M. Ernzerhof, *Phys. Rev. Lett.* 1996**,** 77, 3865

[15] M. S. Liao, S. J. Scheiner, *J. Chem. Phys.*, 2002, *117*, 205

[16] A. Fateeva, A. Calborean, J. Pécaut, P. Maldivi, J.C. Marchon, L. Dubois, *Tetrahedron* 2008, *48,* 10874

[17] M. Veyrat, O. Maury, F. Faverjon, D. E. Over, R. Ramasseul, J. C. Marchon, I. Turowska-Tyrk, W. R. Scheidt, *Angew. Chem*. 1994, *33*, 220

[18] T. Ziegler, A. Rauk, *Theor. Chim. Acta* 1977, *46*, 1

[19] Chem3D Ultra 10.0, CambridgeSoft, www.cambridgesoft.com.

[20] T. Vangberg, A. Ghosh, *J. Am. Chem. Soc*. 1999, *121*, 12154

[21] R. W. Scheidt, M. E. Kastner, K. Hatano, *Inorg. Chem.* 1978, *17*, 706

[22] W. Jentzen, X. Z Song, J. A. Shelnutt, *J. Phys. Chem. B* 1997, *101,* 1684

[23] Anna Castaings, Thesis from University J. Fourier, Grenoble, France, 2006

[24] G. Maheut, A. Castaings, J. Pécaut, L. M. Lawson-Daku, G. Pecsitelli, L. Di Bari, J-C. Marchon, *J. Am. Chem. Soc*. 2006, *128*, 6347

[25] W. Jentzen, E. Unger, X. Z. Song, S. L. Jia, I. Turowska Tyrk, R. SchweitzerStenner, W. Dreybrodt, W. R. Scheidt, J. A. Shelnutt, *J. Phys. Chem. A*. 1997, *101*, 5789

[26] W. R. Scheidt, *Acc. Chem. Res*. 1977, *10*, 339

[27] N. R. Kestner, J. E. Combariza, *Rev. Comput. Chem*.1999, *13*, 99

[28] J. F. Kirner, C. A. Reed and W. R. Scheidt, *J. Am. Chem. Soc*. 1977, *99* , 1093

|29] R. B. Vanatta, C. E. Strouse, L. K. Hanson and J. S. Valentine, *J. Am. Chem. Soc*. 1987, *109*, 1425

[30] P. Turner and M. J. Gunter, *Inorg. Chem*. 1994, *33*, 1406

[31] B. S. Cheng, P. H. Fries, J. C. Marchon and W. R. Scheidt, *Inorg. Chem*. 1996, *35*, 1024

[32] B. S. Cheng and W. R. Scheidt, *Acta Cryst. C*. 1996, *52*, 361

[33] K. Leung, S. B. Rempe, P. A. Schultz, E. M. Sproviero, V. S. Batista, M. E. Chandross C. J. Medforth, *J. Am. Chem. Soc.* 2006, *128*, 3659

[34] M. S. Liao, J. D. Watts and M. J. Huang, Inorg. Chem. 2005, *44*, 1941

[35] R. J. Cheng, S. H. Chang and K. C. Hung, Inorg. Chem. 2007, *46,* 1948

[36] N. R. Kestner , J. E. Combariza, *Rev. Comput. Chem*. 1999, *13*, 99

[37] V. Vetere, C. Adamo, P. Maldivi, Chem. Phys. Lett. 2000, *325*, 99

[38] M. Swart, J. Chem. Theor. Comput. 2008, *4,* 2057

[39] L. M. Lawson-Daku, A. Castaings, J. C. Marchon, *Inorg. Chem*. 2009, *48*, 5164

Chapter IV
Modeling of hybrid molecule-Si systems

Introduction

The generic structure of a hybrid system used in this work consists on redox-active components (i. e. the molecule itself), the linkage components and the surface, semiconducting in our case.

Thus monolayers of redox-active molecules, such as ferrocenes (Fc) and porphyrins ($ZnAB_3$), are formed on the semiconductor Si surface and the stable charged states of the molecules are utilized to store information. Our purpose has been to understand the main parameters (molecule, linker) which govern the charge transfer between semiconducting Si surface and redox molecules and the electrical behavior of such systems. This theoretical investigation was conducted in parallel with experimental studies on the chemical and physical properties of devices incorporating such Si surface covalently modified with molecules. (coll. LETI: B. De Salvo, J. Buckley, Tiziana Pro). In order to describe and understand the electron transfers and to correlate them to experimental data, one key property of the electronic structure needs to be studied: the alignment and relative positions of the frontier orbitals of the molecule with respect to the gap of the Si substrate [1-3]. We thus need to describe properly the molecular factors that affect this alignment, and correlate them with experimental data.

The main difficulty in such systems is their hybrid nature, being built up from molecules that are essentially local species interacting with an infinite system. The method that we will choose to describe the gap on such systems will thus be a crucial feature. This difficulty has been already pointed out in literature studies [1, 4]. In this context, we used two theoretical approaches. One was based on a molecular description,

using Si small aggregates in place of a Si surface, yielding a molecular orbital description of some relevant features: Homo-Lumo gaps, charge localization or structural properties. The other approach was focused on periodical calculations, with molecules grafted on 'infinite' Si surface. The resulting DOS were compared to molecular results, and discussed in the light of experimental data on electrical properties.

We will start this study with a brief description of semiconductor Si surfaces (small aggregate and slab reconstructed surface), having in view that the self-assembled monolayers of redox molecules are modelled first on a small aggregate of Si and after on 'infinite' surface.

IV.1. Si surface

In this paragraph, we will first remind about some general concepts on semiconductors electronic structure, on the problem of surface reconstruction, on the recent theoretical methods developed to describe such systems, and then we will present our own results.

IV.1.1. Some general concepts [5-8]

In bulk materials, the highest energy band that contains electrons is called the valence band, whereas the lowest energy empty band is called the conduction band. The band gap is the difference in energy between the valence and conduction bands (resp. noted VB and CB) and this region is forbidden for electrons. Figure IV.1 shows these bands and the energy gap for a typical solid material. The valence electrons and the band structure determine the physical and chemical properties of a material.

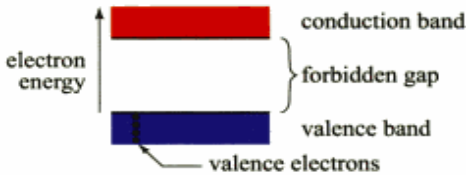

Figure IV.1. Schematic representation of electron energy bands in a typical solid materials

Once we know the band structure, we still need to find out which energy levels are occupied and whether specific bands are empty, partially filled or completely filled.

The energy level indicated by E_f in figure IV.2 is called the Fermi level. An electron with this energy has an equal probability of location in the valence band and the conduction band. The Fermi level E_f in a p-type semiconductor is situated near the valence band E_v, while it is close to the conduction band E_c in an n-type semiconductor.

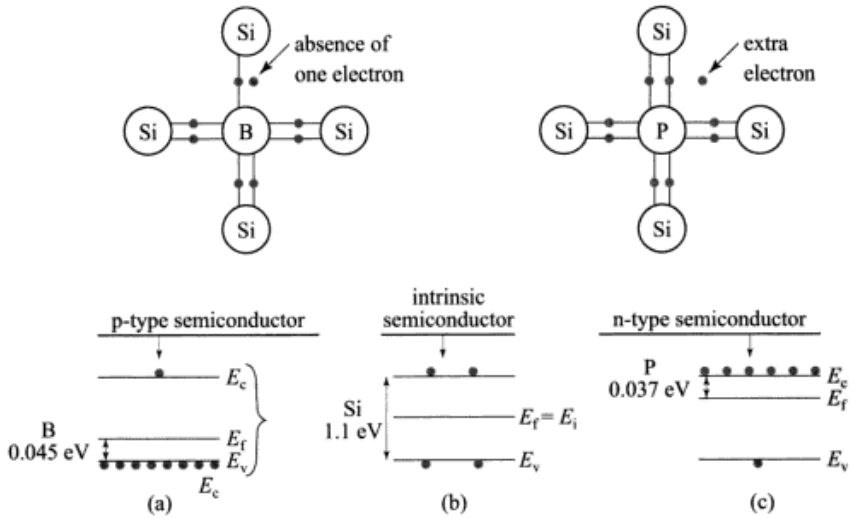

Figure IV.2. Energy band diagrams for p-type, intrinsic, and n-type semiconductor materials

For an intrinsic semiconductor like silicon, the Fermi level is essentially halfway between the VB and CB. Although no conduction occurs at 0 K, at higher temperatures a finite number of electrons can reach the CB and provide some current.

One of the early issues in silicon research was to understanding the spatial and energetic distribution of electrons within a semiconductor. This entails solving the so-called energy band problem, which is, determining the energy of an electron as a function of its wave vector k. The wave vector is a quantum number for tagging the quantum states of an electron in a crystal. In the figure IV.3 are the energy bands for silicon in the diamond crystal structure.

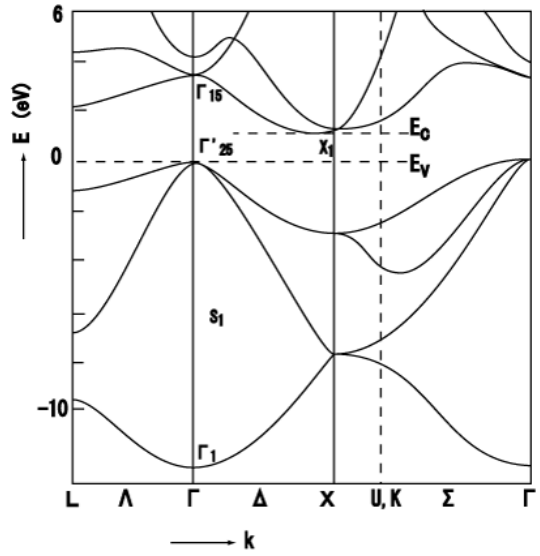

Figure IV.3. More complex representation of band structure in silicon showing wavevector dependence.

The energy is plotted as a function of the wavenumber, k, along the main crystallographic directions in the crystal, since the band diagram depends on the direction in the crystal. The energy band diagrams contain multiple completely-filled and completely-empty bands. In addition, there are multiple partially-filled bands. Empty bands do not contain electrons. In this diagram, the topmost energy of the valence band is labelled E_v and the bottom energy in the conduction band is labelled E_c. The top of the VB is not directly below the bottom of the CB (E_v is for an electron travelling in direction Γ, E_c in direction X), so silicon is called an indirect gap material. For an electron to be excited from the VB to the CB, it needs an energy $E_c - E_v$ and a change in direction/momentum.

Partially filled bands do contain electrons as well as available energy levels at slightly higher energies. These unoccupied energy levels enable carriers to gain energy when moving in an applied electric field. Electrons in a partially filled band therefore do contribute to the electrical conductivity of the material.

Crystal surfaces represent a special type of plane defect. Much of the understanding of solids is based on the fact that these are perfectly periodic in three dimensions; for example the electronic and vibrational behaviour can be described in great detail using methods that rely on this periodicity. The introduction of a surface breaks this periodicity

in one direction and can lead to structural and also subsequent electronic changes. When the crystal lattice is abruptly terminated by a surface, the atoms cannot fulfil their bonding requirements, as illustrated for a silicon surface in figure IV.4.

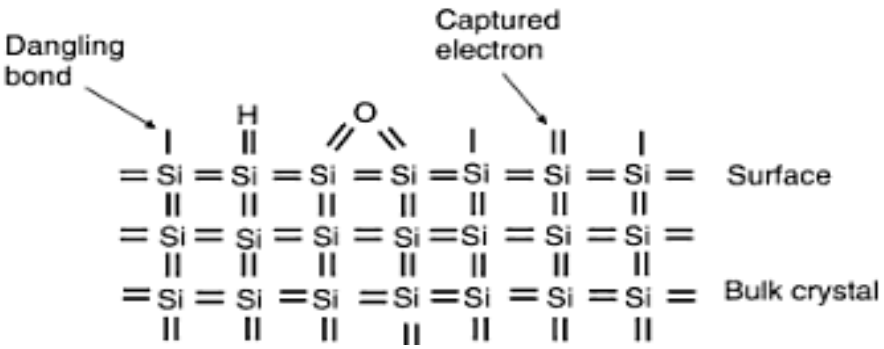

Figure IV.4. Schematic representations of possible defects occurring at the surface of silicon

Each silicon atom in the bulk of the crystal has four covalent bonds, each bond with two electrons. The Si atoms at the surface are left with dangling bonds, that is, bonds that are half full, having only one electron. These dangling bonds look for atoms to which they can bond.

Atoms from the environment can therefore bond with Si atoms on the surface. For example, a hydrogen atom can be captured by a dangling bond and hence become absorbed, or chemisorbed. A foreign atom or molecule is adsorbed if it chemically bonds with the atoms on the surface. If an adsorbed molecule or atom has significant electron modifications relative to its state in the gas phase to form a chemical bond with the surface (covalent or ionic), it is said to be chemisorbed. On the other hand, if it is held on the surface only by van der Waals forces, relying on the polarizability of the molecule, it is said to be physisorbed. Clearly, physisorption produces weak bonds while chemisorption often produces strong bonds.

Several surfaces for Si may be considered (1 0 0), or (1 1 1) or (1 1 0), etc… as found in Si technology (nanowires, MOSFET, …). In our case, all experimental devices were fabricated using Si (1 0 0) so we have focused here on this surface type orientation.

Since the impressive growth of studies made on semiconducting nanostructures (nanowires, quantum dots) yielding new physical effects due to confinement properties [Sorokin], many efforts have been devoted to the development of theoretical methods able to model the main structural and electronic properties. Whereas ab initio (DFT) is reserved for small clusters [9, 10], many semiempirical methods have developed, such as Extended Hückel[11], and more especially tight-binding (TB) methods [12-15]. One of the essential parameter that these methods aim at reproducing is the gap between valence and conduction bands, that is, for bulk Si, *ca* 1.2 eV [16].

IV.I.2. Modeling of Si with molecular approach

We have studied several small aggregates of (Si 1 0 0) with different sizes (figure IV.5): 34 atoms of Si, then 51 and finally 64 atoms. All the studied surfaces were saturated with hydrogens using a (2 X 1) reconstruction which is usual for this surface [17]. We have generated these small aggregates starting from a Si (1 0 0) slab surface that was studied before in the simulation laboratory (LSCDP) of CEA/LETI by P.Blaise.

All calculations were carried out in the framework of Kohn-Sham formalism, using ADF software package [18-20]. The basis sets were made of Slater-type orbital double-zeta functions including one polarization function for H, and double zeta functions for Si atoms. A [Ne] frozen core were used for Si. GGA using Becke 88 [21] and Perdew 86 [22] exchange and correlation functionals were used for all calculations. A small aggregate representative of a Si (1 0 0) configuration, made of 34 atoms of Si saturated with hydrogens was constructed as in the reference [4].

The computed gap is very large in comparison with the experimental bulk Si gap, due to confinement effects [12]. Nevertheless as expected it decreases from 3.6 eV to 3.0 eV when the size increases from 34 to 51 and 64 atoms. In figure IV.5 are shown the optimized structures with their corresponding gaps.

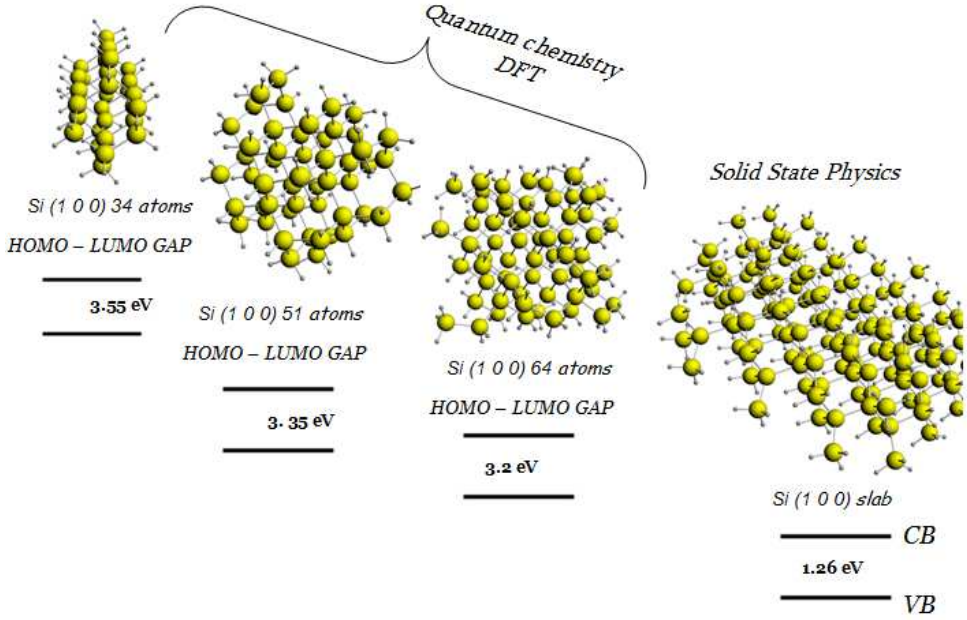

Figure IV.5. Optimized structures with their confinement effects

It is observed that the gap is decreasing while increasing the cluster size, but this is due essentially to the LUMO level. The HOMO energy does not change very much with the size of the cluster whereas the LUMO is down shifted. In figure IV.6 are shown the homo and lumo as a function of size.

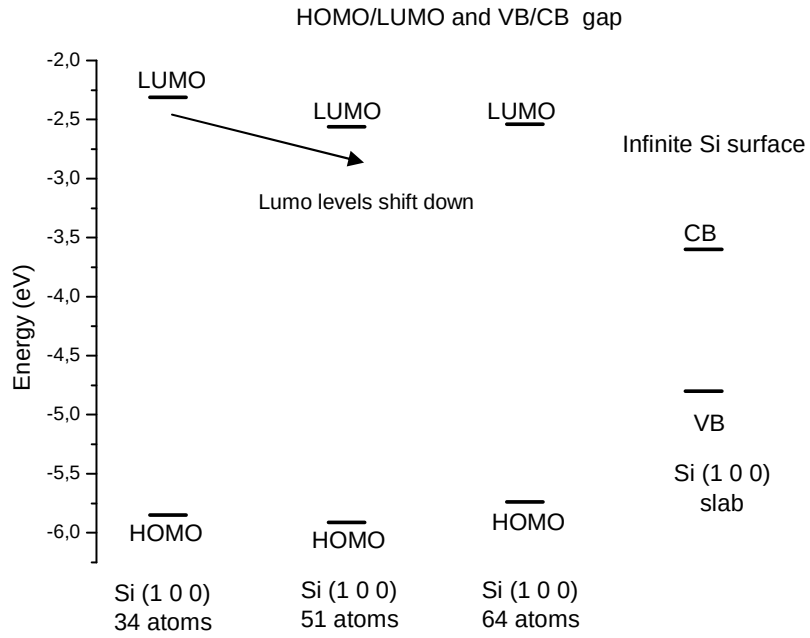

Figure IV.6. HOMO/LUMO gaps and VB/CB gaps shifting

As expected, the Si band gap cannot be reproduced by a HOMO-LUMO gap issued from quantum chemistry approach (≈ 1.14 eV). Moreover, it is known that band gaps are generally too large when computed by LDA or GGA functionals. However, by using a small cluster we hope to be able to be representative in term of atomic structures and accuracy of molecular levels.

IV.1.3. Periodical calculations of Si (1 0 0)

For reproducing the experimental Si gap, a band structure calculation is required using periodical calculations of Si (1 0 0) surface. One of the most widely used techniques for first principles theoretical modeling of semiconductor surfaces is the super cell implementation of plane waves and/or atomic orbitals based pseudopotential methods, within the density functional scheme. It is the case here, with the use of the SIESTA software package [23]. For investigating the extended electronic states in Si slab surfaces, core electrons were frozen with their nuclei and the interaction between valence electrons and ion cores is represented by norm conserving pseudopotentials of the Troullier-Martins form [24]. The interaction between valence electrons is treated within generalised gradient approximation (GGA) based on the density-functional theory approach. Exchange correlation functional of Perdew-Burke-Ernzerhof (PBE) [25] combined with a double zeta + polarization (DZP) basis sets were used.

We have started to reconstruct a slab of Si (1 0 0) oriented surface that was saturated with hydrogens above and below the surface. In figure IV.7 is shown the initial structure made of 5 Si monoatomic slabs in the c direction and periodically repeated in the a and b direction.

When a surface of tetrahedrally bonded semiconductor is created, at least one bond containing two spin-paired electrons is ‘cut’. Such a ‘cut’ or ‘dangling’ bond contains less than two spin paired electrons. The lake of electron pairing make dangling bonds unstable, and surface atoms seek new coordinates to minimize the free energy of the system.

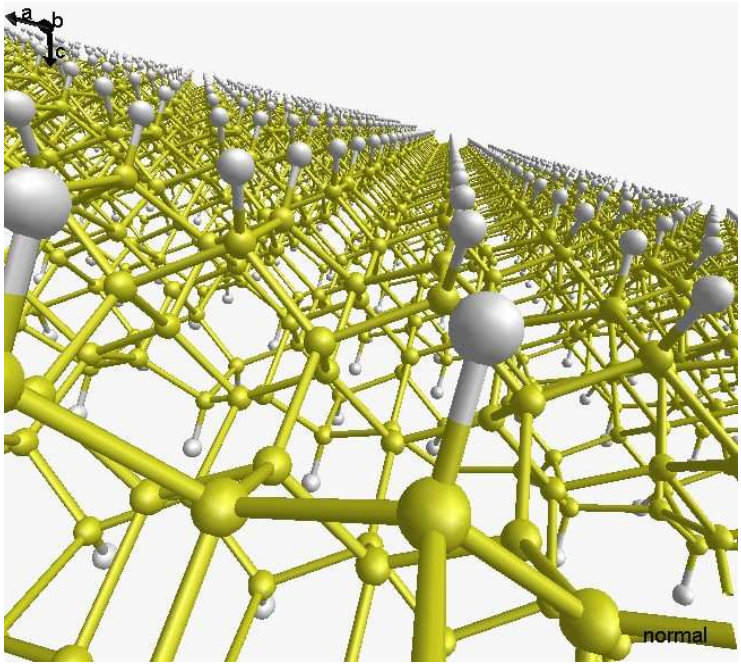

Figure IV.7. Slab Si(1 0 0) before reconstruction

Adaptation of new atomic coordinates leads the surface to relax and reconstruct. In figure IV.8 is shown the reconstructed surface of Si (1 0 0) after performing the relaxation of all the atomic coordinates using a conjugate gradient minimization technique. We can see that we have obtained the well known Si (1 0 0) – (2x1) reconstruction type [26].

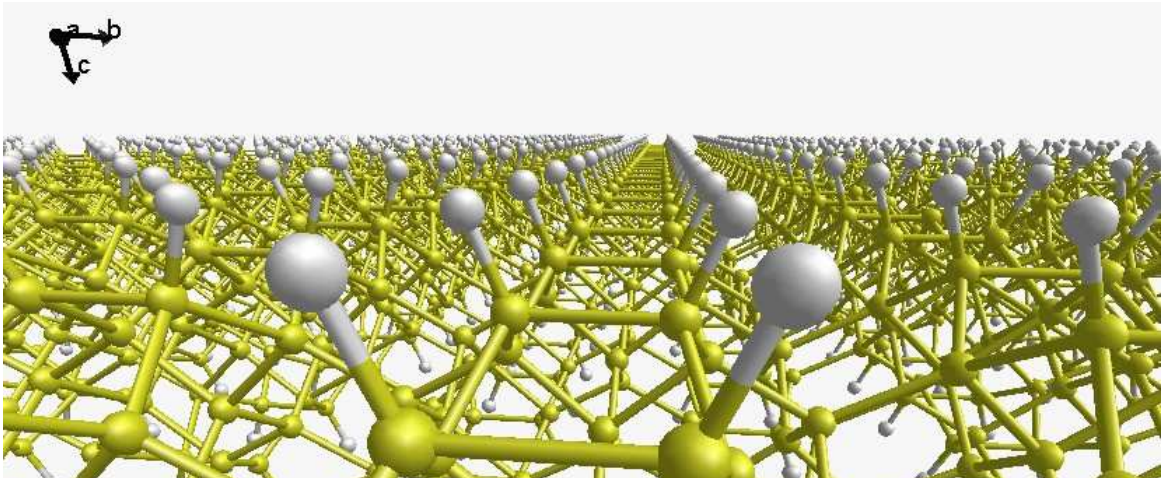

Figure IV.8. Slab Si (1 0 0) after reconstruction

After reconstruction of the surface, the calculated gap between the valence and conductance band reproduces very well the experimental gap (≈ 1.26 eV instead of ≈1.2 eV (exp. at room temperature). This agreement with the experiment is clearly fortuitous and is due to two compensative effects:

1. The gap is usually underestimated and close to 0.5 eV for bulk Si when one uses DFT in the LDA or GGA form.
2. The gap is here overestimated by some tenths of eV because of the reduced thickness of the slab in the c direction, normal to the surface.

Unfortunately, because of periodicity, these calculations are made in gas phase, and a solvent will be very difficult to manage in these conditions. SIESTA is not able to do this kind of calculations. In table 1 are summarized the computational tools that were used for this study with their limits.

Table 1. Surface interpretation and limits with ADF and SIESTA

Theoretical Approach	GAP	Chemical Bonding / Surface reactivity	Solvent	Functionals
Solid State Physics / SIESTA	~ exp. value	Representative of a (100) reconstructed surface	Unable to treat solvent effects	LDA, GGA
Quantum Chemistry / ADF	Overestimated due to 3D confinement	Accurate description of bonding	Able to treat a solvent	LDA, GGA, Hybrid

The limits of computational approaches can be seen, whatever the theoretical approach, ADF for small aggregates, or SIESTA for periodical calculations. The goal will be to extract the significative informations from each of the chosen tools and to compare the results. Even if the gap of small aggregate is much larger than the experimental bulk Si, the

properties of the surface concerning the chemical reactivity and bonding for a Si (100) surface orientation could be the same.

In the following discussions we will use for grafting of redox molecules the small aggregate of 34 atoms and the reconstructed infinite surface. We will turn now to the redox active molecular systems grafted on Si, which were of two types: ferrocene and Zn TPP, with various lengths of tether group for the attachment to the Si surface. We will summarize first the main significant experimental results on each system, then we will develop our modelling of the systems.

IV.2. Ferrocene grafted on Si

As mentioned in Chapter 1, the first reference hybrid system that was investigated was Ferrocene (Fc) grafted on Silicon surface, because it did not necessitate too much synthetic efforts. Two types of linker were used: either a vinyl group (called direct grafting) or a long aliphatic chain teminated by a triazole, with two chain lengths: C_6 and C11 (called indirect grafting). They were studied with a cluster of 34 Si atoms, in gas phase and in acetonitrile solvent.

We will start this description by summarizing the main experimental features obtained on the self-assembled monolayers of ferrocene attached on Si surface.

IV.2.1.Main experimental properties of ferrocene grafted on Si

Cyclic Voltammetry (CyV) measurements were performed in CEA/LETI/D2NT laboratory, by Tiziana Pro [27], in the group of B. de Salvo. This technique was used in order to check the electrochemical response of molecules/silicon systems. Redox energies and the properties related to different spacers were extracted and shown here.

As a technical detail, a solution of tetrabutylammonium hexafluorophosphate in propylene carbonate (Bu_4NPF_6/PC, 1.0 M) was used as supporting electrolyte, with

Platinum as counter electrode and Saturate Calomel Electrode (SCE) as reference electrode. The functionalized Si surface played the role of the working electrode.

The CyV characteristics of ferrocene directly grafted (Fc-Si) and ferrocene grafted with linker Fc-$N_3(CH_2)_{11}$ on Si surface, are shown in figure IV.9 (a, b). For Fc-Si the scan rate was varied from 0.1 V/s to 1 V/s (figure IV.9 a). As can be seen, the oxidation wave (corresponding to the transfer of electrons from the molecules to the Si) and the reduction wave (corresponding to the electrons tunnelling back to the molecules from the Si) of Fc molecules without linker, clearly appear.

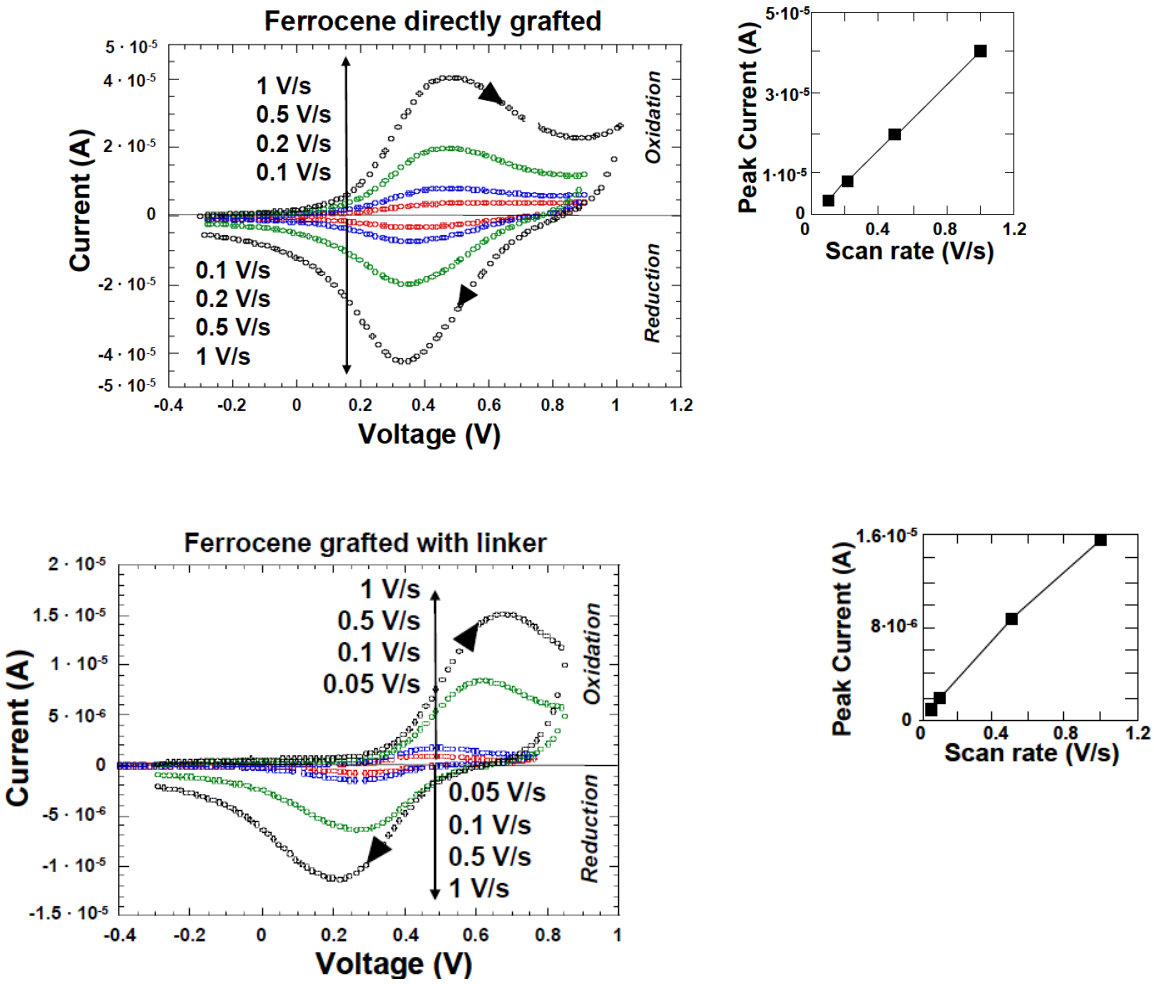

Figure IV.9. (a) left - CyV trace of Fc directly grafted at different scan rate, right - peak current versus scan rate; (b) left- CyV trace of Fc grafted with C11 linker at different scan rate, right - peak current versus scan rate

The monolayer exhibits a reduction peak at 0.34 V (V_{red}) and an oxidation one at 0.47 V (V_{ox}), with a 0.5V/sec scan rate. In the case of ferrocene grafted with linker, the scan rate was varied from 0.05 V/s to 1 V/s; the monolayer exhibits a reduction peak at 0.27 V and an oxidation one at 0.61 V, with a 0.05V/s scan rate. Nevertheless, the average value $(V_{red}+V_{ox})/2$ remain constant regardless of the scan rate. Hence the value found for Fc directly grafted is 0.4 V and for Fc grafted with linker is 0.44 V, given here against the saturated calomel electrode [27]. Converted to NHE by adding 0.248 V to the precedent values, we obtained 0.648 V/ NHE for Fc-Si and 0.688 V/NHE for the Fc-C11 linker.

Another important feature is the shift between oxidation and reduction voltages. For Fc-Si system, the redox process is almost reversible whatever the scan rate ($\Delta V = V_{ox} - V_{red}$ = 0.13 V at 0.5 V/s), whereas for Fc-$N_3(CH_2)_{11}$, a shift is visible (($\Delta V = V_{ox} - V_{red}$ = 0.34 V at 0.05V/s). A similar shift is observed for the C6 linker.

In figure IV.9 right, the oxidation peak current is plotted versus the scan rate. The linear dependence confirms that the oxido-reduction process is related to the species grafted on the electrode. The area under the current peaks, normalized by the product of voltage scan rate and the electron charge, provides a measure of the coverage of the molecules on Si surface. The value obtained for Fc directly grafted is equal to $6.4x10^{13}$ molecules/cm^2, and for Fc grafted with linker is $7.6x10^{13}$ molecules/cm^2.

Conductance-voltage (C-V) and capacitance-voltage (G-V) measurements were performed for Fc directly grafted and Fc grafted with C_6 and C_{11} linker at different frequencies. The resulting plots exhibit peaks, both in capacitance and conductance, associated with redox property of the molecules. [27, 28]. The results are summarized in figure IV.10. Note that when the Si surface is covered with long aliphatic chains without redox center, no peak has been observed.

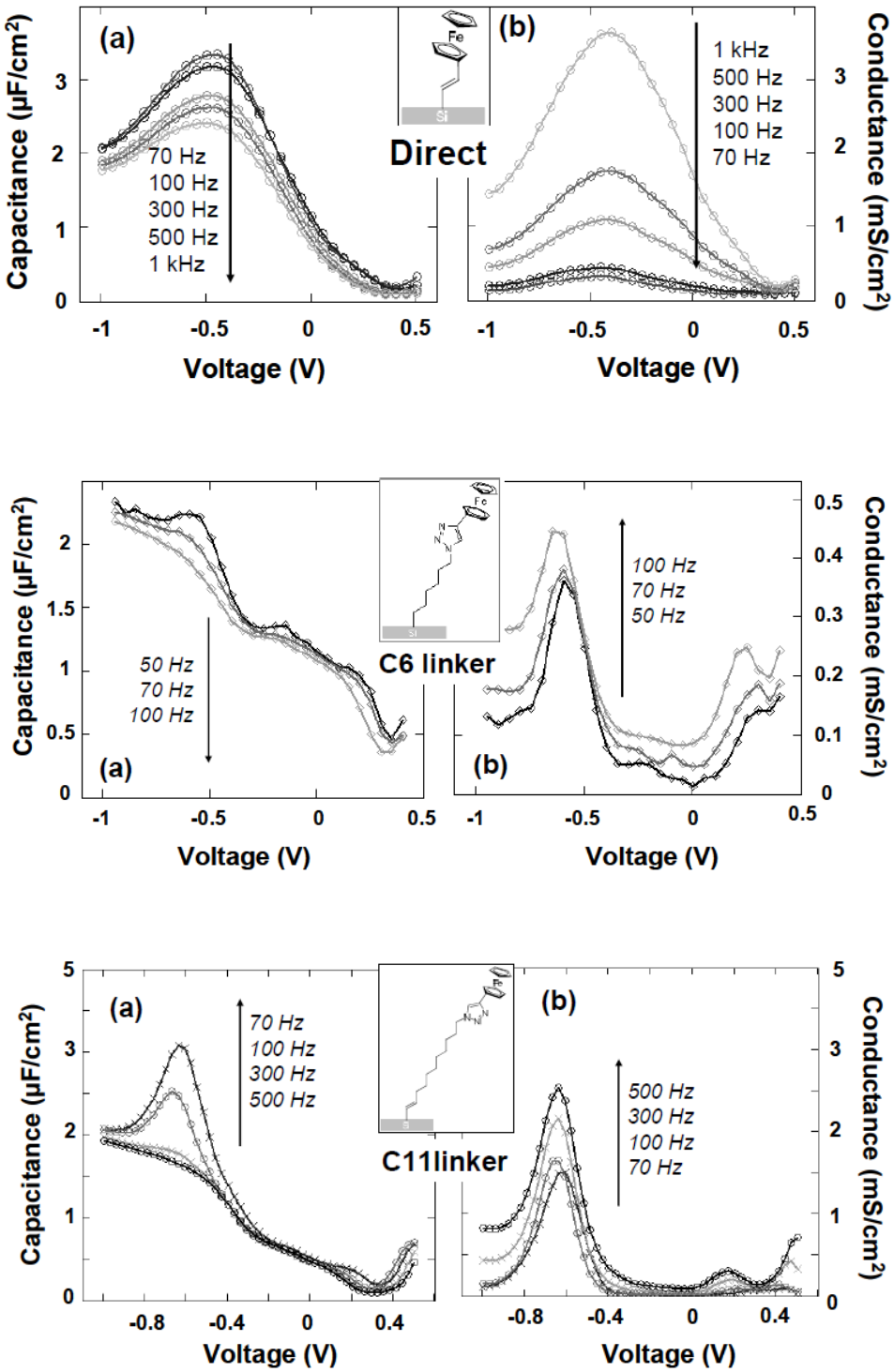

Figure IV.10. Impedance results for Fc directly grafted (top), Fc grafted with C_6 linker (second), Fc grafted with C_{11}linker (down), for different frequencies: a) C-V, b) G-V

The obtained voltage peak for Fc directly grafted is -0.45 V, whereas for C_6 linker it is -0.6 V and C_{11} linker -0.67 V.

The experimental data shows that a long aliphatic linker increases the shift between oxidation and reduction potentials of Fc grafted on Si, as well as the voltage peak in capacitance, with respect to the vinyl linker. This indicates that the electron transport to/from the molecules is slower than in the case of direct grafting, suggesting that the linker acts as a tunnel barrier. This result is in agreement with others studies that calculated the electronic structures of alkyl chains on Si [29, 30].

Also, the redox peaks exhibit frequency dependence, so the Fc/Si electron transfer. In figure IV.10 it can be observed that the intensity decreases in C-V for increasing frequency, while it increases in G-V, for increasing frequency. This behaviour can be explained by the fact that, at low frequencies the charge movement can occur at a rate comparable to the measurement signal and is reflected by the presence of the peak, while at high frequencies the electron transfer process becomes gradually rate limited until a threshold frequency is achieved at which no peak occurs. The impedance measurements are in good agreement with CyV data, which shows a slower electron transfer for increasing linker length.

IV.2.2. Theoretical molecular study of ferrocene grafted on Si

The ADF molecular approach was used for the characterization of the small models of hybrid ferrocene/ silicon systems.

The case of direct grafting (vinyl-Fc) and indirect grafting ($N_3(CH_2)_6$, and ($N_3(CH_2)_{11}$, were studied with a cluster of 34 Si atoms, first being optimized in gas phase, and after in acetonitrile medium. An interpretation of the electron transfer between the molecules and the Si is shown below for both types of grafting (direct and indirect). Correlations with the experimental data were made and presented here.

IV.2.2.1 Direct grafting

The geometry and electronic structure of species resulting from the grafting of Fc on Si (1 0 0) small clusters were explored by quantum modelling in the framework of DFT. The Amsterdam Density Functional (ADF 2006) program was used, with a generalized gradient approximation (GGA) functional namely Becke 86–Perdew 88, combined with double-zeta Slater basis sets. We have optimized first the reduced and the oxidized species in gas phase, then acetonitrile solvent was used, taken into account through a polarizable continuum model using default parameters of the program. Electronic structures were calculated in both cases, for oxidized (positively charged) and reduced Fc (neutral). In the oxidized form, which is a radical cation with a doublet spin state, the unrestricted formalism was used.

The theoretical redox potential against the normal hydrogen electrode (NHE) was obtained as already described in chapter 3, by computing the bonding energies for grafted ferrocene and the one-electron oxidized (ferrocenium) species.

Hence the calculated redox potential for Fc directly grafted was 0.43 V, with the solvent PCM. In the cyclic voltammetry measurements was obtained a redox potential of ≈ 0.4 V (see precedent paragraph), vs the saturated calomel electrode [27], where +0.248 V must be added for changing to the NHE value. As can be observed, the agreement is still within the usual error (*ca* 0.2 V, see chapter 3) with the experimental redox potential of ferrocene direct grafted. It should be noted that we considered in our model a small aggregate of Si in comparison with a bulk Si in experimental.

In figure IV.11 are shown the main molecular results for the ferrocene molecule direct grafted on Si surface (results in solvent).

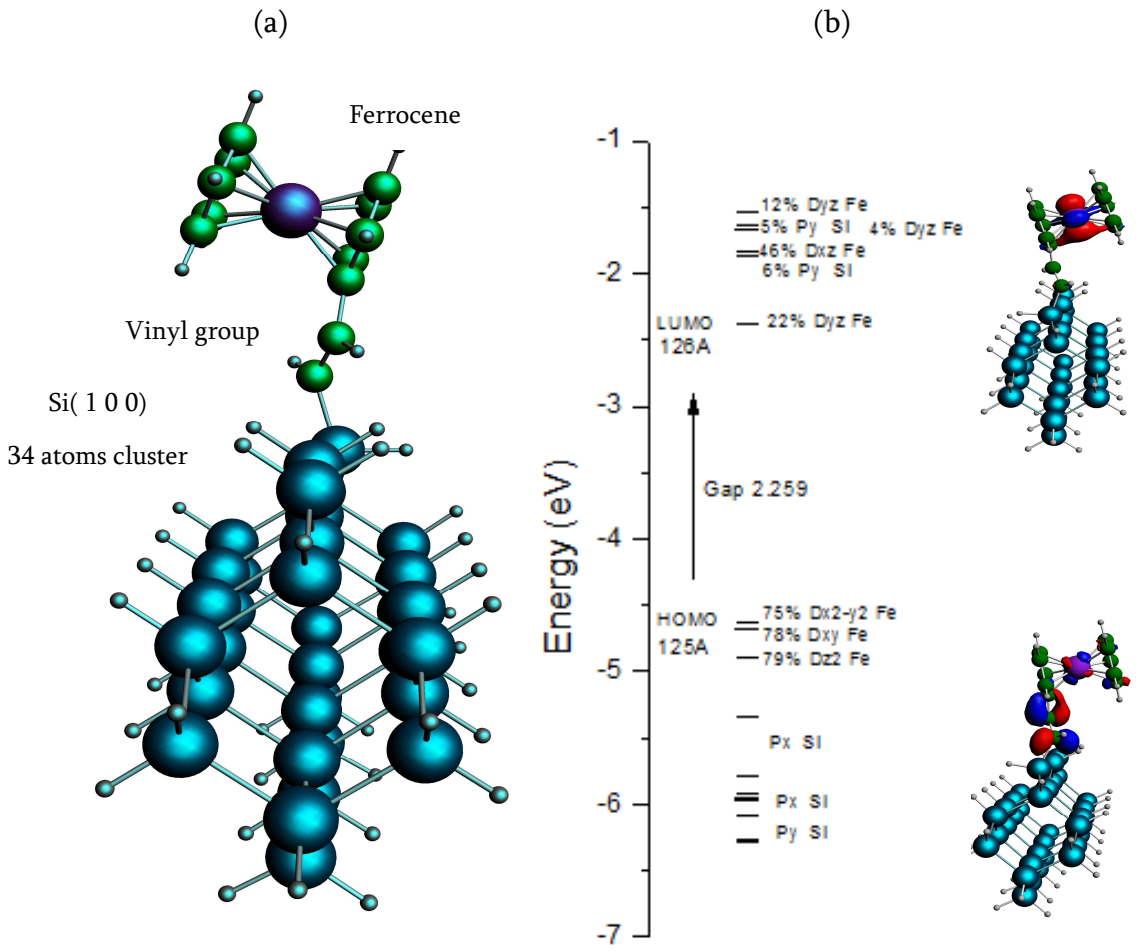

Figure IV.11. (a) Optimized geometry of ferrocene directly grafted on Si 34 small aggregate; (b Schematic molecular orbital diagram.

The geometrical parameters of the ferrocene group were not modified by the grafting. Figure IV.11 b shows the molecular orbital diagram of the species around HOMO-LUMO levels. As can be seen, the HOMO (highest occupied molecular orbital) is located on orbitals centered on the ferrocene + vinyl groups, and more precisely the ferrocene contribution is on the Fe ion. It is important to note that the MOs of the organometallic grafted part and Si cluster do not interact at all. The resulting diagram is the superposition of the two sets of MOs.

For ferrocenium, the diagram keeps the same main features: the SOMO is localized on Fe, and the sets of MOs of the two parts are superposed, without interacting. A Mulliken

charge analysis shows that the positive charge is localized on the Fe (≈0.69). All the carbons and the hydrogens of the molecule or linker give negative values.
Thus the whole results are consistent with the fact that after oxidation, the species holds a positive charge on the molecule. This is in line with the capacitance measurements, where a peak was observed in the presence of ferrocene, meaning that a charge had appeared on ferrocene.

On a more general scheme, the analysis of the molecule on Si cluster allows us to observe the very local distortions of Si levels due to the interaction with a molecule. We are also able to understand better how the levels in the molecule are modified (or not) by the interaction with Si, which is different depending on the type of grafting (direct, indirect). Thus, we need to analyze the levels calculated in the hybrid system on the basis of the two sets, from the molecule and the linker on one side, and from the Si cluster on the other side (figure IV.12).

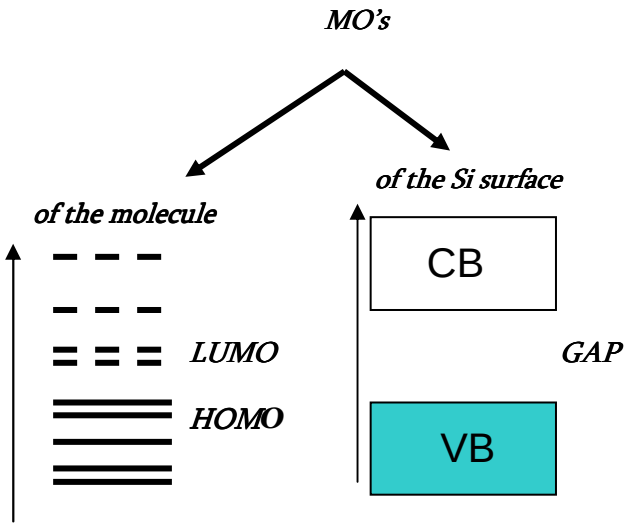

Figure IV.12. Molecular orbital diagram in a hybrid system

In a molecular calculation, the valence and conduction bands (resp. VB and CB on figure IV.8) are in fact a series of closely lying MOs centered on Si. From such a scheme, it is thus possible to analyze the electron transfer between the molecule and the Si and vice versa (figure IV.13).

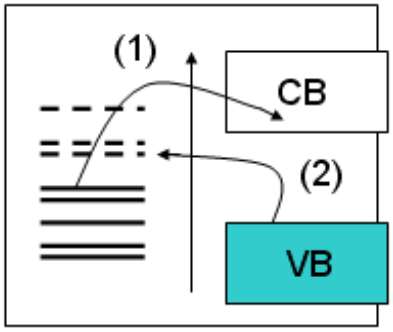

Figure IV.13 Electron transfer from molecule to surface(1) and from surface to molecule(2)

If we consider that the surface is p doped as in the experimental device, the scheme is a bit different. For oxidation, electrons pass from the HOMO level of the ferrocene to the VB of the Si, whereas in reduction, electrons pass from the VB to the LUMO level of ferrocene. The graph shows how the molecule gap is located/ Si gap, then what is the energy gap in order to transfer an electron in a hole (from Si to molecule or vice versa).

The bias applied to the Si substrate in CyV allows to shift the Si levels with respect to the molecular ones, and the transfer process occurs when both Si and molecule levels are aligned.

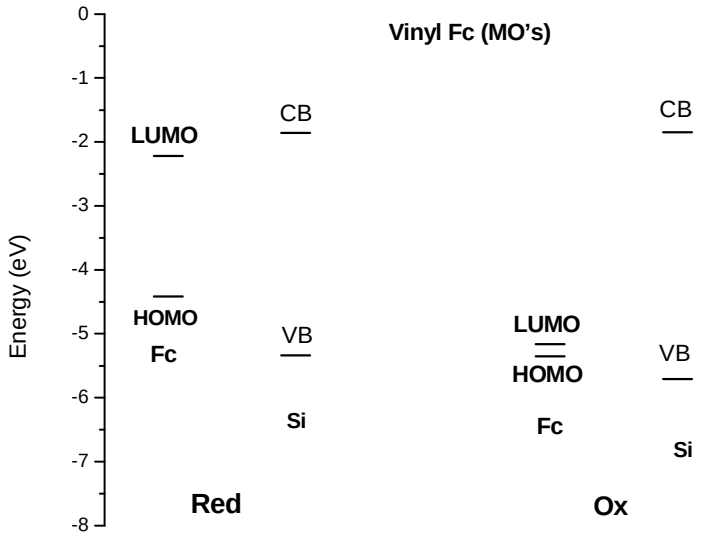

Figure IV.14. Molecule gap / Si gap in ferrocene direct grafted

Figure IV.14 shows that the gaps HOMO-VB of Fc and LUMO-VB of Fc+ are very close in energy, and this leads to similar oxidation and reduction potential values ($V_{ox} \approx V_{red}$). This means that the transfer energies of an electron from the surface to the molecule (≈2.66 eV) or from the molecule to the surface (≈ 2.26 eV) are very close. This is in agreement with cyclic voltammetry measurements especially at low scan rate where the electron transfer should not be limited by the rate of voltage scan.

IV.2.2.2. Indirect grafting

Indirect grafting implies the attachment of the organic molecules with the linkers C_6 and C_{11}. In these cases, we have used the same small aggregate of Si as for direct grafting. The influence of the two linkers was studied and the theoretical results were interpreted in the light of experimental cyclic voltammetry measurements, as before. The computational details are the same as for the direct grafting study.

IV.2.2.2.1. The case of Fc-$N_3(CH_2)_6$ indirect grafting

The redox potential was calculated in the same manner as for ferrocene directly grafted and all results are given from the solvent PCM computations. We obtained a calculated value of 0.64 V/NHE, whereas the experimental value was 0.42 + 0.248 ≈ 0.67 V/NHE [27]. Calculation in that case leads to a very satisfying agreement with the experimental value.

In figure IV.15 (a) is shown the ferrocene molecule grafted on Si surface using the C_6 long linker. Figure IV.15 (b) shows the MO diagram and the HOMO – LUMO occupation in the neutral form. As for direct grafting, the HOMO is localized on ferrocene thus the oxidation leads to a charge held by the ferrocene (and more precisely on Fe). Again, the MOs of the organometallic part and Si cluster do not interact at all. The resulting diagram is the superposition of the two sets of MOs. By comparison with the direct grafting, the HOMO/LUMO gap is increasing for the indirect C6 grafting in the case of neutral species.

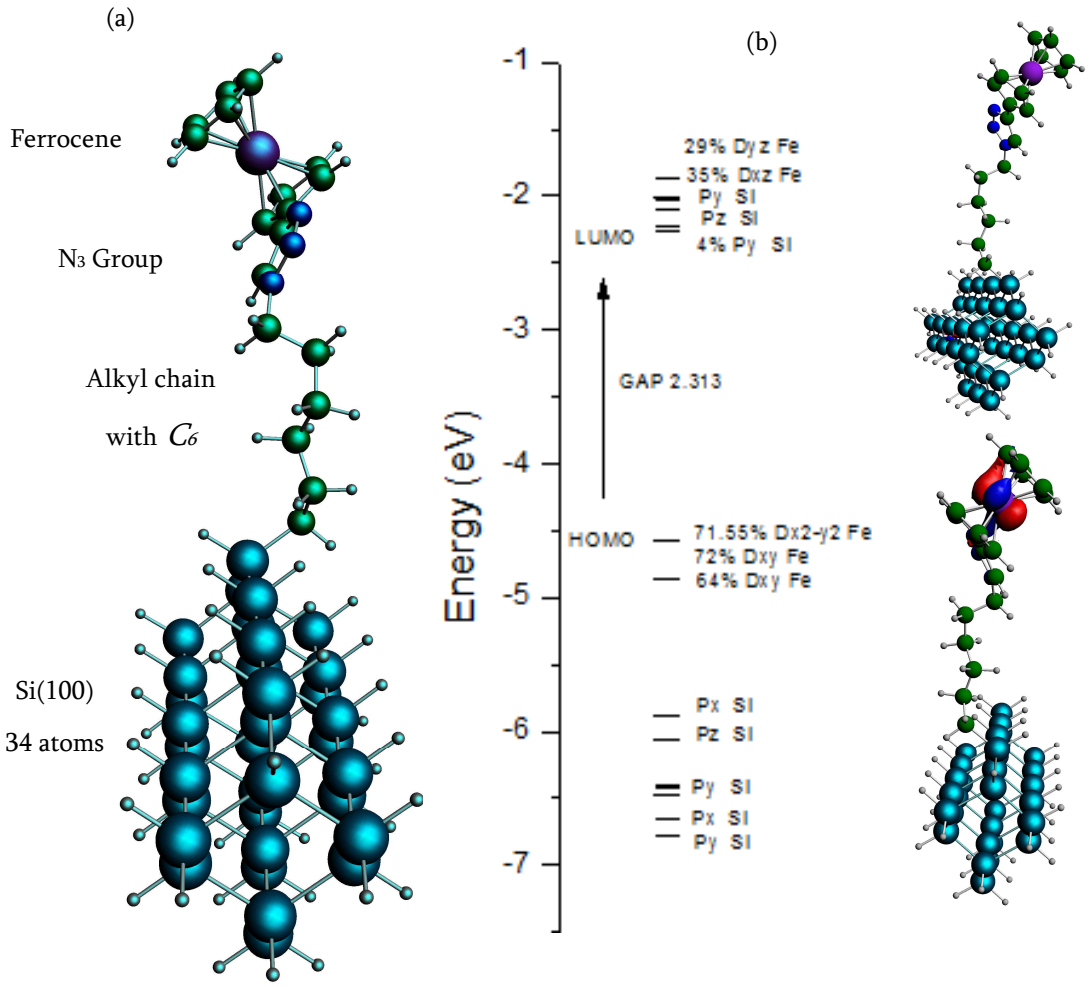

Figure IV.15. (a) geometry structure of Fc-$N_3(CH_2)_6$ indirect grafting; (b) schematic diagram of molecular orbital levels

The transfer of Fc-$N_3(CH_2)_6$ reduced and oxidized species is summarized in figure IV.16.

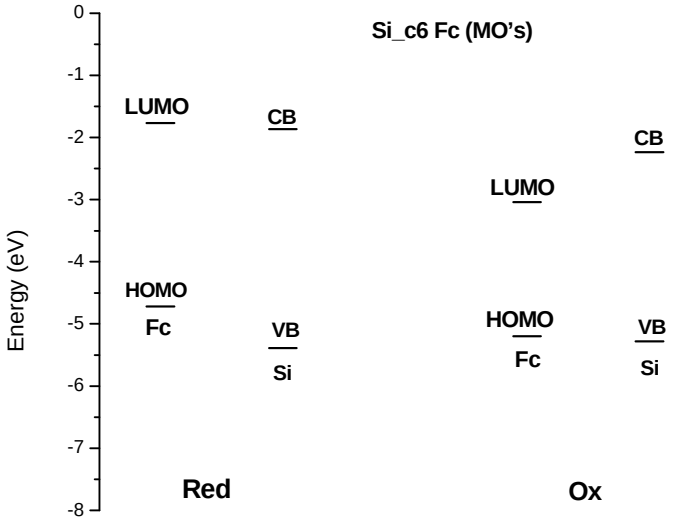

Figure IV.16. Molecule gap / Si gap in Fc-$N_3(CH_2)_6$ indirect grafted

As can be observed in the above diagram, for Fc-$N_3(CH_2)_6$ indirect grafting, the electron transfer is not reversible at the same potential (|Vox|>|Vred|). This could be correlated with cyclic voltammetry measurements where the peaks of oxidation and reduction are shifted. The energy difference for the oxidation transfer is thus ≈ E(HOMO Fc) – E(VB) and for reduction ≈ E(VB) – E(LUMO). For the indirect C6 grafting the computed gaps are: 0.7eV for oxidation potential and 2.2 eV for reduction potential. This could be correlated with cyclic voltammetry measurements where the peaks of oxidation and reduction are shifted.

IV.2.2.2.2. The case of Fc-$N_3(CH_2)_{11}$ indirect grafting

In the case of C11 indirect grafting, we have obtained for the calculated redox potential a value of 0.58 V/NHE, while the experimental one was 0.44 + 0.248 ≈ 0.69 V/NHE. Again the agreement is quite good.

In figure IV.17 (a) is shown the ferrocene molecule grafted on Si surface using a C_{11} long linker with a schematic molecular diagram of the reduced species, figure IV.17 (b).

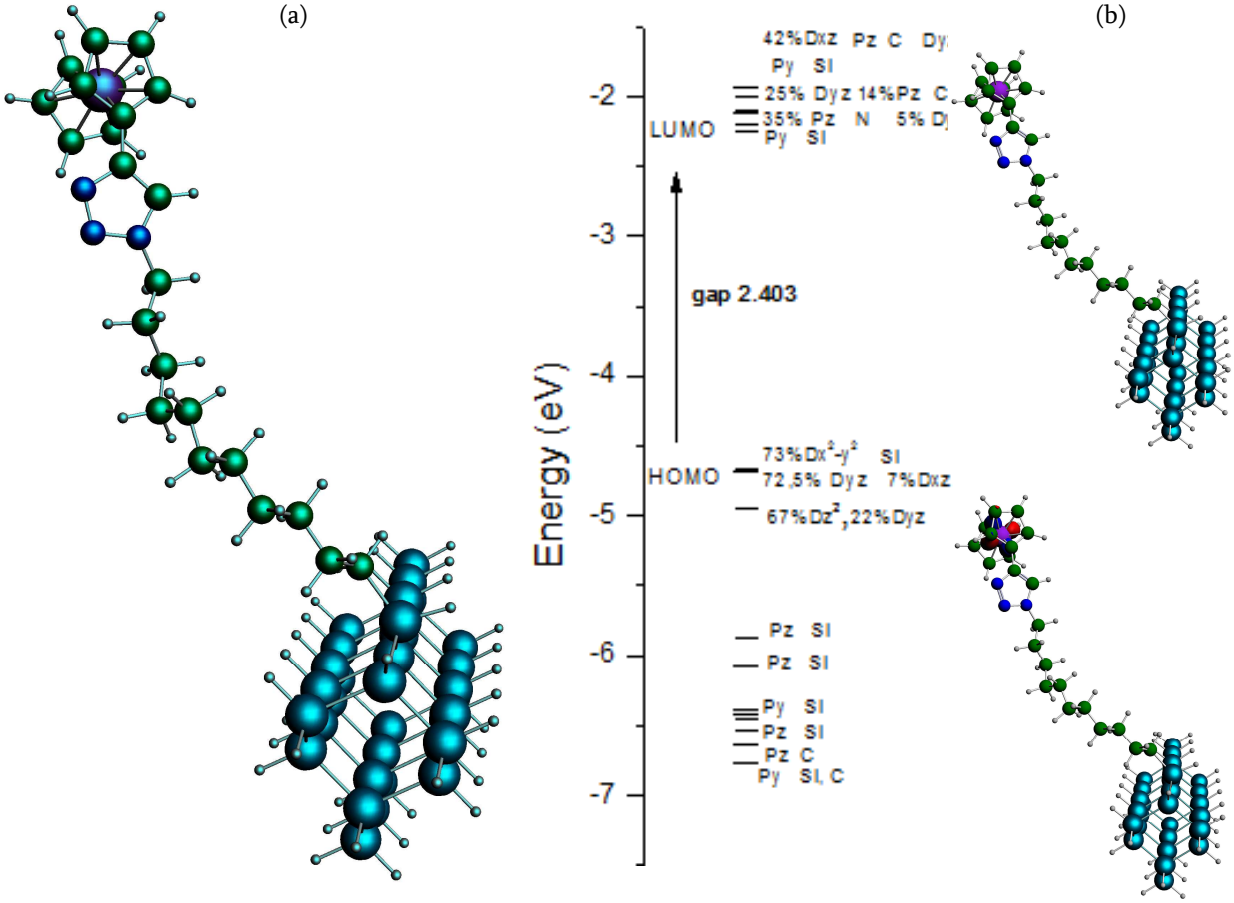

Figure IV.17. (a) geometry structure of Fc-$N_3(CH_2)_{11}$ indirect grafting;(b) schematic diagrams of molecular orbital levels of neutral form

We obtain the same results as for C6 linker: the HOMO is localized on the Fe ion of ferrocene and there is a simple superposition of MOs from each constituent of the system (organometallic and Si parts) (figure IV.17 b). The oxidation leads to a charge held by the ferrocene as in the previous cases. Then, for the long linker C11 indirect grafting, again the HOMO/LUMO gap is increasing in the case of reduced species. This result implies that a higher energy is required to transfer the charge into a hole.

As before, we can align the MOs levels of the molecule and Si gaps, as shown in figure IV.18.

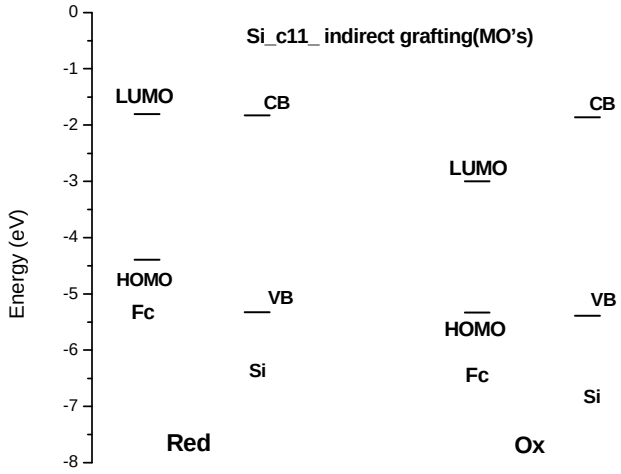

Figure IV.18. Ferrocene gap / Si gap in indirect grafting (C11 linker).

A similar behaviour as in the case of Fc-$N_3(CH_2)_6$ was observed. The electron transfer is not reversible at the same potential (|Vox|>|Vred|). We get the following gaps for the two potentials: 0.9 eV for the oxidation potential and 2.24 for reduction potential. In the experimental cyclic voltammetry measurements a larger shifting on the reduced and oxidized potentials were observed in comparison with the C_6 indirect grafting.

IV.2.2.2.3. Linker effect

The main experimental features of cyclic voltammetry are recalled below on figure IV.19: shows the increasing energy separation E_{red}-E_{ox} versus linker length. Figure IV.19 (b) puts in evidence that the mean energy (E_{red}+E_{ox})/2, versus the linker length is not changed. Since the peak separation increases with the length of the linker, we can assume that the linker acts as a tunnel barrier between Fc and Si.

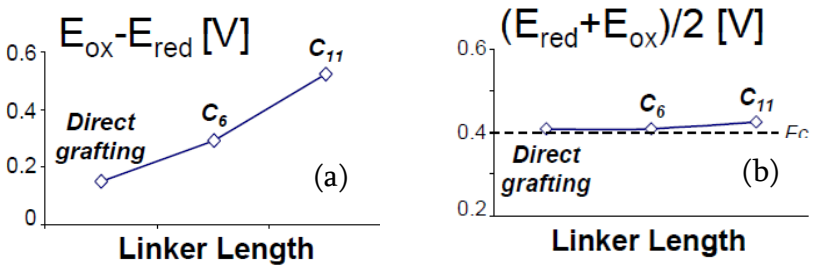

Figure IV.19 a) Separation of energy values E_{ox} and E_{red} function of the length linker;

b) Mean value of redox energy (E_{red}+E_{ox})/2 function of the length linker).

Our theoretical results in terms of alignment of MOs and Si gap are in good agreement with the experimental data shown above. This is shown below on figure IV.20, where we put together the gaps obtained for reduced and oxidized species for the vinyl and N_3-C_{11} linkers. We can compare the influence of the linker on the energy transfers, estimated from the following diagrams.

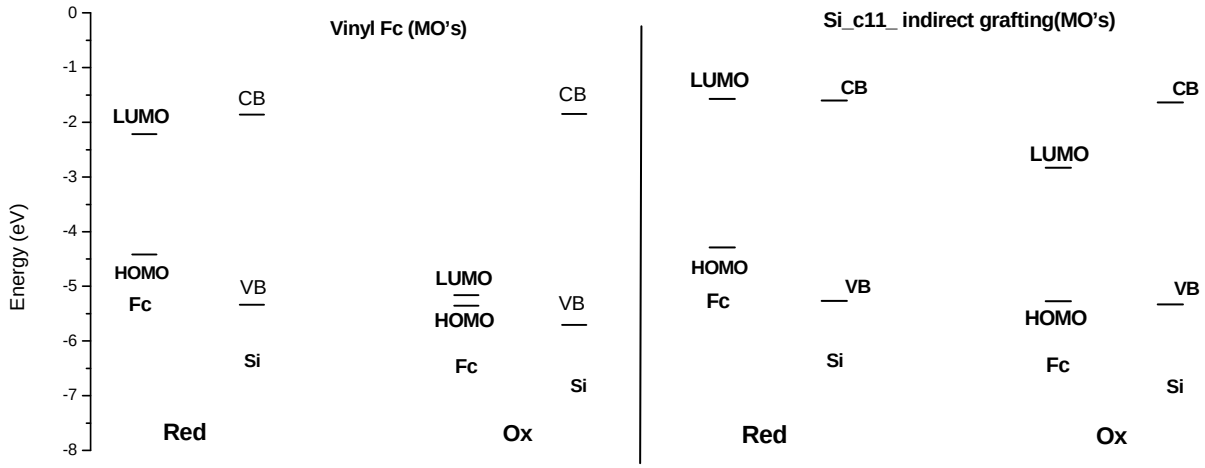

Figure IV.20. Comparison between the levels of molecule and SI around the gap. Left: direct grafting, right: indirect grafting

The energy difference for the oxidation transfer is thus ≈ E(HOMO Fc) – E(VB) and for reduction ≈ E(VB) – E(LUMO). For the direct grafting we get: 0.88 eV for oxidation and 0.19 eV for reduction. For indirect (C11) grafting, we get: 0.9 eV for oxidation and 2.24eV for reduction. This can easily be transformed to calculate the bias shift between oxidation and reduction which is thus ≈0.69 V for direct grafting and ≈ 1.35 V for indirect grafting. We thus are in very good agreement with experimental trends, with a weak shift for direct/vinyl species and a larger one for the indirect grafting. Clearly, this is a qualitative estimate, and we cannot really expect to reproduce completely the whole numbers given by CyV data.

From these results on grafted ferrocene analyzed in terms of molecular properties, we see an excellent agreement of experimental redox potentials with the computed ones. The

small models presented above seem also to reproduce very well the experimental data and various correlations with electrochemical or impedance measurements can be made.

IV.3. Periodical calculations on ferrocene grafted

Periodical calculations were performed for the ferrocene monolayers on a Si slab made of 5 silicon monolayers with the (1 0 0) crystallographic orientation, using SIESTA. We studied the case of a) Fc alone, b) direct grafting (vinyl-Fc), c) indirect grafting with C_6 linker and d) indirect grafting with C_{11} linker.

We have used the reconstructed slab surface of Si described in paragraph I. This surface reproduces well the experimental gap of bulk Si. Also, a sufficiently thick vacuum layer of 4 nm avoids any spurious interactions between repeated cells of grafted monolayer.

The equivalent coverage is given by the area of the supercell in the direction normal to the surface. In our case we have grafted one molecule every 21.72 angström, which gives a coverage of $2x10^{13}$ molecules/cm^{-2} close to the available experimental estimations at $6x10^{13}$ molecules/cm^{-2}.

IV.3.1. Density of States

Although we have an accurate description of the electronic structure of an isolated atom by solving Schrödinger's equation, in a crystal we have to deal with a very large number of atoms, making this equation impossible to solve exactly. Relief comes in the shape of Bloch's theorem, which applies the translational symmetry of the crystal lattice to the electronic structure. This allows us to build a band structure picture of the crystal, where atomic energy levels merge into bands, because of the interference of the atomic states of each of the electrons in the solid. We can now speak also of a density of energy states in the band.

We then employ Density Functional Theory (DFT) in the Kohn-Sham approach to link the relevant electronic structure (such as the d-band in transition metals) to the local

topology of a crystal. First, the ground state Hamiltonian of an N electron system is completely determined by the external potential. DFT links this external potential to the electron density; it follows that the external potential is determined within, an additive constant, by the electron density.

Thus the visualization of this density using techniques of Gaussian smoothing by simulating the possible dispersive effect due to temperature bring us informations on changes in energy levels and their densities depending on the configuration of each studied structure. Moreover, the DOS are used to give an estimation of the gap of the material, or to localize the LUMO and/or HOMO states of a sufficiently isolated system and the relative changes in energy levels that occur in our hybrid systems.

The selected states of projected density of states (PDOS) can bring additional informations in comparison with DOS. It corresponds to the projection of the DOS for each atomic state, (for a given symmetry or species), and it helps to know the contribution of these states in the total density of states. We will show below the resulting PDOS for direct and indirect grafted species.

IV.3.2. PDOS of directly grafted Fc-Si

For the minimization of the system, the super cell implementation of plane waves and/or atomic orbitals based pseudopotential methods, within the density functional scheme were used in the framework of SIESTA code. The core electrons were frozen with their nuclei and the interaction between valence electrons and ion cores is represented by norm conserving pseudopotentials of the Troullier-Martins form. Exchange correlation functional of Perdew-Burke-Ernzerhof (PBE) combined with a double zeta + polarization (DZP) basis sets were used. Geometry optimizations were performed for both species, in the reduced and oxidized forms. In the latter case, an unrestricted formalism was used due to the spin polarisation.

IV.3.2.1. PDOS of Fc-Si

In figure IV.21 is shown the minimized structure of ferrocene monolayers directly grafted on infinite Si (1 0 0) surface.

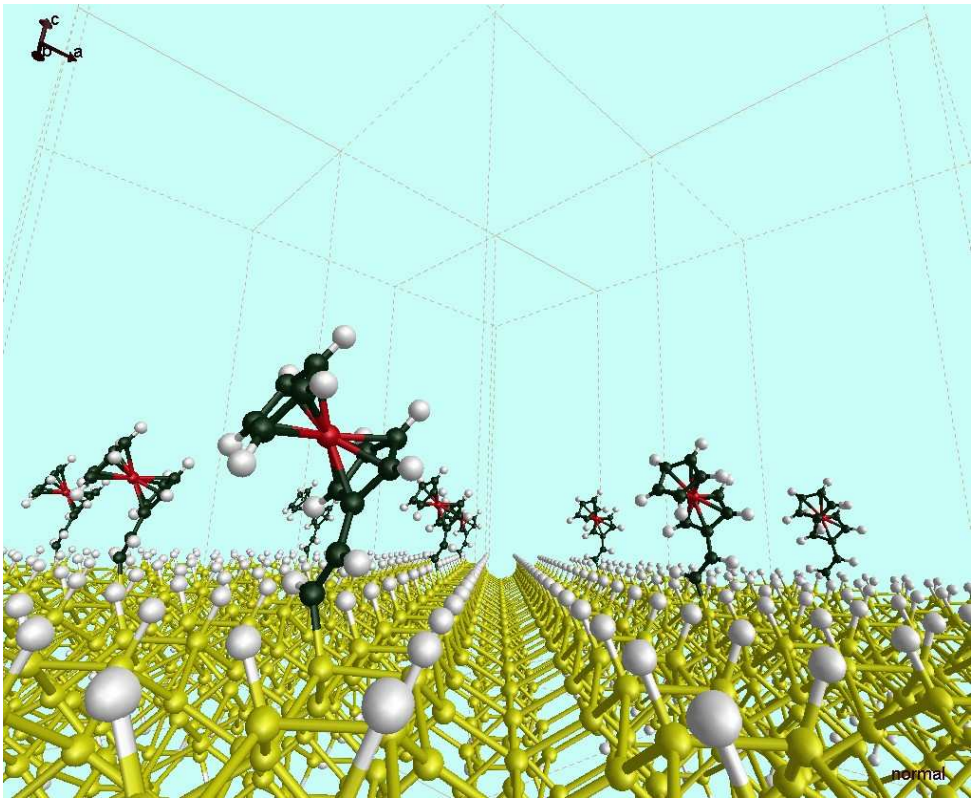

Figure IV.21 Optimized structure of Fc directly grafted

The molecule seems to be stable on the surface, and doesn't collapse during the minimization procedure. After optimization of the structure, the resulting PDOS in reduced form are shown in figure IV.22.

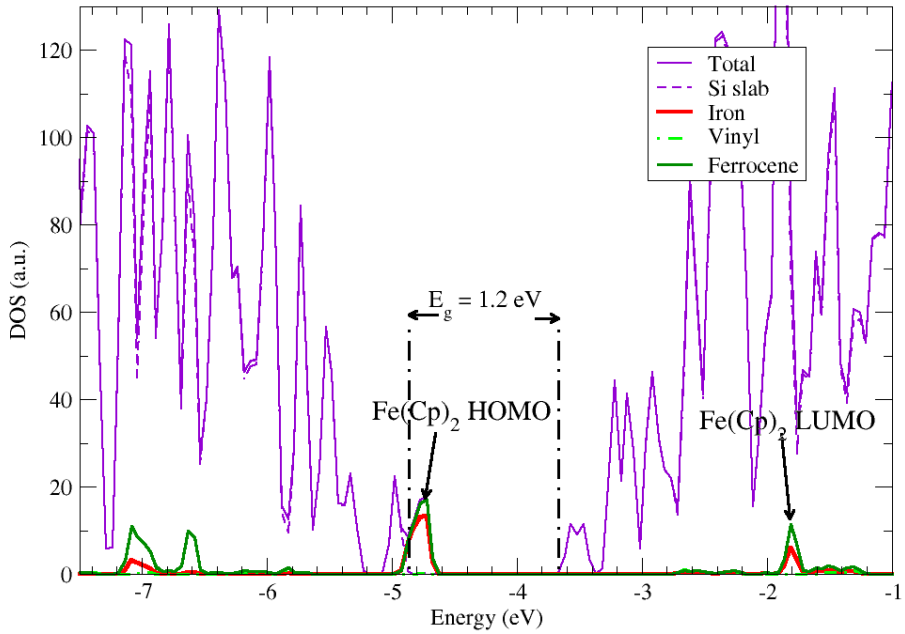

Figure IV.22. PDOS of Fc directly grafted in the reduced form

The total density of states is drawn in violet, and is mainly representative of the silicon slab contribution, where we can recognize clearly a large amount of valence states and conduction states separated by a gap of approximately 1.0 eV, which is 0.2 eV less than the gap calculated for the slab alone. By using the PDOS on silicon and hydrogen atoms of the slab, it can be seen on the above diagram that Si (1 0 0) surface contributes to all the states excepting some states in the gap, close to the effective valence band of silicon. In fact, the HOMO states that belong to ferrocene are the main contributors to the peak close to the valence band, as confirmed by the PDOS on the iron atom. Moreover, we observe that the electronic structure of the surface is not clearly affected by the presence of the molecules that are attached. The density of states of the molecule is not affected by the states of Si surface and is comparable to the isolated molecule: we have recovered the gap for isolated ferrocene, the LUMO states lying deeply inside the conduction band of silicon.

Then, we have minimized the system for the oxidized species $(Fc\text{-}Si)^+$. The resulting PDOS are available in figure IV.23.

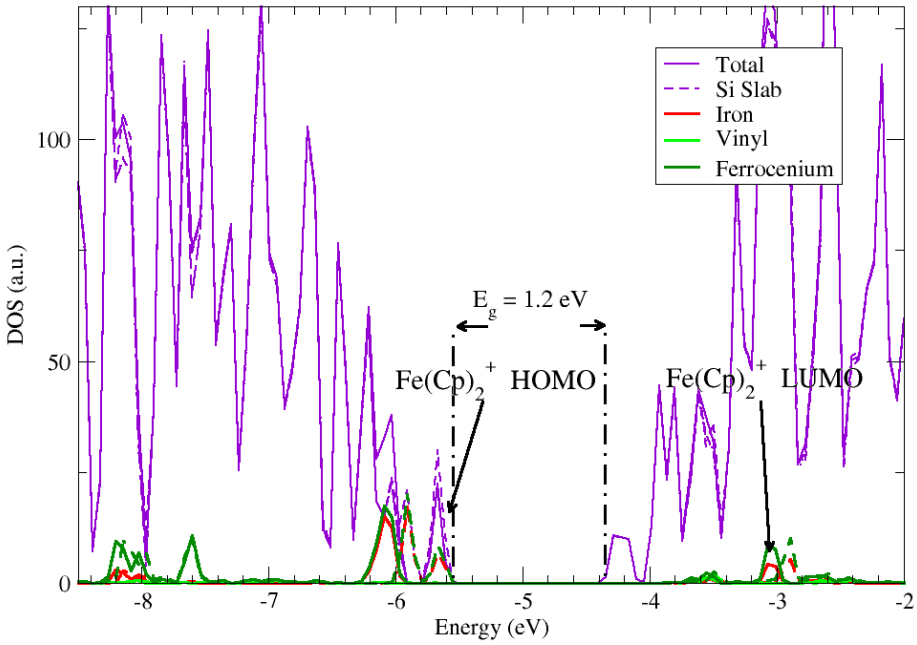

Figure IV.23. PDOS results Fc^+ directly grafted

Even if it remains neutral the Si surface is arbitrary shifted by ≈ 0.73 eV in comparison with the neutral Fc grafted case, due to the periodic boundary conditions where no absolute energy reference exists. The molecular levels are also shifted, but this time due to the lost of one electron, a splitting of ferrocene in two or three levels is observed that corresponds to the splitting observed for the isolated ferrrocenium Fc^+ states. Also, the majority of states correspond to Si states, except for the states of ferrocenium around the VB. The HOMO states are shared between the molecules and the VB of the slab. In comparison to the neutral case, this arrangement clearly indicates that a charge transfer between the molecule and the surface or vice versa is possible, by involving a hole in the valence band. This presumes also about the doping of silicon substrate if one wants to trigger the charge transfer: a p-doped substrate will be more appropriate than a n-doped one.

IV.3.2.2. Comparison with quantum molecular results

The resulting DOS of the two species are compared to molecular results of the small model and discussed in the light of experimental data on electrical properties.

As in the case of molecular description of the small model, the PDOS shows that the HOMO of the system is located on Fc. In both diagrams, the states of the molecule (HOMO) are very close to the valence band (VB) of the surface. The energy states given by the PDOS calculations, match quite well with the molecular orbital levels that are represented in the small system. The main difference comes from the CB of Si which is much higher in the small Si aggregate that in the periodical system. Thus in the small model, the LUMO of the ferrocene part is situated inside the (large) gap of Si whereas here, the CB of Si is lower in energy and thus the LUMO of the Fc part is located much higher than the gap. Taking into account the shifting which always occurs in the oxidized form, the two PDOS are almost similar.

IV.3.3. PDOS of indirect of Fc on Si

IV.3.3.1. The case of Fc-$N_3(CH_2)_6$

The system in both forms, reduced and oxidized, was optimized using the same conditions as for direct grafting. In figure IV.24 is shown the minimized structure of ferrocene monolayers Fc-$N_3(CH_2)_6$ indirectly grafted on infinite Si (1 0 0) surface. The molecule seems to be stable on the surface even if we use a long C_6 linker, and doesn't collapse during the minimization procedure.

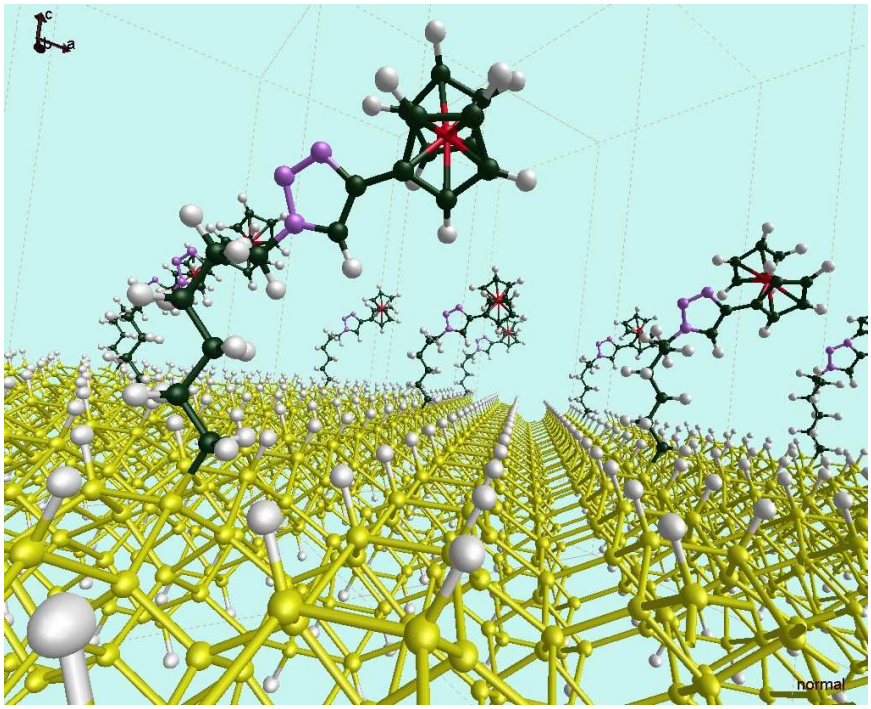

Figure IV.24. Fc-$N_3(CH_2)_6$ monolayers indirect grafted on infinite Si (1 0 0) surface

The resulting PDOS in reduced form are shown in figure IV.25.

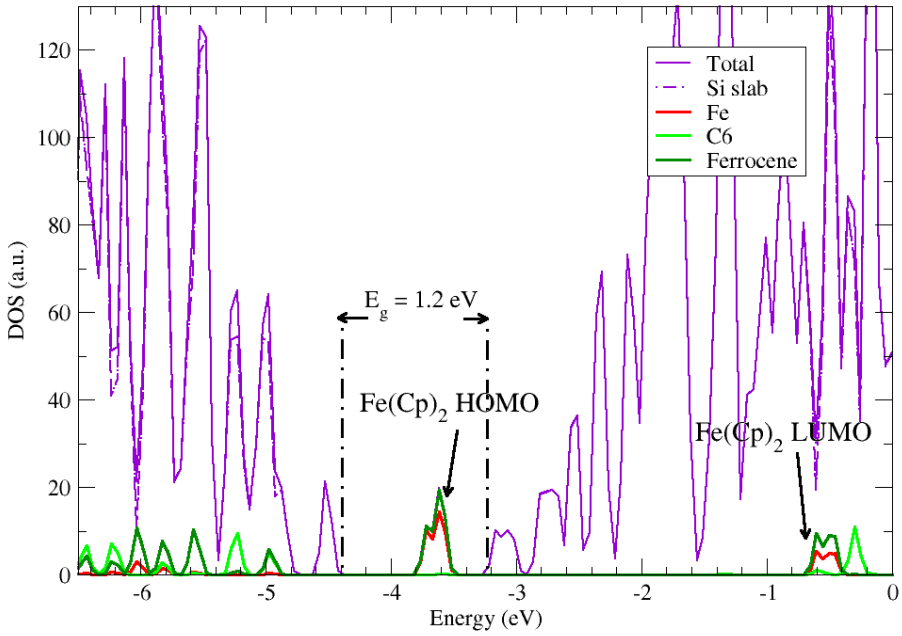

Figure IV.26. PDOS of Fc-$N_3(CH_2)_6$ indirect grafted

The total density is mainly representative of the silicon slab contribution, and a similar gap of Si was obtained. The PDOS on silicon and hydrogen atoms of the slab contributes to all the states excepting some states in the gap, which are shifted closer to the CB of silicon. These latter states are due to the ferrocene part (HOMO) whereas the LUMO states of ferrocene lie deeply inside the conduction band of silicon. The electronic structure of the surface is not affected by the presence of the molecules that are attached. The density of states of the molecule is not affected by the states of Si surface and is comparable to the isolated molecule: we have recovered (after grafting) the gap of isolated ferrocene that.

Then, the minimization of the oxidized species was carried out. The resulting PDOS are available in figure IV.27.

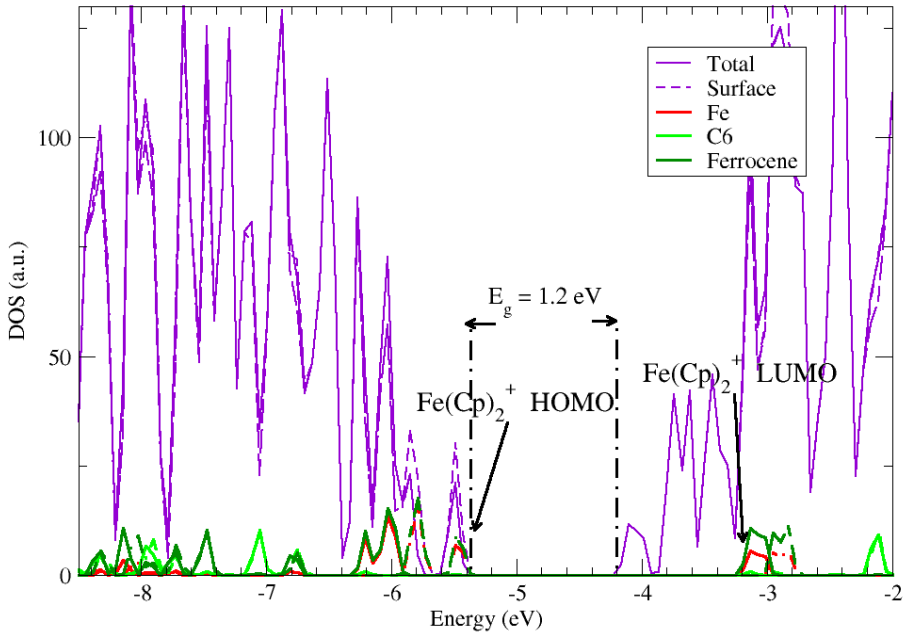

Figure IV.27. PDOS of Fc^{+}-$N_3(CH_2)_6$ indirect grafted

As in the case of direct grafting, the Si surface is again shifted by ≈ 0.73 eV in comparison with the neutral Fc grafted case. Also the molecular levels are shifted, but this time due to the lost of one electron, a splitting of ferrocene in two or three levels is observed that corresponds to the splitting observed for the isolated ferrocenium Fc^{+} states. The Si states

correspond to all the states excepting the states of ferrocenium around the VB. The PDOS shows a similar behaviour as in the description made by the molecular orbital diagram. The HOMO states are shared between the molecules and the VB of the slab.

IV.3.3.2. The case of Fc-$N_3(CH_2)_{11}$

A behaviour close to the Fc-$N_3(CH_2)_6$ species was observed. The minimization of the system was made for the two species, reduced and oxidized. The same theoretical conditions were used for the characterization of this system. In figure IV.28 is shown the minimized structure of ferrocene monolayers Fc-$N_3(CH_2)_{11}$ grafted on infinite Si (1 0 0) surface.

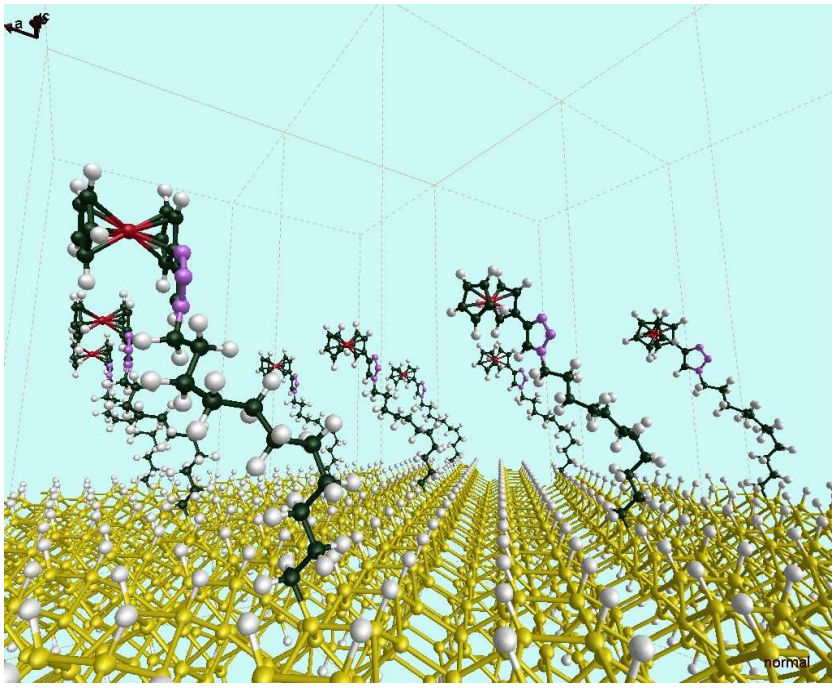

Figure IV.28. Fc-$N_3(CH_2)_{11}$ monolayers indirect grafted on infinite Si (1 0 0) surface

The resulting PDOS in reduced form is available in figure IV.28. The total density is due to the silicon slab contribution, and a similar gap of Si was obtained as in the previous cases. The PDOS on silicon and hydrogen atoms of the slab contributes to all the states

excepting some states in the gap, which are shifted now, in the middle of this gap, almost similar with the case of C_6.

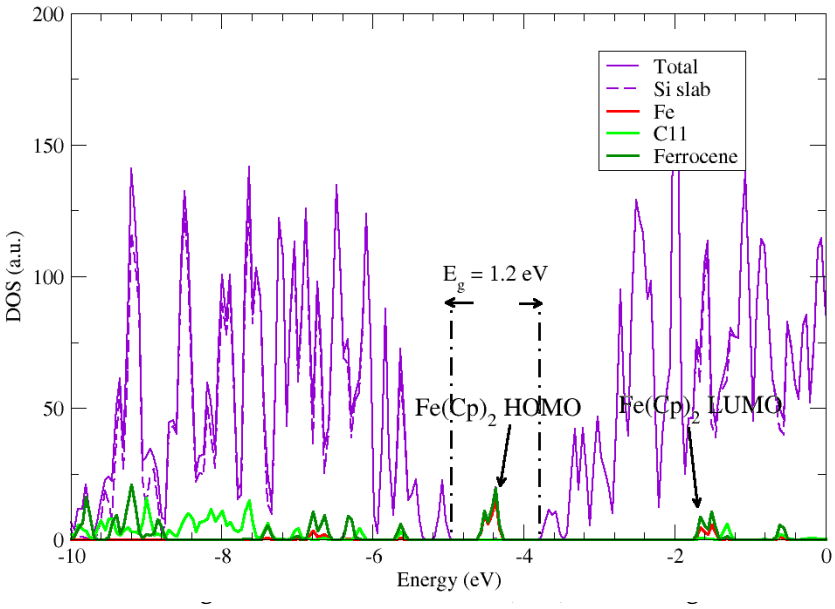

The PDOS is very similar to the one with the C6 linker. In the case of oxidized species Fc^+, the resulting PDOS is available in figure IV.30.

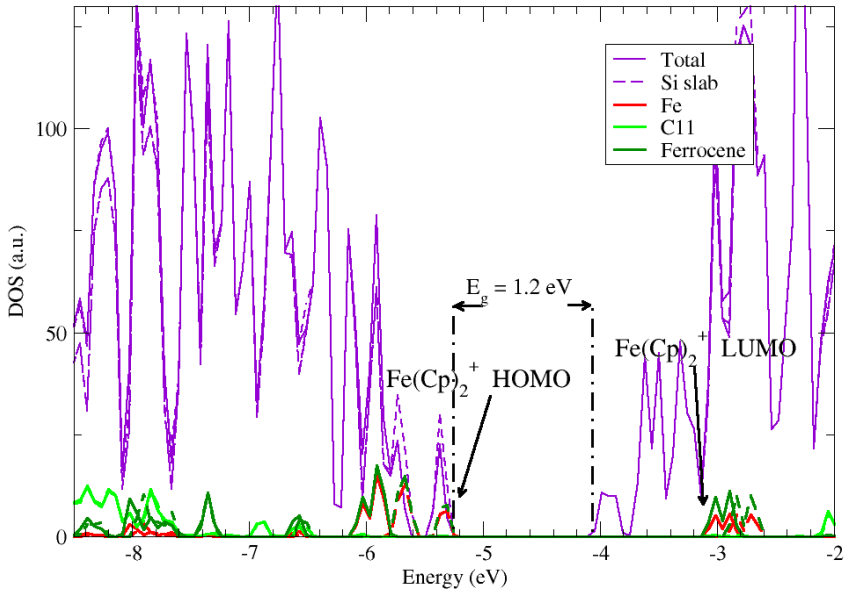

Figure IV.30. PDOS of Fc^+-$N_3(CH_2)_{11}$ grafted on Si (1 0 0)

Again the same PDOS as with the C6 linker is observed.

IV.3.4. Comparison of PDOS between direct grafting and long chains

The C_6 and C_{11} DOS are quite comparable, and show that the main effect of the linker is to increase the energy between the HOMO level of the molecule and the VB of the silicon slab for the neutral case by 0.7 eV approximately when compared to the vinyl case (i.e. direct grafting).

What is also shown is the contribution of the linker, which appears deeply inside the valence band. The C_6 and C_{11} linkers seem to act as a tunnel barrier and also as a modulator of the possible electrostatic dipole between the Fc molecule and the silicon slab: this could explain why the levels of the molecules are shifted inside the silicon gap with a sufficiently long linker. This point should be investigated deeply by evaluating the different molecular dipole intensities, going from the surface to the molecule.

In the case of vinyl direct grafting, the reduced and oxidized species shows a similar arrangement, while for indirect C_6 and C_{11} grafting, a different behaviour between the studied forms was observed. This is similar with small model investigations, where the molecular orbital diagram results shows that a shifting is produced in the case of oxidized species, either is C_6 or C_{11}. This could be an explanation for the cyclic voltammetry, which also describes a shifting in peaks (for reduction and oxidation).

IV.4.Theoretical modeling of porphyrins grafted on Si (1 0 0)

After the study of ferrocene molecules on Si, an investigation of the interaction between a zinc porphyrin namely ZnAB3P and Si surface has been carried out. This porphyrin is derived from a Zn tetraphenyl porphyrin (ZnTPP) with a triple bond or a diazonium group on one of the phenyl groups as tether for further direct or indirect grafting.

Using the same conditions (surface, linkers) as for ferrocene grafting, we have thus investigated the electronic properties of the resulting hybrid systems. Direct grafting (vinyl-Fc) and indirect grafting ($N_3(CH_2)_6$, and ($N_3(CH_2)_{11}$, were studied with a cluster of 34 Si atoms, in gas phase and in acetonitrile solvent. Taking into account the

semiconductor surface, band structure calculations also were performed. As for ferrocene, our modelling will be strongly connected to electrical properties studied experimentally (thesis of T. Pro, CEA/LETI) [27, 28]. We will thus present in a first part the main relevant properties obtained from these experiments.

IV.4.1. Main experimental structural features

The current-voltage characteristics CyV of $ZnAB_3P$-Si (direct vinyl grafting) and $ZnAB_3P$-$N_3(CH_2)_{11}$-Si surfaces, are shown in figure IV.31 a and b. For both monolayers, the scan rate was varied from 0.1 V/s to 1 V/s. Two reduction and oxidation peaks were found, both of them corresponding to single-electron redox reactions.

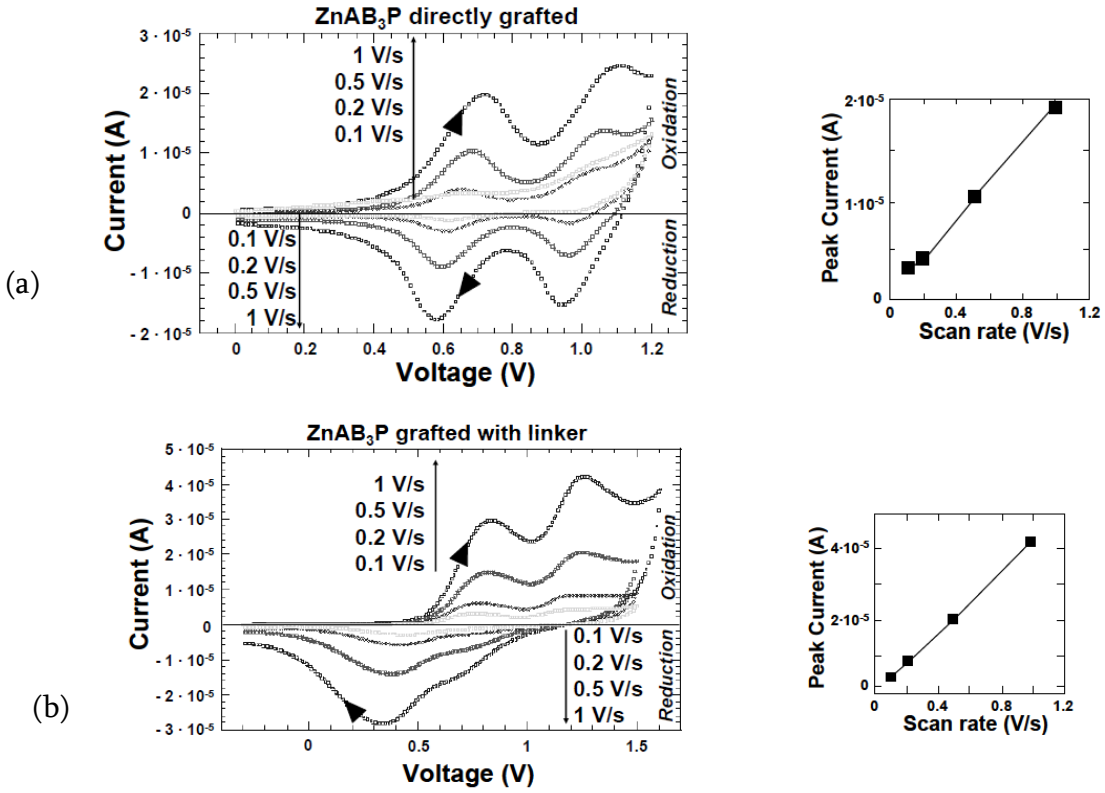

Figure IV.31. a) left - CyV trace of ZnAB3P directly grafted at different scan rate, right - peak current versus scan rate; b) lef t- CyV trace of ZnAB3P grafted with C11 linker at different scan rate, right - peak current versus scan rate. Voltages given vs SCE.

In the case of direct grafting $ZnAB_3P$-Si, the redox potential for the first process is 0.64 V/ SCE, thus 0.888 V/NHE and for the second one : 1.02 V/SCE thus 1.268 V/NHE. These two values are slightly decreased compared to the values obtained for CyV of ZnTPP in solution (First redox potential at 0.9 – 1.19 V/NHE, second one at 1.19-1.59 V/NHE. [29, 30]. This decrease had been already observed for ferrocene (see chap.3 and 4.II). Finally we observe that both redox processes are reversible, the difference between oxidation and reduction voltages are close to 0.09 V.

For $ZnAB_3P$-N_3 $(CH_2)_{11}$-Si (figure IV.31 b) under the same conditions, the first redox potential is 0.61 V/SCE thus 0.858 V/NHE and for the second process: 0.99 V/SCE thus 1.238 V/NHE. The values are very close to the ones obtained for direct grafting. In that case, the indirect grafting leads to shifts in oxidation and reduction peaks of ca 0.45 – 0.5 V. In figure IV.31 a and b (right), the oxidation peak current (the first peak for direct grafting and the second one for indirect grafting) is plotted versus the scan rate. The linear dependence confirms again that the oxido-reduction process is related to species grafted on the electrode.

The same behaviour as for grafted ferrocene is observed, with a peak separation is increased when the grafting is performed with a long alkyl linker, thus giving once again evidence of the effect of the linker over the electron transfer.

Conductance voltage (C –V) and capacitance voltage (G-V) measurements were made. The results of ZnAB3P grafted either directly or with a linker are shown in figure IV.32 a and b.

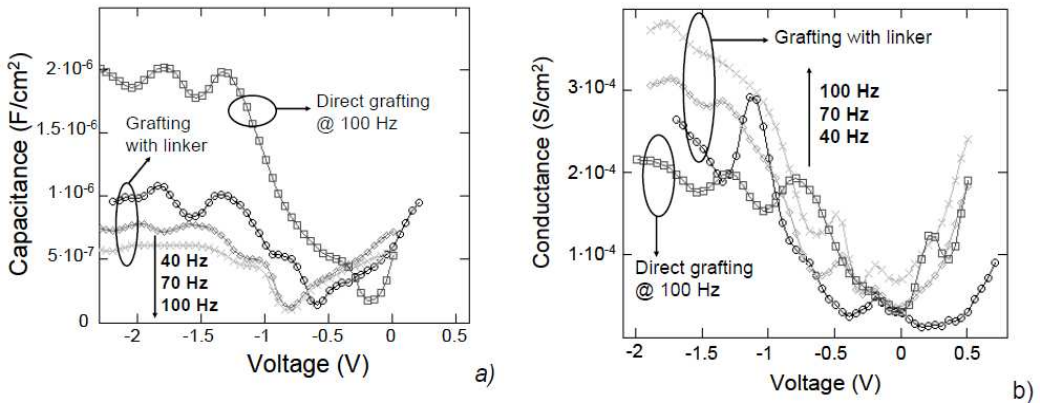

Figure IV.32. C-V tests (a) and G-V tests (b) for $ZnAB_3P$ directly grafted (at 100 Hz) and grafted with linker (40 Hz, 70 Hz and 100 Hz).

A stronger attenuation of capacitance value appears for the indirect grafting, but no shift of the voltage peak can be noted. In the case of direct grafting, two peaks at -1.3 V and -1.8 V were observed at 100 Hz, corresponding to the two redox states of ZnAB3P. For the case of indirect grafting, the peaks were observable at lower frequencies (40 Hz and 70 Hz in figure IV.32-*a*) but no longer at 100 Hz. Those peaks were detected at -1.9 V and -1.6 V at 70 Hz and shifted to -1.8 V and -1.3 V at 40 Hz. For the direct grafting, both redox peaks are visible, at same voltages as in the CyV tests.

For the indirect grafting, only one peak is visible at -1.6 V at 40 Hz and 70 Hz. This fact can be attributed to a slower electron transfer between the ZnAB3P and Si with a linker. ZnAB3P capacitors showed lower robustness compared to Fc capacitors. The presence of the linker influences the capacitance value but not the peak voltage. In the G-V the linker affected the electron transfer as only one redox process took place.

Nevertheless we observe that these redox active species are able to give an electron transfer and are thus good candidates to store charges.

IV.4.2. Theoretical molecular study of porphyrin grafted on Si

The geometry and electronic structure of ZnTPP grafted on a small Si_{34} aggregate were explored in the framework of ADF molecular approach.

We used the same theoretical approach as for ferrocene in order to describe the electronic properties of ZnTPP porphyrins on Si surface. In particular, the first oxidized species being a radical cation was computed in an unrestricted scheme with a doublet ground state. The case of direct grafting (vinyl-ZnTPP) and indirect grafting ($N_3(CH_2)_6$ and $(N_3(CH_2)_{11}$, were studied. After complete geometry optimizations, molecular orbital diagram of the chosen species were described and correlated with the experimental data.

IV.4.2.1. Direct grafting of ZnTPP

Optimized structures were calculated for the first oxidized and reduced ZnTPP. Then, theoretical redox potentials against the normal hydrogen electrode (NHE) were computed as already described.

The theoretical redox potential found for ZnTPP directly grafted is 0.8 V/NHE. In the CyV measurements, the first redox potential was found ≈ 0.89 V/NHE. As for ferrocene the agreement with experimental data is quite good.

In figure IV.33 is shown the structure and MO diagram of ZnTPP directly grafted on Si surface, from solvent calculations.

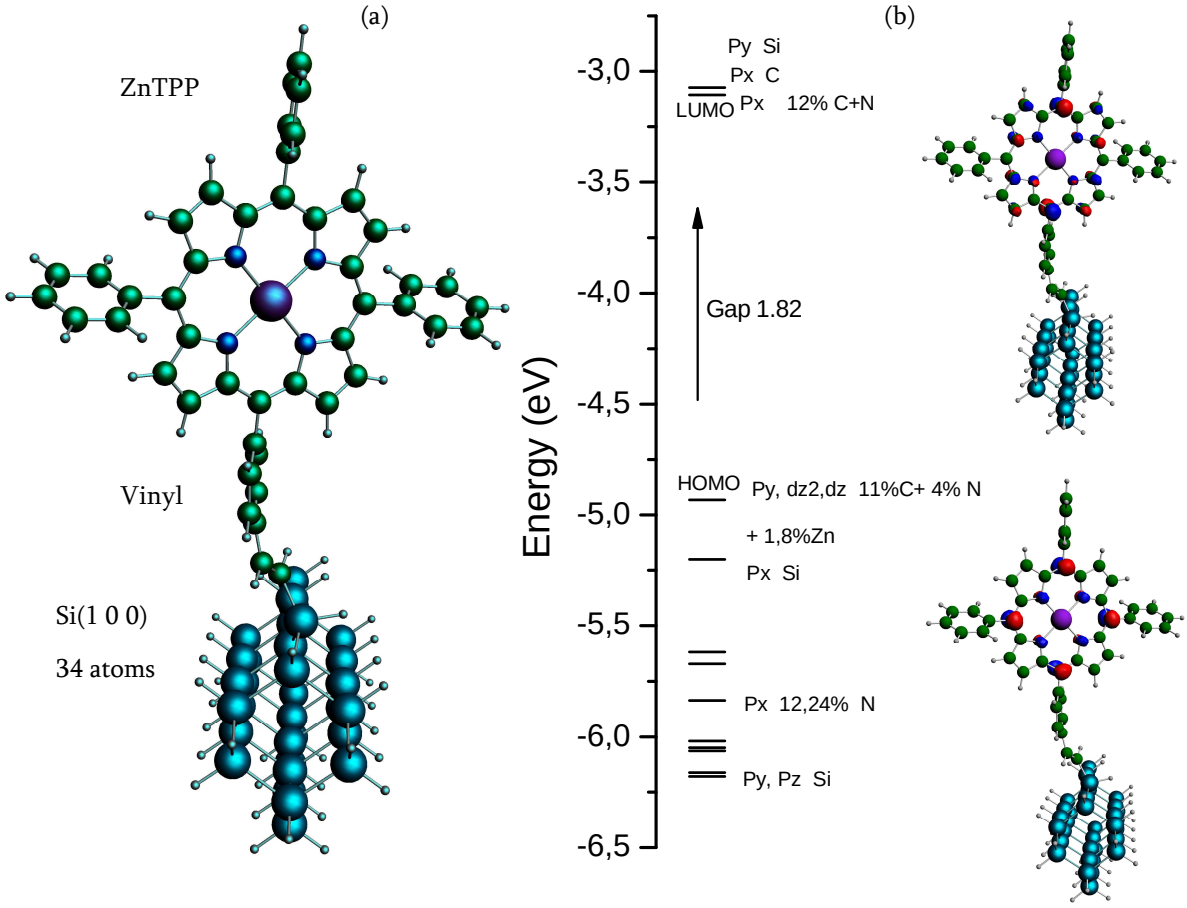

Figure IV.33. (a) geometry structure of ZnTPP directly grafted; (b) MO diagram.

As can be seen on the above diagram (figure 4.30 b), the HOMO (and LUMO) are localized on π-orbitals of the conjugated core of the porphyrin. This means that the HOMO and LUMO of the hybrid species are the same as that of the isolated porphyrin. Thus the oxidation takes place on the porphyrinic core, and this is consistent with the

presence of a charge transfer during capacitance measurements. After oxidation, the relaxed electronic structure of the positively charged system shows that the positive charge is still located on the molecule, by examining the Mulliken charges.

Then, we have studied the electron transfer that could occur in the hybrid system in the reduced and oxidized species. The resulting molecular orbital diagram shows how the levels in the molecule or in the surface are modified after the grafting of porphyrin. The levels given in the hybrid system by the molecule and the linker on one side, and of Si cluster on the other side, were investigated as shown in figure IV.34.

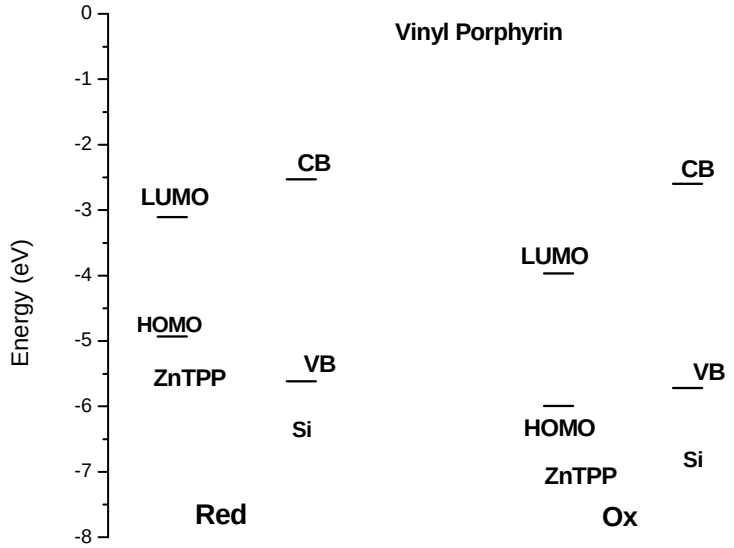

Figure IV.34. Molecule gap / Si gap inZnTPP direct grafted

Again the Si surface is considered as p doped as in the experimental device. The same mechanism as for ferrocene is invoked. For oxidation, an electron is transferred from the HOMO level of the ferrocene to the VB of the Si, whereas in reduction, electron passes from the VB to the LUMO level of ferrocene. The figure shows how the molecule gap is aligned / Si gap. The values for the oxidation transfer and reduction transfer are thus: 1.6 V and 1.73 V.

We can see that the oxidation and reduction bias are thus close to each other. This behaviour can explain the CyV of ZnAB3 directly grafted where a very small shifting

between the oxidation and reduction peaks appears. Also in the conductance voltage and capacitance voltage measurements, both redox peaks of the porphyrin were visible at the same voltage as in CyV.

IV.4.2.2.Indirect grafting of ZnTPP

IV.4.2.2.1 The case of ZnTPP-$N_3(CH_2)_6$ indirect grafting

The ZnTPP molecules were attached on the surface using the C6 long linker. The geometry optimization of ZnTPP molecule grafted on Si surface using C_6 long linker is shown in figure IV.35 (a) and the MO diagram was investigated (figure IV.35 (b)).

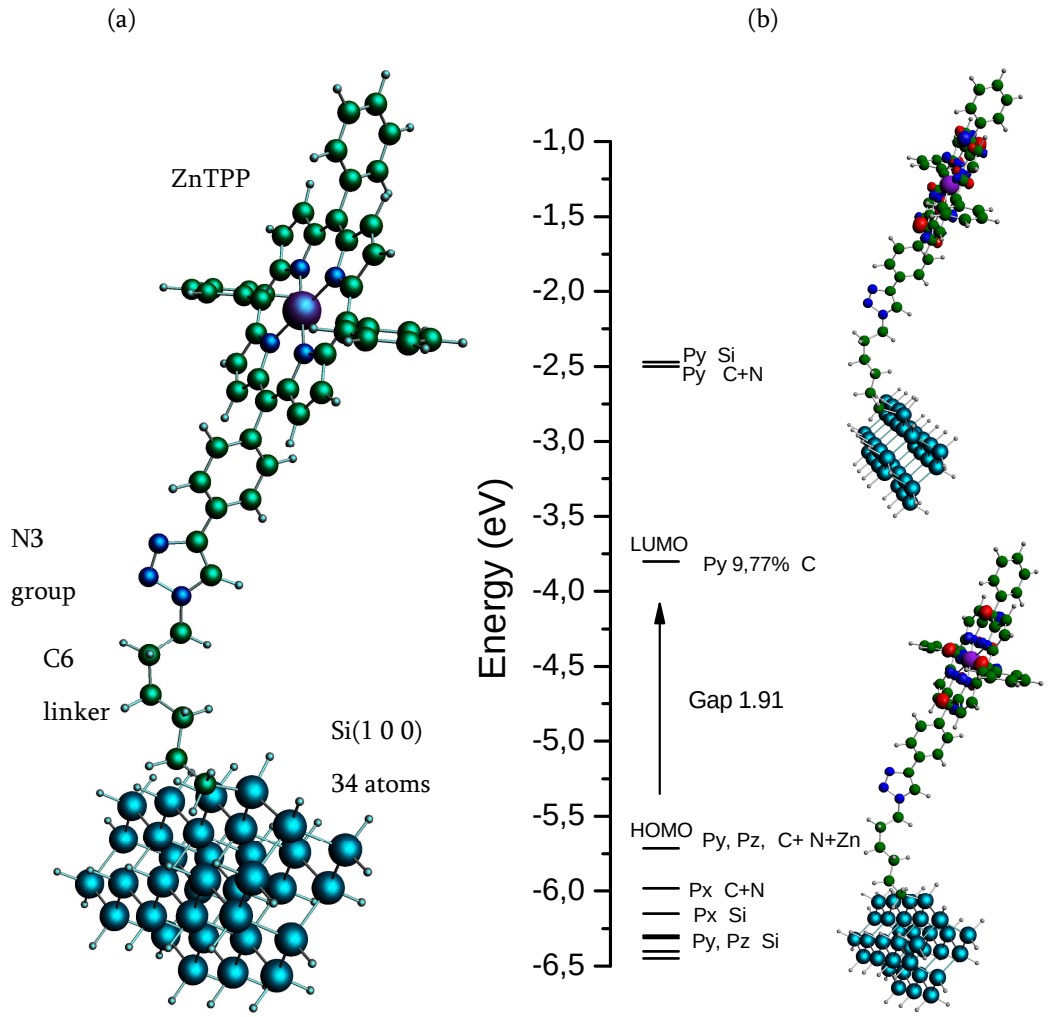

Figure IV.35. (a) Structure of ZnTPP grafted with C6 linker; (b) MO diagram.

As for the vinyl linker, the HOMO is localized on π-orbitals of the porphyrinic core. After oxidation, the Mulliken charges of the relaxed electronic structure shows that the positive charge is located on the molecule. Finally, we have shown on figure IV.36 the alignment of the HOMO-LUMO gap of the molecule with respect to the gap of Si.

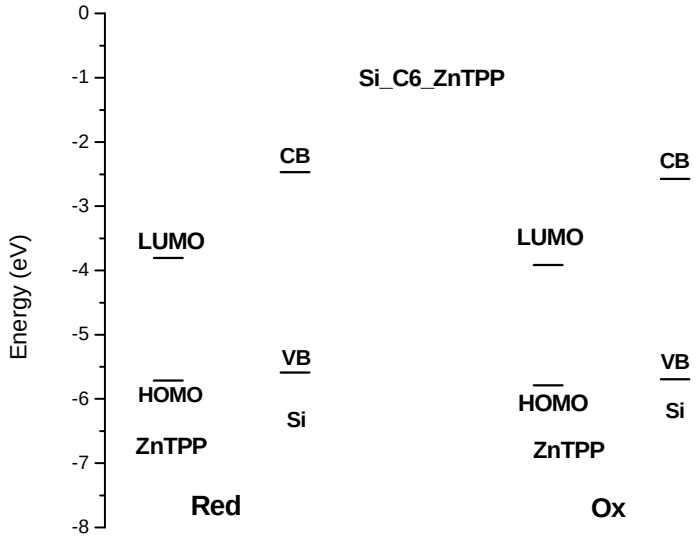

Figure IV.36 Molecule gap / Si gap in ZnTPP indirect grafted

The energy transfers between HOMO-VB and VB-LUMO are: 0.77 V for oxidation potential and 1.68 V reduction potential. This shows again that the difference between the two energy transfers is much higher than with the direct grafting. This could be correlated with cyclic voltammetry measurements where the peaks of oxidation and reduction are more shifted for the indirect grafted species.

IV.4.2.2.2. The case of ZnTPP-$N_3(CH_2)_{11}$

For the oxidized species, no geometry optimization was possible until now either in gas phase or acetonitrile solvent, due to electronic convergence problem. An empty orbital level appears between the occupied ones which give a wrong occupation, and in consequence a wrong total bonding energy. Several smear's were used in order to help the

problems convergence. Smear *N* is half the energy widths (in hartrees) over which electrons are smeared out over orbitals that lie around the Fermi level and that are close in energy. The calculation is still running at this moment. Thus we were not able to calculate the redox potential. We will describe in the following the case of the neutral species of ZnTPP. The geometry optimization of ZnTPP molecule grafted on Si surface using C_{11} long linker is shown in figure IV.37 (a) with its MO diagram (figure IV.37 (b)).

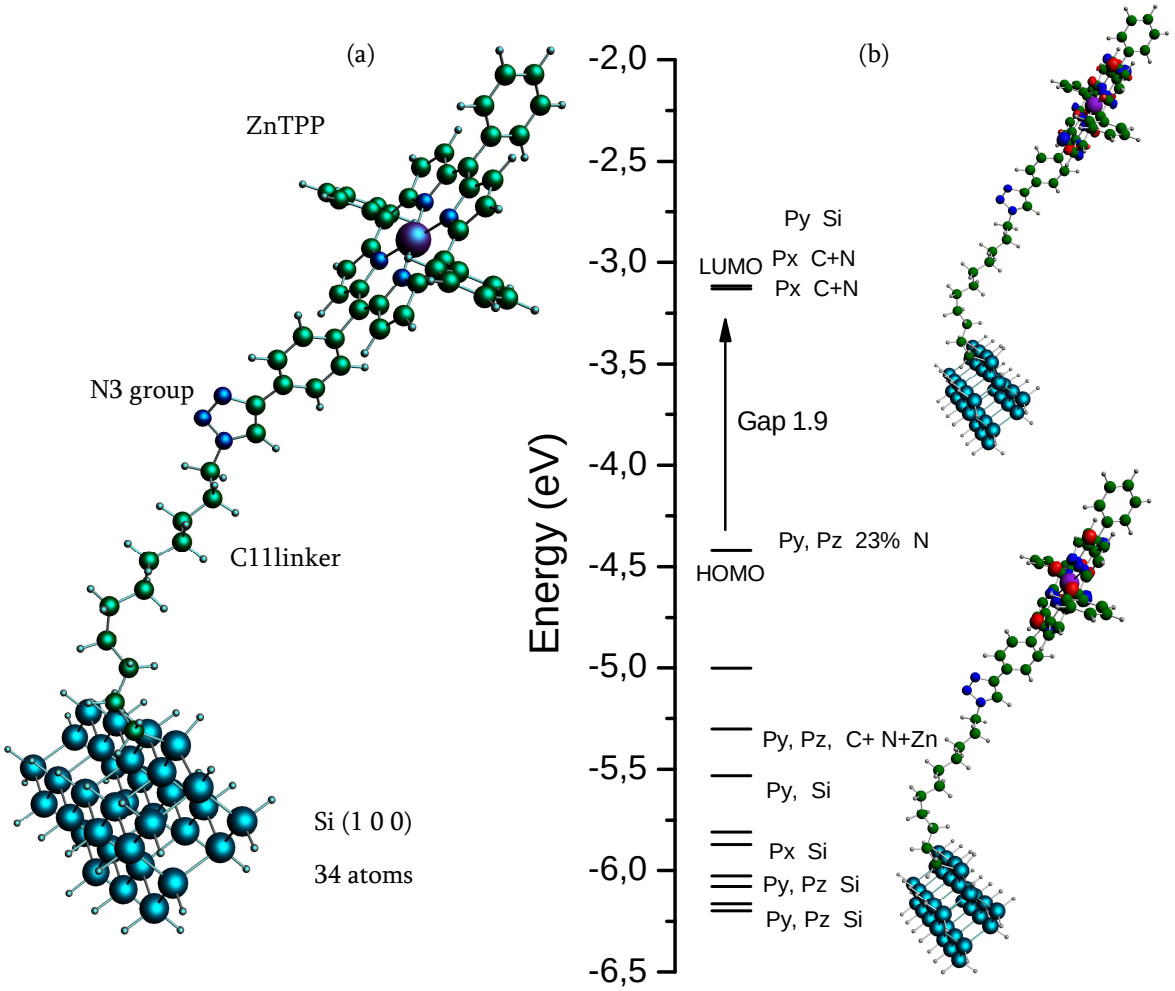

Figure IV.37 (a) Structure of ZnTPP indirect grafted with C11 linker; (b) MO diagram.

As in the case of C6 species, the HOMO is localized on the porphyrinic core, indicating that during oxidation, the positive charge is localized on the conjugated core.

On a more general point of view, our molecular calculations on grafted porphyrins agree with experimental data: redox potentials and trends in the CyV. The small models presented above seem also convenient to reproduce the experimental trends observed on Cyv and impedance measurements: shift of oxidation and reduction peaks, charge transfer on the redox active molecule in capacitance experiments.

IV.4.3. Periodical calculations on porphyrin grafted

Periodical calculations were performed for the ZnTPP monolayer on a Si slab made of 5 silicon monolayers with the (1 0 0) crystallographic orientation. We studied the cases of a) direct grafting (vinyl-ZnTPP), b) indirect grafting with C_6 linker and c) indirect grafting with C_{11} linker. We have used the reconstructed slab surface of Si described in the paragraph I.3. A sufficiently thick vacuum layer of 4 nm avoids any spurious interactions between repeated cells of grafted monolayer.

The equivalent coverage is given by the area of the supercell in the direction normal to the surface. We have grafted one molecule every 21.72 angström, which gives a coverage of $2x10^{13}$ molecules/cm^2 close to the available experimental estimations at $6x10^{13}$ molecules/cm^2.

IV.4.3.1. PDOS of directly grafted ZnTPP

For describing the projected density of states of the studied hybrid systems, the super cell implementation of plane waves and/or atomic orbitals based pseudopotential methods, within the density functional scheme were used with SIESTA.

Geometry optimizations were performed in the reduced (neutral) and oxidized (charged) forms. The calculations were made in gas phase and the same parameters of calculations were used for the porphyrin calculations. In figure IV.38 is shown the optimized structure of the ZnTPP directly grafted on Si slab surface. As for ferrrocene direct grafting, the ZnTPP molecule seems to be stable on the surface, and doesn't collapse during the minimization procedure.

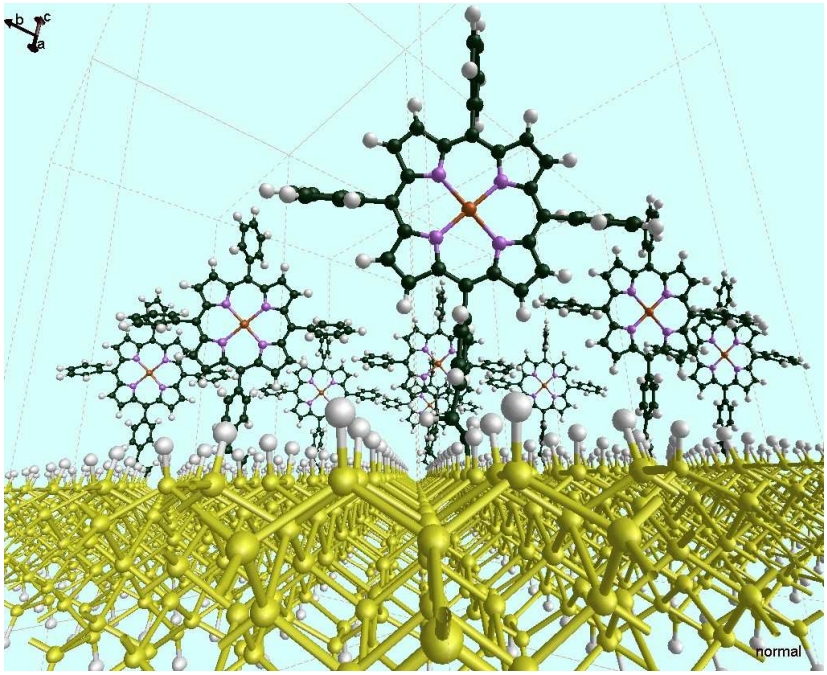

Figure IV.38. Optimized structure of ZnTPP directly grafted

After minimization of the system, the resulting PDOS were extracted and shown below. The reduced (neutral) species computed PDOS are shown in figure IV.39.

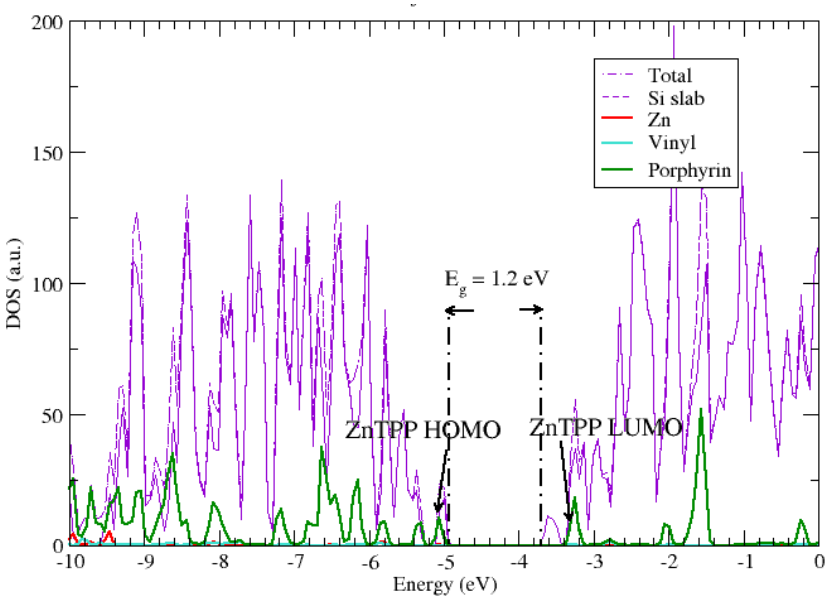

Figure IV.39. PDOS of ZnTPP directly grafted in the reduced form.

The total density of states is mainly representative of the silicon slab contribution. The gap of approximately 1.0 eV due to the VB and CB can be recognized. Silicon and hydrogen atoms of the Si (1 0 0) slab, contributes to all the states of the hybrid system excepting some states in the gap, near to the effective VB of silicon. Some states that belong to ZnTPP are contributors to the peak close to the VB, confirmed by the PDOS on the carbon atoms of the porphyrinic core. The electronic structure of the surface is not clearly affected by the presence of the molecules that are attached. Conversely, the density of states of the molecule is not affected by the states of the Si surface and is comparable to the isolated molecule. We have recovered the gap for isolated ZnTPP, and the LUMO states lie close to the CB of silicon. It was not the case for ferrocene where these states were been found deep inside the conductance band.

The PDOS were extracted also from the charge species $ZnTPP^+$ and are shown in figure IV.40.

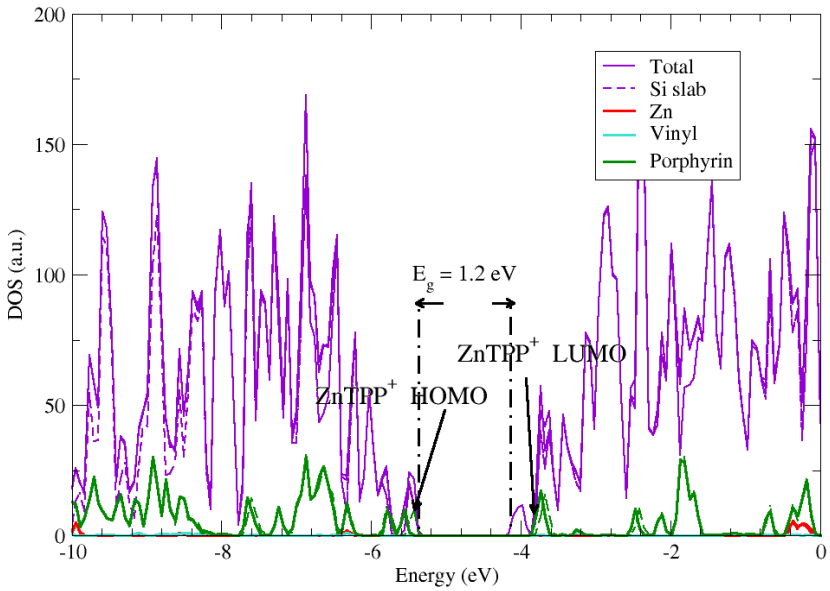

Figure IV.40. PDOS results for $ZnTPP^+$ directly grafted

A splitting of porphyrin states in two or three levels is observed near to the VB, compared to the neutral species. This is similar to the case of ferrocenium directly grafted where this splitting was observed near to the VB for ferrocene charged molecule. As in the molecular

orbital description of the small model of $ZnTPP^+$ directly grafted, the HOMO states are shared between the molecules and the VB of the slab. This arrangement indicates that a charge transfer between the molecule and the surface or vice versa is possible, by involving a hole in the valence band (with a p-doped substrate).

IV.4.3.2. Comparison with molecular computations

The states of the molecule in the DOS are very similar to the levels observed in the MO diagram (same energy levels, same localizations of the orbitals). In turn the Si gap seems not to be perturbed by the molecule. Finally, as already seen on the molecular description, the DOS of the whole system are essentially the simple superposition of the states of the two parts: molecule and Si.

In the case of molecular description of the small model, the PDOS shows that the HOMO of the system is located on the ZnTPP molecule. In both diagrams, the states of the molecule (HOMO) are very close with the valence band (VB) of the surface. We can presume that an electronic transfer can occur between the molecule and the surface or from the surface to the molecule.

Concerning the comparison with the electron transfer diagrams that were made for the small systems, in this case we are not able to do the same because the levels given in density of states are quite approximate. With a quantum chemistry DFT approach we always calculate a finite number of states, while in solid state physics we calculate a finite number of states but per supercell. The DOS are constructed by a simple averaging technique which takes into account any state as if it gives not a precise energy but a Gaussian centered on this energy, which is of course arbitrary.

The advantages of DOS is that is far simpler to analyze when we have many states which are all almost degenerated than to visualize a huge amount of eigenvalues / energies as in a molecular approach (Mo's). When we confronted to sufficiently big objects with many states with some of them almost multiply-degenerated, the DOS is far preferable. This is one of the reasons of using DOS for these types of calculations.

IV.4.3.3. PDOS for indirect grafting of ZnTPP

IV.4.3.3.1. The case of ZnTPP-$N_3(CH_2)_6$

The same theoretical approaches were used for the characterization of the ZnTPP indirect grafting using a C6 long linker. Neutral (reduced) and charged (oxidized) species were studied. In figure IV.41 is shown the minimized structure of ferrocene monolayers ZnTPP-$N_3(CH_2)_6$ grafted on infinite Si (1 0 0) surface. The molecule is stable on the surface, and doesn't collapse during the minimization procedure.

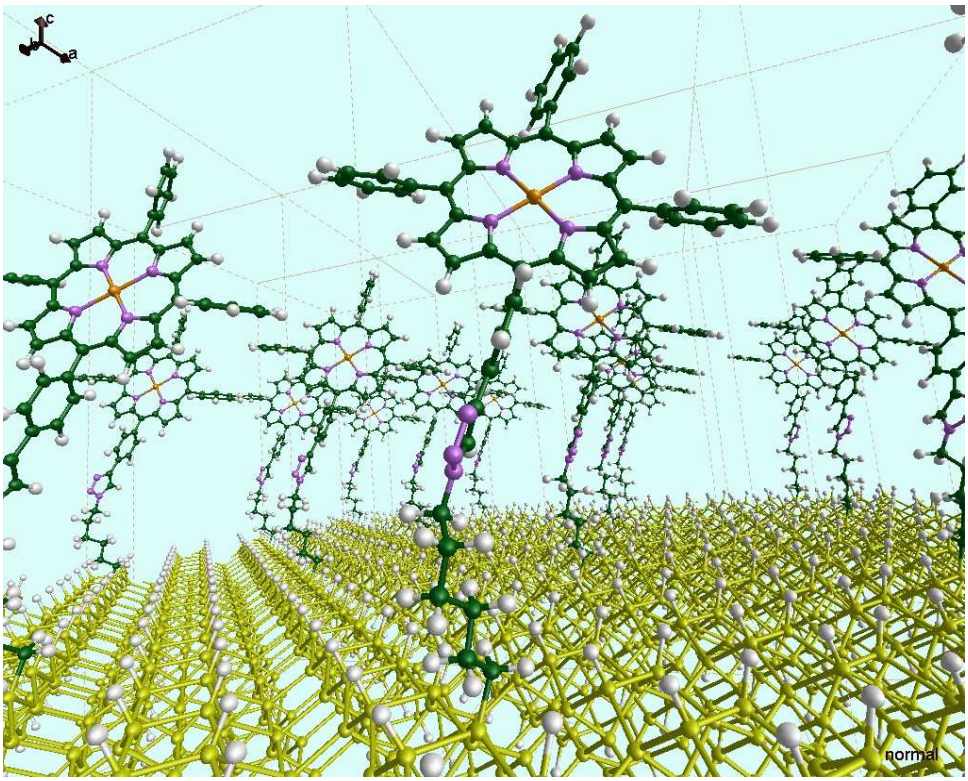

Figure IV.41. ZnTPP-$N_3(CH_2)_6$ monolayer grafted on infinite Si (1 0 0) surface

The resulting PDOS in reduced form is shown in figure IV.41.

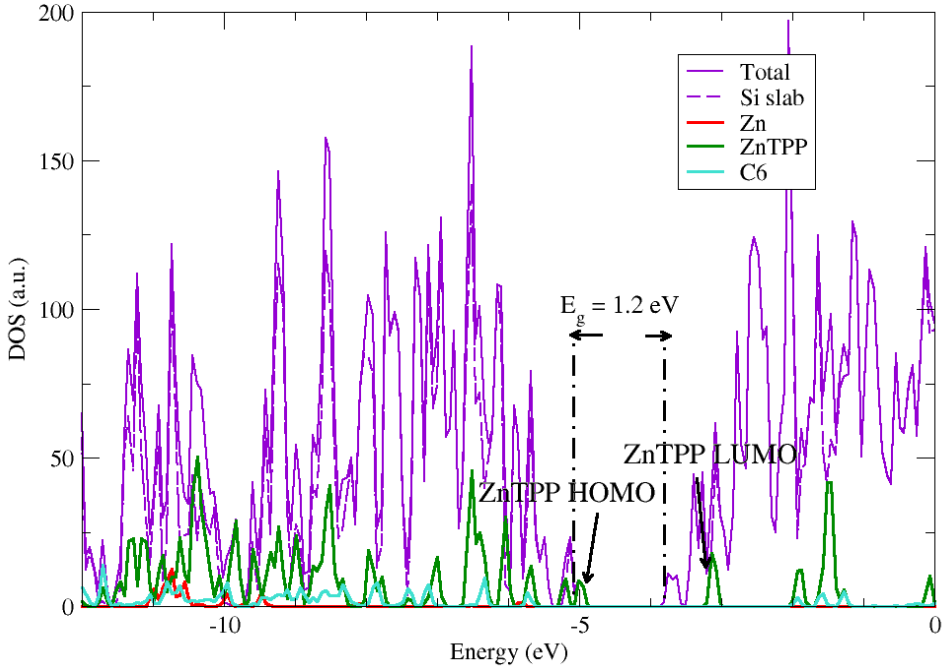

Figure IV.42. PDOS of Fc-N_3 $(CH_2)_6$ grafted

The total density of states in the case of C6 linker is mainly representative of the silicon slab as in the previous cases described above. The Si slab gap of approximately 1.0 eV can be recognized and is 0.2 eV less than the gap calculated for the slab alone. The surface contributes to all the states excepting some states in the gap, close to the effective VB of silicon. The PDOS confirms that the HOMO states belong to ZnTPP, more precisely to the carbon atoms of porphyrin. No changes in electronic structures of the surface or molecule were observed. The density of states of the molecule is not affected by the states of Si surface and is comparable to the isolated molecule.

For the charged (oxidized) species the PDOS were extracted and drawn below (figure IV.43).

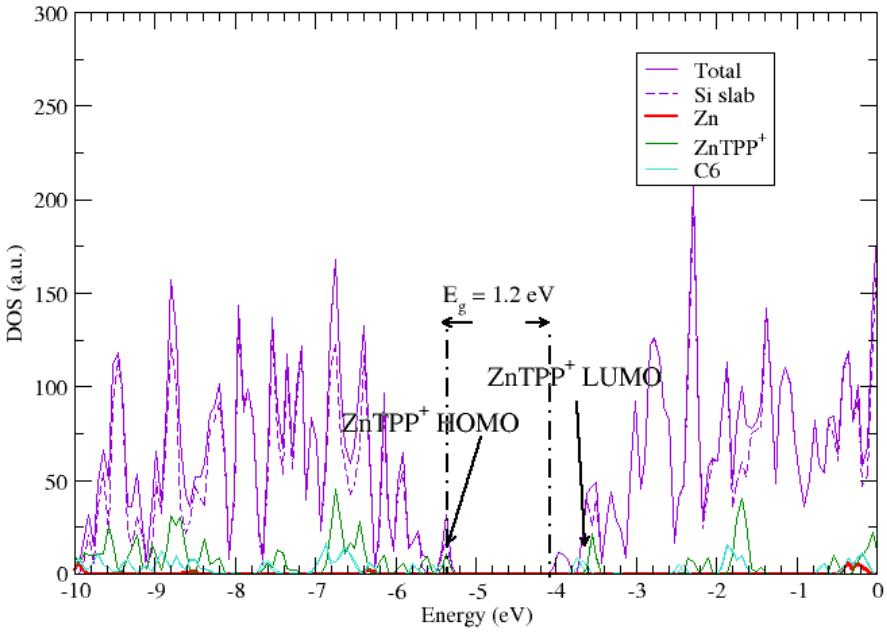

Figure IV.43. PDOS of Fc^{+}-$N_3(CH_2)_6$ grafted.

The usual shifting that appears for the charged species is present, due to the periodic boundary conditions where no absolute energy reference exists and to the loss of one electron. The HOMO levels of the molecules are shifted now inside the VB, and the contribution of the molecules energy states is very low in comparison with the neutral system.

As for molecular orbital diagram, the HOMO states are shared between the molecules and the VB of the slab. This arrangement indicates that a charge transfer between the molecule and the surface or vice versa is possible, by involving a hole in the valence band (p-doped substrate).

IV.4.3.3.2. The case of ZnTPP-$N_3(CH_2)_{11}$

In figure IV.44 is shown the minimized structure of ferrocene monolayers ZnTPP-$N_3(CH_2)_{11}$ grafted on infinite Si (1 0 0) surface. The surface is not affected by the presence of the molecule and the molecule seems to be stable on the surface, and doesn't collapse during the minimization procedure.

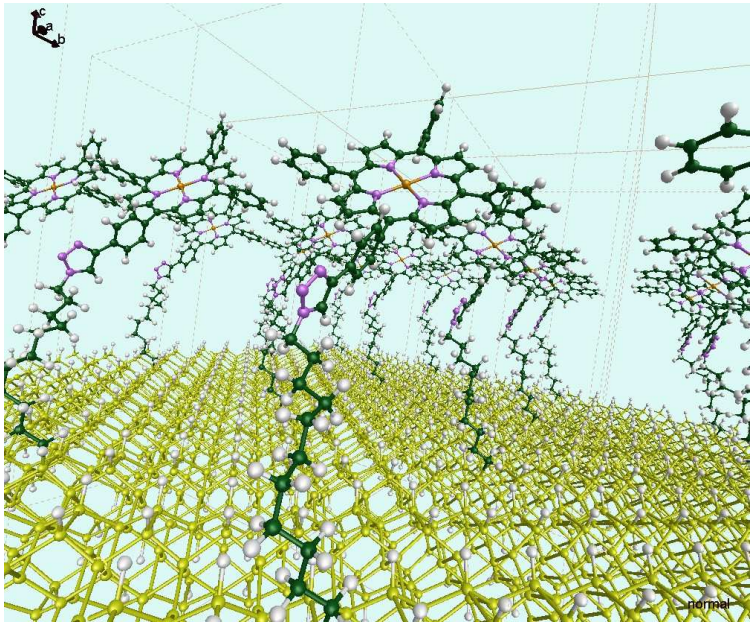

Figure IV.44. ZnTPP-$N_3(CH_2)_{11}$ monolayer grafted on infinite Si (1 0 0) surface

The resulting PDOS in reduced form are available in figure IV.45.

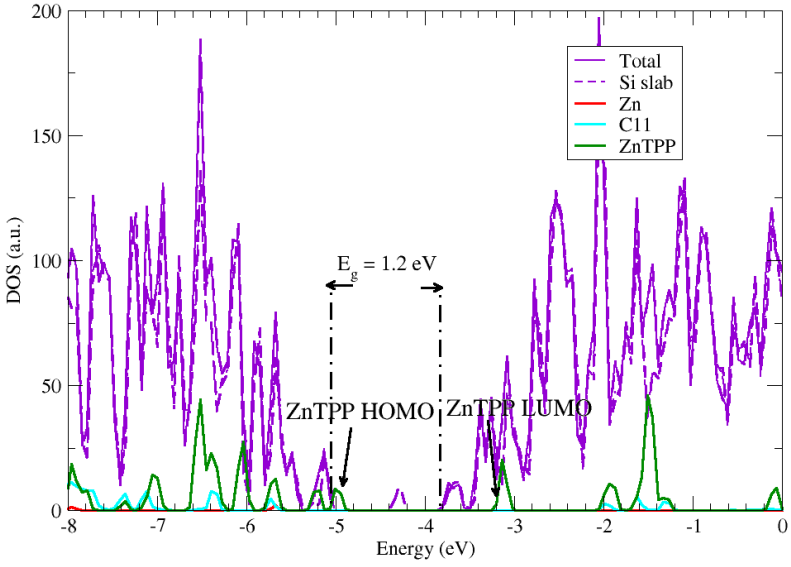

Figure IV.45. PDOS of Fc-$N_3(CH_2)_{11}$ grafted.

The states due to the Si slab contribute to all the states of the system, excepting some energy states around VB that correspond to ZnTPP molecules. A similar arrangement was

obtained as in the case of C6 grafting. The only difference is due to the Si states that appear in the middle. For the moment, no explanation for this behaviour was found.

As in the case of molecular orbital diagram description, the HOMO is localized on the ZnTPP molecule. As for all other species, there is no mutual influence of the density of states of the molecule and of the Si surface. The levels of the molecule are quite similar to those obtained with the molecular calculation.

For the charged (oxidized) species the PDOS are shown in figure IV.46.

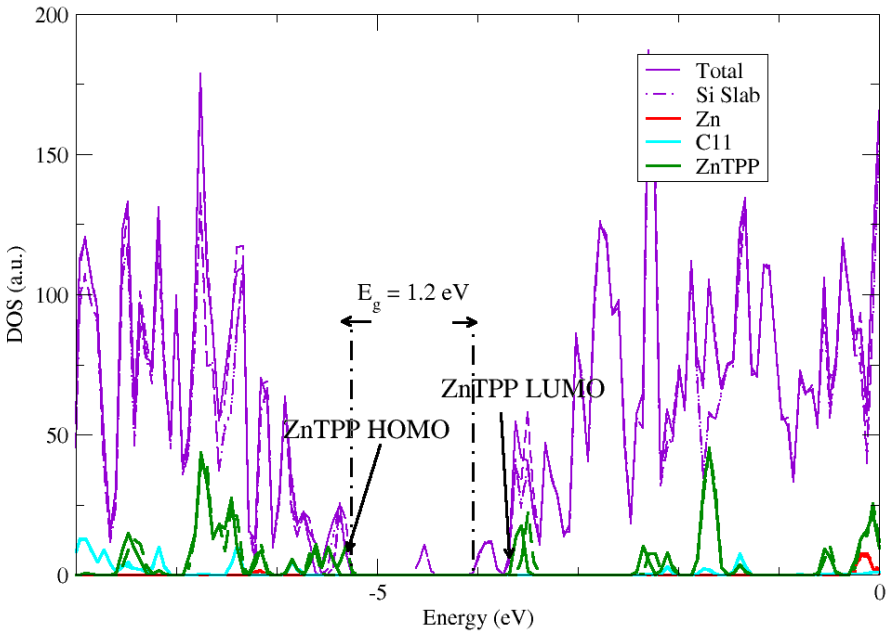

Figure 4.43. PDOS of $ZnTPP^{+}$-$N_3(CH_2)_{11}$ grafted.

As in the case of ferrocene grafted, the C6 and C11 DOS are quite comparable, and show that the main effect of the linker is to increase the energy between the HOMO level of the molecule and the valence band of the silicon slab for the neutral case by 0.7 eV approximately when compared to the vinyl case (direct grafting). For the charged case, the electron transfer is still possible and probably of the same nature that we explained above.

IV.4.3.3.3 Comparison of PDOS for direct and indirect grafting

In all cases, the HOMO of the molecule and the VB are very close in energies. The difference occurs on the LUMO states. The LUMO of the molecule appears deeply inside the valence band. One can conclude that the C6 and C11 linker are almost electronically neutral with respect to the active electronic states near the gap of the silicon slab. Although the gap between VB and HOMO of the molecule is almost zero, the gap between the VB and the LUMO in oxidized species increases with long chain/vinyl. We use the VB in both electron transfers because we refer to the p-doped silicon. Thus this could explain the shift between reduction and oxidation potentials that is experimentally observed.

A similar behaviour of the porphyrins grafted was observed by comparison with the ferrocene molecules grafted, either for direct or indirect grafting.

IV.5. Conclusions

Comparison between molecular and periodical calculations

The use of molecular systems with a small Si aggregate strongly increases the Si gap. But as the MO levels of molecule and Si are not mutually influenced, this does not affect the levels of the molecule. Simply due to a CB much too high in energy, the LUMO of the molecule becomes the LUMO of the whole hybrid system. The MO diagram is constituted by the simple superposition of MO of the molecule and MO of the Si aggregate. In the case of periodical calculations, the correct Si gap is obtained, and in fact this affects the LUMO state of Si which is now the LUMO of the whole system while the LUMO of the molecule lies higher in the CB.

Comparison with experimental data

The computed redox potentials agree very satisfactorily with experimental data, for ferrocene and porphyrin. We reproduce also the fact that it is slightly reduced for the hybrid system compared to the molecule in solution, either for ferrocene or porphyrin. The alignment of HOMO-LUMO and VB/CB of Si are able to correlate with the trends observed experimentally in the shifts between the potentials of oxidation and reduction, depending on the kind of linker.

Finally, the small model described by the DFT molecular approach seems to be able to reproduce the periodical calculations, except for CB of Si, and seems also to be correlated with the experimental data. We have some advantages due to the solvent calculations, which is mandatory in order to calculate redox potentials. Even if we used a very small aggregate of Si, it seems that we are representative in term of chemical reactivity and bonding for a Si (100) surface orientation.

Bibliography

[1] T. Rakshit, G-C. Liang, A. W. Ghost, M. C. Hersam, S. Datta, Phys.Rev.B 2005, *72,* 125305

[2] N. P. Guisinger, M. E. Greene, R. Basu, A. S. Baluch, M. C. Hersam, *Nano Lett.* 2004, *4*, 55

[3] Y. Xue, S. Datta, M. A. Ratner*, J. Chem. Phys*. 2001, *115*, 4292

[4] M. Cossi, M. F. Iozzi, A. G. Marrani, T. Lavecchia, P. Galloni, R. Zanoni, F. Decker, *Phys. Chem. Lett. B,* 2006*, 110*, 22961

[5] P. Siffert, E. Krimmel, *Silicon,* Springer-Verlag New York, 2008

[6] W. C. O'Mara, L. E. Hunt, R. B. Haber, *Handbook of Semiconductor Silicon Technology*, Elsevier Science & Technology Books, 1990

[7] R. Hull, *Properties of Crystalline Silicon*, Institution of Engineering and Technology, 1999

[8] J. Thomas, *Silicon*, Marshall Cavendish Inc, 2001

[9] J. Shoemaker, L. W. Burggraf, M. S. Gordon*, J. Chem. Phys*. 2000, *112*, 2994

[10] A. R. Brown, D. J. Doren, *J. Chem. Phys*. 1999, *110*, 2643

[11] D. Kienle, K. H. Bevan, G.-C. Liang, and L. Siddiqui, J. I. Cerda, A. W. Ghosh, *J. Appl. Phys*. 2006, *100*, 043715

[12] Y. M. Niquet, C. Delerue, G. Allan, M. Lannoo, *Physical Rev. B* 2000*, 62,* 8, 5109

[13] Y. M. Niquet, A. Lherbier, N. H. Quang, M. V. Fernández-Serra, X. Blase, and C. Delerue, *Phys. Rev. B* 2006, *73*, 165319

[14] M. P. Persson, H. Q. Xu, *Nano Lett*. 2004, *4*, 2409

[15] B. Boykin, G. Klimeck, F. Oyafuso, *Phys. Rev. B* 2004, *69*, 115201

[16] M. Weinelt, M. Kutschera, R. Schmidt, C. Orth, T. Fauster, M. Rohlfing, *Appl. Phys. A* 2005, *80*, 995

[17] D.J. Chadi, *Phys. Rev. Lett.* 1979, *43* (1), 43

[18] E. J. Baerends, ADF 2006.01. SCM, Theoretical Chemistry, Vrije Universiteit: Amsterdam, The Netherlands, http://www.scm.com.

[19] C. F. Guerra, J. G. Snijders, G. t. Velde, E. J. Baerends, *Theor. Chem. Acc.* 1998, *99*, 391

[20] G.t. Velde, F. M. Bickelhaupt, S. J. A Gisbergen, C. F. Guerra, E. J. Baerends, J. G. Snijders, T. J. Ziegler, *Comput. Chem*. 2001, *22*, 931

[21] A. Becke, *Phys. Rev. A* 1988, *38*, 3098

[22] J. P. Perdew, *Phys. Rev. B* 1986, *33*, 8822

[23] http://www.icmab.es/siesta/

[24] N. Troullier, J. L. Martins, *Phys. Rev. B*. 1991, *43*, 1993.

[25] J. Perdew, K. Burke, M. Ernzerhof, *Phys. Rev. Lett.* 1996**,** *77*, 3865

[26] G. P. Srivastava, Theoretical Modelling of Semiconductor Surfaces, *Singapore: World Scientific*, 1999

[27] PhD thesis of Tiziana Pro, CEA/LETI, 2009

[28] T. Pro, J. Buckley, K. Huang, A. Calborean, M. Gély, G. Delapierre, G. Ghibaudo, F. Duclairoir, E. Jalaguier, P. Maldivi, B. De Salvo and S. Deleonibus, *IEEE Trends. Nanotech.* 2009**,** *8*, 204.

[29] M-C. Kuo, L-A. Li, W-N. Yen, S-S. Lo, C-W. Lee and C-Y. Yeh, *Dalton Trans.*, 2007, 1433

[30] A. Wahab, M. Bhattacharya, S. Ghosh, A. G. Samuelson, and P. K. Das, *J. Phys. Chem. B* 2008, *112,* 2842

Chapter V
Molecular dynamics

Stability and endurance of the chosen organic molecules are of paramount importance in order to transform this technology from research to development and production. Both ferrocenes and porphyrins are well known to be very stable compounds at room temperature and ambient conditions. However, when these compounds are immobilized on Si surfaces, it is not the stability of molecules by themselves which is important, but that of the entire device consisting of the redox – active unit, the covalent bond that binds it to the surface and the electrolyte solution.

In this light, we have performed some molecular dynamics calculations for the ferrocene grafted on the Si surface for neutral and charged species. Some experimental results obtained by the CEA/LETI laboratory, in the group of B. De Salvo are shown first followed by the theoretical modelling.

V.1. Main experimental structural features

To study the thermal stability of the molecular layer, C-V and G-V tests were performed (at room temperature) on Fc directly grafted capacitors previously submitted to various annealing times and temperatures. Samples were exposed in a standard oven, in ambient. The baking time was fixed at $^1\!/_2$ hour. Figure V.1 shows that the Fc peak in C-V and G-V undergoes attenuation when the annealing temperature is increased [2]. This corresponds to a progressive degradation of the molecular layer, implying a reduction of the number of active Fc molecules on the Silicon surface. At 200°C the monolayer was completely damaged. Note that these experiments are in agreement with the fact that the melting point of Fc is 176°C [1].

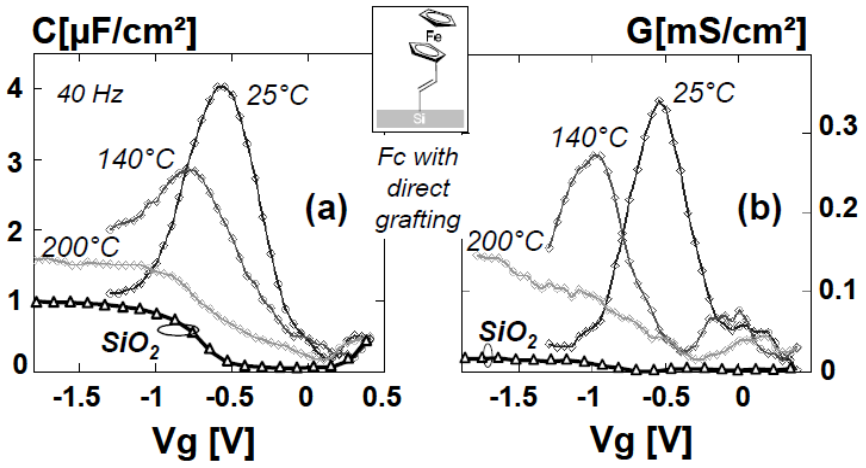

Figure V.1. C-V and G-V on capacitors with Fc directly grafted, previously annealed at room temperature (25° C), at 140°C and at 200°C.

V.2. Theoretical study

V.2.1. Theoretical method

In order to check the stability of our molecules grafted on silicon surface with a realistic coverage we have grafted one molecule every 21.72 angström, which gives a coverage of $2x10^{13}$ molecules/cm^{-2} close to the available experimental estimations at $6x10^{13}$ molecules/cm^{-2} we first have done simplified but accurate minimization of the forces between atoms, employing a conjugate gradient algorithm furnished as a standard within SIESTA. Yet conjugate gradient minimization are known to give easily local minima positions, allowing to investigate deeper the stability of the system at a certain temperature. Thus by doing molecular dynamics at room temperature for some time may help to explore any spontaneous transformation.

Nevertheless, doing molecular dynamics within DFT, at least in the (N V E) ensemble (microcanonical) for its easiness, is very time demanding because of the self-consistent cycles required at each step. So, managing DFT MD for more than a few picoseconds would require months of calculations. That's why we will restrict our self to a pico-second

or less, just to check the stability of the molecules under a spontaneous transformation at room temperature (like a collapse toward the surface for example). A deeper analysis, that is to say longer time scale (nano-second and beyond) would require at least a parameterized force field and/or a kind of a statistical sampling which is out of scope for our study.

All the calculations have been done with a time step of 2 fs, and an initial 400K temperature (Maxwell-Boltzman distribution), leading to a thermalization at approximately 300K due to partition of initial kinetic energy into remaining kinetic energy and some potential energy picked by the system.

V.2.2. Main results on ferrocene grafted

The MD calculations for the vinyl ferrocene grafted are shown in figure V.2.

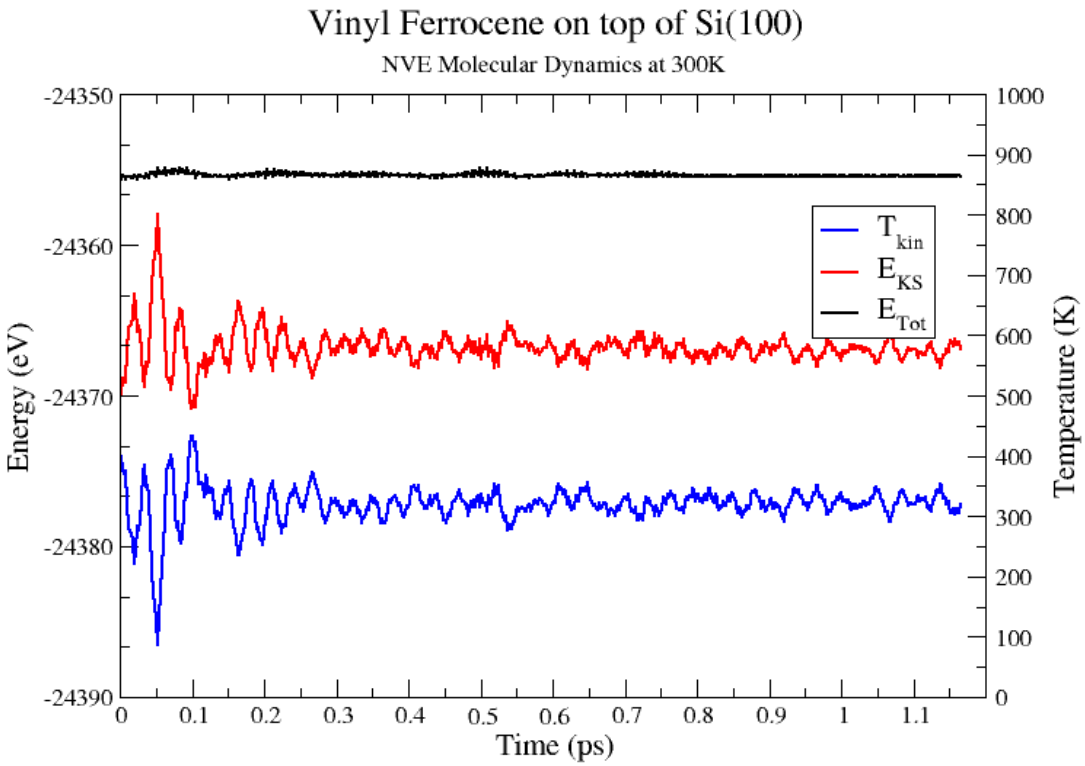

Figure V.2. MD energy oscillations at 300K of vinyl Fc

In the above diagram, the total energy is conserved at least for the five first digits, showing the appropriateness of the time step. The first oscillations – below 0.1 ps – show a typical and fast thermalization of the different freedom degrees of the ensemble, and then after the system is showing mainly atomic vibrations at a mean kinetic energy close to the room temperature. By performing a movie of the molecular dynamics positions, we can see that the main excited vibration modes are localized in the Si-H and C-H bonds, with also a small torsion of the cyclopentadienyle rings. But, globally, the whole ensemble seems to be stable against temperature at 300K.

The case of vinyl ferrocenium was also been investigated. The results are shown in figure V.3.

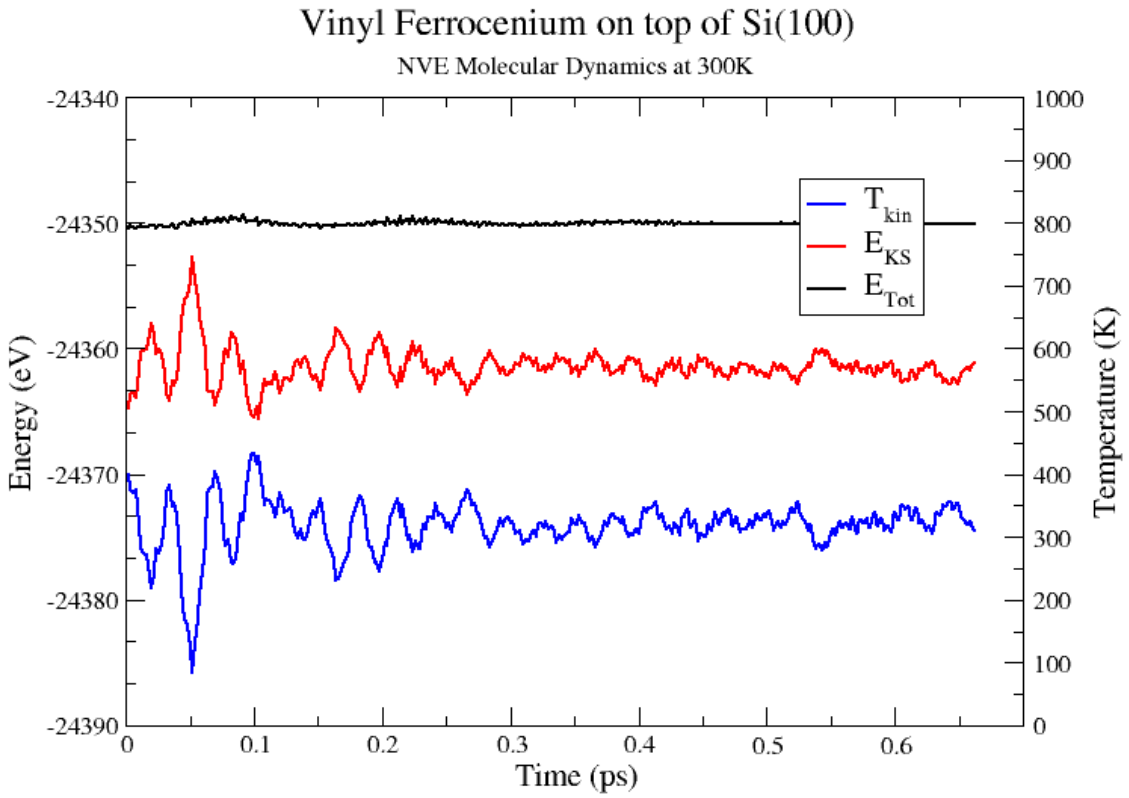

Figure V.3. MD energy oscillations at 300K of vinyl Fc^{+}

The overall situation is globally the same as before for vinyl ferrocene. The time scale is a little bit shorter (for neutral 1.2 ps while for charged is 0.8 ps) in comparison with neutral species due to a more demanding self-consistent cycle for the charged system. Also the

stability of the whole system is questionable due to the charged molecules; in fact in our simulation, SIESTA compensates the charge by a neutralizing background which violates the right treatment of the electrostatic. So, even if the system seems also to be stable after less than a picosecond, we need to mention that the electrostatic treatment is artificial between each molecule.

V.2.3. General trends

The two systems show a relative stability against typical room temperature thermalization on short time scale. This is consistent with experiment, even if it is not a full treatment of the stability question against experiment time scale, it shows at least that the molecules don't collapse spontaneously. Also, because hydrogen bonds seem to react firstly as shown by the D movies visualization (GDIS program was used), by increasing the temperature we should see some hydrogen desorption from the silicon surface – well known in microelectronic for temperature between 600 and 1300K depending on the gas pressure – but also the possibility to break some C-H bonds close to the Iron atom, which could destabilize the whole assembly. These could explain why the observed temperature range [3, 4] is quite low for such systems. A double rotation mechanism of the ferrocene molecule has been observed: one rotation of both cyclopentadienyl rings passing from eclipsed to staggered conformation and one rotation of molecule around the vinyl linker.
Because these calculations demand a lot of time and computational resources, these first calculations made on ferrocene directly grafted should be extended for all the systems that were studied in this work (indirect grafting with C6 and C11 linkers). Also the porphyrins molecules should be investigated in the same manner as ferrocenes.
These types of calculations can bring additional informations regarding the behaviour and stability of molecules on the surface under different temperatures.

Bibliography

[1] A. Salomon, T. Boecking, O. Seitz, T. Markus, F. Amy, C. Chan, W. Zhao, D. Cahen, A. Kahn, *Adv. Mater.* 2007, 19, 445

[2] PhD thesis of Tiziana Pro, CEA/LETI, 2009

[3] http://www.answers.com/topic/ferrocene

[4] M. J. S. Monte, L. M. N. B. F. Santos, M. Fulem, J. M. S. Fonseca, C. A. D. Sousa, J. Chem. Eng. Data 2006**,** 51, 757

Conclusions

We will give here the main objectives, challenges and questions that we wanted to adress in this work, and we will summarize our main findings, and the knowledge that we gained, first about theoretical approaches and secondly on the physical behaviour of the systems.

The present work was the theoretical contribution of a whole project devoted to the design and investigation of hybrid systems for future applications in information storage based on molecular functionalities, and using CMOS technology. This project, lead at the CEA-Grenoble (LETI and INAC), gathers several approaches from fundamental to applied research, and brings together experimentalists and theoreticians. Among the various aspects studied in this context, two were essential for molecular storage of information and its incorporation into CMOS devices: the structural behaviour of molecules under a redox process and the electronic properties of hybrid molecule-Si surface systems.
Our objective was thus to propose theoretical approaches, based on DFT methods best adapted to the issues mentioned above, and to bring helpful interpretations of experimental properties in the light of an electronic structure description. Thus all along this work we have always relied on all possible experimental data relevant to our calculations.

In a first part, we focussed essentially on molecular properties. The aim was to study molecules able to store charges through electron transfer, in particular when the redox process is supposed to induce a change in the structure (molecular redox bistability). It was thus crucial to have methods able both to predict correctly redox potentials for a variety of molecules and to reproduce conformational changes. This study was based mainly on ferrocene derivatives and metalloporphyrins. We showed that standard DFT

computations of redox potentials were in good agreement with experiments provided that a solvent was added (through the PCM method), even with the approximation of neglecting thermodynamic parameters such as the zero-point energy and the entropy changes. From our studies of various porphyrinic derivatives and their structural properties, we also were able to reproduce conformation energy barriers and to have a detailed analysis of their behaviours in various solvents. Unfortunately, the manganese (II) porphyrins need further investigations, and the correct description of the electronic structure is still a challenge at the DFT level, although thanks to CAS approaches, we should be able to solve this point.

The second part was dedicated to the description of molecules grafted onto a Si surface. The modeling of such systems was more challenging than the first part, due to their hybrid nature. Indeed, they combine the molecule - which properties are well localized in space - with a semiconducting surface which properties are essentially due to its periodical nature. This is reflected by the difficulty of finding a reliable univoque way of modeling the whole system. We have thus practiced two different approaches, one from molecular quantum chemistry, the second from periodical solid state calculations. We have isolated the main drawbacks of each method. The former needs to describe the Si surface by a more or less small aggregate: it gives accurate MO levels and allows to handle an environment as a solvent. The drawback is that the Si gap is wrong, with too high energy for the LUMO (≈ bottom of conduction band of Si). Nevertheless the increase in cluster size helps to decrease the Si gap essentially by decreasing the level of the LUMO. In turn, the HOMO and Si valence bands are quite close to what is obtained by periodical calculations. It gives quite good redox potentials (compared to experimental data), as the processes associated are localized on the molecule. It allows also to rationalize some differences in the alignment of gaps (molecule and Si) due to the different nature of the linker. The latter, i. e. periodical calculations, are less accurate to describe molecular levels and are unable to calculate redox potentials, but they give an *a priori* better description of the alignment of gaps. So it helps to scale the molecular calculations and to identify

possible problems about the wrong gap. In our case, both gave the same explanations about the difference in energy transfers due to oxidation and reduction processes. This is essentially due to the fact that we never have to take into account the conduction band, which position given by molecular calculations is clearly not correct. Also an underlying effect which certainly helps is that both groups of energy levels are not really mutually affected and are not coupled. So we can describe the total system as the superposition of two subsystems, the molecule and the Si part. Moreover, an interface electrostatic dipole of molecular origin can be described.

Finally, the conclusions that were drawn here will help to design more efficient simulations of such hybrid systems, and more particularly because we know better the pros and cons of each approach. Other molecular systems should be investigated, for instance with other charge transfer species. Moreover to go further in the description, the transport properties should be evaluated starting from our ab initio calculations that could probably serve directly as valuable inputs for future quantum transport calculations.
Finally, clearly some progress on the properties of potential bistable systems based on manganese II/III redox couple should be realized.

We will recall here the main objectives, challenges and questions that we wanted to adress in this work, and we will summarize our main findings, and the knowledge that we gained, first about theoretical approaches and secondly on the physical behaviour of the systems.

Thus we see that the ability to simulate molecular processes at surfaces - due to the interdisciplinary nature of this field of research at the intersection between chemistry, physics and material science - is thus still a challenge to our present day simulation capabilities.